
The evolution of protoplanetary disks in T Tauri binary systems

Sebastian Daemgen



München 2012

The evolution of protoplanetary disks in T Tauri binary systems

Sebastian Daemgen

Dissertation
an der Fakultät für Physik
der Ludwig-Maximilians-Universität
München

vorgelegt von
Sebastian Daemgen
aus Wuppertal

München, der 13. August 2012

Erstgutachter: Prof. Thomas Preibisch

Zweitgutachter: Priv. Doz. Achim Weiss

Tag der mündlichen Prüfung: 22. Oktober 2012

Contents

Abstract	xi
1 Introduction	1
1.1 Star formation in the Solar neighborhood	1
1.1.1 Observational signatures of T Tauri Stars	3
1.1.2 Young low-mass multiple stars	7
1.2 Protoplanetary disks and their evolution	9
1.2.1 The influence of stellar companions on circumstellar disks	10
1.2.2 A short note on planets in binaries	13
1.3 Open issues and the aim of this thesis	14
1.4 Structure and content of this thesis	15
2 Adaptive Optics spectroscopy	17
2.1 Close visual binaries: the need for high-spatial resolution spectroscopy	17
2.2 A short introduction to Adaptive Optics	18
2.3 Spectroscopy with Adaptive Optics	21
2.3.1 Long-slit spectroscopy with NACO	22
2.3.2 Integral field spectroscopy with SINFONI	24
3 Disk & star parameters of T Tauri binaries of the Orion Nebula Cluster	27
3.1 Observations and data reduction	28
3.1.1 Sample definition	28
3.1.2 NACO imaging: photometry and astrometry	30
3.1.3 Spectroscopy with NACO	34
3.1.4 NIFS-NIRI imaging and spectroscopy	40
3.2 Results	40
3.2.1 Extinctions and color-excess – the color-color diagram	40
3.2.2 Spectral types and veiling	44
3.2.3 Luminosity, effective temperature, and radius	47
3.2.4 Accretion: equivalent width, accretion luminosity, and mass accretion rate	50
3.3 Discussion	54
3.3.1 Stellar parameters and sample biases	54

3.3.2	Disk evolution around the components of visual ONC binaries	57
3.3.3	Is the existence of an inner disk linked to planet formation in binaries?	66
3.4	Conclusions	67
4	Disks and stellar parameters in Chamaeleon I binaries	69
4.1	Observations and data reduction	70
4.1.1	Sample definition	70
4.1.2	NACO imaging: photometry and astrometry	71
4.1.3	SINFONI H+K-band IFU spectroscopy	77
4.2	Results	82
4.2.1	The color-color diagram: photometric extinctions and color excesses	82
4.2.2	Spectral types, extinction & veiling	87
4.2.3	Effective temperatures & luminosities: the HR-diagram	94
4.2.4	Accretion	97
4.2.5	The new companion candidate to T 33 B	99
4.3	Discussion	100
4.3.1	Stellar parameters & sample biases	100
4.3.2	The evolution of disks in Cha I binary components	105
4.4	Conclusions	114
5	Binary disk evolution across different star-forming regions	117
5.1	The combined results from various star-forming regions	118
5.1.1	The decay of the disk frequency in binaries with age	118
5.1.2	Differential disk evolution	123
5.1.3	The independence of mass accretion rate and binarity	125
5.1.4	Binary disk evolution vs. planet formation	127
5.2	Summary	128
6	Conclusions & outlook	131
A	Statistical evaluation of the disk frequency	135
A.1	Derivation of the formulae	135
A.1.1	The probability density for k disks in n targets	136
A.1.2	The weighting factors $p(k D)$	136
A.1.3	Application to the ONC	139
B	Best-fit spectral templates	141
B.1	ONC K-band spectra and best-fit templates	141
B.2	Best fit spectral templates for all Cha I spectra	155
	Bibliography	171
	Acknowledgements	181

List of Figures

1.1	Star formation	2
1.2	Emission line spectrum of a T Tauri star	4
1.3	Near-IR excess in T Tauri stars	6
1.4	Disk fraction as a function of SFR age	10
2.1	Schematic diagram of an Adaptive Optics system	19
2.2	Slit losses as a function of FWHM	23
3.1	NACO H-band imaging of ONC binaries	31
3.2	Target component spectra	38
3.3	Color-color diagram of the ONC binary components	41
3.4	Equivalent widths of Na I and Ca I as a function of spectral type	45
3.5	Contour plot of χ^2 as a function of extinction and K-band excess	47
3.6	Example of spectral type fitting	48
3.7	HR-diagram of the ONC targets	49
3.8	Brackett-gamma equivalent width as a function of near-IR excess	51
3.9	Target component spectral types	54
3.10	Extinction in primary and secondary components	55
3.11	Relative ages of primary and secondary in ONC binaries	56
3.12	Binary separation as a function of component accretion type	59
3.13	Distance to Theta 1 Ori C as a function of accretion type	61
3.14	Mass ratios of ONC binaries vs. binary separation	62
3.15	Distribution of accretion luminosities	64
3.16	Mass accretion rates versus stellar mass	65
4.1	NACO Ks-band imaging of Cha I binaries	74
4.2	NACO Ks-band imaging of triples with unresolved components	75
4.3	NACO Ks-band imaging of the newly discovered binary T 33 B	75
4.4	Stellar PSF traced in SINFONI data cube	81
4.5	SINFONI spectroscopy of Cha I binaries	83
4.6	Color-color diagrams	86
4.7	Comparison of Cha I target components to dwarf and giant spectra	88
4.8	Willing's Q and I_{H_2O} index	89

4.9	Comparison of Cha I target components to dwarf and giant spectra	91
4.10	Spectroscopic versus photometric extinctions	94
4.11	HR diagram of Cha I target components with models of Siess et al.	95
4.12	HR diagram of Cha I target components with models of Palla & Stahler	96
4.13	Br-gamma absorption strength in dwarfs	97
4.14	Relative motion of T 33 Ba and Bb	100
4.15	Spectral types histogram	102
4.16	Primary versus secondary extinction	103
4.17	Primary age versus secondary age	104
4.18	Near-infrared excess $E(Ks-L')$ of primary and secondary components	107
4.19	Brackett-gamma emission vs. near-infrared color excess $E(Ks-L')$	108
4.20	Accretion status as a function of binary separation	109
4.21	Mass ratio as a function of binary separation	111
4.22	Mass accretion rate as a function of stellar mass	112
4.23	Mass accretion rate as a function of binary separation	113
5.1	Decay of accretion and inner dust disk frequencies of binary components with age	120
5.2	Accretion type as a function of binary separation	124
5.3	Mass accretion rate as a function of stellar mass for different SFR	126
A.1	Probability density function	136
B.1	Target spectra and best-fitting dwarf templates of ONC targets	141
B.2	Target spectra and best-fitting dwarf templates of Cha I targets	155

List of Tables

3.1	ONC targets and observations	29
3.2	Relative photometry and astrometry of the observed binaries	33
3.3	Non-resolved photometry of the observed binaries	34
3.4	Individual component apparent magnitudes	35
3.5	Spectral features identified in the observed spectra	37
3.6	Individual component properties	42
4.1	Cha I targets and observations	72
4.2	Individual component apparent magnitudes	78
4.3	Spectroscopic individual component properties	92
4.4	Equivalent widths of Brackett-gamma in dwarfs	98
5.1	Fraction of dust and accretion disks of binary components in different SFR	119
A.1	Accretion	137

Abstract

Binary stars are among the most common outcome of star formation. However, many details remain to be explored of how binarity influences the evolution of primordial circumstellar disks, the birthplaces of planets. Tidal interactions and irradiation can change disk geometries and lifetimes, dust properties, and thus the conditions for planet formation.

This thesis presents high-spatial resolution near-infrared photometric and spectroscopic observations of 52 visual multiple stars with projected separations of 25–1000 AU in the Orion Nebula Cluster and Chamaeleon I star-forming regions. It represents the largest coherent study of protoplanetary disks around the individual components of T Tauri binary stars in the two regions, and is among the largest of its kind in nearby star-forming regions to date. The data are used to infer individual stellar (e.g. effective temperature, luminosity, age, mass) and binary parameters (separation, component mass ratio). These are brought into context with disk parameters of each component: ongoing accretion is inferred from the strength of Brackett- γ emission and the existence of hot dust at the inner rim of the circumstellar disk is measured from near-IR excess emission.

The new results show a significant reduction of the frequency of accretion disks around binary components compared to single stars in the same regions. The effect is strongest in close binaries with <100 AU projected separation where the frequency of accretors among the binary components is less than $1/2$ of the single star accretor fraction. While these close systems also show a mild reduction of targets with hot circumstellar dust, wider binaries have a dust disk fraction comparable to single stars. The derived mass accretion rates were measured to not depend on the fact that stars are accompanied by binary companions at separations of ~ 100 – 1000 AU.

The new results are put into context with findings from the fields of star formation, disk evolution, and planet formation to derive the following conclusions: (a) Binary components form simultaneously. Capture is not the major binary formation process. (b) Disk evolution is accelerated in binary stars of separations <100 AU compared to single stars of the same mass. (c) Opposite to single star disk evolution, the disk around the less massive component has on average a shorter lifetime than the more massive component's disk. (d) While the lifetime of a disk depends on the diameter of a disk, mass accretion rates are independent of a disk's size and lifetime. A possible reason is a decoupling of inner and outer disk properties. (e) The correlation of disk and planet statistics around binary components supports a rapid formation of gas planets with masses $\gtrsim 1 M_{\text{Jup}}$ (through e.g. disk fragmentation) and a slower process (e.g. core accretion) for lower-mass planets.

Zusammenfassung

Doppelsterne gehören zu den am häufigsten gebildeten Objekten im Sternentstehungsprozess. Dennoch ist der Einfluss von stellaren Begleitern auf die Entwicklung zirkumstellarer Scheiben, dem Geburtsort der Planeten, bisher wenig verstanden.

Die vorliegende Arbeit beschreibt und diskutiert Nahinfrarotbeobachtungen von 52 stellaren Vielfachsystemen mit projizierten Abständen von 25 bis 1000 Astronomischen Einheiten (AE) in den Sternentstehungsregionen des *Orion Nebula Cluster* und *Chamaeleon I*. Damit handelt es sich um die größten homogenen Studien protoplanetarischer Scheiben in T Tauri-Doppelsternen in diesen beiden Regionen und um eine der umfangreichsten Untersuchungen dieser Art bisher. Die aufgenommenen Beobachtungsdaten erlauben die Bestimmung von individuellen stellaren (z.B. Effektivtemperatur, Leuchtkraft, Alter, Masse) und Systemparametern (Abstand der Komponenten, Massenverhältnis). Zusätzlich dient die Detektion von Brackett- γ -Emission als Anzeichen für aktive Akkretion während zirkumstellarer Staub in der inneren Scheibe mittels Nahinfrarotfarbexzess nachgewiesen wird.

Die Ergebnisse zeigen, dass der Anteil an Doppelsternkomponenten mit intakter Akkretionsscheibe signifikant geringer ist als der von Einzelsternen vergleichbarer Masse in beiden Regionen. In engen Systemen mit weniger als 100 AE projiziertem Abstand ist die Akkretionsscheibenhäufigkeit auf etwa die Hälfte des Einzelsternwertes reduziert. Heißer Staub in der inneren Scheibe ist in engen Doppelsystemen < 100 AE jedoch nur leicht verringert und für > 100 AE identisch zu der von Einzelsternen. Die gemessenen Massenakkretionsraten in Doppelsternkomponenten erweisen sich als ununterscheidbar von denen in Einzel- und Doppelsystemen anderer Sternentstehungsregionen.

Die gesammelten Daten lassen folgende Schlüsse zu: (a) Die Komponenten von Doppelsternen entstehen vorrangig gleichzeitig, was gegen *Einfang* ursprünglich isolierter Komponenten als hauptsächlichen Doppelsternenstehungsmechanismus spricht. (b) Scheiben in Doppelsternen enger als ~ 100 AE entwickeln sich, und verschwinden, schneller als Einzelsternscheiben. (c) Im Gegensatz zur Scheibenentwicklung in Einzelsternen ist die Lebenszeit einer Scheibe um die masseärmere Komponente eines Doppelsterns kürzer als die um den Primärstern. (d) Während die Lebenszeit einer Scheibe durch ihren äußeren Durchmesser (also indirekt durch den Doppelsternabstand) bestimmt wird, sind die Massenakkretionsraten universell. Dies ist ein Hinweis auf eine Entkopplung der Entwicklung der inneren und äußeren Scheibe. (e) Die Parallelen in der Häufigkeit von Scheiben um Komponenten von Doppelsternen und der Detektion von Planeten in vergleichbaren Systemen legt einen schnellen Planetenentstehungsprozess für massereiche ($> 1 M_{\text{Jup}}$) Gasplaneten nahe (z.B. *disk fragmentation*) und einen langsameren Prozess (z.B. *core accretion*) für masseärmere Planeten.

Sheldon: I'm a physicist. I have a working knowledge of the entire universe and everything it contains.

Penny: Who's Radiohead?

Sheldon: I have a working knowledge of the important things.

(The Big Bang Theory, CBS, 2009)

Chapter 1

Introduction

The question of how stars form is among the oldest questions asked by astronomers, and two facts seem to have crystallized from investigations over the last few decades: (a) a significant fraction of stars forms in binary systems and (b) at birth, almost every star is surrounded by a circumstellar disk¹. Accordingly, binary star formation and the evolution of their disks must be a significant part of stellar formation research and any comprehensive theory must be able to explain the observed binary star properties such as mass ratios, separations, and disk lifetimes. In addition to star formation itself, the disk material is the basic ingredient for planet formation. And although the existence of more than 50 planets in binary systems is known today, it is not clear how and why some of their characteristics are different from single star planets, like the observation that planetary masses are a function of binary separation (Roell et al. 2012; Duchêne 2010). Exploration of the preceding phase of circumstellar disk evolution will provide information about the conditions that planets experience when forming in a binary system.

In the following I will summarize part of what is known in the area of (multiple) star formation research in order to prepare the discussion of the topic of this thesis, *the evolution of protoplanetary disks in T Tauri binary systems*.

1.1 Star formation in the Solar neighborhood

There are a number of regions within the nearest few hundred parsec from the Sun that harbor large amounts of interstellar gas and dust. These *molecular clouds*, and the dense cores within, provide the location and basic ingredients for the formation of stars and planets. The fact that we can still observe high-density molecular clouds means that these regions have not yet lost all their material to the production of stars and planets or been blown away by strong nearby radiation sources. This, in turn, indicates the relative youth of stars associated with these particular regions, which are typically called *Young Stellar Objects* or YSOs.

¹irrespective of binarity

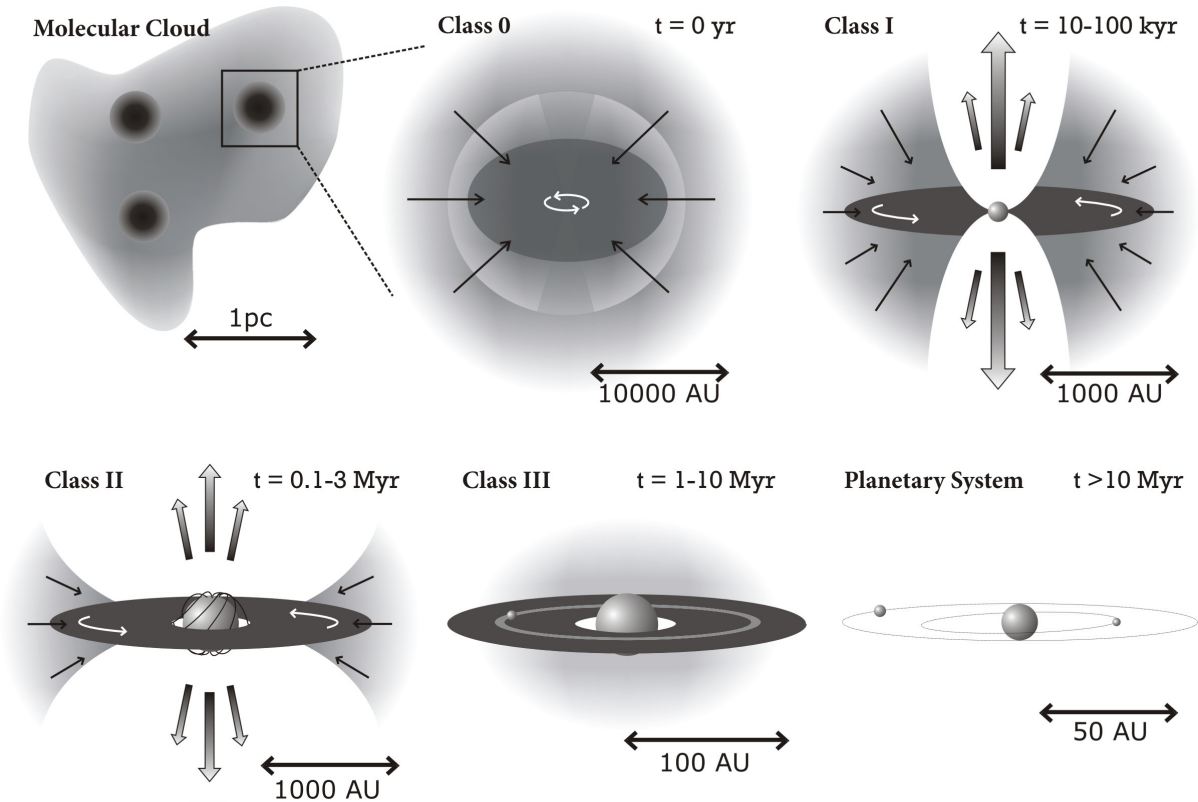


Figure 1.1: Principle stages of star formation as originally proposed by [Shu et al. \(1987\)](#) with the new classifications by [Lada \(1987\)](#) and [Andre et al. \(1993\)](#). Overdense regions in the molecular cloud collapse to a starless core (Class 0) which subsequently forms a protostar in its center (Class I). Through angular momentum conservation, any initial rotation will result in the formation of a disk around the forming star accompanied by strong outflows along the rotation axis. After a few hundred kyr the star becomes visible at optical and near-infrared wavelengths (Class II), surrounded by an optically thick disk. Outflows and accretion cease within a few Myr after the collapse and the star's circumstellar disk evolves to an optically thin disk (Class III) and a planetary system may form.

To name a few examples of nearby *star-forming regions* (SFR): molecular clouds in Ophiuchus, Taurus-Auriga, Chamaeleon, and Orion, in order of increasing distance to the Sun, have been targeted by a large number of studies to investigate the birth and early evolution of stellar and sub-stellar objects. Within these regions, the evolution from an initial so called *molecular cloud core* to a fully grown star can be described by a model first proposed by [Shu et al. \(1987\)](#) which was later refined and complemented by a number of follow-up studies (see [McKee & Ostriker 2007](#), and references therein).

The basic picture is sketched in Fig. 1.1. When part of the molecular cloud becomes gravitationally unstable, a runaway collapse process is triggered. To satisfy angular momentum conservation, any initial rotation of the cloud will cause the rapidly rotating infalling material to flatten to a disk-like structure around a dense proto-stellar core with potential for further fragmentation into a multiple star system. This stellar progenitor is

usually called a *protostar* or, after the classification scheme of Lada (1987) using infrared spectral slope indices², a *Class I* object. This stage is characterized by a stellar core surrounded by a disk of primordial cloud material, both of which are deeply embedded in a dense molecular cloud core. These objects, about 0.1 Myr after the initial cloud collapse, are often accompanied by strong outflows along the stellar rotation axis powered by the disk magnetosphere, the disk, or the star itself (e.g. Bouvier et al. 2007).

Until an age of 1–10 Myr, the continuing accretion of material from the envelope and disk will have cleared the surroundings of the young star to reveal the stellar photosphere to the observer. This is called the *Class II* stage and members of this class are named depending on their mass: stars with masses above $\sim 2 M_{\odot}$ and up to $\sim 8 M_{\odot}$ are called *Herbig Ae/Be* stars (see Herbig 1960) and stars of lower mass after their prototype T Tau, *T Tauri stars*, which was later refined to *classical T Tauri Stars* (CTTS). The latter show, in addition to possible outflows and a peculiar near-infrared signature caused by the combined emission from the stellar photosphere and a circumstellar disk (see Fig. 1.3), a wealth of strong emission lines. These are mostly from Hydrogen, but also Helium, Calcium, and a few weaker lines are seen in emission (e.g. Muzerolle et al. 1998b). The responsible mechanism, *magnetospheric accretion* (briefly outlined in Sect. 1.2), ceases within a few Myrs and leaves behind a *Class III* star that shows only a weak signature of circumstellar dust and weak emission lines. The designative name for low-mass stars of this category is “weak-line T Tauri Stars” (WTTS). The contraction of the central stellar object has now come to a halt, and the star nearly reached its final size and mass on the main sequence.

As T Tauri stars, both weak-line and classical, are the subject of this thesis, I will discuss them in further detail in the following Sect. 1.1.1.

1.1.1 Observational signatures of T Tauri Stars

The class of T Tauri stars was first phenomenologically defined by Joy (1945) and later refined by Herbig (1962) and Bastian et al. (1983) to contain highly variable late-type (later than *F*-type) stars with peculiar emission line spectra, associated with bright and dark nebulosity. In addition, it has been found that T Tauri stars, in particular WTTS can be associated with strong X-ray emission and high stellar rotation velocities on the order of $v \sin i \approx 10 \text{ km s}^{-1}$ (e.g. Pallavicini et al. 1981). A detailed physical explanation of all the phenomena at work is still part of current research, although first attempts to describe the basic principles of were made soon after their discovery (e.g. Lynden-Bell & Pringle 1974; Rucinski 1985; Hartigan et al. 1994, and references therein).

In the following I will discuss the observables of T Tauri stars in a little more detail and also give some background on the underlying mechanism of magnetospheric accretion.

² $\alpha_{\text{IR}} = d \log \lambda F_{\lambda} / d \log \lambda$ is measured between ~ 2 and $\sim 20 \mu\text{m}$. Class I: $\alpha_{\text{IR}} > 0$, Class II: $-1.5 < \alpha_{\text{IR}} < 0$, Class III: $\alpha_{\text{IR}} < -1.5$.

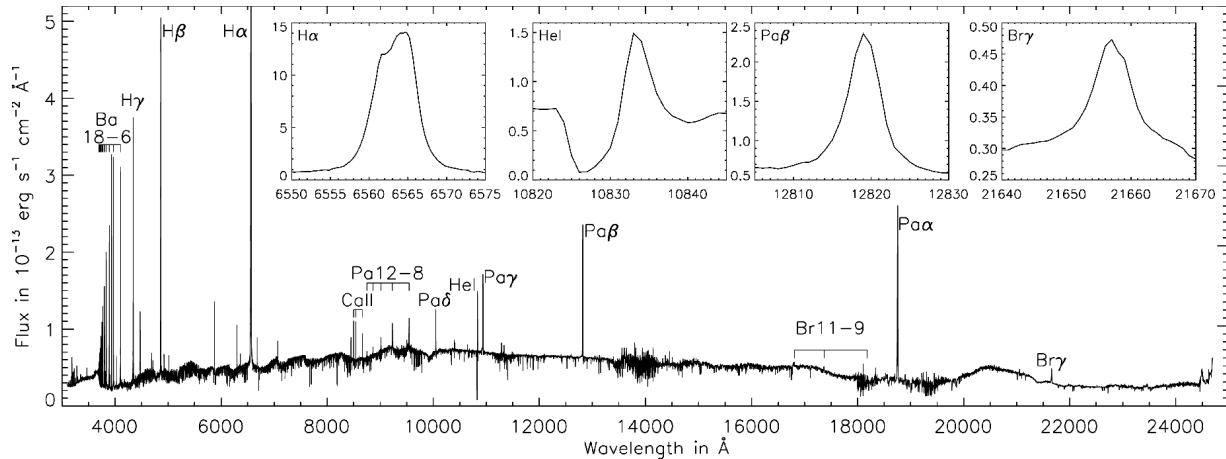


Figure 1.2: The star TW Hya observed with X-shooter as an example of a typical emission line spectrum of a CTT star in the optical and near-infrared wavelength range. (Figure from N. Rudolf, pvt. comm.).

Emission lines in T Tauri spectra: magnetospheric accretion

In Fig. 1.2 we see a typical representation of an emission line spectrum of a T Tauri star. The most prominent line is typically the Balmer- α or $H\alpha$ line at 6563\AA . Other lines frequently found in emission include hydrogen lines such as Paschen- β (12800\AA), and Brackett- γ ($\text{Br}\gamma$, 21665\AA), as well as Helium (HeI , 5876\AA), the Sodium doublet (NaI , 5890\AA), Oxygen (OI at 7773\AA and 8446\AA), and the Calcium triplet (CaII) at 8542\AA (Muzerolle et al. 1998b). The excitation of these to the strong levels observed is assumed to be a consequence of the accretion of disk material onto the star channeled along magnetic field lines.

As was inferred from the strong Zeeman broadening and circular polarization of magnetically sensitive lines, T Tauri stars are usually host to strong magnetic fields powered by a convective dynamo (Bouvier et al. 2007; Reiners 2012). The first measurements by Basri et al. (1992) found values of $\gtrsim 1\text{ kG}$ for the weak-line T Tauri star Tap 35 and many more measurements have been made in the meantime suggesting typical magnetic field strengths of several 100 Gauss up to values of more than 5 kG ⁽³⁾ (Reiners 2012; Bouvier et al. 2007). The existence of strong fields provides the basis to explain most of the observed features of T Tauri stars in the framework of *magnetospheric accretion*:

The associated dense magnetic fields sweep up the material in the inner disk and channel it along their field lines towards the stellar surface. The removal of disk material causes a truncation of the disk at the corotation radius, i.e., the radius at which the Keplerian velocity of circumstellar material is the same as the speed of the magnetospheric field lines which themselves are coupled to the stellar rotation. While material inside this radius is accelerated towards the star through gravitational attraction, material outside

³compare this to the Solar dipole field of a few Gauss and the maximum field strength inside Sun spots of up to 3 kG (Babcock 1961; Borrero & Ichimoto 2011)

the corotation radius is flung outward (Bouvier et al. 2007). The accreted gas – essentially freely falling from the corotation radius at a few stellar radii down to the stellar surface – is accelerated to very high velocities. The accumulated kinetic energy is finally radiated away as hot continuum emission when the material shocks at the stellar surface.

The effects of this mechanism are readily observable. (a) broad emission lines are produced by the fast-moving hot gas in the accretion flow and (b) continuum emission in excess of the stellar and disk emission, typically referred to as *veiling* since absorption lines in the stellar photospheric spectrum appear “filled up”, i.e., veiled. The very good match between the predictions of the magnetospheric accretion model and observations make this the currently favored model of accretion in T Tauri stars. Most previously proposed models such as “boundary layer accretion” (Lynden-Bell & Pringle 1974) appear to be obsolete. The inferred mass accretion rates from the magnetospheric accretion model are consistently on the order of 10^{-10} – $10^{-7} M_{\odot}\text{yr}^{-1}$ in the T Tauri star mass range (e.g. Natta et al. 2006).

H α as an accretion indicator. As emission lines are the most easily accessible feature of accretion, many studies use the equivalent width, or the width at 10% peak height, of H α emission. The use of H α is slightly compromised by the fact that emission is not purely generated by accretion but also by chromospheric activity. It has been found, however, that stable lower limits exist below which one can assume that emission is mostly of chromospheric origin and the line strengths above can be used to infer accretion. These are $\sim 5\text{\AA}$ for K-type, $\sim 10\text{\AA}$ for early M stars and $\gtrsim 20\text{\AA}$ for the H α equivalent widths of stars later than M5 (measured by Barrado y Navascués & Martín 2003 from H α measurements of T Tauri stars with no signs of accretion). These are the limits that can be applied to distinguish classical (i.e. accreting) from weak-line (i.e. not accreting) T Tauri stars.

The use of Brackett- γ as an accretion indicator. Accretion measurements in this thesis rely on the presence or absence of Br γ emission to decide whether a T Tauri star is still in the early phase of active accretion or already ceased to accrete and moved on to the subsequent weak-line T Tauri phase. The use of Br γ instead of the defining H α feature is necessary because of the observational constraints that apply to the observations in this thesis. While optical extinctions can be very high particularly in the centers of star forming regions, near-infrared observations can penetrate the dense interstellar material making it possible to observe young stars in more obscured parts of the cloud. Within the three near-infrared bands that are most easily accessible from ground-based observations (*J*, $\lambda_c^J=1.25\mu\text{m}$; *H*, $\lambda_c^H=1.65\mu\text{m}$; *K*, $\lambda_c^K=2.2\mu\text{m}$), Br γ is located in the latter band. Although it is known that the weaker strength of Br γ can cause false negative detections of emission, Br γ returns adequate information about the accretion characteristics of T Tauri stars (Antoniucci et al. 2011) and the resulting statistics can be corrected with information from multiwavelength observations covering more than one accretion indicator (see Sect. 3.3.2). A detailed comparison of different accretion indicators including Br γ can be found in Antoniucci et al. (2011).

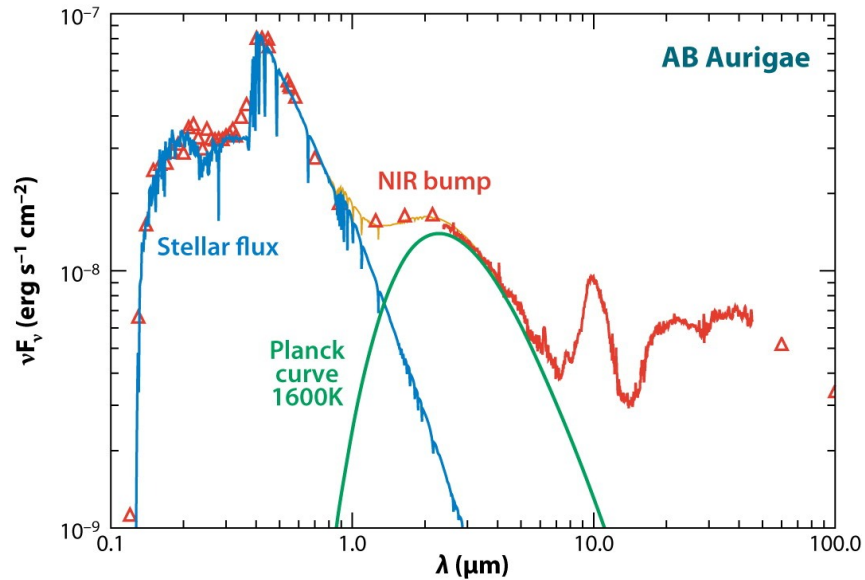


Figure 1.3: The near-IR spectrum of T Tauri and Herbig Ae/Be stars, illustrated here by the example of AB Aurigae. This shows the inherently composite nature of the spectrum consisting of a stellar part and a bump caused by hot (1600 K) dust at the inner rim of the disk (Figure from [Dullemond & Monnier 2010](#)).

Near-infrared excess

Although 99% of the disk material around a T Tauri star is made up of gas, the near- and far-infrared continuum radiation at $\lambda \gtrsim 2.3 \mu\text{m}$ is dominated by the signature of optically thick dust. The most prominent feature in this wavelength range is the near-infrared emission in excess over a pure stellar spectrum. Fig. 1.3 shows an example for such a spectrum, which can be described as a composite of a stellar spectrum and a ~ 1600 K blackbody. The extra radiation has its origin in the inner rim of the circumstellar dust disk. Inside the radius at which the temperature gradient imposed by the heating from the central star exceeds the sublimation temperature of the highly abundant primordial silicates⁴ (~ 1600 K, [Duschl et al. 1996](#)) the disk becomes optically thin. This is equivalent to the existence of an inner hole in the dust disk – first proposed by [Bertout et al. \(1988\)](#) – of a few tenths of AU in size. An inner hole also explains why most T Tauri stars show radiation from a disk *and* the stellar photosphere, independently of the viewing angle onto the disk. Only in the few cases where the disk is viewed almost edge-on, the stellar light suffers from high extinctions when passing radially through part of the disk material.

Observationally, near-infrared excess can be easily detected by the characteristic colors of T Tauri stars. [Meyer et al. \(1997\)](#) found that the dereddened colors of their sample of 30 classical T Tauri stars align tightly around straight lines in $(J-H)-(H-K)$ and $(H-K)-(K-L)$ color-color diagrams respectively. This distinguishes them from weak-line T Tauri

⁴The disk composition is assumed to be initially approximately that of the interstellar medium

stars which lie close to the dwarf locus. Representations of these linear relations called *Classical T Tauri Star locus* or *CTTS locus* are shown in Figs. 3.3 and 4.6.

Photometric variability

As was noticed already in the original definition by Joy (1945), T Tauri stars are subject to strong and mostly irregular variability on timescales from hours to months and years. This is true for the broad-band photometry at all wavelengths (radio to X-ray) as well as for the superimposed emission features. On top of a periodic signal due to star spots and modulated by stellar rotation, the reason for this type of variability is stellar youth apparent through coronal flaring and variable accretion and/or extinction (Herbst et al. 1994).

The extensive simultaneous multiwavelength studies of Carpenter et al. (2001, 2002) find that the bulk of T Tauri stars shows photometric variability on the order of 0.2 magnitudes in JHK_s and ~ 0.05 mag in the respective near-infrared colors. The long term *ROTOR* study of 72 CTTS over 20 years by Grankin et al. (2007) find a similar picture in the optical: wavelength range variability of CTTS is typically $\lesssim 0.4$ mag in V band. Similarly, accretion signatures vary. For example, Nguyen et al. (2009) show for the $H\alpha$ 10% width and $\text{Ca II-}\lambda 8662$ that the derived mass accretion rates vary on the order of 0.35–0.65 dex.

While variability can be used to identify young stellar objects, it also makes observations more complex. Only simultaneous observations can guarantee a proper derivation of, e.g., colors and their correlation with accretion features. And only repeated measurements can reveal the range of values that the parameters of a particular target can assume. Whenever observations at different epochs are taken, one has to account for the possibility that the star under consideration is in a state of weak or strong accretion and the derived numbers may not reflect its typical or average activity.

1.1.2 Young low-mass multiple stars

In their seminal studies, Duquennoy & Mayor (1991), Fischer & Marcy (1992), and Raghavan et al. (2010) determined the parameters of solar-type and lower-mass main-sequence multiple stars. Around half of all G-type and 42% of all M-type stars are found to be multiples with typical separations between a few and a few hundred AU with a slight tendency towards more equal mass components with decreasing primary mass. The picture of young stars in nearby clusters and associations is similar to some degree, though with a few peculiarities owing to the partly dense stellar environment and the dynamically young state of star forming regions.

Multiple stars in nearby star-forming regions

The existing high-spatial resolution binary surveys of a number of star-forming regions draw a partly inhomogeneous picture. While some regions such as the Orion Nebula Cluster

(ONC) and Lupus show companion star fractions that are comparable to the fraction in the field (in the same separation and spectral type range, [Duchêne 1999](#)), others including Taurus-Auriga and Ophiuchus show binary fractions that are up to twice as high ([Leinert et al. 1993](#); [Prosser et al. 1994](#); [Brandner et al. 1996](#); [Padgett et al. 1997](#); [Petr et al. 1998](#); [Duchêne 1999](#); [Köhler et al. 2006](#)). Furthermore, mass ratios seem to vary from one region to another and there is evidence for a radial dependence of binary parameters on the distance to the densest parts of star forming clusters. For example, while typical binary separations are ~ 40 AU in nearby star forming regions ([Simon et al. 1995](#)), binaries in the center of the Orion Nebula Cluster appear to be, on average, tighter than their counterparts in the cluster’s outskirts ([Reipurth et al. 2007](#)). Some of these observations can be explained by the increased chance of dynamical interactions with other cluster members or with passage through the gravitational potential well in the cluster center. Others are likely a direct consequence of the formation process of these “dynamically young” multiple stars which have had only little time for interaction after their formation in regions of low stellar density.

In addition to binaries (i.e. multiples consisting of 2 stars) higher-order multiples also exist in significant numbers. For example, [Correia et al. \(2006\)](#) find 7 triples and 7 quadruples among their 52 observed systems in several star forming regions. For reasons of dynamical stability, these multiples often take the form of *hierarchical* multiples, i.e., they consist of a close binary system orbited by a wide component which itself can be multiple. In the further course of this thesis, I will usually not make a clear distinction between binaries and higher-order multiples since the hierarchy allows me to treat, e.g., triples as two binaries: the close binary system and another binary consisting of the combined close system and the wide tertiary component.

The formation of multiple stars

From the observation that we find at least as many binaries in young star-forming regions as in the field we can infer that binary formation must have happened before an age of at most a few Myr. However, the mechanisms at work are not yet understood. Since the details of binary star formation do not have direct consequences for the results of this thesis they will not be discussed in depth here. I will give only a short summary of the current scenarios and the interested reader is recommended to consult the comprehensive review by [Tohline \(2002\)](#) or, more recently, [Goodwin et al. \(2007\)](#).

The main mechanisms proposed to explain the currently observed population of binaries are *capture*, *prompt breakup*, and *delayed breakup* as well as variations thereof. While capture of an initially unrelated body appears to be too inefficient to be responsible for the high binary fraction observed, the currently preferred mechanism is that of prompt breakup, i.e. direct cloud fragmentation into multiple bodies which can be further divided into rotational and turbulent fragmentation. Delayed breakup, in contrast, implies the formation of an initially stable central object which fragments at a later stage due to subsequently emerging instabilities. Due to the complex physics involved, currently no

simulations can reproduce all observed binary parameters and it is up to future studies to prove either mechanism to be more or less likely at work in multiple star formation.

Observational evidence with implications for the binary formation process comes, for example, from optical and near-infrared studies. The high fraction of binaries with coeval components, deduced by comparing component luminosities and effective temperatures with theoretical isochrones, is a clear indication for simultaneous formation through fragmentation (e.g. Hartigan et al. 1994; Brandner & Zinnecker 1997; White & Ghez 2001; Kraus & Hillenbrand 2009). Furthermore, there are indications that grain evolution is indeed similar for both components of a binary (Skemer et al. 2011), again suggesting simultaneous formation of all binary components during the same process.

1.2 Protoplanetary disks and their evolution

In addition to the mostly phenomenological definition in the last section it will be fruitful to discuss the physical properties of T Tauri stars a little bit more. As it is the most striking characteristic of the class of T Tauri stars, I will focus here on the circumstellar disk. The evolution and lifetime of primordial circumstellar disks is particularly worthwhile to discuss since it not only reflects the timescale for the formation of the star itself, but it also dictates the maximum time available for planet formation. An alternative name for *circumstellar disk* which does justice to the fact that planets may form from the primordial disk material (see e.g. Sect. 1.2.2) is *protoplanetary disk*. Both terms will be used synonymously in the following, however with a preference for “protoplanetary” when the formation of planets is discussed.

We learned briefly in Sect. 1.1 that disks are formed in the early evolution of a star to satisfy angular momentum conservation during collapse. First direct imaging evidence that circumstellar material actually takes the shape of a disk came from observations with the *Hubble Space Telescope* (HST) which shows dark disk-like structures in front of the bright nebular background of the Orion Nebula (O’Dell et al. 1993; McCaughrean & O’dell 1996). The exact distribution and evolution of material in these disks has since been discussed in many theoretical studies (Dullemond & Monnier 2010, and references therein).

Optical, near-infrared, and sub-mm observations seem to have secured the following facts about protoplanetary disks: (a) initial disk masses are correlated with the central star mass with typical values of $M_{\text{disk}} \approx 100M_{\oplus}$ (Natta et al. 2000; Wyatt 2008), (b) disk sizes are typically found to be on the order of a few ten to a few hundred AU (Dutrey et al. 1996; Vicente & Alves 2005; Williams & Cieza 2011), and (c) disks have lifetimes of at most ~ 10 Myr (Haisch et al. 2001; Fedele et al. 2010). The latter fact is nicely visible in Fig. 1.4. It suggests an exponential decay of disk frequency with cluster age with a time constant of $\sim 2\text{--}3$ Myr.

It should be emphasized again that a disappearing near-infrared signature provides information only about the absence of an *inner* disk. It has been shown, however, that the presence of an inner disk is well linked to detections of the disk at longer wavelengths probing the disk on AU scale (mid-IR) and the total disk material (sub-/mm) (Cieza et al.

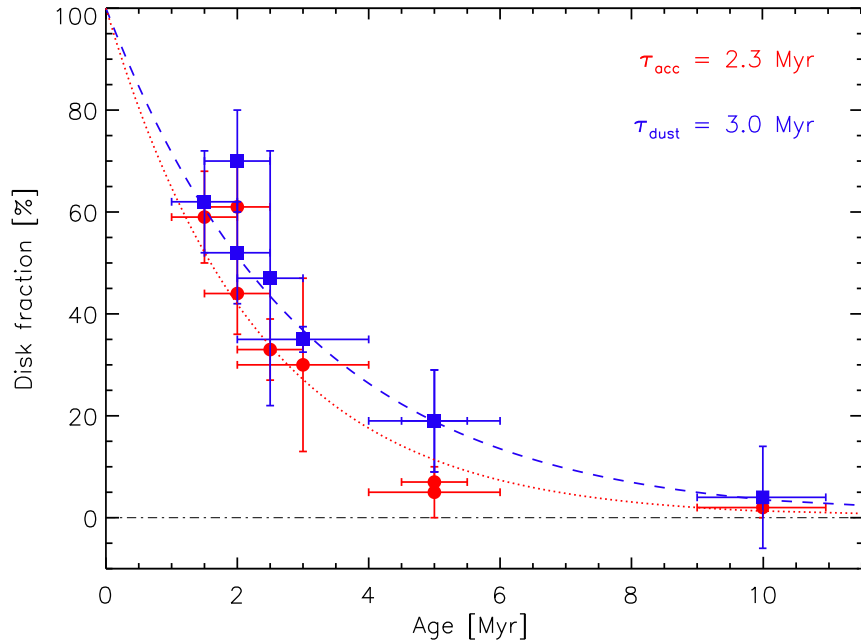


Figure 1.4: The decay of disk frequency with the age of the star-forming region. Blue squares show the fraction of objects with IRAC [3.6]–[8.0] excess in each star-forming region, indicating the presence of hot dust in the inner disk. Red circles show the fraction of targets with H α excess, i.e., ongoing accretion. The blue dashed line and red dotted line show the best fit exponential decay to the two distributions (after Fedele et al. 2010).

2007; Andrews & Williams 2005). The conclusion from the combination of observations at different wavelengths: After the formation and evolution of a disk over a timescale of up to 10 Myr the disk disperses very rapidly within less than 0.5 Myr (Cieza et al. 2007). Predictions of the onset of disk dispersal for an individual target cannot yet be made and it remains unclear why some stars lose their disk already before an age of 1 Myr and some retain their disks up to several times this age.

1.2.1 The influence of stellar companions on circumstellar disks

The most striking impact of a stellar companion on the evolution of a circumstellar disk is the truncation of the disk through tidal interaction. This was first theoretically discussed by Papaloizou & Pringle (1977) and Artymowicz & Lubow (1994) who derive a maximum outer disk radius that is roughly 1/3 of the binary separation for an equal mass binary⁵ with vanishing orbital eccentricity.

Despite the seemingly simple direct consequence – a smaller than usual circumstellar disk – the implications of stellar binarity for disk evolution are complex and mostly lack confident predictions by theory. To explore the implications of the existence of stellar

⁵For mass ratios $q < 1$, the primary disk is a bit larger and the secondary disk a bit more strongly truncated.

companions to disk-bearing stars, observational evidence was gathered in a number of recent studies. Most of these rely on rather small samples or are compiled from heterogeneous sources that make an interpretation difficult. Though, building on this evidence new studies, including the present thesis, will help to substantiate (or invalidate) the following hypotheses with better statistics.

The evolution of the *inner* disk in binaries

A lot of our knowledge about the evolution of circumstellar disks comes from optical and near to mid-infrared studies of spatially resolved and unresolved binaries. These provide information mostly about the innermost parts of the disk, less than a few AU from the star, where the high temperatures and ongoing accretion processes produce significant radiation in the 0.5–20 μm regime. These inner disk surveys can stand on their own but can also be interpreted with respect to the finding that the existence of an inner disk is in general correlated with the existence of dust material in the outer disk (Andrews & Williams 2005).

T Tauri binaries come in all combinations of disk/no-disk. The absence of T Tauri binaries with only one component surrounded by a disk, as inferred from the accretion indicator Bry and from $K-L$ excess, led Prato & Simon (1997) to the conclusion that mixed systems are rare. Although this was shortly later confirmed using H α (Duchêne et al. 1999), both studies suffered from small sample sizes and possibly from observing a star forming region (Taurus) that is not representative for the general evolution of disks in binaries. As was discussed by Monin et al. (2007), Taurus does show a slightly lower fraction of mixed pairs than other regions ($\sim 10\%$ of Taurus binaries are mixed), but in general a high abundance of mixed pairs of around 20% was found by larger studies in several regions and with good statistics (White & Ghez 2001; Hartigan & Kenyon 2003; Prato et al. 2003).

Disks in binaries are shorter lived. As expected by theory (see considerations in e.g. Monin et al. 2007), it was observed that close binaries lose their disks earlier than wide binaries and single stars. This was inferred from the observation that only few binaries with separations $\lesssim 40$ AU show signs of disk presence (Bouwman et al. 2006; Cieza et al. 2009; Kraus et al. 2012). Under the likely assumption that there is no systematic preference for binaries to form earlier than singles in the same cluster, disk evolution in most close binaries must have finished already before an age of ~ 1 Myr, while single stars were found with disks up to much longer timescales of several Myr. Interestingly, 1/3 of all close binary components do not lose their disk early. Part of these can be explained by the fact that usually only minimum (projected) binary separations are known and the factual binary separation is much wider than it appears. Other proposed mechanisms are the feeding from circumbinary reservoirs or the same, currently unexplained, process that determines why some single star disks disappear after 1 Myr and others only after 5 Myr.

Despite shorter observed disk lifetimes, Monin et al. (2007) argue that planet formation in binaries is still possible, which corroborates with the discovery of planets in close binary systems with separations as small as 20 AU (Eggenberger & Udry 2010, see also Sect. 1.2.2).

The disk around the less massive component disappears first. The number of mixed pairs with an accreting primary was found to be significantly higher than the number of mixed pairs with an accreting secondary (White & Ghez 2001; Monin et al. 2007). Considering that the components of a binary are usually coeval (Hartigan et al. 1994; Brandner & Zinnecker 1997; White & Ghez 2001; Prato et al. 2003; Kraus & Hillenbrand 2009), this can be used as an indicator that disks around the less massive binary component evolve faster than primary disks. Although this is against the trend that less massive single stars retain their disks for longer (Carpenter et al. 2006), it might be explained by the more severe truncation of the less massive components' disks and a consequential earlier disk exhaustion. Alternatively, it could be that some observational studies are biased by the possibility that the more massive primaries are stronger accretors (White & Ghez 2001) and thus more easily detected. The trend for more strongly accreting primaries, however, was not confirmed by all subsequent studies (e.g. Prato et al. 2003).

Disk parameters co-evolve in binary components. Similar to the observation that binary components are of similar age, it was also observed that other disk-related stellar parameters are more similar between the components of a binary than between randomly paired single stars. Optical and near-infrared studies find that accretion luminosities, mass accretion rates, near-infrared excess, and dust grain evolution are similar between the components of binaries at all separations (Hartigan & Kenyon 2003; McCabe et al. 2006; Skemer et al. 2011).

Another observation was made by White & Ghez (2001), who find that close systems with separations < 200 AU are less often mixed pairs than wider binaries. This leads to the interpretation that disk evolution is synchronized in close systems, while in wide systems it is not. Explanations for this phenomenon range from a similar angular momentum distribution at birth to feeding of the individual disks from a circumbinary reservoir.

Mass accretion rates show no dependence on binary parameters. The mass accretion rate inferred from H α observations by Hartigan & Kenyon (2003) suggest that there is no difference between components of binary stars and singles. Another surprising result given the rather different environment that a truncated disk poses to the sustainment of a disk. The interpretation of this observation is difficult (see also Question 3 in Sect. 1.3).

The cold outer disk material in binaries

There are a few studies that use sub-/mm observations to assess the evolution of the cold outer disk material in binary stars. Since spatially resolved observations of close binaries are difficult to obtain for a significant number of binaries, most of the previous studies observe cold dust and gas with no information about whether the circumstellar material is located around either binary component or in a circumbinary reservoir. Only very few and recent studies acquired spatially resolved radio data for a large number of targets.

The early, though spatially unresolved study of Osterloh & Beckwith (1995) finds for a sample of around 50 T Tauri binaries that 1.3 mm emission from close (< 100 AU sepa-

ration) binary stars is significantly weaker than from wider binaries and single stars. This finding is in good agreement with the expected truncation of disks through tidal interactions and was confirmed by studies of [Andrews & Williams \(2005\)](#) and [Harris et al. \(2012\)](#). In addition to component disk truncation, [Jensen et al. \(1996\)](#) find that the mass of circumbinary disks around < 100 AU binaries can be at most $\sim 5 M_{\text{Jup}}$, although a few exceptions with circumbinary disks of higher mass do exist (e.g. GG Tau, [Dutrey et al. 1994](#)).

A recent study uniquely capable of assessing the differential evolution of disks in binaries was published by [Harris et al. \(2012\)](#), who present high-spatial resolution sub-/mm interferometry of 23 binaries in Taurus, 14 of which have spatially resolved disk detections. Surprisingly, the measured individual disk sizes do not agree with theoretical predictions of tidal disk truncation. This indicates that not only truncation but also other processes (for example accretion) must be involved in the determination of disk parameters like their size.

1.2.2 A short note on planets in binaries

If the conditions imposed on a circumstellar disk by the presence of a stellar companion are not entirely hostile to planet formation, we expect to see at least some binaries with planetary systems. Owing to the efforts of several dedicated observing programs (e.g. [Eggenberger et al. 2007](#); [Daemgen et al. 2009](#); [Eggenberger & Udry 2010](#); [Muterspaugh et al. 2010](#); [Roell et al. 2012](#)), we know of more than 50 stellar binary systems which are host to planets (for a recent list see [Roell et al. 2012](#)) and an additional number of new candidates will likely come from the evaluation of recently acquired data from the Kepler satellite (see e.g. [Adams et al. 2012](#)). Since most of the properties of these planets are determined during their formation, they must reflect the conditions in the circumstellar disk. Hence, studying the population of planets in binaries will contribute additional information about disk evolution in binaries.

While many interesting studies of planets in binaries were published in the recent years, I would like to focus on one interesting finding in particular. More information can be found in the short discussion in Sect. 3.3.3 and, e.g., the article by [Eggenberger & Udry \(2010\)](#).

[Duchêne \(2010\)](#) compiled the projected separations and minimum planet masses of all planets found around a binary component known at the time. The striking feature in the $m \sin i$ -separation diagram is the absence of close (< 100 AU) binaries with planets below $1 M_{\text{Jup}}$. Although an observational bias cannot be ruled out completely⁶, this observation can possibly give information about the planet formation process in binaries. Together with the finding that in close binaries the disk evolution timescale is shorter than in wide binaries, this could point to a different formation process for high- and low-mass planets respectively. For example, if low-mass planets are formed by a rather slow process (like core accretion, see e.g. [Pollack et al. 1996](#)) and higher mass planets are formed before the

⁶The detection of planets in binaries with the radial velocity technique is particularly difficult in close binary systems and the signature of low-mass planets may remain hidden in the binary signal.

rapid dispersal of close binary disks (e.g. via gravitational instability, [Boss 1997](#)), then this signature would be expected. With the currently rapid increase of highly sensitive observations targeting planets and disks it will soon be possible to place strong constraints on the planet formation process in binaries and thus planet formation in general.

1.3 Open issues and the aim of this thesis

The previous sections give a brief summary of today’s knowledge about the formation and evolution of protoplanetary disks in low-mass binary stars. The current picture of binary star formation, however, is still incomplete and ever evolving. This thesis presents the largest spatially resolved study of T Tauri binaries in a clustered star forming region, the Orion Nebula Cluster, and the most complete study of inner disks around binary components in Chamaeleon I. It aims at addressing some of the currently open questions that naturally arise from the increasing set of observations and theoretical expectations about stellar formation with focus on multiple systems. In particular, I will address and attempt to answer the following items:

■ **Are disks around components of visual T Tauri binaries in the ONC and Cha I shorter-lived than single star disks?**

The presence and properties of disks around single stars in nearby star-forming regions including the ONC and Cha I have been subject of many previous studies. The derived fractions of single star accretors of $\sim 50\text{--}55\%$ in the ONC and $\sim 44\%$ in Cha I agree well with the suggested decay of disk frequency in [Fig. 1.4](#). The inferred timescales for disk evolution set the timescales available for the formation of the stars themselves and for planet formation. The evolution of material in disks around the components of binary stars is disturbed and disks are truncated. This influence can cause disks to evolve on different timescales with implications for star and planet formation. This thesis presents an assessment of the frequency of binary components with ongoing accretion and/or hot circumstellar dust with the help of the currently two largest nearly-simultaneous spatially-resolved photometric and spectroscopic observations of binaries in the ONC and Cha I. The measured disk frequencies are compared to the corresponding single star values in order to measure the impact of binarity in a separation range of $\sim 25\text{--}1000$ AU.

■ **What is the lifetime of disks around the components of T Tauri binaries?**

To infer the lifetimes of disks around the individual components of binary stars, measurements of the evolution of binary disk frequency in star-forming regions at various ages are required. The new data of this thesis allow me to infer the fraction of visual binary components with projected separations of $\sim 25\text{--}1000$ AU with accretion and/or hot inner dust disks at the ages of the ONC (~ 1 Myr) and Cha I ($\sim 2\text{--}3$ Myr). The evolution of disk frequency of the individual components of binaries with SFR age can be measured. This provides the currently best estimate of the average time until circumstellar disks around

individual binary components dissolve. This evolution is compared to the single star disk frequency, which is known to decay approximately exponentially with a time constant of 2–3 Myr.

■ Is the mass accretion universal, i.e., independent of binarity or star forming region?

The mass accretion rates of low-mass single stars in various star-forming regions are known to be consistently on the order of $\sim 10^{-9}$ to $\sim 10^{-7} M_{\odot} \text{yr}^{-1}$. The environments of disks around the components of T Tauri binary stars of separations up to a few 100 AU are, however, significantly different to that of single stars: disks are smaller, less massive, and their evolution is disturbed by the gravitational and radiative influence of the stellar companion. Is accretion, i.e., the transport of material from the disk onto the stellar surface, sensitive to those changes at the outer edge of the disk? Or is it primarily determined by the conditions in the innermost parts of the disk where the accretion overflow takes place and which are barely influenced by the presence of a stellar companion? The present data are used to measure the mass accretion rates in the individual components of ~ 25 –1000 AU binaries. Correlations with component masses and binary separations are explored to statistically assess the influence of binarity on mass accretion rates.

1.4 Structure and content of this thesis

This thesis analyzes and discusses the evolution of protoplanetary disks around the individual components of T Tauri binary stars in nearby star-forming regions. The discussion of these observations and the implications for the field of binary disk evolution in low-mass binary systems are organized as follows.

Chapter 2 introduces *adaptive optics spectroscopy* with which a major part of the observational data were acquired. The chapter explains why near-infrared adaptive optics observations are required for this project and summarizes the basic principles of the technique. Details are provided about the impact of the use of adaptive optics on spectroscopic observations with a long slit and an integral field unit by the examples of *NACO* and *SINFONI* instruments on ESO's *Very Large Telescope* (VLT), respectively.

Chapter 3 presents a near-infrared photometric and spectroscopic study of the individual components of 26 T Tauri binaries in the Orion Nebula Cluster, the currently largest study of this kind in a clustered star-forming environment. The strength of Br γ emission is used to infer the presence and strength of active magnetospheric accretion in each stellar component. $H-K_s$ color excess indicates the presence of hot circumstellar dust. These disk and accretion indicators are brought into context with the simultaneously derived stellar component ages and masses as well as projected binary separations and mass ra-

tios. Differential disk evolution, mass accretion rates, and implications for the formation of planets around the components of binaries with $\sim 100\text{--}600$ AU in the ONC are discussed.

Chapter 4 presents the currently largest nearly-simultaneous $1.25\text{--}3.5$ μm photometric and spectroscopic study of spatially resolved multiple stars in the Chamaeleon I star forming region. The presence of hot circumstellar dust is inferred from $K_s\text{--}L'$ color excess and ongoing accretion is indicated by Br γ emission for each individual binary component. The data return spectral types, luminosities, masses, and ages of all stellar components which are discussed in terms of their influence on the presence of disks and the measured mass accretion rates in binaries of separations between $\sim 25\text{--}1000$ AU.

Chapter 5 compares the findings of the ONC and Cha I studies in this thesis and supplements these with literature data from surveys of the Taurus star-forming region. Conclusions about the measured disk frequencies are brought into context with the age of the respective population and with binary separations to measure disk evolution timescales.

Chapter 6 summarizes the conclusions from the previous sections. An outlook is presented and future studies to extend our insight into the evolution of protoplanetary disks around the components of low-mass binary stars are proposed.

Chapter 2

Adaptive Optics spectroscopy

Most of the observational data of this thesis require observations in the near-infrared with an angular resolution as high as possible. The currently most efficient technique to observe a large number of targets close to the theoretical resolving limit of today's largest ground-based telescopes is *Adaptive Optics* (AO) which can be combined with both imaging and spectroscopic observations. This chapter gives a short introduction to the scientific and technical aspects of high-spatial resolution spectroscopy with AO. As most observations were taken with *NAOS-CONICA* (NACO) and *SINFONI* on ESO's *Very Large Telescope* (VLT), these two instruments will serve as examples for the implementation of the techniques of *long-slit* and *integral field* AO spectroscopy, respectively.

2.1 Close visual binaries: the need for high-spatial resolution spectroscopy

In order to disentangle the effects of stellar, binary, and disk parameters on disk evolution, investigations of binaries must study the individual stellar components for their disk properties. While unresolved, combined-light studies can determine the presence of *at least one* disk in a binary system they cannot give information about whether the more or less massive component is host to the circumstellar material or both. The important correlation of the individual disk lifetimes with stellar mass¹ is thus inaccessible with unresolved observations. In addition, there is evidence that mixed systems with only one accreting component exist in probably all star-forming regions (Monin et al. 2007). The underlying mechanisms that determine the *relative* speed of disk evolution require further study with necessarily spatially resolved binary observations.

One of the most interesting ranges of binary separations for the study of the evolution of circumstellar disks is the range between ~ 10 AU and a few times 100 AU. On one hand, the observed binary separation distribution of young stars peaks at ~ 30 AU (Lein-

¹In binaries, individual component disk sizes are a function of binary separation and component masses (Artymowicz & Lubow 1994). The smaller a disk, the shorter is its expected lifetime (Monin et al. 2007).

ert et al. 1993), which renders this range particularly worthwhile studying as binaries are most common with these separations. On the other hand, while the truncation of the outer disk to $\sim 1/3$ of the binary separation (Artymowicz & Lubow 1994) is stronger the closer the binary system and is most severe in systems with separations < 100 AU, wide systems $\gg 100$ AU are not expected to significantly alter disk evolution (Monin et al. 2007). Binaries with separations in the range of ~ 10 – 1000 AU accordingly contain both disks with significant truncation and disks with rather unchanged properties. These binary separations are therefore suited to explore a wide range of possible impacts of stellar companions with the outer disk material.

The nearest star-forming regions are located at ~ 140 – 160 pc from the Sun. At this distance, the closest binaries in the identified separation range appear with angular separations of down to $\sim 0''.1$. This is below the seeing limit of ground-based observations and accordingly spatially resolved observations require either the use of space-based observatories or high-spatial resolution techniques from the ground. While inner disk signatures (accretion/circumstellar dust at ~ 1000 K) are strongest in the optical and near-infrared wavelength range, the longer near-IR wavelengths enable the observer to more deeply penetrate the regions of strong extinction, which are a common feature of star-forming regions. The currently most efficient method for near-IR observations at high spatial resolution is *Adaptive Optics*. While it enhances angular resolutions from the seeing limit ($\gtrsim 0''.5$ at the best observing sites) to close to the theoretical diffraction limit ($\sim 0''.06$ at $\lambda = 2 \mu\text{m}$ on an 8 m telescope) it also provides sufficient sensitivity to observe faint low-mass stars at > 100 pc at a good signal to noise ratio (SNR) and can be combined with both imaging and spectroscopic instruments. Observations with the latter are required for the study of disks in binaries to measure accretion signatures such as emission lines and simultaneously obtain a measurement of the spectral type and extinction of the target source.

In summary, observations for the purpose of studying the evolution of inner circumstellar disks around low-mass stars require imaging and spectroscopy at high spatial resolutions at near-infrared wavelengths. This is done most efficiently for a large number of targets with ground-based observations supported by adaptive optics.

2.2 A short introduction to Adaptive Optics

Adaptive optics are by now a well-established part of astronomical instrumentation. Every large ground-based observatory operates AO facilities to extend the range of application of their instruments to observations at high angular resolution. This section will therefore only summarize the basics of this technique and the interested reader is recommended to refer to the pertinent literature (e.g. Beckers 1993; Hartmann 1998; Davies & Kasper 2012, and references therein). The focus of this chapter shall be on the use of adaptive optics with near-infrared spectroscopy, which is described in the subsequent sections.

The Earth's atmosphere is subject to turbulences caused by patches of air of different temperatures, densities, and humidity, causing a constant change of the refractive index n which necessarily pass the line of sight between an observer on Earth and a celestial object

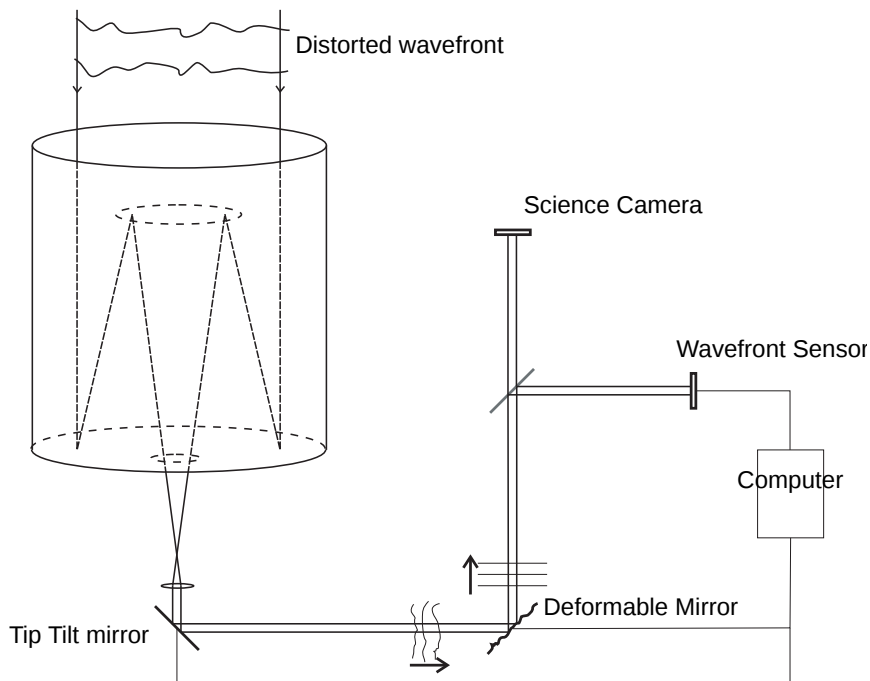


Figure 2.1: Schematic diagram of an Adaptive Optics system integrated into the light path of a telescope. The distorted light enters the telescope, is reflected via the tip-tilt mirror and a deformable mirror onto a beam splitter that redirects part of the light to a wavefront sensor and lets the rest pass to the science camera. The signal from the wavefront sensor is measured, interpreted, and forwarded to the tip-tilt and deformable mirrors which flatten the incoming wavefront.

of interest. The imposed chaotic wavefront distortions of these *turbulence cells* – caused by the fact that the speed of light in air is a function of temperature – cause a *seeing-induced* full width at half-maximum $\text{FWHM}_{\text{seeing}} = \lambda/r_0$ which is equal to a value of $\sim 0''.7$ at a wavelength of $\lambda = 2.2 \mu\text{m}$, assuming the canonical value of $r_0^{2.2\mu\text{m}} \approx 0.6 \text{ m}$ for the size of the turbulence cells, called *Fried parameter* r_0 (see e.g. [Fried 1965](#); [Glindemann et al. 2000](#)). This is rather large compared to the width of the ideal diffraction limited *point spread function* (PSF) of a circular telescope aperture of width D , called *Airy function*, of

$$\text{FWHM}_{\text{Airy}} = 1.03 \frac{\lambda}{D} \quad (2.1)$$

which returns a more than ten times better resolution of $\text{FWHM} = 0''.06$ at $\lambda = 2.2 \mu\text{m}$ with current 8 m telescopes. While the theoretical diffraction limit becomes smaller with decreasing wavelength the seeing limit is larger at optical wavelengths due to the wavelength dependence of the Fried parameter of $r_0 \propto \lambda^{6/5}$ ([Fried 1965](#); [Karo & Schneiderman 1978](#)).

To recover the full angular resolution power of large ground-based telescopes, adaptive optics are included in the light path after entering the telescope and before light enters the science part of the instrument. A sketch of the basic setup is presented in Fig. 2.1. The basic principle relies on the fact that the shape of the distorted wavefront can be

measured and corrected in real-time. Reflection off a *deformable mirror* (DM)², adapted to assume the measured shape, leaves the reflected wavefront ideally with no atmospherically induced aberrations. The quality of the correction is limited by the fact that turbulent changes in the atmosphere happen on rather short timescales. The typical *coherence time* $\tau_0 \approx r_0/|v|$, i.e., the time during which the aberrations through the atmosphere can be assumed to be constant, is on the order of a few times 10 ms (assuming a wind speed v of a few 10 ms^{-1} , Beckers 1993; Glindemann et al. 2000). This is the maximum time that is available between measuring the shape of the wavefront and its correction. Corrections that are applied slower than the coherence time can at best partly correct the imposed aberrations since the atmosphere already changed significantly.

The demands on the wavefront measuring routine are accordingly high: at a rate of up to 1 kHz it needs to take an acquisition of the incoming wavefront, determine its shape, and pass this information to the deformable mirror. This requires a suitable wavefront reference which is ideally (i) a point source above the atmosphere (to be able to assume that the undisturbed wavefront is approximately flat and passed all of the medium that generates the turbulences), (ii) which provides enough light to be imaged with millisecond snapshots, and (iii) that is close enough to the scientific object of interest to experience the same aberrations. This is usually provided by a star within $30''$ of the science target³ with a minimum brightness determined by the used instrumentation, e.g., $V < 16.7 \text{ mag}$ or $K < 12\text{--}13 \text{ mag}$ in the case of NACO/VLT (see Sect. 2.3.1).

To measure the shape of the wavefront, so-called *wavefront sensors* are used which receive part of the light reflected from the deformable mirror. Three principally different designs are currently favored: *Shack-Hartmann*-type, *curvature sensing*, and *Pyramid wavefront sensors*. The first two are used by the NAOS (Sect. 2.3.1) and SINFONI (Sect. 2.3.2) adaptive optics modules, respectively. Shack-Hartmann wavefront sensors use arrays of lenses (so called *lenslets*) to measure the distortion of individual parts of the wavefront. While the undistorted wavefront passing the lenslet array creates a regular pattern of spots on a CCD, wavefront aberrations cause a displacement of the individual spots. This displacement is converted into a distortion model which is used as an input signal for the actuators of the DM. Curvature sensing exploits the fact that a distorted wavefront will not focus exactly in the focal plane like in the undistorted case. Measurement of an increase of the intensity in front of or behind the focal plane indicates the degree and shape of a distortion and is passed on to the DM to correct the incoming wave. Limitations of both techniques are the high demand on computing power to update the correct shape of the DM within a coherence period and the limited number of actuators that can be placed

²The “Tip” and “Tilt” signals, i.e., uniform gradients of the wavefront in x and y direction, often require the use of a separate optical component, e.g., a *Tip-Tilt mirror*, since they are typically too large for correction with the DM.

³The quality of the correction is a function of the size of the *isoplanatic angle*, i.e., the angle under which two sources show correlated atmospheric aberrations, and the angular distance between the reference and science target. The closer the reference the better the correction. Ideally the reference and science target are identical.

on the DM to correct for high-order aberrations⁴.

The performance of adaptive optics can be measured by means of the *Strehl Ratio*, which is defined as the ratio of the measured and theoretical, purely diffraction-limited peak flux of a point source. While seeing-limited Strehl ratios are typically less than a few per cent, AO-corrected observations can improve the Strehl ratio to more than 40% at $\lambda = 2 \mu\text{m}$, depending on reference source brightness and seeing conditions. At these high Strehl ratios, the angular resolution is nearly identical to the theoretical resolution power of the telescope (see e.g. [Le Louarn et al. 1998](#)). The correction is wavelength-dependent due to an increase of the coherence times and lengths with wavelength. Accordingly, high Strehl ratios are mainly obtained at infrared wavelengths, while optical corrections require comparably large instrumental and computing effort to achieve even minor improvements. Already over a wavelength range from $\sim 2.2 \mu\text{m}$ (*K*-band) to $\sim 1.25 \mu\text{m}$ (*J*-band), the typical Strehl value can decrease from ideally $\gtrsim 50\%$ down to $\lesssim 10\%$. A Strehl ratio $< 100\%$ implies that the detected flux is not distributed in the shape of an ideal *Airy* pattern. In fact, the shape of an AO PSF can be described as a superposition of a diffraction-limited core and a seeing-limited “halo”.

The above describes the basic concept and characteristics of reducing the impact of atmospheric turbulence on ground-based astronomical observations with adaptive optics. Constraints on the applicability of this concept to a particular scientific question arise, however, for example from the limited sky coverage due to guide star magnitude limits, the improvable Strehl ratio in particular at short wavelengths, or the small isoplanatic angle. Concepts to tackle these and other points do exist and are either already in use or are currently being installed (*Laser guide star AO, ground-layer AO*; e.g. [Wizinowich et al. 2006](#); [Rabien et al. 2010](#)), have proven their feasibility (*multi-conjugate AO*; [Beckers 1988](#); [Marchetti et al. 2003](#)), or are planned for special purposes such as the direct imaging of planets (*extreme AO*; e.g. [Sauvage et al. 2010](#)).

2.3 Spectroscopy with Adaptive Optics

The gain of the use of AO for observations of close visual binary stars is obvious: the high spatial resolution allows to separately obtain spectral information from both components of a binary. Additionally, most of the light is concentrated into the central peak of the PSF which is equivalent to an increase of the S/N. In the following I will discuss the implications of the use of adaptive optics for stellar spectroscopy with a long slit by the example of NACO (Sect. 2.3.1) and the principally different method of integral field spectroscopy with SINFONI (Sect. 2.3.2).

⁴The number of actuators limits the number of different aberration *modes* that can be generated with a DM. The higher the number of actuators/modes, the more detailed can be the match of the DM with the actual wavefront shape.

2.3.1 Long-slit spectroscopy with NACO

NACO, short for NAOS-CONICA, is an imaging and spectroscopy instrument at the VLT consisting of the *Nasmyth Adaptive Optics System* (NAOS) operated in the visible and infrared, and the *CONICA* camera sensitive at all near-infrared wavelength bands between ~ 1 and $5\ \mu\text{m}$ (Lenzen et al. 2003; Rousset et al. 2003). Among other observing modes, spectroscopy is offered as grism spectroscopy with a long slit of dimensions $0''.086$ or $0''.172 \times 28''$ with a spectral resolution of $R=400\text{--}1400$ for wavelengths between ~ 1 and $\sim 4\ \mu\text{m}$.

Wavelength-dependent slit losses. A prominent feature uniquely attributable to the use of AO in spectroscopy is a wavelength dependence of the PSF in Strehl ratio and shape, owing to the wavelength-dependent efficiency of the AO correction. This has implications for both integral field and long-slit spectroscopy, but in particular the latter can suffer from wavelength-dependent *slit losses*, i.e., the fact that only the central part of the light bundle can pass if the PSF is significantly wider than the slit. While wavelength-*independent* slit losses can easily be calibrated, the induced slope on the extracted science spectra can mimic a different level of interstellar extinction than actually present (see Sect. 3.2.2 for the derivation of extinction in NACO spectra of ONC binary components). It is therefore important to have control over the impact of slit losses on the extracted spectral slope.

The magnitude of the wavelength-dependent losses can be estimated with, e.g., the information from the NACO manual⁵ that a NACO Strehl ratio in *K*-band ($2.2\ \mu\text{m}$) can be larger than 30% under good conditions while in *J*-band ($1.25\ \mu\text{m}$) only a few per cent may be achieved. If we assume good observing conditions, values of 40% at $2.2\ \mu\text{m}$ and 10% at $1.25\ \mu\text{m}$ are reasonable. The corresponding FWHM of $0''.075$ in *K*-band and $0''.059$ in *J*⁶ combined with the use of the $0''.086$ wide slit of NACO imply that considerably more flux in *J*-band passes the slit than at *K* wavelengths. While a simulation of AO PSFs is highly complex (e.g. Tristram & Prieto 2005), an order-of-magnitude estimate of the slit losses as a function of FWHM was simulated using Gaussian PSFs, shown in Fig. 2.2. The inferred 11% slit loss at a FWHM of $0''.059$ (i.e. *J*-band) and 21% slit loss at FWHM = $0''.075$ (*K*-band) support the qualitative considerations about the wavelength dependence of the slit losses.

Since slit losses also depend on the – timely variable – Strehl ratio of the individual observations, calibration of the spectra can be complicated. This is particularly true when a wide spectroscopic wavelength range is assumed as in the above example. Observations of binary components in the Orion Nebula Cluster in this thesis, however, use a short wavelength range of $\sim 2\text{--}2.5\ \mu\text{m}$. The effect of wavelength-dependent slit-losses is accordingly significantly smaller. To estimate the magnitude of the wavelength-dependent slit losses for these observations, we conservatively assume that the FWHM increases from $0''.07$ to $0''.08$ from the blue ($\sim 2\ \mu\text{m}$) to the red edge ($\sim 2.5\ \mu\text{m}$) of the observation (estimated from the increase of the FWHM between *J* and *K*-band from $0''.06$ to $0''.075$). Approximation

⁵<http://www.eso.org/sci/facilities/paranal/instruments/naco/doc/>

⁶Simulated with the NAOS preparation software, <http://www.eso.org/sci/observing/phase2/SMGuidelines/NAOSPS.html>

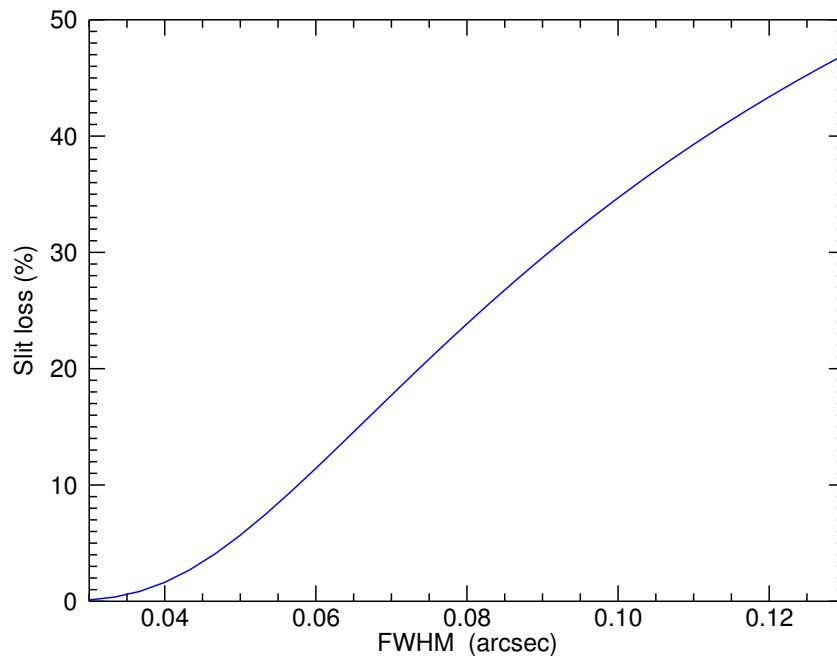


Figure 2.2: Slit losses as a function of the FWHM of a Gaussian PSF. The simulations estimate the fraction of light that does not pass the spectroscopic slit assuming the instrumental parameters of NACO, i.e., a $0''.086$ wide slit and a pixel scale of $0''.01326 \text{ pix}^{-1}$.

with a Gaussian function enables me to estimate the change change in slit loss to be $\sim 5\%$ (Fig. 2.2). This would induce an artificial slope in the spectra which can be falsely interpreted as a reduced extinction of $\sim 0.8 \text{ mag}$, smaller than the typical uncertainty in this study (see Sect. 3.2.2 for the derivation of extinction from NACO slit spectra). In addition, the increase of 5% is only an upper limit since the composite AO PSF is not Gaussian but keeps a significant fraction of its light in the wings of the airy pattern and the seeing-limited halo which has a size independent of the Strehl ratio (and will thus be truncated to the same degree by the slit) and the real increase of FWHM within K -band is likely smaller than the anticipated conservative $0''.01$. The real change of slit-losses between $2 \mu\text{m}$ and $2.5 \mu\text{m}$ is accordingly likely $\ll 5\%$ and will only add to the noise budget of the derived parameters with no significant consequences for the scientific considerations in this thesis.

Line shape. In addition to a wavelength dependence, AO PSFs are subject to temporal and spatial variability. The resulting line shapes are functions of the wavelength and slit width and their Strehl ratio-dependent composite shape. This complex structure has implications for the spectral resolution: while the line wings have a spectral resolution defined by the slit width, the line cores with widths smaller than the slit have a higher spectral resolution (see also the NACO manual). The implications of AO spectroscopy for the line shapes do not influence the results of this thesis – neither is the measurement of line shapes part of the analysis nor does it have significant impact on the relative absorption strengths used for spectral classification.

Wavelength shifts. The small FWHM of the PSF at small wavelengths is of importance for an accurate wavelength calibration, in particular when the FWHM is smaller than the width of the slit. A displacement of the peak in dispersion direction is interpreted as a wavelength shift which is wavelength-dependent as it correlates with the FWHM. In case an absolute measurement of e.g. radial velocities is *not* part of the scientific program (as in this thesis), this shift can be removed at the wavelength calibration stage.

The above effects can make a flux and wavelength calibration of AO slit spectra complicated or impossible. Depending on the scientific purpose, however, part of the effects can be ignored because they have no or negligible impact on the results. For the purpose of this thesis, stellar and disk characterization through spatially-resolved spectroscopy of visual binaries, the two latter effects (peculiar line shape and wavelength shifts) have no impact on the results. Slit-losses may appear, however, with only negligible wavelength dependence. This is sufficient for the purpose of this thesis where no direct spectral flux-calibration is required.

2.3.2 Integral field spectroscopy with SINFONI

SINFONI consists of a curvature sensing adaptive optics module and the *SPectrometer for Infrared Faint Field Imaging* (SPIFFI) in an *integral field unit* (IFU) design (Eisenhauer et al. 2003; Bonnet et al. 2004). SINFONI integral field spectroscopy uses an *image slicer* which divides the field of view of SPIFFI into 32 equal stripes (called *slitlets*) by reflection off its structured surface. These stripes are rearranged by another image slicer into a single long “pseudo”-slit on a Rockwell Hawaii 2k×2k IR detector array, each projected onto 64 pixels. The thus collected information can be reconstructed to form an *image cube* which contains both spatial information in a 64×32 grid of rectangular pixels and spectral information for each spatial pixel, spread over 1024 pixels in *z*-direction.

While some of the implications of adaptive optics for long-slit spectroscopy do not apply here (no slit-losses or artificial wavelength shifts), others do apply and a thorough calibration of the stellar spectra requires careful attention to the details.

Line shape. As in the long-slit case, line shapes are a function of many parameters including Strehl ratio and wavelength and are barely predictable. As they are of minor importance for the conclusions of this thesis, the shape is disregarded and assumed to have no effect on other inferred parameters.

The wavelength dependence of the FWHM and spatial location. The wide wavelength range used for the observations of visual binaries in the Chamaeleon I dark cloud of 1.45–2.45 μm results in a strongly wavelength-dependent PSF shape including significant variations of the FWHM, ellipticity, and centroid location of stellar objects in the data. The FWHM and centroid vary by up to 1 pixel in *x*- and *y*-direction as is illustrated in Fig. 4.4. The details of a spectral extraction which uses adaptive extraction ellipses to

conserve the *relative* flux at all wavelengths are presented together with the description of the data reduction of the SINFONI observations of Cha I binaries (Sect. 4.1.3).

The great advantage of IFU spectroscopy over long-slit observations with AO are the absence of slit losses whose magnitude is hard to accurately predict as a function of wavelength, in particular when the spectral range is wide. The remaining direct consequence of AO use – a wavelength-dependent PSF – can be determined offline and corrections can be applied during post-processing.

Chapter 3

Disk & star parameters of T Tauri binaries in the Orion Nebula Cluster

(Daemgen, Correia, & Petr-Gotzens 2012)*

To obtain a census and explore the evolution of dust and accretion disks in binary stars, observations were taken in two nearby star forming regions, the Orion Nebula Cluster (ONC) and Chamaeleon I (Cha I). While the former is a representative member of the class of strongly clustered regions at a very young age of ~ 1 Myr (Hillenbrand 1997), the latter is about twice as old and more disperse with only a low chance for stellar encounters. Both different environments will imprint their unique signatures on the evolution of binaries and disks, making both interesting candidates for further investigations of disk evolution in binary stars. This chapter will discuss the Orion part of the study.

The Orion Nebula Cluster has been targeted by a wealth of studies (for an extensive review see Bally 2008), some of the major attractions being its bright *Orion Nebula Cluster*, a high stellar density of up to 5×10^4 stars per pc^3 in the center (McCaughrean & Stauffer 1994), and its physical proximity of only 414 pc (Menten et al. 2007). In addition, four OB-type stars mark the center in form of the so-called *Trapezium*. The existence of these short-lived stars corroborates with the youth of the cluster of only ~ 1 Myr (Hillenbrand 1997) which is also indicated by the variability, X-ray emission (see Reipurth 2008, for references), and high disk content of its stellar members of 55–90% (Hillenbrand et al. 1998). An interesting feature of this cluster is the large abundance of *proplyds*. These are *protoplanetary disks* that are directly visible either as bright externally irradiated flattened structures around stars or as dark silhouettes in front of the bright background nebulosity (O’Dell & Wen 1994; McCaughrean & O’dell 1996) – historically the first excellent indication that circumstellar material indeed takes the shape of a disk.

Not only proplyds, but also indirectly observable disks were subject of a number of studies (e.g. Hillenbrand et al. 1998; Lada et al. 2000; Da Rio et al. 2010) as well as the binary content of the ONC (Prosser et al. 1994; Padgett et al. 1997; Petr et al. 1998; Simon et al. 1999; Köhler et al. 2006; Reipurth et al. 2007). Interestingly, the multiple star fraction of the ONC ($8.8 \pm 1.1\%$ for binary separations of 67.5–675 AU, Reipurth et al. 2007)

*This chapter depends on collaborative work which I had the opportunity to take the lead of. In particular I was responsible for the data reduction, interpretation, and discussion, as well as the composition of the manuscript.

is lower than that in the field, while other young regions like Taurus have a significantly higher (almost a factor of 3) multiple star content at roughly the same age (Duchêne 1999).

3.1 Observations and data reduction

3.1.1 Sample definition

We observed 20 visual binaries in the ONC from the binary census of Petr (1998) and Köhler et al. (2006). Data for 6 additional binaries come from observations by Correia et al. (2012, *in prep.*). All targets are listed in Table 3.1. The projected separations range from $0''.25$ to $1''.1$, which corresponds to ~ 100 – 400 AU at the distance of the ONC. Magnitude differences of the binary components range from 0.1 to ~ 3 mag in H and K_s -band.

All of our targets are members or very likely members of the ONC, which were mostly identified based on their proper motion (Hillenbrand 1997, and references therein). Targets without proper motion measurements ([HC2000] 73, TCC 15, TCC 55) or those with low proper-motion membership probability (JW 235, JW 566, JW 876) were confirmed to be young stars, thus likely members based on their X-ray activity (Hillenbrand & Carpenter 2000; Reipurth et al. 2007; Getman et al. 2005). No further information is available for two targets, [AD95] 1468 and [AD95] 2380, but our spectroscopy shows late spectral types (SpT) at moderate luminosity and extinction for these and all other targets, ruling out foreground and background stars. Common proper motion with the ONC and signs of youth combined with small angular separation of the components render it likely that all binaries are gravitationally bound. However, chance alignment of unrelated members of the Orion complex cannot be excluded. A possible example might be TCC 15, whose secondary shows almost no photospheric features but strong Br γ and He I emission, suggesting a highly veiled nature of this component. This makes it a candidate member of the Orion BN/KL region, which is in the line of sight of the ONC but slightly further away (~ 450 pc) and probably younger (Menten et al. 2007). However, the chance of finding an unrelated stellar component at the separation measured for this binary ($1''.02$) is only $W=8\%$ given a projected density of ~ 0.03 stars/arcsec² in the center of the ONC (Petr et al. 1998). In the following, we treat TCC 15 as a physical binary.

We also searched the literature for possible spectroscopic pairs among our binary components and found that among the 11 binaries that had been surveyed (Tobin et al. 2009; Fűrész et al. 2008), two are spectroscopic binary candidates (see Table 3.1). Both had already been excluded from our statistical analysis for other reasons (see discussion in Sect. 3.2.4 for JW 260; JW 974 was not observed with spectroscopy). Spectroscopic binarity cannot be excluded for the other targets, since no published spectroscopic binary surveys exist and our observations are of too low spectral resolution to detect spectroscopic pairs. In the following, we treat these binary components as single stars.

Table 3.1 lists all targets including the dates of their observation, the instrument used, and the observational mode. Furthermore, we provide the projected distance to the massive and bright θ^1 Ori C system, which is at the center of the ONC.

Table 3.1: Targets and observations

Name ^a	dist. to θ^1 Ori C [']	Obs. with	Imaging or Spectroscopy	Imaging Filters ^b	SB ^c	Date (UT)
[AD95] 1468	7.18	NACO	I&S	<i>JH</i>	no	Feb 09, 2005
[AD95] 2380	6.92	NACO	I&S	<i>JH</i>	no	Jan 06, 2005
JW 235	6.85	NACO	I&S	<i>JH</i>	no	Dec 19, 2004
JW 260	9.00	NACO	I&S	<i>JH</i>	SB1	Dec 19, 2004
JW 519	0.80	NACO	I	<i>JHK_s</i>		Feb 07 & 09, 2005
JW 553	0.52	NACO	S			Dec 07, 2004
JW 566	7.17	NACO	I&S	<i>JH</i>		Dec 08, 2004 & Feb 17, 2005
JW 598	0.71	NACO	S			Dec 08, 2004
JW 648	1.00	NACO	I&S	<i>JHK_s</i>		Feb 07 & 17, 2005
JW 681	1.25	NACO	S		no	Jan 06, 2005
JW 687	2.06	NACO	I&S	<i>JH</i>		Feb 09, 2005 & Dec 07, 2004
JW 765	14.09	NACO	I	<i>JH</i>	no	Feb 07, 2005
JW 876	14.45	NACO	S		no	Jan 08, 2005
JW 959	7.98	NACO	S		no	Jan 08, 2005
JW 974	14.96	NACO	I	<i>JH</i>	SB2?	Nov 19, 2004
[HC2000] 73	2.30	NACO	S			Jan 05, 2005
TCC15	0.50	NACO	S			Dec 29, 2004
TCC52	0.46	NACO	S			Dec 08, 2004
TCC55	0.49	NACO	S			Jan 10 & 11, 2005
TCC97	0.42	NACO	I	<i>JHK_s</i>		Feb 07, 2005
JW 63 ^d	8.95	GEMINI	I&S	<i>JHKL'</i>		Feb 16 & 19, 2008
JW 128 ^d	6.10	GEMINI	I&S	<i>JHKL'</i>		Feb 17 & 19, 2008
JW 176 ^d	4.67	GEMINI	I&S	<i>JHKL'</i>	no	Feb 24 & Mar 7, 2008
JW 391 ^d	2.81	GEMINI	I&S	<i>JHKL'</i>		Feb 19, 2008
JW 709 ^d	3.53	GEMINI	I&S	<i>JHKL'</i>		Feb 18 & 20, 2008
JW 867 ^d	5.79	GEMINI	I&S	<i>JHKL'</i>	no	Feb 23, 2008

^a Identifiers are suitable for use with the simbad database (<http://simbad.harvard.edu/simbad/>). References: *AD95*: Ali & Depoy 1995; *JW*: Jones & Walker 1988; *TCC*: McCaughrean & Stauffer 1994; *HC2000*: Hillenbrand & Carpenter 2000.

^b Photometry for this study was obtained in these filters and has been listed in Table 3.2. If fewer filters than the complete set of *JHK_s* has been indicated here, photometry has been added to Table 3.2 from literature sources when available.

^c Spectroscopic binary status. References: Tobin et al. (2009); Fűrész et al. (2008).

^d From Correia et al. (2012, *in prep.*).

3.1.2 NACO imaging: photometry and astrometry

Twenty of our 26 targets were observed with the NAOS-CONICA instrument (NACO; Lenzen et al. 2003; Rousset et al. 2003) at UT4/VLT in the time from November 2004 to February 2005. Of those, 16 were observed in spectroscopic mode and 11 in CONICA imaging mode (see Table 3.1). All observations were executed using the adaptive optics system NAOS where the targets themselves could be used as natural guide stars. Depending on the brightness of a target, either an infrared or visual wavefront sensor was used.

Observations and data reduction

We employed the S13 camera of NACO with a pixel scale of 13.26 mas/pixel and $13''.6 \times 13''.6$ field of view. Each imaged target binary was observed in J and H filters and three of these additionally in K_s . Observations of the same target in different filters were obtained consecutively to minimize the effects of variability. The *full width at half maximum* (FWHM) of the observations are typically $0''.075$ in J , $0''.065$ in H , and $0''.068$ in K_s -band. All observations were made in a two-offset dither pattern with a $5''$ pointing offset to allow for sky subtraction with total integration times varying between 60 s and 360 s per target and filter, depending on the brightness of the target components.

Imaging data were reduced with custom *IRAF*¹ and *IDL*² routines according to the following procedure. A low amplitude (< 10 ADU), roughly sinusoidal horizontal noise pattern—probably 50 Hz pick-up noise at read-out—was removed from all raw images by subtracting a row-median (omitting the central region containing the signal) from each column. We cropped each image to a 400×400 pixel ($\equiv 5''.3 \times 5''.3$) sub-region of the original 1024×1024 pix preserving all flux from each target multiple. For each target and filter there were at least two dithered images that undergo the same corrections, which were then used for sky subtraction. Bad pixel correction and flat fielding were applied, the latter using lamp flats taken with the NACO internal calibration unit. All reduced images per object and filter were then aligned and averaged. The fully reduced images in H -band are presented in Fig. 3.1.

Photometry and astrometry

Relative aperture photometry for all targets observed with NACO was obtained by applying the PHOT task in the *IRAF* *daophot* package to each of the reduced binary star images. The aperture radius was varied from 2 to 20 pixels to find a possible convergence of the magnitude difference of primary and secondary. The differential photometry of most binaries converged for aperture sizes of 3 to 6 pixels allowing determination of their magnitude differences with uncertainties of $\Delta\text{mag} \lesssim 0.03$. For the binaries that did not converge but followed a monotonic decrease in their magnitude difference with aperture size, we

¹Image Reduction and Analysis Facility, <http://iraf.noao.edu/>

²Interactive Data Language, <http://www.exelisvis.com/>

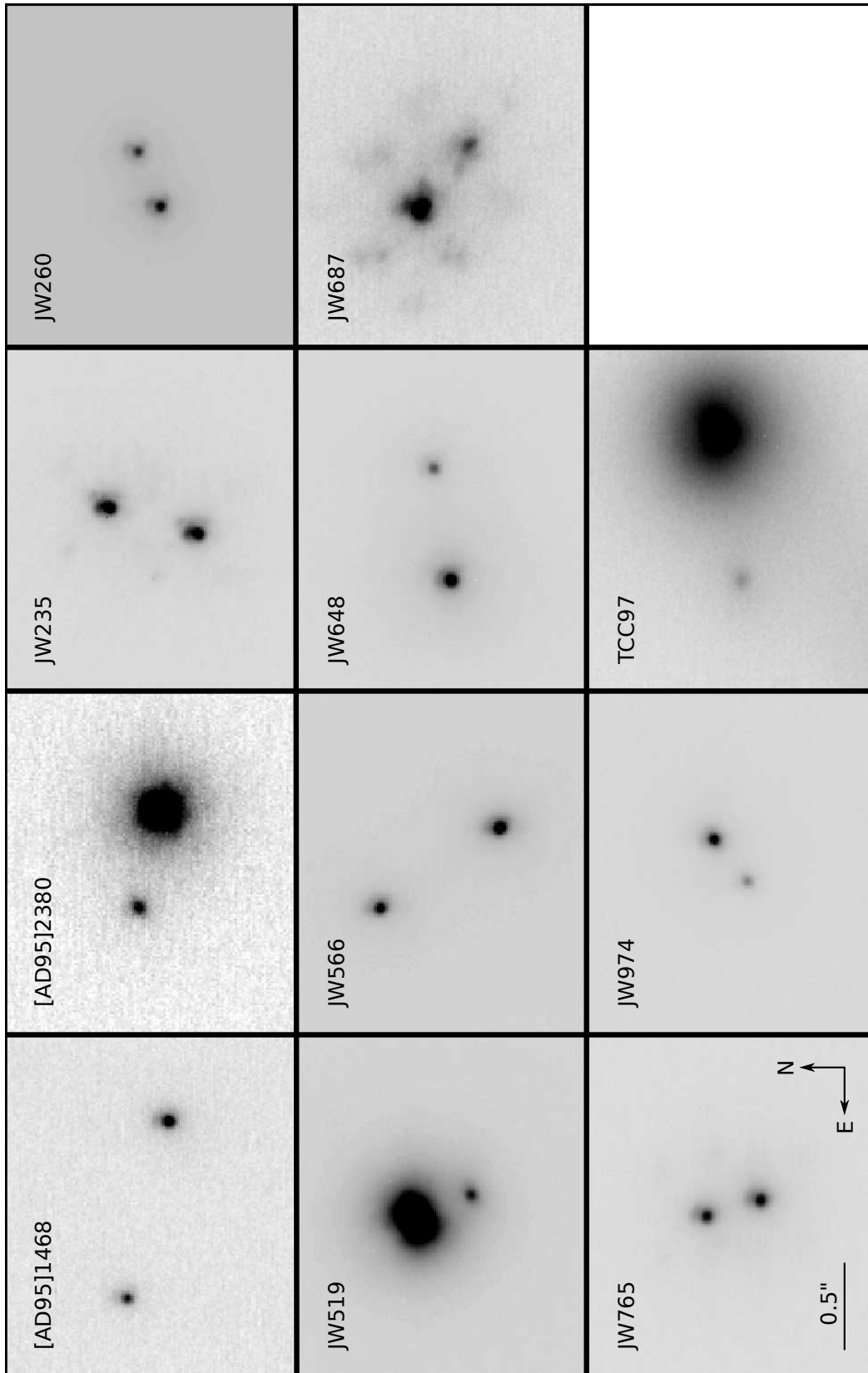


Figure 3.1: NACO *H*-band images of all ONC targets observed with NACO imaging. The intensity scale is linear and adapted to best depict both components.

32 3. Disk & star parameters of T Tauri binaries of the Orion Nebula Cluster

assigned a value of Δmag by averaging the results for apertures of sizes between 3 and 6 pixels. The uncertainty was estimated according to the slope of each individual curve.

The DAOFIND task in DAOPHOT returned sufficiently accurate astrometry for all targets. The pixel data were transformed into physical angles and separations using the pixel scale of 0.013260 arcsec/pixel and the rotation offset of 0° . The resulting relative photometry and astrometry are listed in Table 3.2.

The procedure was successful for all binaries observed with NACO, although we found peculiarities for two targets. The image of the brighter component of JW 519 has an elongated shape (see Fig. 3.1) that is not seen in the companion point spread function (PSF). We therefore conclude that we have found evidence of an unresolved third component in the JW 519 system. Unfortunately, the close separation of the system does not allow us to determine any of the separate parameters of the individual components. The photometry of JW 519 in Tables 3.2 and 3.4, as well as all further evaluation, therefore treats this likely triple as a binary. The primary of TCC 97 is surrounded by a proplyd that was first identified by O’Dell et al. (1993). Since this feature is detected in our images, our aperture photometry averages only the smallest useful apertures of 3–5 pixel radius (instead of 3–6) to exclude as much of the disk flux as possible.

A special photometry routine was applied to the target binaries JW 553, [HC2000] 73, and TCC 55, which used photometry of several reference stars in the same exposure. In particular for JW 553 and TCC 55, this procedure leads to more accurate photometry in the environment of strong nebulosity and high stellar density close to the cluster center. The photometry of JW 553 and TCC 55 uses fully reduced J , H , and K -band mosaics of the Trapezium region (Bouy et al. 2008) observed with the MCAO demonstrator *MAD* (Marchetti et al. 2007). A reference PSF was computed from 4–8 stars within $\sim 9''$ of the target binary. With this PSF, we obtained instrumental photometry for all stars in the vicinity of the target using the *IRAF daophot* package. Observed apparent magnitudes of the reference stars together with our measured relative magnitudes were then used to derive the apparent magnitudes of the target binary components. Similarly, PSF photometry of [HC2000] 73 was derived using ADONIS (Petr 1998) exposures making use of the PSF and apparent magnitude of the nearby star θ^2 Ori A (Muench et al. 2002).

Most photometry in this thesis was obtained in the NACO and 2MASS JHK_s filter systems. Since these two filter sets are very similar, no transformations had to be applied. Some photometry, however, was performed in different filters. We checked the compatibility of the 2MASS K_s and the ADONIS and *MAD* K filters used for some of the systems and relative magnitudes (see Tables 3.2 and 3.3). Comparing 39 young stars in the ONC (with similar properties as the target sample) for which both ADONIS K and K_s photometry are available (Petr 1998), we found an average offset of only 0.01 ± 0.23 mag between K and K_s . The Gemini/NIRI K -band photometry of late-type stars is compatible with that of the K_s -band with $K - K_s = 0 \pm 0.05$ mag (Daemgen et al. 2007). We therefore did not apply any corrections to our K -band magnitudes. Some of the relations used in Sect. 3.2.1 (i.e. the dwarf, giant, and CTT loci) were transformed to the 2MASS system using the relations in Carpenter (2001). In the following, we thus assume that all photometry is compatible with the 2MASS filter system.

Table 3.2: Relative photometry and astrometry of the observed binaries[†]

Name	ΔJ [mag]	ΔH [mag]	ΔK_s [mag]	ΔK [mag]	sep ^a [$''$]	PA ^b [$^\circ$]	Ref.
[AD95] 1468	0.75 ± 0.10	0.66 ± 0.02	0.10 ± 0.05		1.08	76.9	T,1
[AD95] 2380	$\gtrsim 2.5^c$	2.62 ± 0.03	2.99 ± 0.15		0.59	77.6	T,1
JW 235	0.46 ± 0.02	0.10 ± 0.02	0.47 ± 0.15		0.35	163.6	T,1
JW 260	0.53 ± 0.02	0.40 ± 0.02	0.17 ± 0.05		0.35	292.2	T,1
JW 519 ^e	2.8 ± 0.2	2.8 ± 0.2	2.6 ± 0.1		0.36	204.3	T
JW 553	2.1 ± 0.3	3.2 ± 0.3	3.19 ± 0.10		0.384 ± 0.004	248.1 ± 0.3	2
JW 566	0.20 ± 0.03	0.39 ± 0.02	0.78 ± 0.02		0.86	33.8	5
JW 598				3.19	0.9		4
JW 648	1.12 ± 0.03	1.16 ± 0.03	1.23 ± 0.02		0.68	278.7	T
JW 681				1.53	1.09	214	3,4
JW 687	1.63 ± 0.05	1.15 ± 0.07^d	0.53 ± 0.07		0.47	232.6	T
JW 765	0.08 ± 0.02	0.12 ± 0.01	0.06 ± 0.10		0.33	16.5	T,1
JW 876			0.50 ± 0.05		0.49		1
JW 959			0.07 ± 0.03		0.34		1
JW 974	1.16 ± 0.04	1.26 ± 0.04	1.41 ± 0.05		0.32	128.7	T,1
[HC2000] 73	0.48 ± 0.09	1.13 ± 0.06		1.52 ± 0.07	0.71	266.2 ± 0.5	4
TCC 15	2.5 ± 0.3	3.3 ± 0.3	3.65 ± 0.1		1.022 ± 0.004	288.2 ± 0.3	2
TCC 52	1.61 ± 0.03	1.56 ± 0.03	1.64 ± 0.02		0.52	39.24	5
TCC 55	1.0 ± 0.1^f	2.2 ± 0.3	1.26 ± 0.10		0.256 ± 0.004	153.1 ± 0.3	2
TCC 97	1.8 ± 0.15	1.8 ± 0.15	1.4 ± 0.2		0.88	98.5	T

[†] Reproduced here are only the targets observed with NACO. The photometry of the six additional targets observed with Gemini/NIRI can be found in [Correia et al. \(2012, in prep.\)](#).

^a Uncertainty in the separation: $\Delta \text{sep} = 0''.01$ unless otherwise noted.

^b Position angle uncertainty: $\Delta \text{PA} = 0.5^\circ$ unless otherwise noted.

^c The companion to [AD95] 2380A is detected with less than 3σ significance in J -band. The number quoted here is a lower limit.

^d This number is an average of two independent measurements that differ by 0.16 magnitudes.

^e The elongated shape of JW 519's primary suggests the primary to be binary itself. The photometry for JW 519, however, is based on the assumption of a single central object since separate components cannot be identified.

^f Reanalysis of MAD data published in [Bouy et al. \(2008\)](#).

REFERENCES. (T) This thesis; (1) [Köhler et al. 2006](#); (2) [Bouy et al. 2008](#); (3) [Reipurth et al. 2007](#); (4) [Petr 1998](#); (5) ESO archival data 074.C-0637(A). Reduction and photometry are described in Sect. 3.1.2.

34 3. Disk & star parameters of T Tauri binaries of the Orion Nebula Cluster

Table 3.3: Non-resolved photometry of the observed binaries

Name	J^{sys} [mag]	H^{sys} [mag]	K_s^{sys} [mag]	K^{sys} [mag]	Ref.
[AD95] 1468	13.92 ± 0.11	12.48 ± 0.18	11.23 ± 0.08		3 ^a
[AD95] 2380	13.9 ± 0.02	11.39 ± 0.03	9.88 ± 0.02		3 ^a
JW 235	12.10 ± 0.15	11.11 ± 0.15	10.50 ± 0.15		2
JW 260	8.19 ± 0.15	7.60 ± 0.15	7.23 ± 0.15		2
JW 519	12.07 ± 0.01	11.07 ± 0.01	10.61 ± 0.01		1
JW 553	10.56 ± 0.10	9.49 ± 0.05		9.05 ± 0.10	b
JW 566	11.49 ± 0.04	9.97 ± 0.05	8.86 ± 0.03		3 ^a
JW 598	10.87 ± 0.04	9.57 ± 0.05	8.93 ± 0.11		2
JW 648	10.97 ± 0.03	9.91 ± 0.02	9.28 ± 0.01		1
JW 681	12.78 ± 0.01	11.82 ± 0.01	11.07 ± 0.11		1
JW 687	11.94 ± 0.01	10.50 ± 0.01	9.70 ± 0.03		1
JW 765	11.76 ± 0.15	11.04 ± 0.15	10.81 ± 0.15		2
JW 876	9.31 ± 0.02	8.45 ± 0.03	8.03 ± 0.02		3 ^a
JW 959	9.36 ± 0.02	8.84 ± 0.03	8.63 ± 0.02		3 ^a
JW 974	12.42 ± 0.02	11.78 ± 0.03	11.41 ± 0.02		3 ^a
[HC2000] 73	12.59 ± 0.05	11.72 ± 0.03	10.99 ± 0.03		b
TCC 15	12.96 ± 0.03	11.14 ± 0.01	10.25 ± 0.01		1
TCC 52	8.64 ± 0.04	7.56 ± 0.04	6.72 ± 0.04		2
TCC 55	15.10 ± 0.14	13.27 ± 0.14		11.15 ± 0.14	b
TCC 97	13.13 ± 0.03	12.44 ± 0.02	11.77 ± 0.01		1

^a If no other reference could be found *and* if the distance to θ^1 Ori C is larger than $5'$, 2MASS values were used.

^b System magnitudes were derived from the component magnitudes (Table 3.4).

REFERENCES. (1) Muench et al. 2002; (2) Carpenter et al. 2001; (3) 2MASS, Cutri et al. 2003.

The relative photometric and astrometric results are given in Table 3.2. Together with literature values for the integrated photometry in Table 3.3, component magnitudes were derived, which are listed in Table 3.4.

3.1.3 Spectroscopy with NACO

NACO was used in grism-spectroscopy setup using the S27 camera and an 86 mas wide slit. The wavelength coverage is $2.02\text{--}2.53\ \mu\text{m}$ with a spectral resolution of $R \sim 1400$ and a resolution of 27 mas/pix in the spatial direction. The slit was aligned with the binary separation vector to simultaneously obtain spectra of both stellar components. All binaries were observed in an ABBA nodding pattern with a $12''$ nod throw, performing several

Table 3.4: Individual component apparent magnitudes[†]

Name		J [mag]	H [mag]	K_s [mag]
[AD95] 1468	A	14.36 ± 0.11	12.95 ± 0.18	11.93 ± 0.08
	B	15.11 ± 0.13	13.61 ± 0.18	12.03 ± 0.08
[AD95] 2380	A	...	11.48 ± 0.03	9.95 ± 0.02
	B	...	14.10 ± 0.04	12.94 ± 0.14
JW 235	A	12.65 ± 0.15	11.81 ± 0.15	11.04 ± 0.16
	B	13.11 ± 0.15	11.91 ± 0.15	11.51 ± 0.18
JW 260	A	8.71 ± 0.15	8.17 ± 0.15	7.90 ± 0.15
	B	9.24 ± 0.15	8.57 ± 0.15	8.07 ± 0.15
JW 519	A	12.15 ± 0.02	11.15 ± 0.02	10.70 ± 0.01
	B	14.95 ± 0.19	13.95 ± 0.19	13.30 ± 0.09
JW 553	A	10.66 ± 0.12	9.55 ± 0.06	9.11 ± 0.04^a
	B	13.18 ± 0.09	12.70 ± 0.06	12.21 ± 0.13^a
JW 566	A	12.15 ± 0.04	10.54 ± 0.05	9.29 ± 0.03
	B	12.35 ± 0.04	10.93 ± 0.05	10.07 ± 0.03
JW 648	A	11.30 ± 0.03	10.23 ± 0.02	9.58 ± 0.01
	B	12.42 ± 0.04	11.39 ± 0.03	10.81 ± 0.02
JW 687	A	12.16 ± 0.01	10.82 ± 0.02	10.22 ± 0.04
	B	13.79 ± 0.04	11.97 ± 0.05	10.75 ± 0.05
JW 765	A	12.47 ± 0.15	11.73 ± 0.15	11.53 ± 0.16
	B	12.55 ± 0.15	11.85 ± 0.15	11.59 ± 0.16
JW 876	A	8.56 ± 0.03
	B	9.06 ± 0.04
JW 959	A	9.35 ± 0.02
	B	9.42 ± 0.03
JW 974	A	12.74 ± 0.02	12.08 ± 0.03	11.67 ± 0.02
	B	13.90 ± 0.04	13.34 ± 0.04	13.08 ± 0.04
[HC2000] 73	A	13.13 ± 0.06	12.05 ± 0.03	11.23 ± 0.03
	B	13.61 ± 0.07	13.18 ± 0.05	12.75 ± 0.06
TCC 15	A	13.06 ± 0.04	11.19 ± 0.02	10.29 ± 0.01
	B	15.56 ± 0.27	14.49 ± 0.29	13.94 ± 0.10
TCC 52	A	8.86 ± 0.04	7.79 ± 0.04	6.94 ± 0.04
	B	10.47 ± 0.05	9.35 ± 0.05	8.58 ± 0.04
TCC 55	A	14.45 ± 0.08	12.67 ± 0.17	10.96 ± 0.03^a
	B	15.45 ± 0.10	14.84 ± 0.31	12.22 ± 0.08^a
TCC 97	A	13.32 ± 0.04	12.63 ± 0.03	12.03 ± 0.04
	B	15.12 ± 0.13	14.43 ± 0.13	13.43 ± 0.16

[†] The photometry of the six targets observed with Gemini/NIRI is listed in [Correia et al. \(2012, in prep.\)](#).

^a These values are derived from K -band system magnitudes instead of K_s (see Table 3.3).

36 3. Disk & star parameters of T Tauri binaries of the Orion Nebula Cluster

nod cycles for the faintest targets. Total exposure times per target were 120–2600 s. Spectroscopic standards of B spectral type were observed with the same camera setup, close in time and at similar airmass to enable us to remove telluric features. These standard spectra were reduced and extracted in the same way as the target exposures.

Spectroscopic exposures were reduced with *IDL* and *IRAF* routines including flat fielding, sky subtraction, and bad pixel removal. Lamp flats taken with an internal flat screen were fitted along the dispersion axis and divided. The extraction and wavelength calibration of the reduced target and standard exposures were performed using the *apextract* and *dispcor* packages in *IRAF*. The two-dimensional spectrum was traced with a fourth order polynomial and extracted through averaging over a 10 pixel-wide ($\sim 0''.27$) aperture centered on the ~ 4 pixel-wide (FWHM) trace of each target component. The subsequent wavelength calibration uses exposures of an argon arc lamp extracted in the same traces. All nodding exposures of the same target component were then aligned and averaged. The final extracted and calibrated spectra span a wavelength range of 20320–25440 Å with a resolution of 5 Å/pixel.

To allow for accurate telluric-line removal, intrinsic spectral features of the standard stars had to be removed. These were the Brackett- γ (Br γ , 21665 Å) and the He I (21126 Å) absorption lines, where the latter was only observed for spectral types B0 and B1. The removal of in particular the Br γ line is crucial because we aim to measure the equivalent widths of Br γ emission in the target spectra. Therefore, the Br γ line was carefully modeled according to the following scheme. Two telluric lines blend into the blue and red wings of Br γ at the spectral resolution of our observations. We modeled these tellurics by averaging the fluxes in the Br γ region (before telluric removal) of those target component spectra that showed neither absorption nor emission in Br γ . The telluric standard flux was divided by the thus generated local telluric model, allowing us to fit the remaining Br γ absorption line with a Moffat-profile and remove its signature. The cleaned standard spectra were then divided by a blackbody curve of temperature T_{eff} according to their spectral type (Cox 2000) to obtain a pure telluric spectrum, convolved with the instrumental response of NACO.

We observed a wavelength-dependent mismatch of the wavelength calibrations output from *IRAF dispcor* between the target stars and the corresponding telluric standards of up to about one pixel. To guarantee a good match of the positions of the telluric features, we used the tellurics themselves to fine-tune the wavelength calibration of the standard spectra. A customized *IDL* routine computes the local wavelength difference by means of cross correlation and corrects the mismatch accordingly. Since the tellurics are the strongest features in all our spectra, this method results in a good match between the telluric features of the target and reference, and telluric features could be removed reliably.

Flux uncertainties in the derived spectra as needed for the χ^2 minimization method described in §3.2.2 were estimated from the fully reduced and extracted target spectra by performing local computation of standard deviations. The final reduced and extracted component spectra contain a noisy (signal-to-noise ratio (SNR) smaller than 20/pix) region redwards of ~ 25000 Å caused by the low atmospheric transmission at these wavelengths. The region with $\lambda > 25120$ Å was excluded from any further evaluation. The set of

Table 3.5: Spectral features identified in the observed spectra

λ_c [Å]	Width [Å]	Species	Transition
14 877.5		Mg I	$3d^3 D_{1,2,3}^o - 4f^3 F_{2,3,4}^o$
15 025.0		Mg I	$4s^3 S_1^o - 4p^3 P_2^o$
15 040.2	*	Mg I	$4s^3 S_1^o - 4p^3 P_1^o$
15 168.4		K I	$3d^2 D_{3/2} - 4f^2 F_{5/2}^o$
15 740.7		Mg I	$4p^3 P_0^o - 4d^3 D_1$
15 765.8	*	Mg I	$4p^3 P_2^o - 4d^3 D_3$
15 888.4		Si I	$4s^1 P_1^o - 4p^1 P_1$
16 719.0		Al I	$^2 P_{1/2}^o - ^2 D_{3/2}$
16 750.5	*	Al I	$^2 P_{3/2}^o - ^2 D_{5/2}$
17 110.1		Mg I	$4s^1 S_0 - 4p^1 P_1^o$
20 338.0		H ₂	$\nu = (1-0) S(2)$
20 587.0		He I	$2p^1 P^o - 2s^1 S$
21 066.6		Mg I	$4f^3 F_{2,3,4}^o - 7g^3 G_{3,4,5}^o$
21 098.8		Al I	$4p^2 P_{1/2}^o - 5s^2 S_{1/2}$
21 169.6		Al I	$4p^2 P_{3/2}^o - 5s^2 S_{1/2}$
21 218.0		H ₂	$\nu = (1-0) S(1)$
21 661.2	56	H I	$n = 7 - 4$ (Br γ)
21 785.7		Si I	
21 825.7		Si I	
21 903.4		Ti I	$a^5 P_2 - z^5 D_3^o$
22 062.4	116	Na I	$4p^2 P_{3/2}^o - 4s^2 S_{1/2}$
22 089.7	*	Na I	$4p^2 P_{1/2}^o - 4s^2 S_{1/2}$
22 614.1	91	Ca I	$4f^3 F_2^o - 4d^3 D_1$
22 631.1	*	Ca I	$4f^3 F_3^o - 4d^3 D_2$
22 657.3	*	Ca I	$4f^3 F_4^o - 4d^3 D_3$
22 814.1		Mg I	$4d^3 D_{3,2,1} - 6f^3 F_{2,3,4}^o$
22 935.3	170	¹² CO	$\nu = (2-0)$ band head
23 226.9	170	¹² CO	$\nu = (3-1)$ band head
23 354.8		Na I	$4p^2 P_{1/2}^o - 4d^2 D_{3/2}$
23 385.5		Na I	$4p^2 P_{3/2}^o - 4d^2 D_{5/2}$
23 524.6	170	¹² CO	$\nu = (4-2)$ band head
23 829.5	170	¹² CO	$\nu = (5-3)$ band head

Photospheric features of late-type stars between 14500 Å and 25000 Å. Integration widths are listed here for all lines that have equivalent widths measured in this thesis. Lines marked with asterisks blend into the line with the next shortest wavelength (the respective previous line in the list); these lines were integrated together when used for equivalent width measurements. The transition information is composed from Prato et al. (2003), Cushing et al. (2005), Kleinmann & Hall (1986), and the NIST Atomic Spectra Database (<http://www.nist.gov/pml/data/asd.cfm>).

38 3. Disk & star parameters of T Tauri binaries of the Orion Nebula Cluster

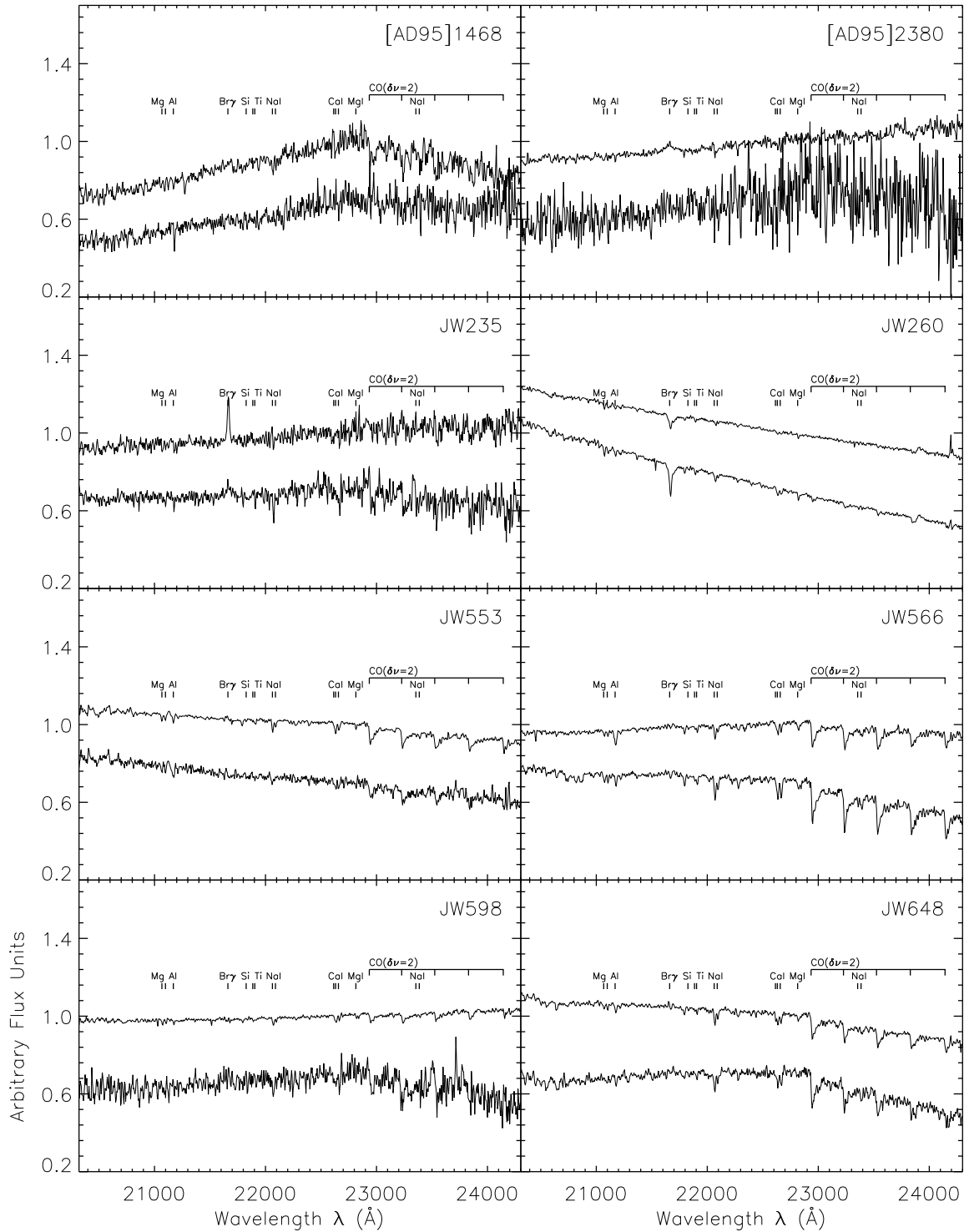


Figure 3.2: Spectra of the primary (top spectrum in each panel) and secondary component (bottom spectrum) of all targets observed with NACO spectroscopy (Gemini/NIFS spectra are displayed in [Correia et al. \(2012, in prep.\)](#)). Primary spectra are normalized at $2.2 \mu\text{m}$, and the secondaries are arbitrarily offset. The position of the most prominent lines in [Table 3.5](#) are indicated.

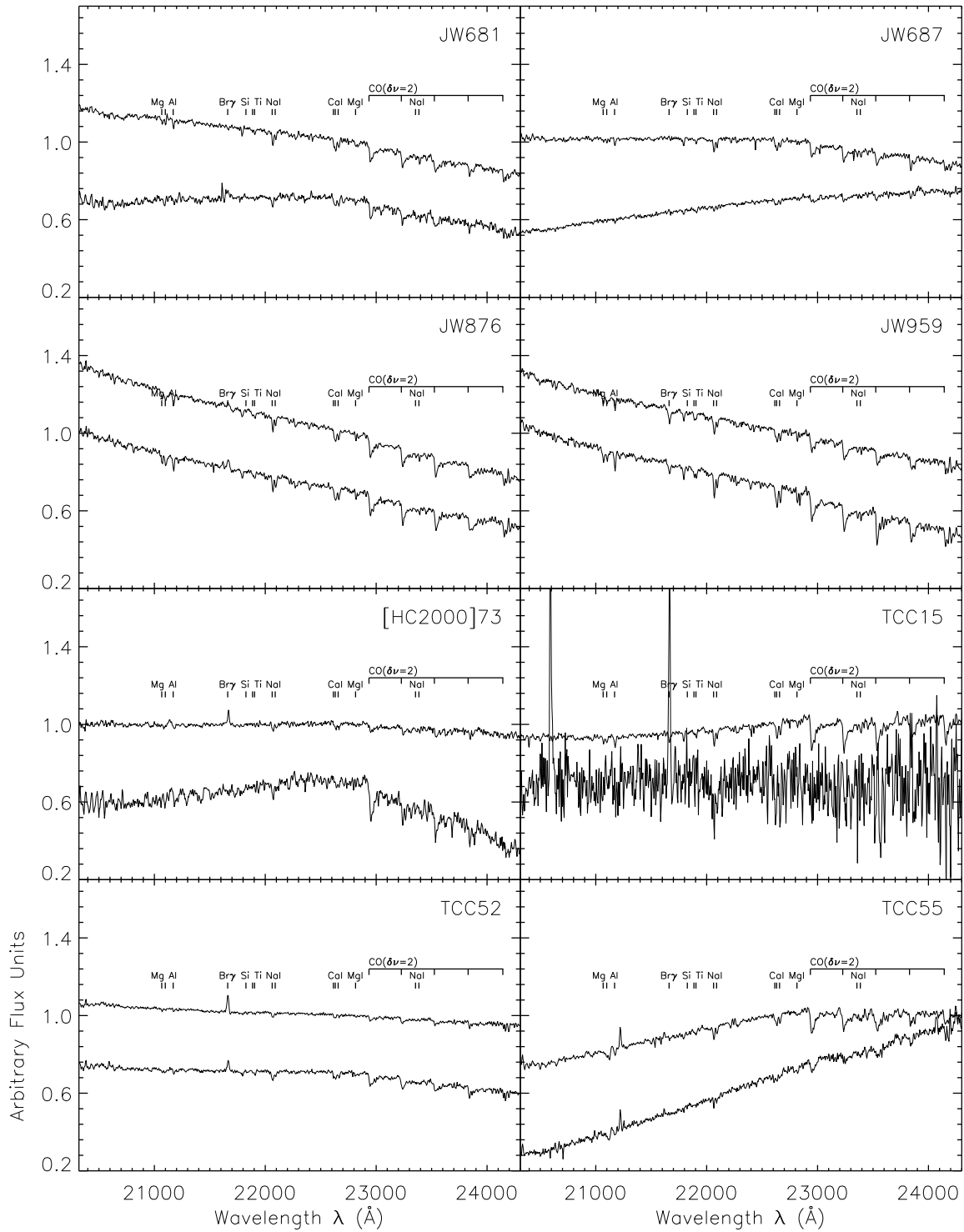


Figure 3.2: (ctd.)

reduced and extracted spectra consists of one spectrum for each target component in the spectral range of 20320–25120 Å with a resolution of 5 Å/pixel. All final reduced spectra are displayed in Fig. 3.2. The positions of the most prominent absorption and emission features are overplotted and listed in Table 3.5.

Flux calibration

To enable us to extract line luminosities and mass accretion rates (see Sect. 3.2.4), spectra were flux-calibrated. This was achieved by comparing the K_s -band photometry from Table 3.4 with synthetic photometry obtained by convolving the measured spectra with the 2MASS K_s filter curve and integrating with $zp(F_\lambda) = 4.283 \times 10^{-7}$ for the zeropoint³. Since the K_s filter curve extends to slightly bluer wavelengths than our NACO spectra, spectra were extrapolated. To estimate the impact of our linear extrapolation on the integration result, we assumed several extrapolations with different slopes (up to unreasonable values). The resulting variation in $L_{\text{Br}\gamma}$ is small, mainly because the extrapolated part coincides with the steep edge of the filter and was kept as an additional uncertainty.

3.1.4 NIFS-NIRI imaging and spectroscopy

The observations with NIRI photometry and NIFS spectroscopy at Gemini North are described in Correia et al. (2012, *in prep.*). We used the reduced and extracted but non-telluric corrected spectra of Correia et al. (2011) and performed the telluric correction using the same method as for our NACO observations. Furthermore, since the NIFS spectra are of higher spectral resolution ($R \approx 5000$) than both our NACO observations and the template spectra, we smoothed the NIFS spectra with a Gaussian kernel to a resolution of $R \sim 1400$. These steps were included to guarantee that a coherent evaluation of all data is possible. The six target spectra observed with NIFS that were included in this study will be presented in Correia et al. (2012, *in prep.*).

3.2 Results

3.2.1 Extinctions and color-excess – the color-color diagram

Using the component magnitudes of Table 3.4, we composed a $(H - K_s)$ - $(J - H)$ color-color diagram (Fig. 3.3). We compared our data with the loci of dwarfs and giants (Bessell & Brett 1988) and the location of classical T Tauri stars (CTTs locus; Meyer et al. 1997) that had both been converted to the 2MASS photometric system. Extinctions were derived by dereddening to the CTTs locus along the interstellar reddening vector (Cohen et al. 1981) and are listed in Table 3.6.

Most targets are located in the region accessible from the dwarf and CTTs loci by adding extinction. However, three groups of targets have rather peculiar locations in the diagram:

³http://www.ipac.caltech.edu/2mass/releases/allsky/doc/sec6_4a.html

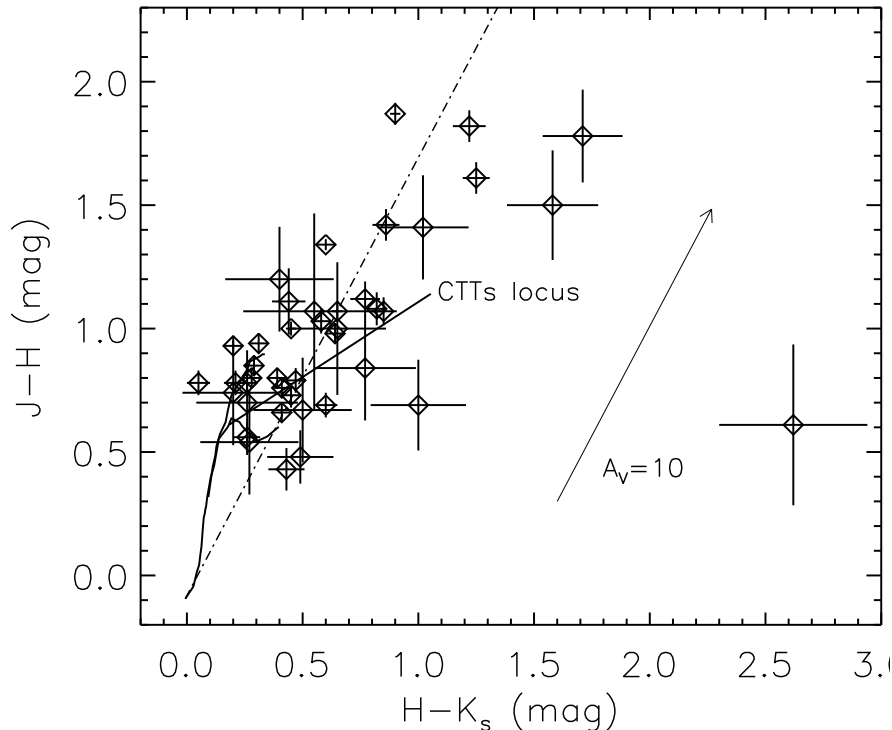


Figure 3.3: Color-color diagram of the target binary components. The CTTs locus (Meyer et al. 1997), the dwarf and giant locus (Bessell & Brett 1988), and a reddening vector of 10 mag length are overplotted, after conversion to the 2MASS photometric system (Carpenter 2001). Targets to the right of the dash-dotted line have an IR color excess.

i) two of the targets with among the smallest of $H-K_s$ values, the secondaries of JW 63 and JW 176, have no intersection with either the dwarf or giant locus along the dereddening direction. *ii)* There are some targets (the secondaries to JW 553, [HC2000] 73, and TCC 97) that are significantly below the CTTs locus. Targets in this location in the color-color diagram have been observed before (see e.g. Fig. 20 in Robberto et al. 2010). *iii)* The outlier TCC 55B in the bottom-right of the plot. Most of these peculiar locations can be explained by the intrinsic photometric variability of young stars of ~ 0.2 mag (Carpenter et al. 2001) and the fact that photometry was not taken simultaneously. Furthermore, colors are known to depend on the inclination of a possible disk (Robitaille et al. 2006) – a parameter that cannot be determined with our data. All peculiar objects were assigned an extinction of 0. Using expected dwarf colors from Bessell & Brett (1988), we then derived the color excesses

$$E_{J-H} = (J-H)_{\text{obs}} - 0.11A_V - (J-H)_0 \quad (3.1)$$

and E_{H-K_s} for all objects (Table 3.6).

We compared our extinction measurements with optical data from Prosser et al. (1994). Their sample contains six spatially resolved binaries that are also part of our sample

42 3. Disk & star parameters of T Tauri binaries of the Orion Nebula Cluster

Table 3.6: Individual component properties of all targets with detectable photospheric features

Name	Comp.	SpT	T_{eff} [K]	A_V [mag]	r_K ($F_{K_{ex}}/F_{K_*}$)	L_* [L_{\odot}]	age ^a [Myr]	M_* ^a [M_{\odot}]
[AD95] 1468	A	M4 ± 1	3270 ± 150	3.7 ± 1.1	0.00 ± 0.29	0.11 ± 0.03	4.0 ± $^{4.0}_{1.4}$	0.23 ± $^{0.05}_{0.05}$
	B	0.5 ± 1.3
[AD95] 2380	A
	B
JW 235	A	0.0 ± 1.0
	B	M3 ± 3	3420 ± 440	5.7 ± 0.9	0.73 ± 0.65	0.62 ± 0.16	1.0 ± $^{2.0}_{0.9}$	0.35 ± $^{0.23}_{0.17}$
JW 260	A	G0 ± 1	6030 ± 170	0.0 ± 1.1	0.20 ± 0.04	18.0 ± 5.5	3.5 ± 0.5	2.5 ± $^{0.2}_{0.3}$
	B	F7 ± 3	6320 ± 210	0.0 ± 1.1	0.00 ± 0.04	12.1 ± 3.7	4.0 ± 0.5	2.3 ± $^{0.2}_{0.2}$
JW 553	A	K7 ± $^{1}_{2}$	4060 ± 250	3.0 ± 0.1	0.22 ± 0.06	5.2 ± 1.5	0.35 ± $^{0.35}_{0.32}$	0.8 ± $^{0.3}_{0.2}$
	B	M1 ± 3	3710 ± 440	1.4 ± 1.7	1.72 ± 0.57	0.16 ± 0.02	8 ± $^{32}_{5}$	0.57 ± $^{0.13}_{0.3}$
JW 566	A	K7 ± 1.5	4060 ± 280	4.4 ± 1.1	0.02 ± 0.05	1.3 ± 0.2	1.2 ± $^{1.8}_{0.5}$	0.75 ± $^{0.35}_{0.23}$
	B	M1.5 ± 2	3705 ± 290	0.0 ± 0.3	0.00 ± 0.05	1.2 ± 0.1	0.9 ± $^{0.5}_{0.7}$	0.48 ± $^{0.2}_{0.13}$
JW 598 ^b	A	K5 ± 2	4350 ± 380	4.4 ± 0.4
	B	M2 ± 4	3560 ± 570	5.0 ± 0.4	0.01 ± 0.44
JW 648	A	M0 ± 1	3850 ± 170	2.3 ± 0.1	0.06 ± 0.05	1.7 ± 0.1	0.7 ± 0.2	0.57 ± $^{0.13}_{0.12}$
	B	M3.5 ± 2	3340 ± 290	2.3 ± 0.3	0.00 ± 0.14	0.49 ± 0.04	1.0 ± 0.8	0.30 ± $^{0.11}_{0.10}$
JW 681	A	M1 ± 1.5	3710 ± 220	8.1 ± 0.6 ^c	0.09 ± 0.06
	B	M3.5 ± 4	3340 ± 550	7.6 ± 1.2 ^c	0.26 ± 0.15
JW 687	A	M2.5 ± $^{0.5}_{1}$	3490 ± 150	6.1 ± 0.1	0.43 ± 0.10	1.7 ± 0.1	0.10 ± 0.05	0.38 ± $^{0.05}_{0.06}$
	B	M2 ± 1	3560 ± 150	7.4 ± 0.4	1.62 ± 0.27	0.54 ± 0.06	1.3 ± $^{0.5}_{0.4}$	0.39 ± $^{0.06}_{0.06}$
JW 876	A	M0.5 ± 1	3790 ± 210	2.3 ± 0.6 ^c	0.02 ± 0.06
	B	M1.5 ± 3	3630 ± 440	0.0 ± 1.0 ^c	0.38 ± 0.13
JW 959	A	K3 ± 3	4730 ± 450	3.0 ± 0.8 ^c	0.27 ± 0.10
	B	K3 ± 2	4730 ± 370	5.6 ± 0.7 ^c	0.00 ± 0.08
[HC2000] 73	A	M2 ± 1	3560 ± 150	1.1 ± 0.5	1.63 ± 0.28	0.21 ± 0.03	3.5 ± $^{3.0}_{1.0}$	0.38 ± $^{0.10}_{0.06}$
	B	M7 ± 1	2880 ± 140	0.0 ± 0.5	0.01 ± 0.24	0.08 ± 0.01	0.6 ± $^{3.0}_{0.4}$	0.09 ± $^{0.05}_{0.05}$
TCC 15 ^b	A	K4 ± 2	4590 ± 290	10.6 ± 0.4	...	2.7 ± 0.3	1.8 ± $^{3.2}_{1.0}$	1.5 ± $^{0.2}_{0.5}$
	B	3.0 ± 2.8
TCC 52	A	M0.5 ± 2	3790 ± 300	0.7 ± 0.3	4.42 ± 0.36	10.4 ± 0.9	0.01 ± $^{0.20}_{0.01}$	0.6 ± $^{0.3}_{0.2}$
	B	M2 ± 1	3560 ± 150	2.0 ± 0.4	0.80 ± 0.12	3.1 ± 0.4	0.05 ± $^{0.15}_{0.04}$	0.39 ± $^{0.08}_{0.05}$
TCC 55	A	M3 ± 1	3420 ± 150	3.0 ± 0.7	0.14 ± 0.10	0.09 ± 0.02	6 ± $^{6}_{2}$	0.29 ± $^{0.07}_{0.06}$
	B	0.0 ± 0.7
JW 63	A	K7 ± 2	4060 ± 320	2.0 ± 0.3	0.00 ± 0.05	1.3 ± 0.1	1.2 ± $^{1.8}_{0.5}$	0.75 ± $^{0.4}_{0.25}$
	B	M3 ± 2	3420 ± 290	3.2 ± 0.3	0.00 ± 0.21	0.84 ± 0.07	0.7 ± $^{0.5}_{0.6}$	0.33 ± $^{0.15}_{0.10}$
JW 128	A	M0 ± 2	3850 ± 390	2.2 ± 0.2	0.00 ± 0.11	1.6 ± 0.1	0.7 ± $^{1.0}_{0.6}$	0.56 ± $^{0.39}_{0.19}$
	B	M0 ± 2	3850 ± 390	0.8 ± 0.2	0.00 ± 0.13	0.89 ± 0.06	1.2 ± $^{2.5}_{0.5}$	0.57 ± $^{0.40}_{0.19}$
JW 176	A	K7 ± 2	4060 ± 320	3.2 ± 0.2	0.02 ± 0.16	3.5 ± 0.2	0.45 ± $^{0.45}_{0.40}$	0.75 ± $^{0.40}_{0.25}$
	B	M0 ± 2	3850 ± 390	4.0 ± 0.2	0.00 ± 0.19	2.8 ± 0.2	0.45 ± 0.40	0.58 ± $^{0.40}_{0.21}$
JW 391	A	M0.5 ± 3	3790 ± 440	1.2 ± 0.2	0.71 ± 0.31	1.1 ± 0.1	0.9 ± $^{1.6}_{0.8}$	0.52 ± $^{0.40}_{0.10}$
	B	M3.5 ± 2	3340 ± 290	0.1 ± 0.2	0.00 ± 0.22	0.15 ± 0.01	3.5 ± $^{3.5}_{1.5}$	0.28 ± $^{0.12}_{0.11}$
JW 709	A	K7 ± 2	4060 ± 320	1.7 ± 0.2	0.00 ± 0.24	0.94 ± 0.06	1.8 ± $^{3.2}_{0.9}$	0.76 ± $^{0.40}_{0.25}$
	B	K7 ± 1	4060 ± 250	1.6 ± 0.2	0.00 ± 0.11	0.69 ± 0.05	3.0 ± $^{4.0}_{1.6}$	0.78 ± $^{0.25}_{0.23}$
JW 867	A	M1 ± 1	3710 ± 150	0.1 ± 0.3	0.13 ± 0.12	0.89 ± 0.08	1.0 ± $^{0.4}_{0.2}$	0.48 ± $^{0.10}_{0.10}$
	B	M2.5 ± 1	3490 ± 150	0.0 ± 0.3	0.02 ± 0.11	0.77 ± 0.07	0.9 ± $^{0.2}_{0.6}$	0.37 ± $^{0.06}_{0.06}$

^a Results from comparing T_{eff} and L_* with the models of Siess et al. (2000).

^b The spectral features allow us to assign a spectral type, but the spectral fitting routine was unable to match the overall continuum shape of this target, in particular for a strong increase at $\lambda > 24000 \text{ \AA}$.

^c These extinction values were derived from our spectral fitting instead of photometry, since our photometric information was incomplete.

Table 3.6: Individual component properties of all targets with detectable photospheric features (ctd.)

Name	Comp.	R_* [R_\odot]	E_{J-H} [mag]	E_{H-K_s} [mag]	$W_{\text{Br}\gamma}$ ^a [Å]	disk prob.	$\log(L_{\text{acc}}/L_\odot)$	\dot{M}_{acc} [$10^{-9} M_\odot \text{yr}^{-1}$]
[AD95] 1468	A	1.04 ± 0.05	0.43	0.47	1.48 ± 0.50	0.50	-1.92 ± 0.21	2.2 ± 1.44
	B	(<1.62)	0.05
[AD95] 2380	A	(1.00 ± 0.19)	0.97
	B	(<3.51)	0.01
JW 235	A	(5.13 ± 0.47)	1.00
	B	2.24 ± 0.29	-0.04	-0.26	3.67 ± 0.93	0.84	-1.37 ± 0.18	$11 \pm \frac{9}{8}$
JW 260	A	3.89 ± 0.11	0.29	0.19	-2.52 ± 0.15	0.00
	B	2.91 ± 0.10	0.44	0.43	-4.05 ± 0.15	0.00
JW 553	A	4.63 ± 0.28	-0.01	-0.03	<0.54	0.00	< -1.11	< 18
	B	0.97 ± 0.12	-0.14	0.26	<2.04	0.00	< -2.68	< 0.14
JW 566	A	2.33 ± 0.16	0.49	0.78	0.64 ± 0.19	0.70	-1.01 ± 0.05	$12 \pm \frac{6}{4}$
	B	2.61 ± 0.20	0.21	0.29	<0.70	0.13	< -1.30	< 11
JW 598	A	(<0.34)	0.00
	B	<2.08	0.07
JW 648	A	2.90 ± 0.13	0.16	0.30	<0.52	0.33	< -1.43	< 7.6
	B	2.09 ± 0.18	0.21	0.14	<0.84	0.12	< -1.76	< 4.9
JW 681	A	<0.50	0.00
	B	1.18 ± 0.26	0.90
JW 687	A	3.58 ± 0.15	0.03	-0.06	<0.61	0.02	< -1.56	< 10
	B	1.93 ± 0.08	0.34	0.49	<1.34	0.00	< -1.67	< 4.2
JW 876	A	<0.55	0.47	< -0.87	...
	B	1.30 ± 0.24	0.99	-0.97 ± 0.04	...
JW 959	A	-1.86 ± 0.27	0.00
	B	-0.81 ± 0.25	0.00
[HC2000] 73	A	1.21 ± 0.05	0.34	0.51	3.68 ± 0.37	1.00	-1.78 ± 0.16	$2.1 \pm \frac{1.1}{1.0}$
	B	1.17 ± 0.06	-0.22	-0.02	<1.36	0.00	< -2.64	< 1.2
TCC 15	A	2.63 ± 0.17	0.09	0.06	(-0.79 ± 0.21)	0.00
	B	(16.69 ± 2.73)	1.00
TCC 52	A	7.50 ± 0.59	0.36	0.59	8.00 ± 0.56	1.00	0.39 ± 0.20	$1230 \pm \frac{950}{830}$
	B	4.61 ± 0.19	0.28	0.40	2.04 ± 0.25	1.00	-0.49 ± 0.07	$153 \pm \frac{42}{34}$
TCC 55	A	0.87 ± 0.04	0.86	1.23	<0.72	0.00	< -2.19	< 0.7
	B	(<0.68)	0.00
JW 63	A	2.32 ± 0.18	-0.06	-0.10	<1.02	0.00	< -1.54	< 3.6
	B	2.62 ± 0.22	-0.16	-0.44	<1.17	0.09	< -1.76	< 5.5
JW 128	A	2.81 ± 0.28	-0.05	-0.05	<1.28	0.06	< -1.21	< 12
	B	2.12 ± 0.21	0.07	0.14	<1.26	0.09	< -1.40	< 5.9
JW 176	A	3.80 ± 0.30	-0.04	-0.08	<1.50	0.02	< -0.81	< 31
	B	3.75 ± 0.38	-0.18	-0.26	<1.47	0.02	< -0.93	< 30
JW 391	A	2.42 ± 0.28	0.21	0.35	12.91 ± 0.45	1.00	-0.12 ± 0.11	$140 \pm \frac{120}{50}$
	B	1.16 ± 0.10	0.20	0.11	1.41 ± 0.48	0.58	-2.20 ± 0.22	$1.1 \pm \frac{0.8}{0.8}$
JW 709	A	1.97 ± 0.16	-0.00	-0.01	<1.01	0.00	< -1.66	< 2.3
	B	1.68 ± 0.10	-0.01	-0.02	<0.97	0.06	< -1.87	< 1.2
JW 867	A	2.29 ± 0.09	0.16	0.24	1.03 ± 0.31	0.80	-1.50 ± 0.12	6.0 ± 2.3
	B	2.41 ± 0.10	0.14	0.19	2.41 ± 0.29	1.00	-1.05 ± 0.05	23 ± 4.8

^a Positive values indicate emission lines, negative values indicate Br γ in absorption. Values in parantheses are lower limits since no correction for veiling τ_K was possible.

(JW 553, JW 598, JW 648, JW 681, JW 687, TCC 15⁴). Using the observed $V - I$ colors and an estimate of $(V - I)_0$ derived from our measured effective temperatures and the 1Myr stellar evolutionary model of Baraffe et al. (1998), we calculated extinctions as $A_V \approx [(V - I) - (V - I)_0]/0.4$ (Bessell & Brett 1988). The results are consistent with our near-infrared extinction measurements usually to within ~ 1.0 mag, except for JW 687 A, where we find a substantially larger A_V from the optical data than from our NIR measurements. This discrepancy for this target, however, could be explained by its large veiling value (optical veiling can reduce the measured $V - I$ color and thus the derived extinction).

3.2.2 Spectral types and veiling

Owing to the young age of the targets in our sample, the stars are still contracting, hence their surface gravities ($\log g$) are lower than those of main sequence stars. However, to find appropriate templates for spectral classification and the estimation of both the visual extinction A_V and near-infrared continuum excess in K -band (veiling, r_K), one needs to find templates with physical conditions as close as possible to the pre-main sequence stars in this sample. Since no comprehensive catalog of pre-main sequence spectra at a spectral resolution of $R = 1400$ or higher exists, we compared our target spectra to those of dwarfs and giants using a method similar to that shown in Prato et al. (2003). We measured the equivalent widths of the T_{eff} and $\log g$ -sensitive photospheric features Na I, Ca I, $^{12}\text{CO}(2-0)$, and $^{12}\text{CO}(4-2)$ (wavelengths see Table 3.5) for all target component spectra as well as dwarf and giant spectra from the IRTF spectral library (Rayner et al. 2009; Cushing et al. 2005) in a spectral range between F2 and M9. Fig. 3.4 demonstrates that dwarf spectra are more suitable templates for our sample than giant stars in the same spectral range. We note that veiling reduces the equivalent widths of spectral lines according to $W_\lambda^{\text{measured}} = W_\lambda/(1+r_K)$ (see also Sect. 3.2.4) and points in Fig. 3.4 would move towards the origin if the veiling is high. It would therefore be necessary to only compare targets with small r_K , which is only possible after the veiling was determined using the templates. However, we see that not only the distribution of $r_K < 0.2$ targets but all targets are well-congruent with the dwarf locus, indicating that dwarfs are suitable for the determination of the stellar parameters of our pre-main sequence stars. We also considered intermediate solutions between dwarfs and giants as possible templates. Despite the possibly closer match in $\log g$ of pre-main sequence stars, no improvement in the resulting match with our target equivalent widths could be seen. Thus, in order to minimize additional noise sources, we used dwarf templates for the evaluation that we now describe.

Spectral types, spectroscopic extinctions, and veiling were simultaneously determined by a χ^2 minimization method that modifies the template spectra according to

$$F^*(\lambda) = \left(\frac{F_{\text{phsph}}(\lambda)}{c} + k \right) e^{-\tau_\lambda} \quad (3.2)$$

⁴Prosser et al. (1994) list the brighter component in V as the primary of binary. We show, however, that it is of later spectral type than its companion. Accordingly, our designation swaps both components with respect to the Prosser et al. paper.

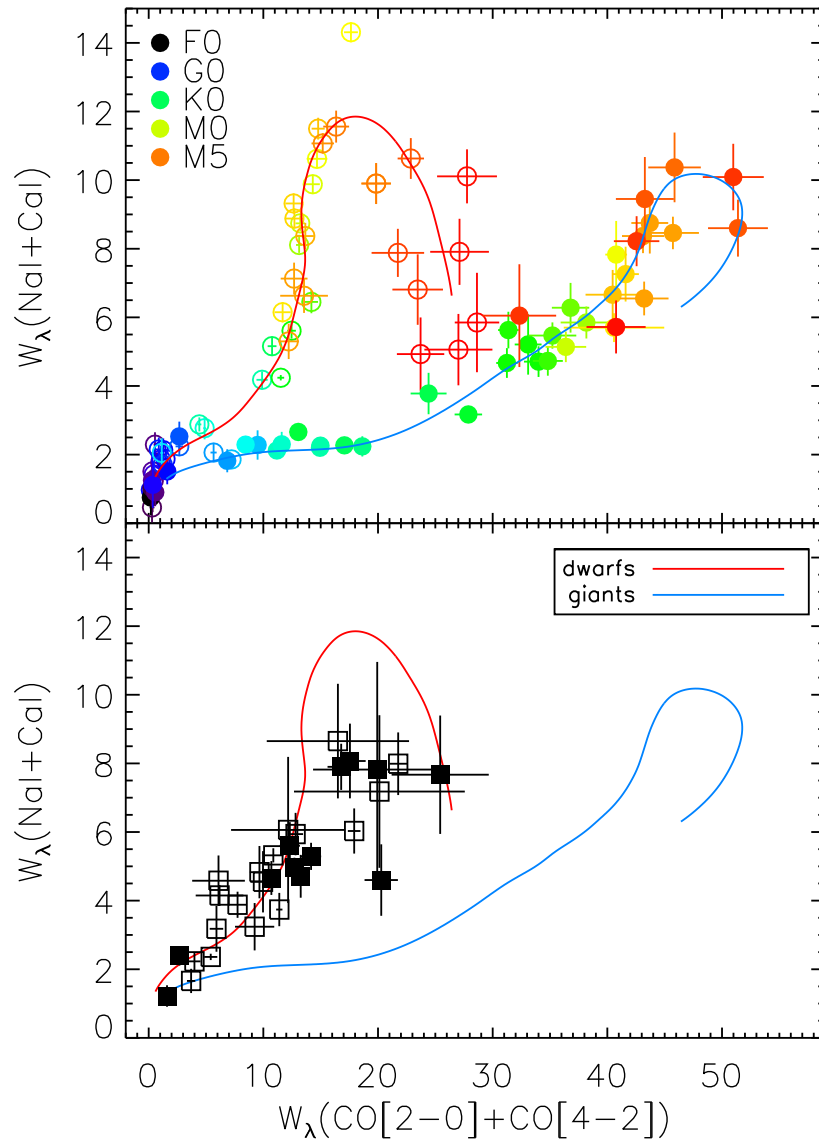


Figure 3.4: *Top*: The equivalent widths of Na I+Ca I versus CO[2-0]+CO[4-2] as an indicator of T_{eff} and $\log g$ for dwarf (open circles) and giant (filled circles) template spectra from the IRTF spectral library. Spectral types are color-coded according to the legend in the upper left. The red and blue lines guide the eye to the two relations. *Bottom*: The same plot including the derived dwarf and giant relations (red and blue curve) as in the top panel, overplot with the ONC target components. Open symbols show targets with high veiling $r_K > 0.2$, filled symbols $r_K < 0.2$. Two targets, TCC 15B and [AD95] 2380B, are off bounds at high $W_\lambda(\text{Na I}+\text{Ca I})$.

46 3. Disk & star parameters of T Tauri binaries of the Orion Nebula Cluster

(cf. Prato et al. 2003) with $\tau_\lambda = (0.522/\lambda)^{1.6} A_V^{\text{spec}}$, where F_{phsph} is the photospheric flux of the templates and k is the K -band excess in units of $F_{\text{phsph}}(2.2\mu\text{m})/c$, i.e. the excess over the photospheric flux at $2.2\mu\text{m}$ normalized with a constant c . We introduce the extinction variable A_V^{spec} , since it is typically not identical to the photometric extinction A_V . The excess k is assumed to not vary strongly with wavelength within the limits of K -band, i.e., it is $k(\lambda) = \text{const}$. Although some of the targets show evidence of a slightly stronger excess towards the red edge of the K -band, the theoretically slightly poorer fit of line depth at the long wavelength end does not have a strong impact on the resulting k since it is determined from the best fit to the entire wavelength range of our spectra. For each template spectral type, the three variables A_V^{spec} , k , and c were modified with 120–160 steps each within a reasonable range of values and we found a minimum value of

$$\chi^2 = \frac{1}{n - \text{dof} - 1} \sum_{i=1}^n \frac{(F_i - F_i^*)^2}{\Delta F_i^2} \quad (3.3)$$

where n is the number of pixels in the spectrum, $\text{dof} = 3$ the degrees of freedom, and F_i , ΔF_i , and F_i^* the flux in the i -th pixel of the target spectrum, its measurement error, and the modified template spectrum, respectively. The minimum of the χ^2 distribution (see Fig. 3.5) was compared for different spectral types and the nine best-fitting solutions (spectral type along with the corresponding optimal combination of A_V^{spec} , k , c) when examined by eye. Spectral types were selected by comparing the overall shape of the continuum and the strength of several photospheric absorption lines of the modified (Eq. 3.2) best-fit templates. Uncertainties in the spectral type were estimated from the range of spectra that could possibly fit the data. This resulted in a typical uncertainty of one or two subclasses. The uncertainty in k was determined from the error ellipse in a three-parameter χ^2 -minimization at $\chi_{\text{min}}^2 + 3.5$ (Wall 1996).

An example of the best-fit result for one of our target binaries is shown in Fig. 3.6. The best template fits of all spectra for which spectral parameters could be determined are shown in Appendix B.1. From the excess flux k , the K -band continuum excess r_K is calculated to be

$$r_K = \frac{k}{F_{\text{phsph}}(2.2\mu\text{m})/c} \quad (3.4)$$

The results from the spectral fitting are summarized in Table 3.6. Some spectra do not show any photospheric features and no estimation of the spectral type was possible. These target components are marked with ellipses in the spectral type-dependent columns of Table 3.6.

Despite the wide range of extinction values derived from the photometric and spectroscopic determination, we did not force the χ^2 minimization to match the photometric A_V values from Sect. 3.2.1 for the following reason. In the χ^2 fitting routine, the determination of the other parameters (spectral type, veiling, normalizing constant c) does not depend on the value chosen for A_V as long as it has reasonable values. While spectral types are mainly determined by line ratios, veiling is sensitive to line depths; both signatures are not strongly influenced by extinction. However, forcing A_V to a particular value typically produces poor fits and hence A_V is kept as a free parameter.

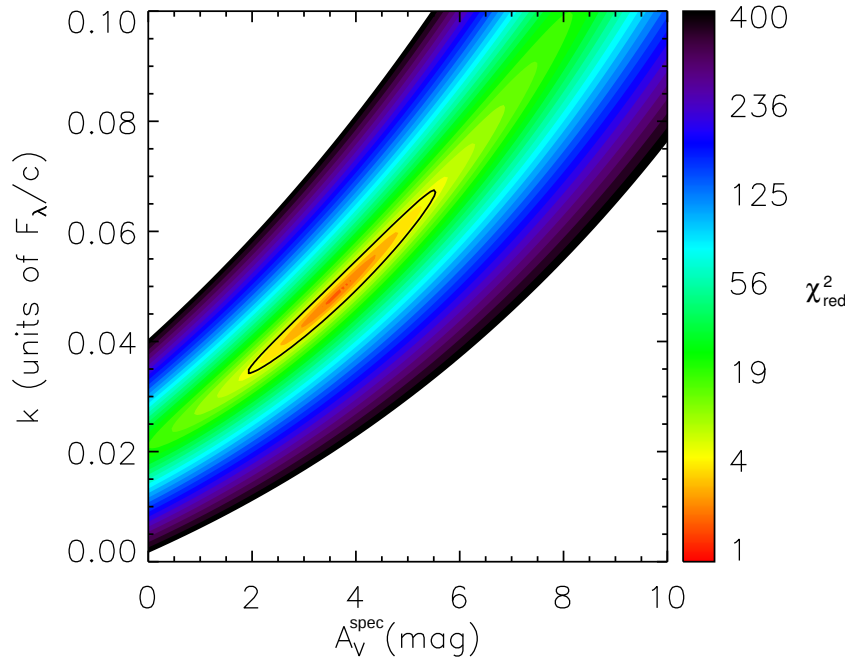


Figure 3.5: Contour plot of reduced χ^2 as a function of spectroscopic extinction A_V^{spec} and K -band excess k of the best template fit to JW 553B. The color bar on the right measures the level of reduced χ^2 , white areas in the plot mark regions of reduced $\chi^2 > 400$. The black contour marks the location of the level $\chi^2 = \chi_{\text{min}}^2 + 3.5$.

We only use the photometric extinctions listed in Table 3.6 for further evaluation. Exceptions are JW 681, JW 876, and JW 959 where no photometric extinctions could be measured and our best estimates for A_V come from spectroscopy with an uncertainty determined from the fitting error ellipse that is similar to the uncertainty in k .

3.2.3 Luminosity, effective temperature, and radius

Luminosities L_* of our target components were derived from bolometric magnitudes by applying bolometric corrections BC_J (Hartigan et al. 1994) to the measured J -band magnitudes with a distance to Orion of 414 ± 7 pc (Menten et al. 2007) and J -band extinctions of $A_J = 0.27A_V$ (Cohen et al. 1981). The J -band was chosen to help us minimize the impact of hot circumstellar material, which mainly contributes flux at longer wavelengths (K and L -band) i.e. closer to the maximum of the $T \sim 1500$ K blackbody emission from the inner dust rim (Meyer et al. 1997). The resulting luminosities are listed in Table 3.6, along with effective temperatures T_{eff} derived from their spectral types and SpT– T_{eff} relations (earlier than M0: Schmidt-Kaler 1982; later or equal to M0: Luhman et al. 2003). Luminosity uncertainties were propagated from the magnitude, extinction, and distance uncertainties but do not include any of the intrinsic variability of the targets since we

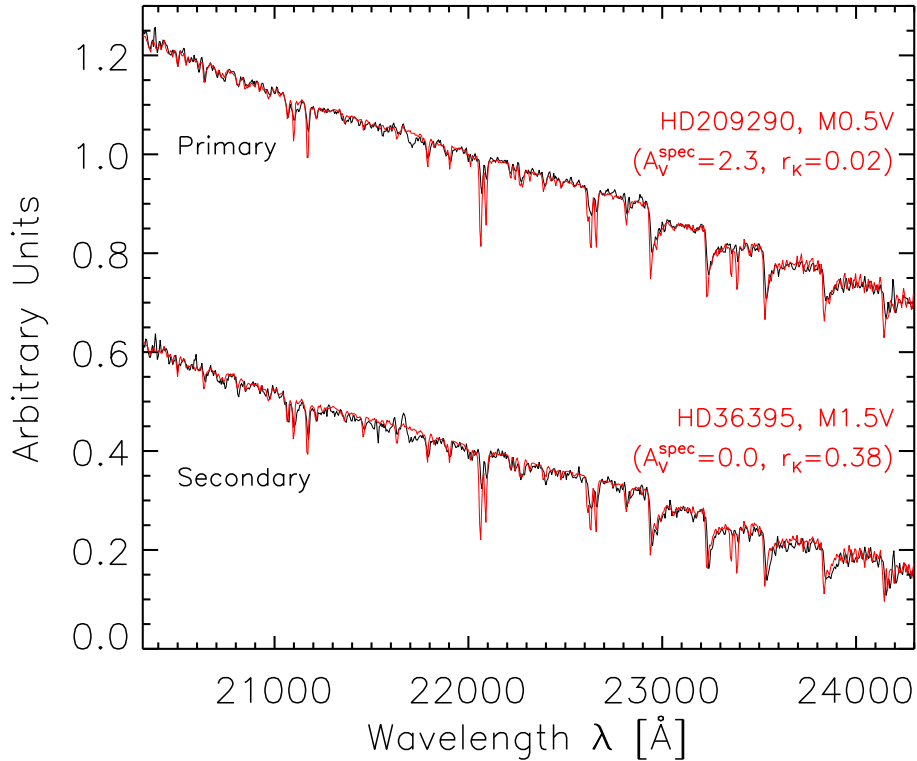


Figure 3.6: The result of the spectral template fitting for the primary and secondary component of JW 876. The black curves show the spectrum of the primary and secondary component respectively, offset for clearer visibility. The red curves are the corresponding best-fit models from the IRTF spectral library, modified according to Eq. (3.2) with extinction and veiling values from Table 3.6. Best-fit results for all targets in Appendix B.1.

cannot estimate the magnitude of the effect for any individual target component⁵. We estimate, however, an average impact of variability by varying M_J by 0.2 mag (Carpenter et al. 2001) and rederiving the luminosity of each target. We observe a difference in the derived luminosities of up to 20% with a sample median of 0.08 dex. This is twice as large as the typical propagated random uncertainties. Stellar radii R were then calculated from L_* and T_{eff} from the basic relation

$$L_* = 4\pi R^2 \sigma T_{\text{eff}}^4 \quad . \quad (3.5)$$

The HR diagram: ages and masses

Effective temperatures and luminosities were used to derive ages and masses by comparison with evolutionary tracks from Siess et al. (2000). Fig. 3.7 shows the position on the HR-diagram of all components with measured T_{eff} and L_* . The derived masses are – except

⁵The variability of a few of the target binaries was observed by Carpenter et al. (2001), although they did not resolve the individual components.

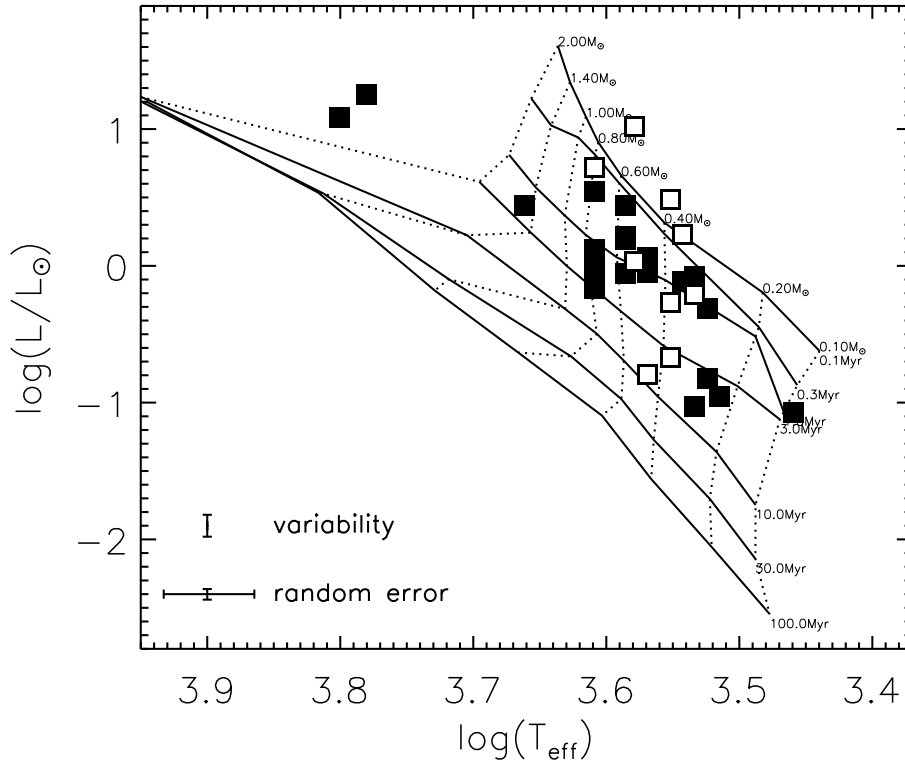


Figure 3.7: HR-diagram with evolutionary tracks from [Siess et al. \(2000\)](#). Open symbols are target components with high veiling $r_K > 0.2$, filled symbols have $r_K \leq 0.2$. Typical uncertainties from random errors and the resulting uncertainty from 0.2 mag intrinsic photometric variability ([Carpenter et al. 2001](#)) are shown in the lower left. For the determination of the parameters (age & mass, see Table 3.6), more tracks and isochrones were used than shown in the plot; they were omitted for a clearer illustration.

for three targets – below $1 M_\odot$, and ages are found to be in the range of 10^4 – 10^7 yr, with an average of 0.97 Myr. One object, the secondary component of [HC2000] 73, has an estimated mass of $0.09 \pm 0.05 M_\odot$, indicating that it is a possible substellar object. The details of this binary are discussed in an accompanying paper ([Petr-Gotzens & Daemgen 2012, in prep.](#)).

It is apparent that the targets that are classified as the youngest, are those with the highest veiling. Their high luminosities thus probably do not represent extreme youth but are rather an indication of hot circumstellar material contributing near-infrared flux even in J -band. This is not properly accounted for when extracting ages from the HR diagram because the infrared-excess in the J -band is unknown for our targets and therefore not subtracted from their brightness. A consequence is the apparent non-coevality of binary stars with at least one component with high veiling, as discussed in Sect. 3.3.1 and Fig. 3.11. Furthermore, apparently old ages can be caused by underestimated extinctions, making these targets appear underluminous and thus too old. However, since the evolutionary tracks for stars of a certain mass are almost vertical ($T_{\text{eff}} \approx \text{const}$) in this part of the HR

diagram, the uncertainty in luminosity does not translate into an equally large uncertainty in mass.

3.2.4 Accretion: $W(\text{Br}\gamma)$, L_{acc} , and \dot{M}_{acc}

The accretion activity of each target component was inferred from the Br γ emission feature at 21665 Å. Our measurements are described in this section.

Equivalent widths of Br γ emission

We measured the equivalent width of the Br γ line

$$W_{\text{Br}\gamma} = \int_{\text{Br}\gamma} \frac{F_\lambda - F_c}{F_c} d\lambda \quad (3.6)$$

in an interval of width 56 Å around the center of Br γ (which was individually fit and re-centered between 21654 Å and 21674 Å) for all target components. The integration interval was chosen to ensure that we include as much line flux as possible, while minimizing the influence from the continuum noise around the line at the spectral resolution of our observations. The continuum F_c was determined from a linear fit to the local pseudo-continuum in a region of width 130 Å shortward and longward of the integration limits. The above definition of equivalent width (Eq. 3.6) returns positive values for emission lines and is negative in case of absorption.

To assess the significance of Br γ emission, we inferred the noise level at the position of Br γ from the surrounding continuum. This allowed us to derive a measure for the probability of the presence of a gaseous accretion disk in a binary component (see Appendix A).

The procedure of measuring equivalent widths was performed in two stages. In the first stage, the method was applied to the uncorrected spectra to serve as a measure of accretion disks (Appendix A), where we sought to assess the significance of the measured emission features and thus do not wish to introduce additional uncertainties by means of further modifications of the spectra. However, spectral features were reduced in strength when veiling was imposed on the spectrum and thus the Br γ equivalent width had to be corrected for r_K to represent the actual emission emitted from the accretion process. This required a second step of either calculating

$$W_\lambda = W_\lambda^{\text{measured}} \cdot (1 + r_\lambda) \quad (3.7)$$

as inferred from eqs. (3.2) and (3.6), or applying Eq. (3.2) with r_K values from Table 3.6 to the reduced spectra (for which extinction does not change the equivalent width and can be assumed to be equal to zero for this calculation). Both options returned very similar results. We chose to modify the spectra and remeasure $W_{\text{Br}\gamma}$ to also obtain good estimates for the continuum flux noise, which does not necessarily transform in the same way. The results for this measurement of the actual equivalent widths of the Br γ emission are listed in Table 3.6. When r_K was unknown, no correction was applied and values in Table 3.6 correspond to lower limits of $W_{\text{Br}\gamma}$.

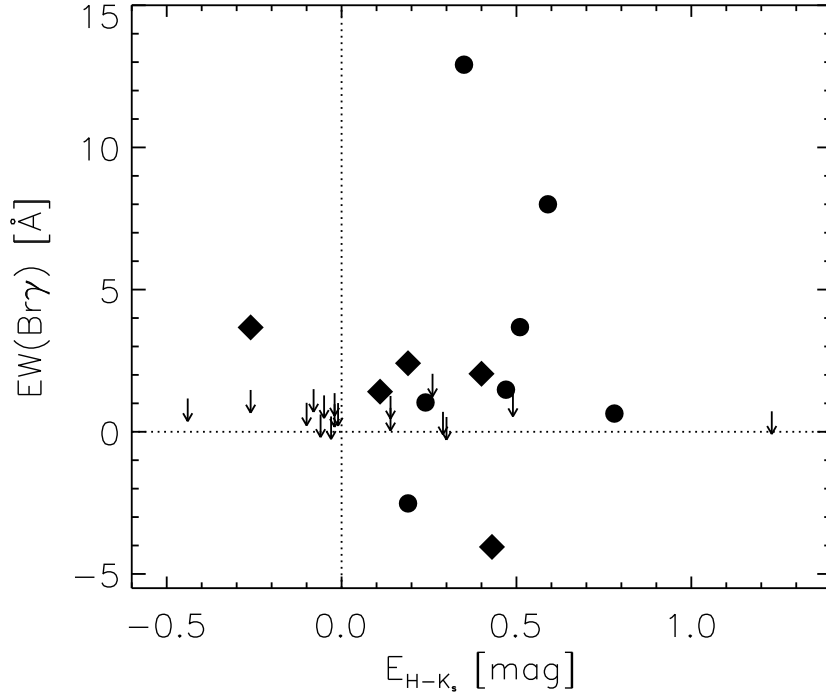


Figure 3.8: Veiling-corrected Bry equivalent width as a function of NIR excess in $(H-K_s)$ color. Circles represent primary, and diamonds secondary binary components. The detection limits of target components with insignificant equivalent widths are marked with arrows.

Bry equivalent widths versus NIR excess

We compared the color excesses E_{H-K_s} , which measure the existence of hot circumstellar material around each binary component (Cieza et al. 2005), with our veiling-corrected Bry emission values. Fig. 3.8 shows that, while all but one target with significant emission in Bry exhibit a NIR excess, the opposite is not true and many targets with NIR excess are found that do not show significant signs of hydrogen emission. This imbalance is well-known and discussed further in Sect. 3.3.2.

The figure shows some interesting features. It seems that there is a slight systematic offset in the calculated excesses relative to the origin, as we see a number of targets clustering around $E_{H-K_s} \approx -0.03$. Assuming that these are targets with no significant color excess, we can infer a small mismatch between the color scales of the theoretical and measured values used to derive E_{H-K_s} . This is partly a consequence of using dwarfs for the theoretical colors $(H-K_s)_{\text{theor}}$ instead of pre-main sequence stars. When using the colors of pre-main sequence stars derived by Luhman et al. (2010), we measured an average shift of 0.015 mag towards redder $H-K_s$ colors that moved the accumulation of low color-excess components towards the origin. Since this correction was small and the Luhman et al. spectral sequence does not cover all spectral types of our sample, we use color-excesses derived from the dwarf colors. In addition, the anticipated systematic offset was negligible compared to the possible photometric variability of ~ 0.2 magnitudes (Carpenter et al.

2001). Although variability does not change our (qualitative) conclusions, it might be a reason for the position of the targets with negative excess with and without significant Br γ emission.

Targets in the bottom right quadrant display Br γ in absorption; since we also detect a NIR emission excess, there is a possibility that Br γ emission generated by accretion cancels with part of the absorption feature. To estimate the real emission strength, one could measure and subtract the strength of Br γ absorption from photospheric standards of the same spectral type. This concerns, however, only the components of JW 260, a binary that was excluded from the discussion and conclusions owing to its earlier spectral type. We thus skip a more thorough evaluation of the accretion state of this binary here.

Br γ line luminosity and mass accretion rates

For target components with full knowledge of extinction and veiling, we calculated Br γ line luminosities and the mass accretion rate \dot{M}_{acc} . The accretion luminosity was derived through

$$\log(L_{\text{acc}}) = (1.26 \pm 0.19) \log(L_{\text{Br}\gamma}/L_{\odot}) + (4.43 \pm 0.79) \quad (3.8)$$

(Muzerolle et al. 1998a) where the Br γ line luminosity is defined as

$$L_{\text{Br}\gamma} = 4\pi r^2 \int_{\text{Br}\gamma} (F_{\lambda} - F_c) d\lambda \quad (3.9)$$

in the same integration limits used for the equivalent width and using a distance to the ONC of $r = 414 \pm 7$ pc (Menten et al. 2007). After correcting the calibrated spectra for veiling and extinction, the data was multiplied with the filter curve, integrated over K_s -band, and converted to L_{acc} according to Eq. (3.8). Uncertainties were estimated from error propagation of all involved parameters including the extrapolation error and the empirical uncertainties in Eq. 3.8. A source of additional uncertainty that we could not quantify in greater detail from our observations is variability. Since the photometry was not taken simultaneously with our spectral observations, the calibration of our spectra might suffer from additional uncertainty when these young targets were observed in different states of activity. Since we had no estimate of the size of this effect for an individual target, we did not introduce any correction but wish to caution that individual accretion luminosities might be offset from the true value. However, assuming that the effect of variability in the accretion luminosities is random, the sample statistics should not be biased.

The mass accretion rate was calculated according to Gullbring et al. (1998) as

$$\dot{M}_{\text{acc}} = \frac{L_{\text{acc}} R_*}{GM_*} \left(\frac{R_{\text{in}}}{R_{\text{in}} - R_*} \right) \quad , \quad (3.10)$$

for a stellar radius R_* and mass M_* from Table 3.6, and the gravitational constant G , assuming that material falls onto the star from the inner rim of the disk at $R_{\text{in}} \approx 5R_*$. The accretion luminosities and mass accretion rates are listed in Table 3.6.

Is the Br γ emission generated by magnetospheric accretion?

The main source of Br γ emission in T Tauri stars is often assumed to be magnetospheric accretion (e.g. Beck et al. 2010). However, mechanisms such as stellar wind, disk wind, outflow, or photoevaporation of the disk by a nearby high-mass star can also contribute to the Br γ emission observed in low-mass stars (Hartmann et al. 1990; Hartigan et al. 1995; Eisner et al. 2010). While the emission region from magnetospheric accretion should be located close to the stellar surface, the sources of most other mechanisms are expected to be located further away at several stellar radii or even in the outer parts of the disk. Detecting a spatial displacement of the Br γ emitting region from the star locus would refute the possibility of magnetospheric accretion as the origin of the emission and render other explanations more likely.

To test this, we used the sky-subtracted raw frames of the spectral observations, showing the spectral traces of both components of each target binary. The orientation of the images is such that the dispersion direction is roughly aligned along the columns of the detector, while the spatial information is aligned along the rows. In each row, we fit two Gaussians to the two profiles of the component spectra, thus measuring the spatial location and width of the spectral profile of the targets in each wavelength bin of size $\sim 5 \text{ \AA}$. Depending on the SNR of the individual observations, the locations of the trace center can be determined to an accuracy of 0.008–0.10 pixels, which, at the spatial resolution of the observations of $\sim 0.027 \text{ arcsec/pix}$, corresponds to $\sim 0.1\text{--}1.1 \text{ AU}$ at the distance of the ONC.

We found no significant offset at $\lambda(\text{Br}\gamma)$ from the rest of the trace for any of the targets in which we observed Br γ in emission. Neither did we detect extended emission in excess of the width of the spectral trace at similar wavelengths. This indicates that the emission indeed originates from a small region close to the stellar surface and is likely to be the product of magnetospheric accretion. However, extended or displaced emission may well be generated mainly perpendicular to the slit. In this case, a displacement of the emission peak could be observed in the dispersion direction. Since we did not measure frequency shifts of spectral features, we cannot exclude this possibility for any individual target component.

While the Br γ emission seems to come from a region close to the star for all targets, we observed one target (TCC 55) in which emission at $\lambda(\text{H}_2) = 21218 \text{ \AA}$ comes from an extended region around the star, rather than the star itself. We observed at least three diffuse H $_2$ emitting regions along the slit, each several pixels wide, one of them apparently surrounding the binary. We used K-band images from the MAD instrument (Petr-Gotzens et al. 2008) to investigate the surrounding area for possible emission sources close to this target located only $0'.49$ from $\theta^1 \text{ Ori C}$. We identified bow-shocks coinciding with the location of the H $_2$ features in the spectra. The diffuse emission around the binary itself might represent the remaining material of a proto-stellar envelope, which would be indicative of a young evolutionary state (i.e. Class I) of the binary.

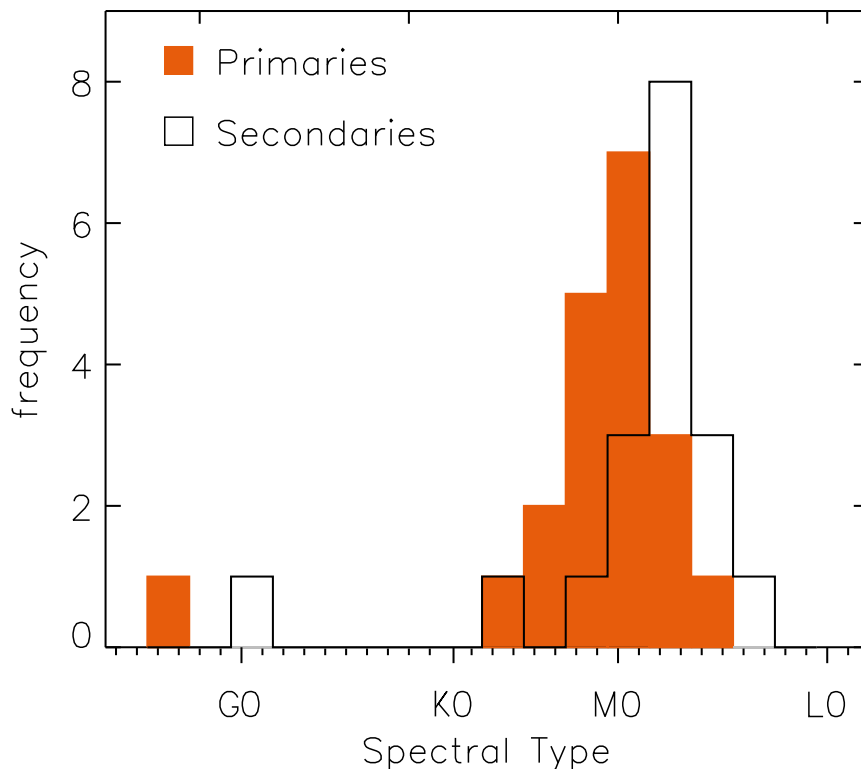


Figure 3.9: Number of target components per spectral type. Solid orange: primaries. Black outline: secondaries. The distributions of primaries and secondaries are only slightly different in spectral types.

3.3 Discussion

3.3.1 Stellar parameters and sample biases

To detect possible biases in the numbers derived from the components of our binary sample, we discuss the degree to which the populations of primaries and secondaries differ and whether they are typical of the ONC population.

Spectral types

It is known that the strengths of accretion parameters correlate with the mass of a star, which (considering the limited spread in age) can be represented by the typically more tightly constrained spectral type⁶. In Fig. 3.9, we see that the spectral type distribution of the primaries peaks at slightly earlier spectral types of M0–M1 than the secondaries (M2–M3). This difference is significant at 98%, according to a Kolmogorov-Smirnov (K-S) test. However, both distributions are indistinguishable from the spectral types of the entire ONC population (Hillenbrand 1997), with K-S probabilities for different distributions of

⁶That accretion signatures do correlate with spectral type can be seen from e.g. Table 7 in White & Ghez (2001).

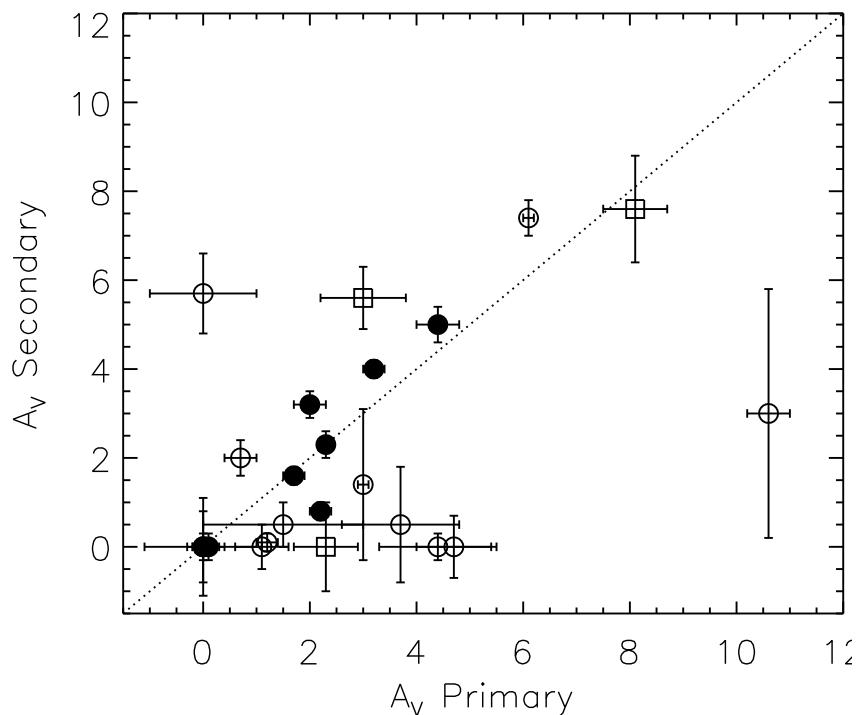


Figure 3.10: Extinction of the primary versus versus secondary components. Circles show targets with A_V determined from the dereddening of the CTT locus. Squares show the spectroscopically determined extinctions of JW 681, JW 876, and JW 959, because photometric extinctions could not be measured. Filled symbols indicate targets with both components having a low veiling $r_K < 0.2$. The dashed line corresponds to equal extinctions.

65% and 57% for primaries and secondaries, respectively. This means that both primaries and secondaries are 'typical' members of the ONC, whereas the primary and secondary spectral type distributions deviate slightly and differences in the derived parameters (such as accretion rates and Br γ -emission strength) can partly be attributed to the – on average – earlier spectral types of the primaries.

Relative extinctions and ages

Interstellar extinction through embedding in the Orion molecular cloud expresses itself as a spatially variable source of extinction that is, nevertheless, very similar for all components of a stellar multiple. An additional source of extinction that can be very different even for components of the same binary can be caused by circumstellar material such as a (nearly edge-on) circumstellar disk, obscuration by the other component's disk, or a remaining dust envelope.

In Fig. 3.10, we can identify and verify the impact of the different sources of extinction. Binaries composed of two low-veiling components have similar extinctions, according to the level of embedding in the cloud, whereas binaries with high-veiling components do not display such correlation. This might be due to dust material from a disk that is detected

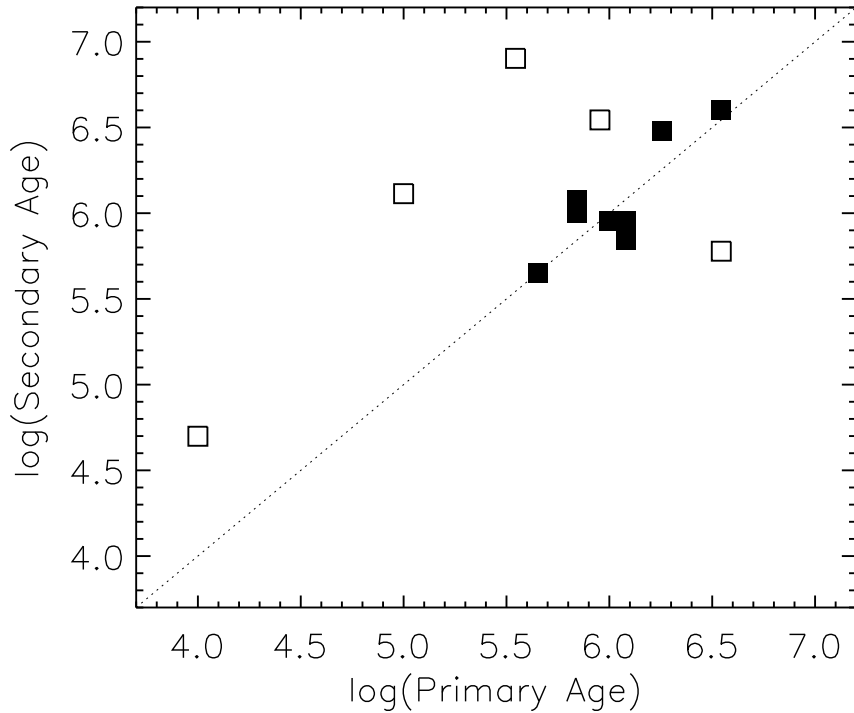


Figure 3.11: Relative ages for the primary and secondary components of all target binaries where both components could be placed in the HR diagram. Filled squares show targets where both components exhibit low veiling $r_K < 0.2$. Targets with open squares have at least one component with strong veiling $r_K \geq 0.2$, thus it is likely that the age estimation from the HR diagram is biased, since extra luminosity from accretion makes the targets appear brighter and thus younger.

by means of its hot-continuum emission from magnetospheric accretion, i.e., veiling (e.g. [Bouvier et al. 2007](#)). In particular, the magnitude of extinction is a strong function of the angle under which the system is observed with close to edge-on disks causing a strong reddening of the NIR colors ([Robitaille et al. 2006](#)). However, our observations do not enable us to determine the inclinations of the circumstellar disks, hence conclusions about disk orientation and alignment cannot be drawn.

The stellar components within a binary are close to being coeval. Fig. 3.11 shows a well-defined correlation of primary and secondary ages for those binaries with little or no veiling. The five binaries with at least one component of $r_K \geq 0.2$ are clearly located off the sequence of coeval binaries, which is probably due to a non-negligible amount of veiling in the J -band for targets with high r_K values. In our present study, we did not attempt to derive accurate absolute ages for our sample, but testing for equal ages within binaries does serve two purposes: *i*) A sanity check. Assuming that binary components do form reasonably close in time ([Kraus & Hillenbrand 2009](#)), we confirmed that our derived T_{eff} and L_* were accurately determined because they result in reasonable values when placed in an HR-diagram. We inferred that the derived parameters (e.g. L_{acc} , \dot{M}_{acc}) are of sufficient quality to help us derive the conclusions of this paper. *ii*) The derived parameters have no

age dependence. Since there is no systematic difference between the primary and secondary age of the binaries, we were able to exclude any dependence on age of the derived relative parameters between the populations of the primaries and secondaries. *iii*) Coequality is consistent with the physical binarity.

While we derived ages $\tau = \log(\text{age})$ that span a range of $\sim 5.5 \leq \tau \leq \sim 6.5$ even for the well-behaved class of low- r_K binaries, this can probably not be attributed to a real age spread. [Jeffries et al. \(2011\)](#) observed no difference in age between stars with and without disks in the ONC, indicating that the age spread must be shorter than the disk lifetime, i.e., significantly more confined than traditionally assumed. We conclude that not only observational uncertainties, but also an intrinsic scatter in the luminosities at constant age must be present. Despite the importance of this observation for the absolute ages of members of star forming regions, we assumed that our *relative* age measurements apply, since the boundary conditions are very similar for both components of the same binary.

3.3.2 Disk evolution around the components of visual ONC binaries

The absolute and differential abundances of disk signatures in the components of our target binaries were found to be a function of binary parameters, as we discuss in the following sections.

The disk fraction of binary components

We derived the fraction of ONC binary components harboring an accretion disk. This number was compared to the single-star disk frequency in the ONC and to binary samples of other star forming regions to expose the effect of binarity and cluster environment on the evolution of circumstellar disks.

The probability density function of the disk frequency was derived in a Bayesian approach as well as the probability of an individual binary component harboring an accretion disk (see Appendix A; individual disk probabilities in Table 3.6). As the strength of disk signatures depends on spectral type (e.g. [White & Ghez 2001](#)), we excluded the binary JW 260 from further evaluation of disk frequencies, since its spectral type is considerably earlier than for the rest of the sample. We measured an accretion disk fraction of $F = 35_{-8}^{+9}\%$ in our sample of 42 spectroscopically observed binary components (Appendix A).

Analyses of the Br γ line are known to return a smaller fraction of accretors than the H α emission feature, which is typically used to decide whether an individual star can be classified as a classical T Tauri star. [Folha & Emerson \(2001\)](#) observed a number of classical T Tauri stars in Taurus-Auriga, measuring NIR emission-line strengths including Brackett- γ signatures. Twenty-four of their targets are in the range of K3–M6 spectral types, comparable to our sample, and three show no emission in Br γ . Hence, a fraction of $f = 0.125$ of all classical T Tauri targets would have to have been misclassified as weak-line T Tauri stars from their Br γ emission. We thus expected a number of $f/(1-f) \times (F \cdot N) \approx 2$ (with $N = 42$ target components) classical T Tauri stars to be classified as non-accreting.

58 3. Disk & star parameters of T Tauri binaries of the Orion Nebula Cluster

The corrected fraction of classical T Tauris among binary star components in the ONC was thus $F_{\text{CTT}} = 40_{-9}^{+10}\%$. Since many studies refer to the fraction of $H\alpha$ -detected classical T Tauri stars rather than the number of accretors from Br γ emission, we used the latter number to compare it with studies of accretion disk frequencies.

Hillenbrand et al. (1998) and Fűrész et al. (2008) found a frequency of accretion disks bearing single stars in the ONC of 50% and 55%, respectively. Both are marginally (1σ and 1.5σ) larger than our measured fraction of $40_{-9}^{+10}\%$. While the Hillenbrand et al. sample was derived from the $I_C - K$ color instead of $H\alpha$ measurements, the Fűrész et al. sample is biased towards classical T Tauri stars making their estimate an upper limit of disk frequency. Both of these findings prevent us from drawing firm conclusions about the difference between the disk frequencies of single stars and binaries. This evidence of a lower disk frequency around 100–400 AU binary components will hence need future confirmation from observations using comparable diagnostics (preferably Br γ) in an unbiased comparison sample.

Similarly, we found evidence of an underrepresentation of dust disks in Orion binaries. Sixteen out of 27 target components (excluding JW 260) with measured $H - K_s$ colors show signs of a dust excess, that is a fraction of $59 \pm 15\%$ compared to the values of 55%–90% found for single stars in the ONC by Hillenbrand et al. (1998) and $80 \pm 8\%$ from Lada & Lada (2003). Since these numbers were derived using indicators other than the $H - K_s$ excess, which is known to typically return a comparably small fraction of dust disks compared to e.g. $K - L$ (Hillenbrand 2005), this evidence cannot be quantified in greater detail.

Our numbers suggest that there is a higher frequency of target components with inner dust disks ($59 \pm 15\%$) than accretion disks ($40_{-9}^{+10}\%$). This discrepancy agrees with observations of single stars in various star-forming regions, where Fedele et al. (2010) concluded that accretion disks decay more rapidly than dust disks in a particular cluster.

The presence of dust and accretion disks around the binary components of our sample is thus consistent with *i*) observations of single stars in a variety of young clusters that dust disks are more abundant than accretion disks in the same cluster and *ii*) the expectation that disk lifetimes are shorter for disks in binary systems than for single stars with comparable properties. The latter is also theoretically motivated by the missing outer disk through dynamical truncation (Artymowicz & Lubow 1994) and the resulting reduced feeding of the inner disk from the outer disk material (Monin et al. 2007). As expected, disk frequency is a function of binary separation (also see Sect. 3.3.2). For example, Cieza et al. (2009) found the component disk frequency in tight < 40 AU binaries of Taurus-Auriga to be significantly lower, at less than one half of the single-star disk frequency. Both their wider binaries (40–400 AU) and our sample (100–400 AU), however, have disk frequencies lower but comparable to single stars, indicating that there is a separation dependent mechanism.

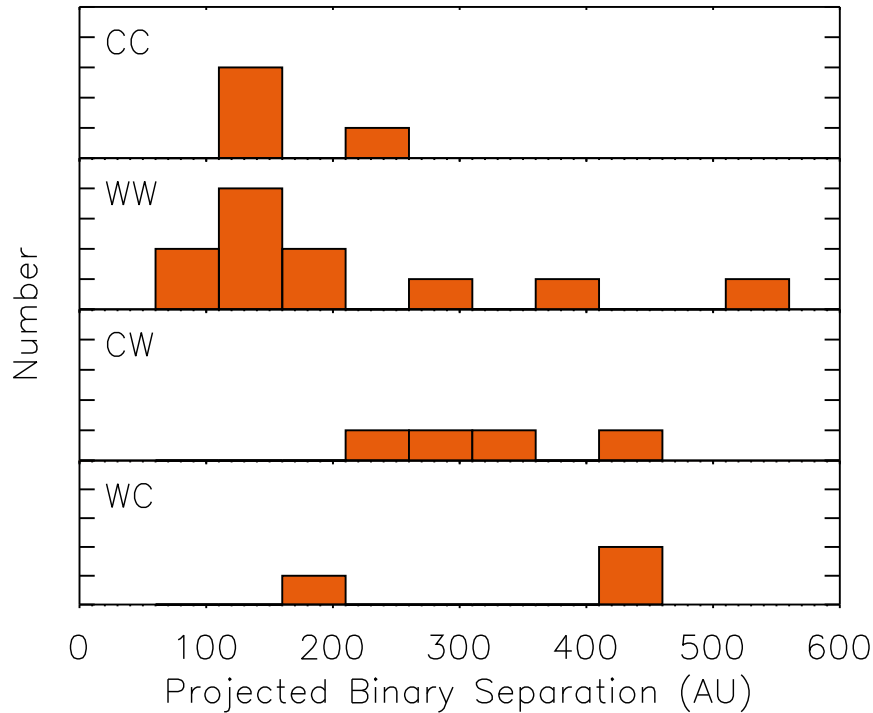


Figure 3.12: Histograms of binary separation as a function of component accretion type (the y-axis tickmarks indicate one binary each). Most of the close binaries are of type WW or CC, i.e., synchronized in their disk evolutionary state.

Synchronized disk evolution in ONC binaries

We detected a significant overabundance of close, $\lesssim 200$ AU pairs of equal emission state, i.e., with both components accreting (CC)⁷ or both components showing no accretion (WW) signatures. This is apparent in Fig. 3.12 and a K-S test indicates 99.5% probability that the separation distribution of equal pairs (CC and WW) differs from the separations of mixed pairs (CW and WC).

To investigate a possible correlation between the synchrony of disks in ONC binaries and their separations, we split our sample into binaries with projected separations larger and smaller than 200 AU. From the content of accreting and non-accreting components in the two separation bins, we predicted the average number of CC, WW, and mixed systems by random pairing, and compare it to our measured distribution. If there were no correlation between the evolution of both components of the same binary, the randomly paired sample of the same number of components (W and C) should be consistent with our observed

⁷To ease the reading of the binary categories, we use the common abbreviations 'C' for accreting components (referring to classical T Tauri Stars), and 'W' for non-accreting components (*weak-line* T Tauri stars) where in the designation of a binary pair (e.g. 'CW') the first position describes the primary (here 'C') and the second the secondary (here 'W') component state. We note, however, that we only refer to the presence of accretion as measured through Bry, which is correlated with but not equal to the the distinction between weak-line and classical T Tauri stars (see also the discussion Sect. 3.3.2).

60 3. Disk & star parameters of T Tauri binaries of the Orion Nebula Cluster

sample. With 18 non-accreting components and 6 accretors in the sample of 12 binaries with separations < 200 AU, we expect an average of $\sim 1.2 \times \text{CC}$, $\sim 6.9 \times \text{WW}$, and ~ 4.1 mixed systems, as predicted by a Monte Carlo simulation. However, we found $3 \pm 1 \times \text{CC}$, $9 \pm 0 \times \text{WW}$, and 0_{-0}^{+2} mixed pairs⁸. This is clearly incompatible with the prediction of random pairing. On the contrary, wide-separation binaries are well described through random pairing with predicted values of $2.2 \times \text{CC}$, $4.1 \times \text{WW}$ and $4.8 \times \text{mixed}$ and measured values of $1_{-0}^{+1} \times \text{CC}$, $3_{-1}^{+2} \times \text{WW}$ and $7_{-2}^{+1} \times \text{mixed}$.

White & Ghez (2001) observed a similar underdensity of mixed pairs among binaries with separations < 210 AU in a sample of 46 binaries in the Taurus-Auriga star-forming association. They concluded that synchronized evolution, which they attributed to the existence of a circumbinary reservoir, can more or less equally replenish the circumprimary and circumsecondary disks, as previously suggested by Prato & Simon (1997).

Can circumbinary disks of sufficient size survive in the ONC and thus be the cause for the synchronization of disk evolution? The typical size of a disk in the Trapezium region is below 200 AU (Vicente & Alves 2005) and only 3 of 149 analyzed systems – the authors claim completeness for large disks > 150 AU at moderate extinctions – were found to have disk sizes > 400 AU. However, circumbinary disks have inner radii of at least twice the binary separation (Artymowicz & Lubow 1994). This requires circumbinary disk sizes of more than 400 AU in diameter for a binary with 100 AU separation and even $\gtrsim 800$ AU circumbinary disks for 200 AU binaries. Assuming that dynamical interactions (Olczak et al. 2006) and photoevaporation (Mann & Williams 2009) are the reason for disk truncation in the ONC, the observed size limits of single star disks should also apply to circumbinary matter. This implies that circumbinary disks of binary systems > 100 AU should not be largely abundant since they are typically truncated to radii below the dynamically induced inner hole radius. These considerations render it unlikely that stable circumbinary disks are the reason for disk-synchronization in the inner regions of the Orion Nebula Cluster. Considering other star-forming regions, one out of currently a handful of systems that were observed with circumbinary material has a separation of larger than 100 AU, UY Aur (see Close et al. 1998; other systems are e.g. GG Tau, Dutrey et al. 1994; V892 Tau, Monnier et al. 2008; the Orion proplyd 124-132, Robberto et al. 2008). Since the current number of directly detected circumbinary disks is still very small, it is not yet clear whether large circumbinary disks can contribute significantly to synchronizing individual component disks in star-forming regions that are less dense than the ONC.

Vicente & Alves (2005) observed no trend in the disk sizes with distance to θ^1 Ori C out to $\sim 4'$, which means that Orion disks are small, independent of their position in the inner ~ 50 arcmin² of the cluster. Furthermore, we would expect to see a larger ratio of CC binaries to WW binaries at large distances from θ^1 Ori C when circumbinary disks are present only in the outer parts of the cluster and transfer a significant amount of material to the individual stellar disks. The distribution of CC and WW in our ONC does

⁸uncertainties are derived from the possibility of a binary changing classification within its 1σ limit of $W_{\text{Br}\gamma}$, i.e., a CC might turn into a CW, if its secondary is classified as C but with an equivalent width that is less than 1σ away from W_{min} .

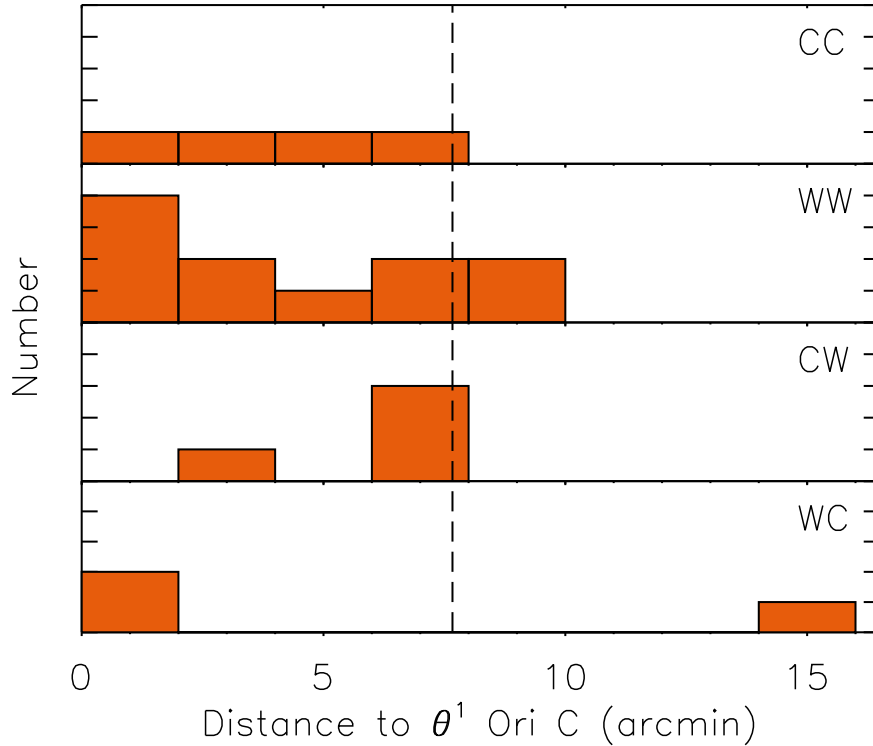


Figure 3.13: Histograms of distance to θ^1 Ori C as a function of accretion type. The histogram shows no indication that binaries of any type are more likely at any distance. The vertical dashed line shows the radius ($460''$; Reipurth et al. 2007) inside which the ratio of wide binaries ($0''.5-1''.5$) to close binaries ($0''.15-0''.5$) drops considerably, probably owing to dynamical interaction.

not, however, increase with distance to θ^1 Ori C (Fig. 3.13). Finally, although in Taurus (Andrews & Williams 2007) more disks with large radii have been observed than in the ONC, probably owing to its weaker dynamical interactions and irradiation, the similarity of the observed parameters (such as the 200 AU limit for synchronization) seems to suggest that the disk feeding mechanism in Taurus binaries is probably similar to that in Orion, i.e., not due to replenishment from circumbinary disks.

What other mechanism could synchronize the circumprimary and circumsecondary disks in $\lesssim 200$ AU systems? Since mass accretion rates are a function of stellar mass (White & Ghez 2001) and disk truncation radii are similar in equal mass systems (Artymowicz & Lubow 1994), synchronization of disk evolution might arise, if close binary systems are preferentially equal mass systems. For 13 binaries of the sample, we were able to derive masses of both binary components (see Fig. 3.14). For these, we observe that all (four) systems with mass ratios of $q > 0.8$ and separations < 200 AU are of WW type, agreeing with the hypothesis of high mass ratios being the cause of synchronized disk evolution. The significance of this result, however, is low. There is a 21% chance that the mass ratios of close (< 200 AU) systems are drawn from the same parent distribution as mass ratios of wider pairs (K-S test). A larger sample of spatially resolved spectroscopic observations of

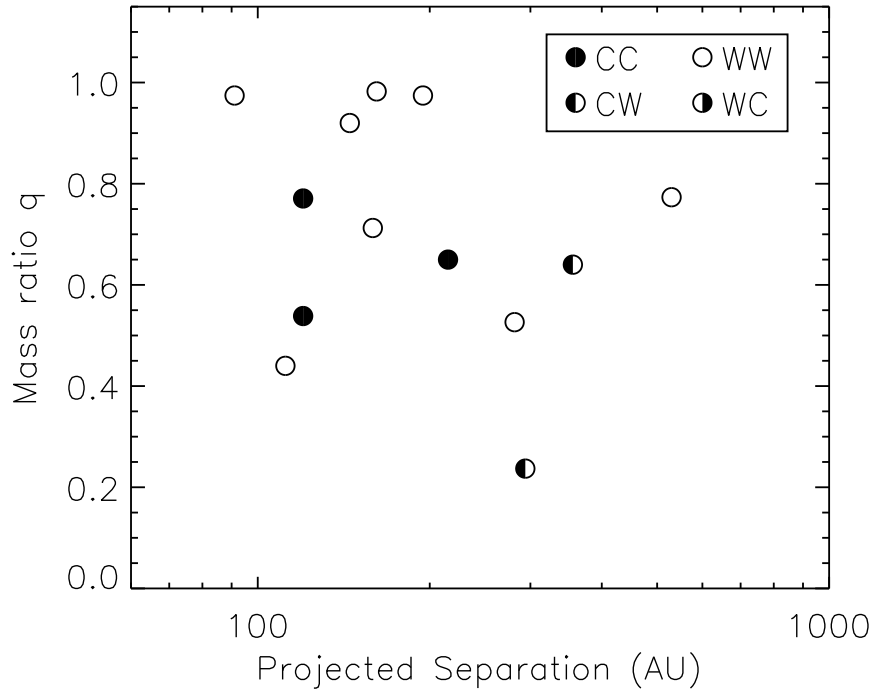


Figure 3.14: Mass ratios of binaries as a function of projected binary separation, indicating whether both binary components are accreting (filled circles, CC), neither component is accreting (open circle, WW), or either component shows signs of accretion (half-open circles = CW and WC). This plot only contains 13 targets, since masses could not be derived for all binary components in the sample. For some target binaries with mass ratios close to 1, the primary (as estimated from the NIR colors and listed in Table 3.4) turned out to be the less massive component. The mass ratios of those targets were calculated as the inverse leading to q -values $\lesssim 1$.

pre-main sequence binaries is needed to decide whether mass ratios are the main driver of the synchronization of binaries closer than 200 AU.

Differential disk evolution in binaries

Mixed pairs with accreting (CW) and non-accreting primaries (WC) – within the uncertainties – are equally abundant: CW pairs appear 4 ± 2 times while WC are measured 3 ± 1 times. Although not statistically significant, this is evidence against a strong preference for primaries to have longer lived disks than the less massive secondary. However, longer lived disks around primaries are suggested by theory since disks around secondaries are truncated to smaller radii (Artymowicz & Lubow 1994) and dissipation times are predicted to scale like R^{2-a} with R the disk radius and $a \approx 1-1.5$ (Monin et al. 2007, and references therein). Monin et al. found that their measured overabundance of $14 \times$ CW versus $6 \times$ WC is consistent with this effect taking place, however, with other factors (i.e. initial disk conditions) having a more a dominant impact on the lifetimes of circumprimary and circumsecondary disks than the differential scaling with R , which is only strong for

binaries with low mass ratios $q \leq 0.5$. Our data agree with this proposed *weak* correlation of the binary mass ratios with the abundance of CW-binaries in Orion, though this result is limited in significance by the small number of mixed systems in our sample.

It is noteworthy that the existence of mixed pairs, together with their property of having wider separations (Fig. 3.12), can introduce difficulties in the interpretation of binary studies that do not resolve their targets into separate components. Cieza et al. (2009) used NIR photometry of unresolved binaries with known separations from several star-forming regions (Taurus, ρ -Oph, Cha I, and Corona Australis) to infer a smaller separation in binaries with no accreting components than in accreting binaries. Besides the proposed shorter disk lifetimes around close binary components, there is an alternative interpretation of their data that they did not discuss. Since they did not resolve binaries into separate components, they were unable to distinguish CC, CW, and WC-type binaries, but merged them all into the category of having at least one disk. As we showed earlier, however, the separation distribution of CW and WC binaries differ significantly from equal-accretion binaries including CC (Fig. 3.12). When joining the three categories with at least one accreting component, the combined separations display a distribution with on average larger separations than the WW distribution. Only from our resolved population, can we interpret this as a lack of mixed (CW+WC) pairs and not a lack of accreting (CW+WC+CC) components in close binaries.

Accretion luminosities and mass accretion rates

Figs. 3.15 and 3.16 show a luminosity histogram and component mass-accretion rates as a function of stellar mass, respectively. In binaries with two accreting components, it is usually the more massive component that has the higher accretion luminosity. Accordingly, we see a tendency for the subsample of primary components to have slightly higher relative accretion luminosities L_{acc}/L_* than the secondaries of our Orion binaries. The derived accretion luminosities agree very well with single stars in the ONC (Robberto et al. 2004; Da Rio et al. 2010) for $\log(L_{\text{acc}}/L_{\odot}) \gtrsim -1.5$, which is the average sensitivity limit of the accretion luminosities derived from our Br γ observations.

Similarly, the mass accretion rates of the ONC T Tauri binary components as a function of stellar mass are (except for three outliers) comparable to those of single stars in the ONC. Fig. 3.16 shows that Orion single stars occupy almost the same area in the $\log(\dot{M}_{\text{acc}})$ - $\log(M_*)$ diagram, with tendency towards slightly lower accretion rates. This tendency is most likely an observational bias, since Robberto et al. (2004) use *U*-band observations with the Hubble Space Telescope that are more sensitive to lower mass accretion rates than our Br γ data. We also overplot stellar components of Taurus binaries (White & Ghez 2001), which have similar mass accretion rates.

Comparable mass accretion rates of singles and binaries in the ONC and Taurus⁹ are not self-evident, considering the different disk populations of the ONC and Taurus. Since disk masses in binaries are lower than in single stars of the same star-forming region because of

⁹Compare also singles in Taurus from Muzerolle et al. (1998a), which are as well at similar accretion rates.

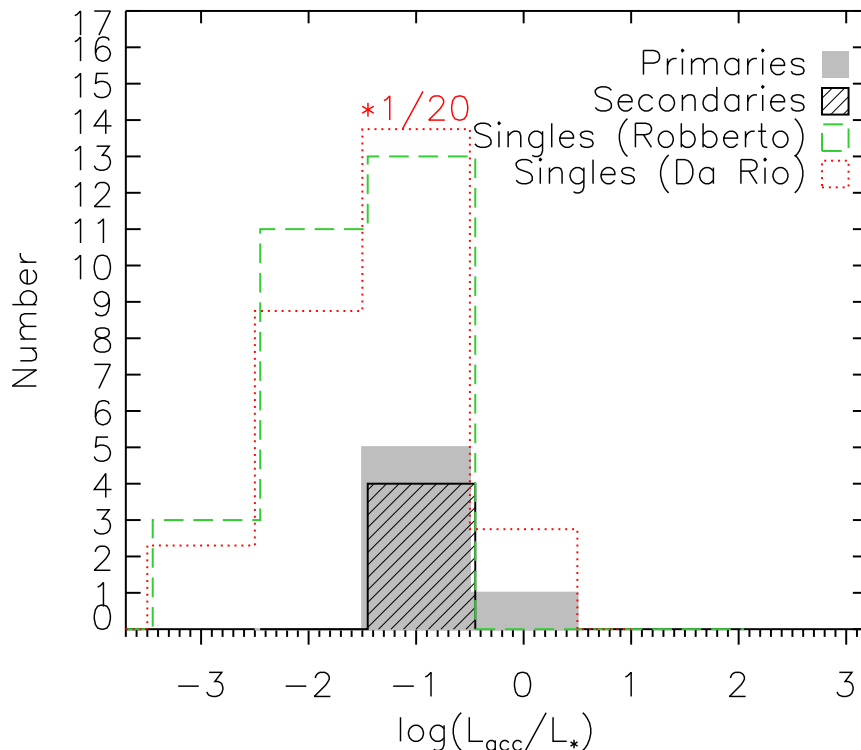


Figure 3.15: Histogram of the accretion luminosities of the primaries (gray shaded area) and secondaries (hatched) calculated from the Br γ emission. For comparison, the accretion luminosity distributions of single stars of Orion from [Robberto et al. \(2004\)](#), (dashed outline) and [Da Rio et al. \(2010\)](#), (dotted outline, scaled by a factor of 1/20 for clear comparability) are overplotted, both limited to the same range of stellar masses as in our binary survey. The distributions are slightly offset relative to each other to make them more visible.

disk truncation ([Artymowicz & Lubow 1994](#)) and disks in Orion are less massive than disks in Taurus ([Mann & Williams 2009](#)), uniform accretion rates indicate either different disk lifetimes or variable efficiency for the replenishment of an existing disk. The hypothesis of shorter disk lifetimes would corroborate the evidence from Sect. 3.3.2 that we observe fewer disks around binary components than were measured for single stars.

Three binary components (TCC 52 A&B, JW 391 A) have comparably high mass accretion rates to the rest of the sample in Fig. 3.16. The responsible mechanism is obscure, since the two respective binaries have no remarkable properties in common relative to other targets. Their mass, separation, and distance to θ^1 Ori C are unremarkable. While JW 391A shows no peculiarity in luminosity, the two components of TCC 52 are found to be the most luminous targets with respect to their mass. The derived very young ages and large radii might indicate an earlier evolutionary stage, i.e. class I, which would agree with the higher mass accretion rates of TCC 52A+B than to older class II components ([Robitaille et al. 2006](#)). Regardless of their properties, it remains possible that all three components were observed in a temporary state of high activity.

To assess whether disks in binaries need significant replenishment to survive in sufficient

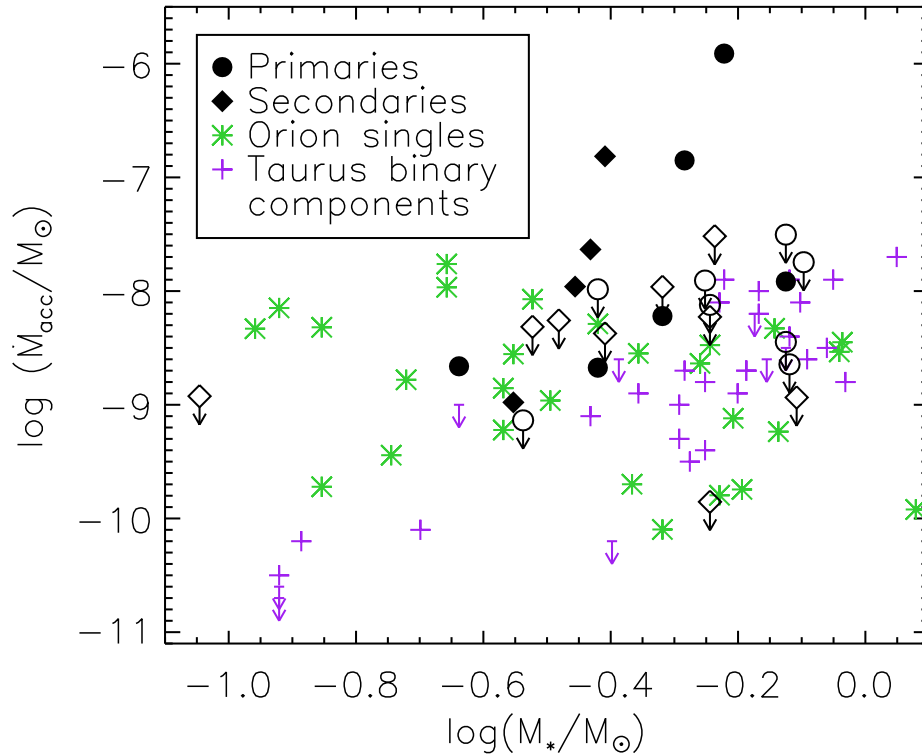


Figure 3.16: Mass accretion versus stellar mass for all significant emitters of the sample (filled symbols) and upper limits to all other targets with measured \dot{M}_{acc} and M_* (open symbols). Primaries are marked with circles, secondaries with diamonds. Green asterisks show the mass accretion rates of single stars in Orion (Robberto et al. 2004), whereas purple plus signs and upper limits marked by arrows are binary components in Taurus (White & Ghez 2001).

quantities, we estimated disk lifetimes $\tau_{\text{disk}} = M_{\text{disk}}/\dot{M}_{\text{acc}}$ from the ratio of disk mass to mass accretion rate and compare it to the age of the star-forming region. To estimate M_{disk} , we compiled upper limits to the total mass of dusty material around both binary components from the literature of millimeter observations (JW 519, JW 681, TCC 52, TCC 97, Mann & Williams 2010; TCC 52, TCC 55, Eisner et al. 2008).

Only for TCC 52 do we have available both mass accretion rates and the total mass of the surrounding (disk) material. The two measurements of total disk mass of TCC 52 disagree at the 1σ -level: $0.0288 \pm 0.0029 M_{\odot}$ are derived by Mann & Williams (2010) and $0.042 \pm 0.009 M_{\odot}$ by Eisner et al. (2008). Nevertheless, we now illustrate that an “order-of-magnitude” estimate is possible when we assume a total disk mass of $\sim 0.03 M_{\odot}$. Disk radii can be estimated from their dynamical truncation radii to be ~ 0.38 and ~ 0.3 times the binary separation for primary and secondary, respectively (Armitage et al. 1999), considering our derived binary mass ratio of $q \approx 0.65$ and $M_{\text{disk}} \propto R_{\text{disk}}$ (e.g. Mann & Williams 2010). This results in individual disk masses of $M_{\text{disk}}^{\text{prim}} \approx 0.017 M_{\odot}$ and $M_{\text{disk}}^{\text{sec}} \approx 0.013 M_{\odot}$. The derived disk lifetimes for these two target components with the highest mass accretion rates of our sample are $\tau_{\text{disk}}^{\text{prim}} \approx 1.4 \times 10^4$ yr and $\tau_{\text{disk}}^{\text{sec}} \approx 8.7 \times 10^4$ yr. Compared to the median

age of the ONC binaries of 1 Myr, derived from Tab. 3.6, this is very short. These high accretion rates could not have been sustained over the entire early evolution process even if the disk masses were initially ten times more massive than we now observe. If both components were not observed at a younger age than assumed or in a short-lived above-average state of accretion, binary component disks would need substantial replenishment to display the strong accretion activity we detect.

3.3.3 Is the existence of an inner disk linked to planet formation in binaries?

Primordial disks like those detected around the binary components in this sample contain the basic material for the formation of planets. Hence, any peculiarities in the evolution of disks in these systems can leave their footprints on the population of planets in binaries, and it should be instructive to compare the properties of planets and disks around the individual components of binaries.

A recent census identified 40 planets in 35 multiple systems (Eggenberger & Udry 2010, and references therein), almost all of which orbit the more massive component of the binary (Mugrauer & Neuhauser 2009). An additional eight planets were claimed to reside in circumbinary (*P-type*) orbits (PSR B1620-26, Rasio 1994; HD 202206, Correia et al. 2005; HW Vir, Lee et al. 2009; NN Ser, Beuermann et al. 2010; DP Leo, Qian et al. 2010b; QS Vir, Qian et al. 2010a; HU Aqr, Qian et al. 2011; Kepler-16, Doyle et al. 2011). Although some of these planets still need confirmation, we note that all latter candidate hosts are spectroscopic binaries with comparably small separations. From the thus composed picture of planet occurrence in binaries (~ 50 planets in multiples, ~ 2 around the less massive component, 8 circumbinary planets), one might suspect that (i) planet formation around the less massive components of binaries is suppressed and (ii) that circumbinary planets are rare, but do exist. These observations might either be caused by selection effects, since spectroscopic binaries and fainter secondary stars are less often targeted by spectroscopic surveys, or be the consequence of peculiar disk evolution in binaries.

In an attempt to carefully evaluate systematical errors and biases, Eggenberger & Udry (2010) discovered an underdensity of planets around stars with close, 35–225 AU stellar companions when compared to single stars with similar properties. This is not seen for wider binaries. The upper limit of 225 AU noticeably coincides with our 200 AU transition to synchronized disk evolution. This suggests a common origin of both effects. To test whether shorter lived disks in close binaries can explain the deficiency of planets in binaries of the same separation range, we derived the disk frequency in both subsamples. Binaries with separations < 200 AU have a slightly smaller fraction of disk bearing components ($34^{+47}_{-23}\%$) than wide > 200 AU pairs ($37^{+49}_{-27}\%$). This difference is, however, not as pronounced as the 1.6 – 2.1σ difference that Eggenberger & Udry (2010) observe for the frequency of planets in the close and wide sample. We concluded that either our sample is not large enough to reveal a significant difference or planet formation in binaries is not strongly correlated with the occurrence of accretion disks.

If the apparent paucity of planets orbiting the less massive components of binaries were not entirely due to selection effects, it could be a consequence of differential disk evolution, which we observe as mixed systems with only one accreting component. If the probability of a star to eventually host a giant extrasolar planet were significantly correlated with the lifetime of its disk, we would expect mainly CW systems, to evolve into circumprimary planetary systems while WC-type binary-disk-systems would preferably evolve into circumsecondary systems. However, we do not observe any significant difference in the appearance of CW systems versus WC (see Sect. 3.3.2). In the same way, we do not see any binaries in which both components are orbited by their individual planets, although the majority of disks evolves synchronously. In agreement with this result are the findings of Jensen & Akeson (2003), who found that disk masses around the primary are always higher than secondary disk masses in four T Tauri binaries, independent of their classification as CC, CW, WC, or WW. Again, a possible explanation could be that the evolution of the inner (accretion) disk is not strongly related to the formation of planets and that other factors dominate the planet formation process.

3.4 Conclusions

We have presented high-spatial-resolution near-infrared spectroscopic and photometric observations of the individual components of 20 young, low-mass visual binaries in the Orion Nebula Cluster. The sample was complemented with similar observations of six additional targets from Correia et al. (2012, *in prep.*). We have measured the relative positions, JHK_s photometry, and K -band spectra including the accretion-indicating Brackett- γ feature in order to derive the projected binary separations as well as the absolute magnitude, spectral type, effective temperature, extinction, veiling, luminosity, and the probability of dust and accretion disks around each binary component. By placing the components into an HR diagram and comparing with pre-main sequence evolutionary tracks, we have estimated the individual age, mass, and radius, as well as the mass accretion rate for each individual component.

Putting the results into context with the star forming environment of the Orion Nebula Cluster and with other young low-mass binary studies, we conclude the following:

1. We have found evidence of a slightly lower frequency of circumstellar disks around the individual components of binaries compared to that around single stars of the ONC, in agreement with theory. We have measured a corrected accretion disk fraction of $40_{-9}^{+10}\%$ for stars in multiple systems of the ONC, which is lower than the $\sim 50\%$ accretion disk fraction of single stars in the ONC found by Hillenbrand et al. (1998). A similar result was found for dust disks, as indicated by NIR excess emission, although with lower significance. As observed for single stars in other clusters, binary components of the ONC have been more often found to contain dust disks than accretion signatures.

2. The evolution of disks around both components of a binary is correlated for binaries with separations of 200 AU and below. This was inferred from our inability to detect any mixed pairs of accreting and non-accreting components with separations < 200 AU, and that the populations of mixed pairs exhibit significantly larger separations (99.5% confidence) than pairs of two accreting or two non-accreting components. We have demonstrated that this synchronization is probably not caused by a feeding mechanism involving a circumbinary disk, but possibly instead closer binaries that harbor equal-mass components.
3. Mixed pairs including an accreting primary and those with an accreting secondary have been observed to be almost equally abundant. In addition to the implication that mixed pairs are common, there is apparently no preference for either the disk of the more or less massive binary component to dissolve first. This points to a *weak* correlation between the binary mass ratio and the presence of a disk around either binary component.
4. We have found that the mass accretion rates of binary components in the ONC do not differ from the accretion rates of single stars and binary components in Orion and Taurus, respectively. Since disk masses and radii of primordial disks in the ONC are – on average – lower, this can potentially lead to shorter lifetimes of disks around binary components, in agreement with our finding of fewer dust and accretion disks than singles of the ONC.
5. We have measured no strong correlation between the existence of planets around the components of main-sequence binaries and the occurrence of accretion features measured around young binary stars in this paper. Although planets seem to be slightly suppressed in binaries of separations smaller than ~ 200 AU (1.6–2.1 σ significance; [Eggenberger & Udry 2010](#)), in wider binaries they are not, and we have not found any equally large differences between the presence of disks in close and wide binary systems.

Chapter 4

Disks and stellar parameters in Chamaeleon I binaries

(In prep. for submission to A&A, Daemgen et al. 2013)

This chapter presents the results from a near-IR high-spatial resolution study of 19 visual binary and 7 triple stars, including one newly discovered tertiary component, with separations between ~ 25 and ~ 1000 AU in the Chamaeleon I (Cha I) star forming region. The analysis uses the individual JHK_sL' photometry, the excess emission in K_s-L' , as well as $H+K$ -band spectroscopy including the wavelength of Brackett- γ ($2.16 \mu\text{m}$) in all individual binary components to infer extinctions, effective temperatures, and the presence of ongoing accretion and hot circumstellar dust around each stellar component of the sample.

As part of the Chamaeleon complex, the Chamaeleon I dark cloud is close to the Sun (160 ± 15 pc; Whittet et al. 1997) with an age distribution peaked between 2 and 3 Myr (Luhman 2007). It thus grants access to – on average – slightly older stars and disks than the ONC and allows adaptive optics to spatially resolve binaries with smaller physical separations. Its ~ 250 currently known stellar and sub-stellar members (Luhman 2008) are loosely clustered around a Northern (Cederblad 112; Cederblad 1946) and a Southern region (Ced 111 & 110) of extinctions up to $A_V=10$ (Cambresy et al. 1997), distributed over a region of several square degrees.

Chamaeleon I is extremely well studied at all wavelengths from X-ray to radio, including its binary (e.g. Ghez et al. 1997; Lafrenière et al. 2008; Nguyen et al. 2012) and disk content (e.g., Luhman et al. 2008; for a review of the region see Luhman 2008). Close to 40 binaries and higher order multiples are known in a separation range between 16 and 1000 AU which implies a multiplicity fraction of about 30% – higher by a factor of ~ 1.9 than in the field and even more than a factor of 2 higher than in the ONC (Lafrenière et al. 2008). Disks are found around $\sim 50\%$ of all members (Luhman et al. 2008), considerably less than in the ONC which fits well with the later evolutionary stage at the older age of the cluster.

While its proximity grants access to spatially resolved visual binaries with separations as close as a few ten AU, the older age of Cha I compared to the ONC makes both studies complementary: The new Cha I data in combination with the study of ONC binaries (Chapter 3) provide access to the investigation of the evolution of protoplanetary disks in binaries with time, subject of Chapter 5.

4.1 Observations and data reduction

4.1.1 Sample definition

Nineteen binaries and 7 triple stars (including one newly discovered tertiary component to T 33 B, for a discussion see Sect. 4.2.5) were observed in the Chamaeleon I star forming region, with both $H+K$ -band spectroscopy and close-in-time JHK_sL' imaging between December 2010 and April 2011. Twenty-four of the targets were selected from the binary survey by Lafrenière et al. (2008) and additionally two likely hosts of sub-stellar companions were included (CHXR 73, Luhman et al. 2006; T 14, Schmidt et al. 2008). This sample of 26 multiples is designed to contain close to all multiples in Cha I in the separation range of $0''.2$ to $\sim 6''$ known at the time of writing, which is equal to ~ 30 – 1000 AU at the distance of Cha I. The separation range was chosen to ensure high-quality spatially resolved observations of the individual binary components with ground-based adaptive optics facilities for in particular the spectroscopic observations. The brighter component of each binary was required to be brighter than $V = 16.7$, $R = 17$, and $K = 13.5$ to serve as the adaptive optics guide star for our NACO and SINFONI observations. All multiples were selected to have at least one component with a spectral type (SpT) in the T Tauri range, i.e., G-type or later. While typically all components of each multiple fulfill this criterion, two binaries have primary stars of comparably early spectral type (T 26 A, G0; T 41 A, B9). These components will be excluded from some of the discussion in Sect. 4.2 to minimize the impact of biases caused by their relatively high mass. Likewise, the two sub-stellar companions to CHXR 73 and T 14 had to be partly excluded since they turned out to be too faint for most of the spectroscopic evaluation in this thesis. They are discussed wherever possible.

All multiples are confirmed members of Cha I, as inferred from their space velocity and indicators of youth (position in H-R diagram, infrared-excess, lithium abundance, stellar activity, Luhman 2004; Luhman et al. 2008). Physical binarity was studied by Lafrenière et al. (2008) and Vogt et al. (2012) through assessment of the local stellar density and co-motion of binary components. While the authors find the probability of chance alignments to be $< 10^{-4}$ for all but the widest binaries, physical association of the wide T 6, T 26, and T 39 multiples was confirmed through multi-epoch imaging data. In addition, the spectroscopy from this study allows me to rule out background giants and I do not detect large changes in separation and position angle for any multiples of the sample, when compared to previously published measurements. The previously undetected companion to T 33 B is discussed and shown to be physically related in Sect. 4.2.5. In the following, I will treat all multiples as physically bound systems.

In every multiple, the brighter component in K_s -band is referred to as the *primary* or “A” component. This is typically in agreement with being of earlier spectral type and thus higher mass than the other members of each system. In two cases (T 39, Hn 4) the inferred mass of the B component is higher than that of the brightest component in K_s ¹.

¹The mass of T 39 B is likely over-estimated due to its spectroscopic binary nature and it may accordingly not be the real primary of the system.

To be consistent with previous publications, I keep the identifiers as they are (the brighter component in K_s is referred to as A) but treat the more massive component as the primary in the analysis of component properties.

Nguyen et al. (2012) examined all but five of our targets for spectroscopic binarity and found CHXR 28 B, T 31 A, and T 39 B to show signs of spectroscopic binarity² (see Table 4.1). Since it is not possible to measure separate spectral or photometric properties of the spectroscopic components from the observations in this thesis, the combined properties will be used where applicable and possible implications of the binary nature highlighted. These targets are excluded from those parts of the discussion where knowledge of the individual component properties is required.

Five of the six triple stars in this sample show a clear hierarchical structure. Whenever binary parameters (like separation, mass ratios, ...) are discussed, these triples are included as two binary stars, one consisting of the close binary system, the other one using the combined characteristics of the close binary (total system mass, center position, ...) to compose a binary with the wide tertiary component. One triple, T 39, does not show a distinct hierarchical structure and is either seen in a projection that veils an existing hierarchy or its components are currently in an unstable non-hierarchical configuration (for a discussion see Lafrenière et al. 2008³). I will include this system as two binaries consisting of the AB and AC components respectively (see Fig. 4.1 for the configuration).

A list of the targets, spectroscopic binarity, and the dates of the observations can be found in Table 4.1.

4.1.2 NACO imaging: photometry and astrometry

Observations and data reduction

All targets were observed with NAOS-CONICA (NACO Lenzen et al. 2003; Rousset et al. 2003) imaging on UT4 of the Very Large Telescope (VLT). The adaptive optics system NAOS always used the brightest multiple component (or the binary itself for close systems) as a guide star. All components of each target were observed in the same field of view in four broad-band filters (JHK_sL') during a single night to minimize the impact of variability. Observations in JHK_s use the N90C10 dichroic and the S13 camera with a pixel scale of 13.26 mas/pix, L' uses the IR wavefront sensor and the L27 camera with 27.1 mas/pix. Typical values of measured FWHM of our point sources are 0''.074 in J , 0''.070 in H , 0''.077 in K_s , and 0''.11 in L' . The derotator was used to keep the North/South direction aligned with the columns of the detector. All targets were observed in a 5-position on-source dither pattern to allow for sky subtraction. Total integration times per target and filter are between 50 and 800 sec in JHK_s -band and equal to 176 sec in L' with the exception of

²Nguyen et al. also report CHXR 47 and Hn 4 as spectroscopic binary candidates. They find, however, that the known visual companions are likely identical to the spectroscopic companions in their data.

³Lafrenière et al. also discuss the weak hierarchy of CHXR 9C and T 31 which is, however, less pronounced than in T 39. An assignment of the “close” and “wide” system is straightforward in these two cases and they will be treated as hierarchical in this thesis.

Table 4.1: Cha1 targets and observations

Identifier	Simbad Name ^a	RA ^b ($h^m s$)	DEC ^b ($^{\circ} ' ''$)	SBC ^c	pre- optics ^d	telluric reference	MJD spectroscopy	phot. ref. JHK_s	L'	MJD photometry
B 53	BYB 53	11 14 50.116	-77 33 40.00	no	0.1	Hip 040105	55589.30224627	HD 110621	HD 75223	55606.34424266
CHXR9C		11 01 18.813	-76 27 01.97	no	0.1	Hip 061193	55571.34166417	S372-S	HD 77281	55557.29178934
CHXR15		11 05 43.278	-77 26 52.99		0.1	Hip 050126	55587.20283114	HD 110621	FS129	55653.12026904
CHXR 28		11 07 56.113	-77 27 26.80		0.1	Hip 050126	55587.21137326	HD 110621	HD 106965	55653.118627437
CHXR 47		11 10 38.045	-77 32 40.81	CHXR28B=SBI? ^e	0.25	Hip 064501	55594.23506763	HD 60778	HD 60778	55666.15952256
CHXR 49		11 11 54.001	-76 19 31.12		0.1	Hip 061193	55589.36918014	HD 110621	HD 60778	55606.24352530
CHXR 68		11 18 20.030	-76 22 00.03		0.25	Hip 060429	55590.19058466	HD 60778	HD 60778	55666.18125080
CHXR 71		11 02 32.947	-77 29 13.50	no	0.1	Hip 050126	55542.34920563	HD 110621	GL347A	55641.08828209
CHXR 73		11 06 28.374	-77 37 33.98		0.1	Hip 033708	55565.35663229			
						Hip 050126	55587.22603233	HD 110621	FS129	55646.12072363
CHXR 79		11 09 18.493	-76 30 30.49	no	0.1	Hip 067042	55588.23978704			
Hn 4		11 05 14.515	-77 11 30.22	(SB2?) ^e	0.25	Hip 061193	55589.34228160	HD 60778	HD 60778	55666.08169563
Hn 21		11 14 25.276	-77 33 05.15	no	0.25	Hip 040105	55592.321034212	HD 110621	GL347A	55641.10665852
ISO 126	ISO-Chal 126	11 08 03.052	-77 38 44.13	no	0.1	Hip 040105	55589.31037568	HD 110621	HD 75223	55606.29302649
T 3	Ass Cha T 2-3	10 55 59.166	-77 24 39.91	no	0.25	Hip 061193	55571.32071327	S708-D, 9141	HD 106965	55610.19226973
T 6	Ass Cha T 2-6	10 58 17.151	-77 17 17.85	no	0.25	Hip 064501	55559.34191219	S372-S, 9137	HD 77281	55602.28873422
T 14	Ass Cha T 2-14	11 04 09.146	-76 27 18.91	no	0.25	Hip 060429	55590.21242836	S708-D, 9141	HD 106965	55590.34649026
T 26	Ass Cha T 2-26	11 07 20.384	-77 38 10.46	no	0.25	Hip 060429	55590.15206476	HD 110621	HD 106965	55653.14097253
T 27	Ass Cha T 2-27	11 07 28.016	-76 52 12.59	no	0.1	Hip 067042	55678.05304754	HD 110621	HD 106965	55653.16332159
T 31	Ass Cha T 2-31	11 08 01.510	-77 42 30.53	T31A=SB2? ^e	0.1	Hip 065181	55569.28001642	HD 110621	HD 106965	55653.20674135
T 33	Ass Cha T 2-33	11 08 14.189	-77 33 52.69	no	0.25	Hip 060429	55590.16543515	HD 60778	HD 60778	55666.039397411
T 39	Ass Cha T 2-39	11 09 13.110	-77 29 13.58	T39B=SBI	0.25	Hip 060429	55590.20255577	HD 60778	HD 60778	55666.05782756
T 41	Ass Cha T 2-41	11 09 50.199	-76 36 48.88	no	0.1	Hip 067969	55589.26156993	HD 110621	HD 75223	55605.33691345
T 43	Ass Cha T 2-43	11 09 54.326	-76 29 24.54	no	0.1	Hip 040105	55589.33528044	HD 60778	HD 60778	55666.11141484
T 45	Ass Cha T 2-45	11 09 59.507	-77 37 06.68	no	0.1	Hip 067969	55589.27490141	HD 60778	HD 60778	55666.13248263
T 51	Ass Cha T 2-51	11 12 24.513	-76 37 07.09	no	0.1	Hip 067969	55589.29062811	HD 60778	HD 60778	55670.07307583
T 54	Ass Cha T 2-54	11 12 42.379	-77 22 23.02	no	0.1	Hip 040105	55589.32408822	S372-S, 9137	HD 77281	55602.31526911

^a Identifier to be used with Simbad (<http://simbad.u-strasbg.fr/simbad/>). If no Simbad name is listed, then the identifier (1st column) can be used with Simbad.
^b RA, DEC according to telescope pointing from data header
^c Spectroscopic binarity reference: Nguyen et al. (2012)
^d SINFONI pre-optics used (see text for definition)
^e The spectroscopic companions to Hn 4 and CHXR 47 are probably identical to the visual companions in this thesis (see Nguyen et al. 2012).

the sub-stellar companion host CHXR 73 with 528 sec. Photometric standard stars were always observed during the same night with the same instrumental setup as the science observations as part of the standard NACO calibration plan.

Pipeline-reduced data products were provided in the ESO data package for all science targets. A sub-sample was compared to images manually reduced with the *NACO pipeline*⁴ in *Gasgano*⁵ with the recommended settings, to confirm their usability for the photometric and astrometric analysis in this thesis. The difference between both reductions was negligible (photometry, noise), thus the provided data products were used for the photometry in this thesis. Manual pipeline reduction, however, was required for the photometric standards, since no reduced data were available. For both, the standards and science targets, the pipeline performs flat fielding using lamp-flats and sky subtraction. After all dithered images per target and filter were shifted and averaged, residual bad pixels were removed by substitution with the median of the surrounding good pixels.

Images of all spatially resolved previously known multiples in K_s -band are shown in Fig. 4.1. The close binary companions in the triple systems T 26 and T 31 could not be resolved. Their binarity is revealed only by their elongated shapes (Fig. 4.2) in these observations with a FWHM of $\sim 0''.07$. The estimated separations are $\lesssim 0''.05$ (T 26B) and $\sim 0''.07$ (T 31B). The tertiary component to T 33 has not been reported before (Fig. 4.3) and its physical association with the system is assessed in Sect. 4.2.5.

Photometry and astrometry

Using a combination of calibrated and differential component photometry, JHK_sL' photometry of all target components was measured.

Differential photometry was obtained through simultaneous aperture photometry of pairs of stars in the image (typically the two binary components). The applied algorithm uses a *differential curve of growth*, i.e., the measured magnitude difference with *IRAF phot* as a function of aperture. The best aperture is defined by the radius at which this curve becomes flat, typically between half the binary separation (to avoid overlapping apertures) and a maximum of ~ 40 pixels in JHK_s and ~ 25 pix in L' . Triple stars allowed the use of accurate PSF photometry with the *daophot* task in *IRAF* using the PSF of the wide tertiary component as a reference. Despite possible isoplanatic effects of the adaptive optics correction, subtraction of the flux-scaled reference resulted in residuals with typical amplitudes $\ll 1\%$ of the original component flux.

Relative astrometry, i.e., separations and position angles, were inferred from the results obtained with *IRAF daofind*, which returns stellar positions with an accuracy of a fraction of a pixel or $\lesssim 0''.01$ respectively⁶. The derotator was used to keep North up, so the inferred position angles are assumed to be absolute.

⁴v4.2.3

⁵v2.4.0, <http://www.eso.org/sci/software/gasgano/>

⁶Inferred from the scatter of binary separations measured in different exposures of the same target

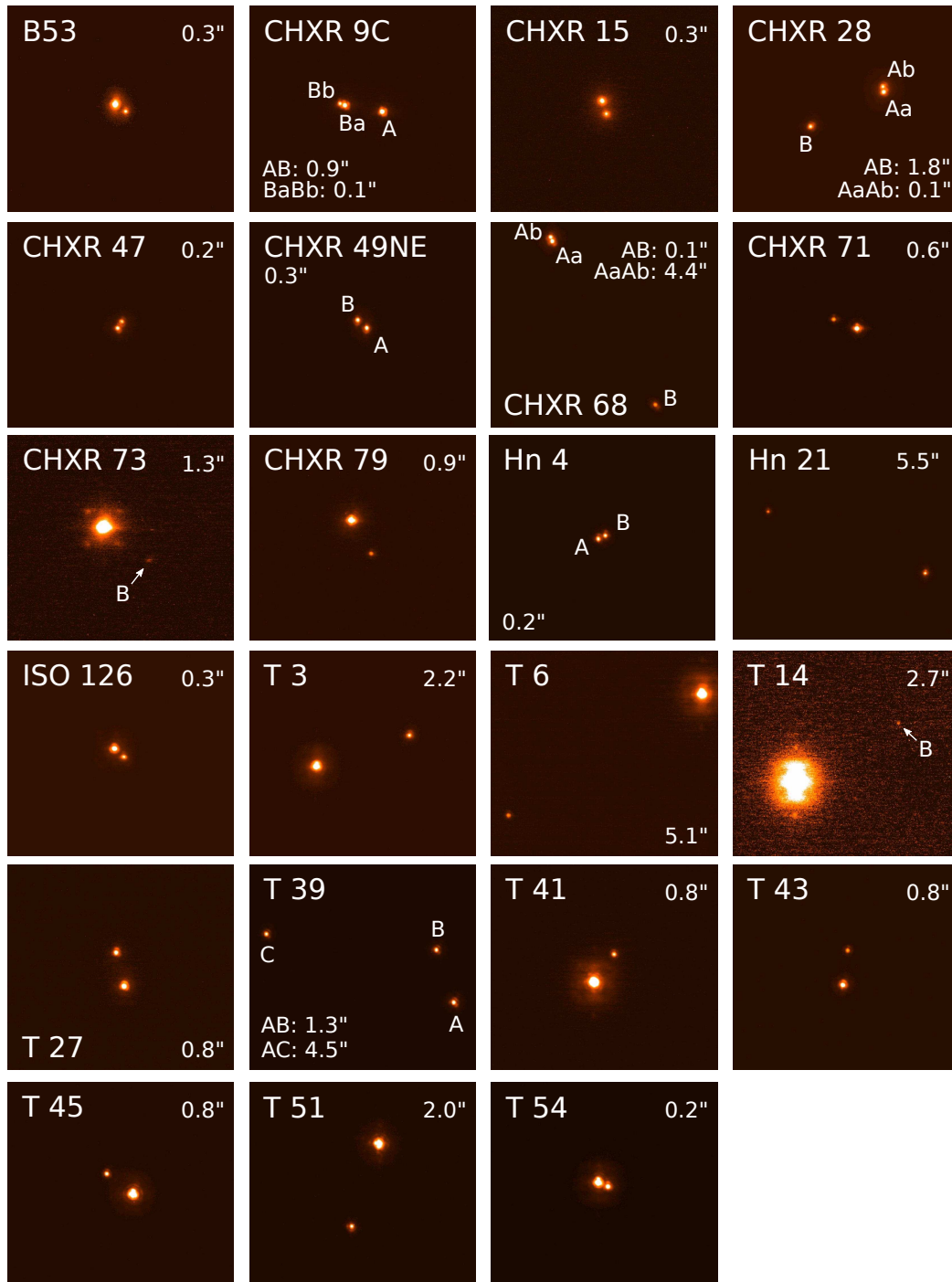


Figure 4.1: NACO K_s -band imaging of all target binaries and triples (except T26, T31, and T33 in Figs. 4.2 and 4.3). The target name and separation between the components is indicated in each subpanel. Components are marked with their component identifier when it is not clear whether they are primary or secondary. All subpanels are $5''.0 \times 4''.6$ in size except for the wide binary Hn21 with $7''.4 \times 6''.8$. The color stretch is linear. North is up and East to the left.

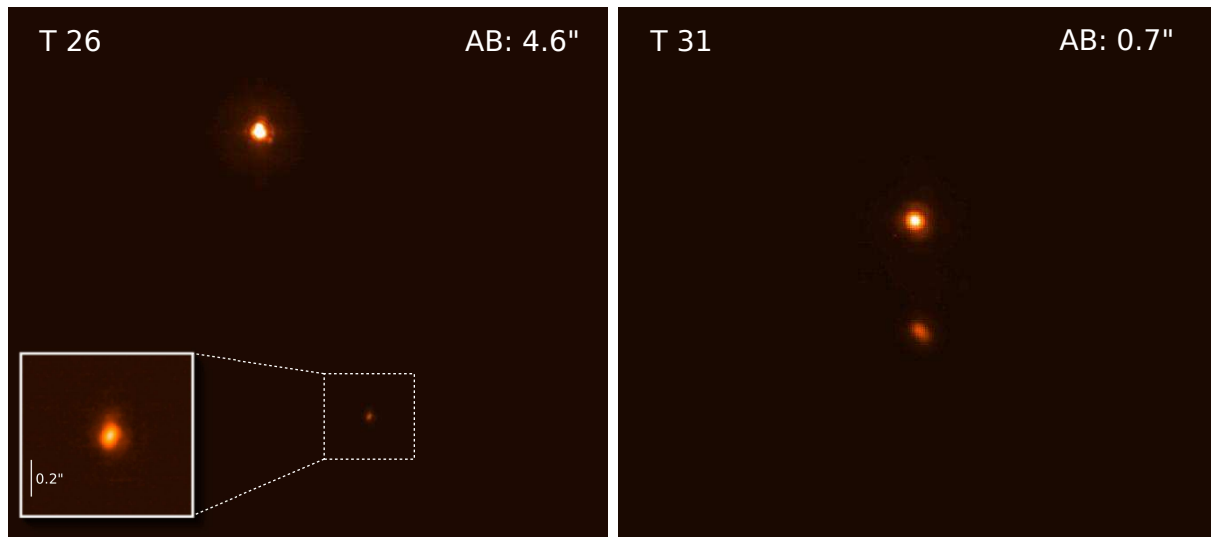


Figure 4.2: The close binary components of these triples (the Southern component in both panels) could not be spatially resolved with NACO K_s -band imaging, despite the good FWHM of $\sim 0''.070$. From the apparent elongation it could be estimated that the separation of T 26 BaBb is not much larger than $0''.05$ and just at the FWHM for T 31 BaBb. Image stretch and orientation as in Fig. 4.1.

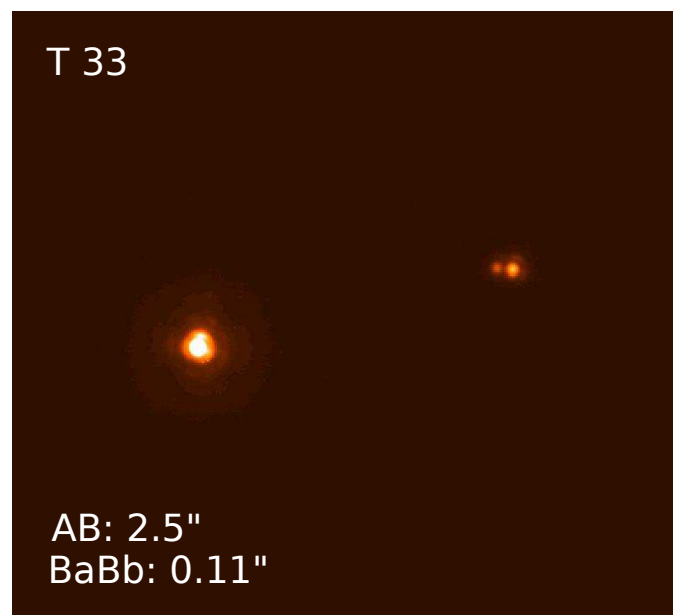


Figure 4.3: K_s -band imaging of T 33 showing the newly discovered faint tertiary component close to T 33 B. Physical association of all three components is discussed in Sect. 4.2.5. Image stretch and orientation as in Fig. 4.1.

The *photometric calibration* was performed with photometric standard stars observed during the same night or a night as close in time as possible⁷. Apertures of $\sim 0''.5\text{--}1''.9$ radius were used, either enclosing one binary component or, for close companions, both components of a binary. The extraction of the standard star photometry used the same individual apertures to avoid the use of aperture corrections. This procedure tacitly assumes that the PSF wings of the standard star and science observations are identical. As AO PSFs are highly variable in time, this might not always be the case. An upper limit for the introduced uncertainty can be estimated from the size of the aperture corrections which are almost exclusively between ~ 0.10 mag and ~ 0.05 mag for these large apertures. The true uncertainty is the difference of the standard star and science star aperture corrections and accordingly small (0.00–0.05 mag), adding to the systematic error budget of the observations. The sky was computed in an annulus of 5 pixel width outside the used apertures. Apparent magnitudes are then calculated under consideration of normalized instrumental magnitudes $m^{\text{inst}} = -2.5 \log(\text{Flux}/t_{\text{exp}})$, airmasses AM , Paranal extinction coefficients⁸ k , and photometric zeropoints zp derived from the standard star observations as:

$$m_{\text{cal}} = zp - m_{\text{sci}}^{\text{inst}} - k \cdot AM_{\text{sci}} = (m_{\text{ref}}^{\text{inst}} + m_{\text{ref}}^0 + k \cdot AM_{\text{ref}}) - m_{\text{sci}}^{\text{inst}} - k \cdot AM_{\text{sci}} \quad (4.1)$$

where $m_{\text{ref}}^{\text{inst}}$ and m_{ref}^0 are the instrumental and literature⁹ magnitudes of the photometric standards, respectively. The resulting photometry is listed in Table 4.2 together with the measured separations and position angles.

Unfortunately, two stars in the sample, T 26 A and T 33 A, turned out to be too bright for observations in L' -band with NACO. Their saturated L' photometry cannot be used for further evaluation. The brown dwarf companion candidate T 14 B remains undetected in J .

All JHK_s photometry presented in this chapter is observed in or converted to the 2MASS system (Cutri et al. 2003), L' photometry is converted to the ESO system when necessary (van der Bliik et al. 1996). As already mentioned in Sect. 3.1.2, photometry with NACO needs no transformation to be compatible with this system and the photometry of the standard stars is available in these filters (see references in ⁹). For all other necessary transformations of JHK_sL' photometry (e.g. CTTS locus, extinction vector; Sect. 4.2.1) the recipes in Bessell & Brett (1988) and Carpenter (2001) were used.

Some targets were observed multiple times for various reasons like bad weather, bad Strehl correction, or a missing photometric reference in one or more filters. The subset of repetitions that returned data of good quality in one or more filters were reduced and measured as described. More than half of all targets with repeated measurements exhibited significant photometric variability of up to ~ 0.2 mag and differential magnitude differences

⁷When no standard was taken during the same night or the standard was not usable. Due to the stability of the calculated zeropoints to ~ 0.02 mag (rms error) over the duration of several nights, this does not introduce significant additional uncertainty.

⁸<http://www.eso.org/sci/facilities/paranal/instruments/naco/tools/library.html>

⁹from the 2MASS catalog (Cutri et al. 2003) and http://www.eso.org/sci/facilities/paranal/instruments/naco/tools/imaging_standards/naco_lw_lp.html

of $\lesssim 0.1$ mag. A scatter of this magnitude can be caused by the intrinsic variability through chromospheric activity of T Tauri stars (see [Carpenter et al. 2001](#)).

Despite occasional re-observations in individual filters, for all targets only one *complete* set of observations exists, i.e., all of JHK_sL' were observed during one night together with photometric references. Those observations are used for the further evaluation.

4.1.3 SINFONI H+K-band IFU spectroscopy

Observations and data reduction

Integral field spectroscopy was obtained with SINFONI ([Eisenhauer et al. 2003](#); [Bonnet et al. 2004](#)) on the VLT. All observations use the adaptive optics module, locked on the brightest multiple component or close binary. The offered $H+K$ configuration was used to obtain simultaneous spectroscopy from ~ 1.5 to ~ 2.5 μm for an array of 32×64 spatial pixels. Depending on the separation of the target binary, one of the 0.25, 0.1, or 0.025 pre-optics was used, resulting in a final spatial pixel scale in the reduced images (after resampling) of $0''.125/\text{pix}$, $0''.05/\text{pix}$, and $0''.0125/\text{pix}$ respectively. The spectral resolution is $R \approx 1500$ with ~ 5 $\text{\AA}/\text{pix}$ in dispersion direction. The angular resolution is variable with wavelength (see discussion below) with a typical FWHM of $\sim 0''.10$ – $0''.25$. This is sufficient to spatially resolve all binaries and wide tertiary components in the sample. All close components in triples, however, are only marginally resolved and only the combined spectra were used for further evaluation. Except CHXR 73, all targets were observed in a 4-position dither pattern. In the two larger scales (0.25 and 0.1) all 4 dithers were on source; the two closest binaries (Hn 4 and CHXR 47) were observed with alternating on- and off-source dithers with the 0.025 pre-optics. Total integration times were 2 min per target. To increase the SNR of the faint secondary around CHXR 73, this target was observed with 16 dither positions totaling 32 min of integration time. Each science observation was accompanied by the observation of a bright telluric standard star of known spectral type (B2 to B6) with identical system settings at similar airmass.

As suggested in the *SINFONI data reduction cookbook*¹⁰, I removed a pattern of dark lines from all science and calibration files – caused by a hard-coded bias-removal of the SINFONI instrument – with the provided *IDL* script. The subsequent reduction of all science and telluric reference frames used the standard *SINFONI pipeline*¹¹ in *EsoRex*¹² according to the *SINFONI pipeline user manual*¹³. Required calibration files were retrieved from the ESO archive¹⁴. The pipeline executes bad pixel removal, flat fielding using a lamp flat, background subtraction, and wavelength calibration. A correction for differential atmospheric refraction was applied to exposures using the pre-optics 0.1 and 0.025. For each set of 4 or 16 dither exposures, the pipeline outputs a *data cube* which consists of

¹⁰Issue 1.0, from <http://www.eso.org/sci/facilities/paranal/instruments/sinfoni/doc/>

¹¹v2.2.9

¹²v3.9.0, <http://www.eso.org/sci/software/cpl/esorex.html>

¹³Issue 16.0

¹⁴http://archive.eso.org/eso/eso_archive_main.html

Table 4.2: Individual component apparent magnitudes

Name	separation ^a [arcsec]	PA ^a [°]	J^b [mag]	H^b [mag]	K_s^b [mag]	L^b [mag]	A_V^{phot} [mag]	$E_{K_s-L'}$ [mag]		
B53	0.28	45	235.8	A	10.80 ± 0.03	10.03 ± 0.04	9.87 ± 0.02	9.66 ± 0.01	0.4 ± 0.5	0.03
				B	11.96 ± 0.05	11.44 ± 0.06	11.30 ± 0.04	10.83 ± 0.03	0.0 ± 0.5	0.21
CHXR 9C	0.90	144	79.7	A	10.83 ± 0.04	10.01 ± 0.03	9.84 ± 0.06	9.76 ± 0.02	0.7 ± 0.6	-0.11
	0.12	19	69.5	Ba	11.15 ± 0.04	10.33 ± 0.03	10.16 ± 0.06	10.08 ± 0.02	0.7 ± 0.6	-0.12
CHXR 15				Bb	11.82 ± 0.04	11.06 ± 0.03	10.84 ± 0.06	10.65 ± 0.02	0.5 ± 0.6	0.00
	0.31	50	198.2	A	11.91 ± 0.03	11.30 ± 0.04	10.99 ± 0.02	10.40 ± 0.04	1.0 ± 0.3	0.20
CHXR 28				B	12.38 ± 0.04	11.80 ± 0.04	11.53 ± 0.02	11.02 ± 0.05	1.1 ± 0.4	0.12
	1.84	294	117.1	Aa	9.99 ± 0.03	9.03 ± 0.04	8.77 ± 0.02	8.62 ± 0.02	2.0 ± 0.5	-0.05
CHXR 47	0.12	20	7.6	Ab	10.44 ± 0.03	9.38 ± 0.04	9.09 ± 0.02	8.81 ± 0.02	2.7 ± 0.5	0.04
	0.17	27	328.9	B	10.46 ± 0.03	9.44 ± 0.04	9.15 ± 0.02	9.00 ± 0.02	2.5 ± 0.5	0.17
CHXR 49NE				A	10.34 ± 0.03	9.42 ± 0.03	8.87 ± 0.03	8.27 ± 0.03	3.6 ± 0.2	0.32
	0.27	43	48.6	B	10.80 ± 0.04	9.83 ± 0.03	9.35 ± 0.04	8.77 ± 0.03	3.6 ± 0.3	0.29
CHXR 68				A	10.99 ± 0.03	10.22 ± 0.04	10.02 ± 0.02	9.64 ± 0.01	1.4 ± 0.3	0.12
	4.40	704	212.1	B	11.09 ± 0.03	10.37 ± 0.04	10.15 ± 0.02	9.73 ± 0.01	0.9 ± 0.3	0.14
CHXR 71	0.09	15	21.9	Aa	10.59 ± 0.03	9.89 ± 0.04	9.61 ± 0.02	9.67 ± 0.04	0.4 ± 0.5	-0.22
	0.56	90	68.5	Ab	10.74 ± 0.03	10.07 ± 0.04	9.84 ± 0.02	9.71 ± 0.04	0.0 ± 0.5	-0.01
CHXR 73				B	11.41 ± 0.03	10.67 ± 0.03	10.40 ± 0.03	10.28 ± 0.03	0.6 ± 0.4	-0.06
	1.29	206	234.6	A	11.55 ± 0.03	10.69 ± 0.04	10.45 ± 0.02	10.24 ± 0.02	1.2 ± 0.5	-0.02
CHXR 79				B	13.12 ± 0.03	12.41 ± 0.04	12.06 ± 0.02	11.27 ± 0.03	0.0 ± 0.3	0.53
	0.88	140	211.0	A	12.64 ± 0.35	11.40 ± 0.04	10.94 ± 0.02	(...) ^c	4.5 ± 2.5	...
Hn 4				B	17.84 ± 0.37	16.35 ± 0.10	15.47 ± 0.16	...	6.7 ± 3.1	...
	0.17	27	295.2	A	11.84 ± 0.04	10.31 ± 0.03	9.32 ± 0.03	8.03 ± 0.03	6.9 ± 0.3	0.76
Hn 21				B	13.84 ± 0.05	12.50 ± 0.04	11.80 ± 0.04	10.87 ± 0.08	5.6 ± 0.4	0.38
	5.48	876	68.5	A ^d	11.65 ± 0.03	10.76 ± 0.04	10.45 ± 0.02	10.17 ± 0.01	1.7 ± 0.5	-0.07
ISO 126				B	11.70 ± 0.03	10.77 ± 0.04	10.47 ± 0.02	10.32 ± 0.01	1.9 ± 0.5	-0.17
	0.28	45	228.8	A	12.09 ± 0.03	11.14 ± 0.04	10.70 ± 0.02	10.18 ± 0.02	3.5 ± 0.3	0.10
T 3				B ^d	12.90 ± 0.04	12.09 ± 0.04	11.56 ± 0.03	10.77 ± 0.03	1.5 ± 0.3	0.38
	2.21	354	288.4	A	12.55 ± 0.03	10.48 ± 0.04	8.87 ± 0.02	6.83 ± 0.02	10.5 ± 0.3	1.87
T 6				B	12.70 ± 0.03	11.21 ± 0.05	10.11 ± 0.04	8.33 ± 0.02	4.3 ± 0.2	1.41
	5.12	819	122.3	A	10.97 ± 0.03	9.64 ± 0.02	8.58 ± 0.03	7.12 ± 0.01	4.9 ± 0.2	1.05
				B	11.62 ± 0.03	10.86 ± 0.02	10.33 ± 0.03	9.55 ± 0.02	1.2 ± 0.5	0.50
				A	8.76 ± 0.04	8.23 ± 0.03	7.70 ± 0.05	6.90 ± 0.01	0.0 ± 0.5	0.76

Table 4.2: Individual component apparent magnitudes (ctd.)

Name	separation ^a [arcsec]	PA ^a [AU]	PA ^a [°]	J^b [mag]	H^b [mag]	K_s^b [mag]	L'^b [mag]	A_V^{phot} [mag]	$E_{K_s-L'}$ [mag]
T 14	2.67	427	299.6	B 12.00 ± 0.08	11.65 ± 0.06	10.95 ± 0.08	10.39 ± 0.02	0.8 ± 0.3	0.26
T 26	4.57	731	201.3	A 9.45 ± 0.02	8.88 ± 0.02	8.48 ± 0.03	7.66 ± 0.01	0.0 ± 0.5	0.72
				B ...	15.01 ± 0.36	16.54 ± 4.16	13.01 ± 0.15
T 27	0.78	125	13.3	A 7.89 ± 0.03	7.06 ± 0.04	6.45 ± 0.02	<i>sat</i>	0.0 ± 0.5	...
				BaBb ^e 11.55 ± 0.04	10.75 ± 0.04	10.24 ± 0.03	9.90 ± 0.04	1.8 ± 0.5	0.01
T 31	0.66	106	182.6	A 11.27 ± 0.03	10.48 ± 0.04	10.08 ± 0.02	9.38 ± 0.03	0.9 ± 0.3	0.50
				B 11.68 ± 0.03	10.99 ± 0.04	10.77 ± 0.02	10.42 ± 0.04	1.1 ± 0.3	0.08
T 33	2.40	384	284.4	A 9.32 ± 0.03	8.17 ± 0.04	7.38 ± 0.02	6.14 ± 0.02	3.0 ± 0.3	0.98
				BaBb ^e 9.74 ± 0.03	8.83 ± 0.04	8.51 ± 0.02	8.24 ± 0.04	1.8 ± 0.5	0.04
T 39	1.25 ^e 4.50 ^g	200 720	18.4 69.9	A 9.65 ± 0.03	8.01 ± 0.03	6.68 ± 0.02	<i>sat</i>	4.3 ± 0.3	...
				B 10.09 ± 0.03	9.27 ± 0.03	9.07 ± 0.04	$\left(L'_{\text{Ba+Bb}} \equiv \right)_f$ $\left(8.60 \pm 0.03 \right)$	0.8 ± 0.4	...
T 41	0.78	125	324.3	A 11.38 ± 0.04	10.56 ± 0.03	10.32 ± 0.07	9.88 ± 0.03	1.0 ± 0.6	...
				B 10.37 ± 0.03	9.67 ± 0.03	9.48 ± 0.03	10.31 ± 0.03	0.0 ± 0.4	-0.59
T 43	0.78	126	352.0	A 10.77 ± 0.03	10.00 ± 0.03	9.83 ± 0.03	10.31 ± 0.03	0.4 ± 0.4	-0.66
				B 11.01 ± 0.04	10.29 ± 0.03	10.09 ± 0.04	9.75 ± 0.03	0.2 ± 0.5	0.14
T 45	0.74	119	51.8	A 7.61 ± 0.03	7.35 ± 0.04	7.28 ± 0.02	7.36 ± 0.01	0.0 ± 0.3	-0.03
				B 11.25 ± 0.28	10.57 ± 0.13	10.27 ± 0.06	9.93 ± 0.04	0.3 ± 2.5	0.09
T 51	1.97	316	161.8	A 11.56 ± 0.03	10.32 ± 0.03	9.55 ± 0.02	8.64 ± 0.03	5.5 ± 0.3	0.45
				B 12.85 ± 0.03	11.75 ± 0.04	11.07 ± 0.02	10.11 ± 0.03	3.6 ± 0.3	0.51
T 54	0.24	38	248.0	A 10.01 ± 0.03	8.93 ± 0.03	8.16 ± 0.03	7.06 ± 0.03	3.2 ± 0.2	0.78
				B 11.78 ± 0.03	10.99 ± 0.03	10.59 ± 0.03	10.10 ± 0.04	2.3 ± 0.2	0.11
T 54	0.24	38	248.0	A 9.32 ± 0.03	8.67 ± 0.03	8.28 ± 0.02	7.15 ± 0.03	0.0 ± 0.5	1.03
				B 11.39 ± 0.03	10.72 ± 0.03	10.38 ± 0.03	9.66 ± 0.03	0.0 ± 0.5	0.53
T 54	0.24	38	248.0	A 8.65 ± 0.04	8.24 ± 0.03	8.24 ± 0.06	8.19 ± 0.01	0.0 ± 0.5	0.02
				B 10.16 ± 0.05	9.66 ± 0.03	9.65 ± 0.06	9.51 ± 0.02	0.0 ± 0.5	0.04

^a Separation uncertainties are $\Delta \text{sep} = 0''.01$, $\Delta \text{PA} = 0.5^\circ$. Projected separations in AU assume a distance to Cha I of 160 pc (Whittet et al. 1997). For hierarchical triples, separations between a wide component and the close pair are given as well as the separation of the close components.

^b Uncertainties are statistical errors from the differential photometry. Systematic uncertainties from relative aperture photometry are ~ 0.1 mag.

^c Due to a saturation of the reference star, no calibrated L' photometry could be measured. The magnitude difference is $\Delta L' = L'_B - L'_A = 4.69 \pm 0.19$.

^d These components are also known as Hn 21 E (primary) and Hn 21 W (secondary).

^e These previously known visual binary components could not be resolved with our NACO AO observations. System photometry is listed.

^f These components are not separated in the L' -band images. The combined photometry returns $L'_{\text{Ba+Bb}} = 8.60 \pm 0.03$.

^g As no clear hierarchy is visible, sep. and PA of the secondary and tertiary components with respect to the primary are given.

2172 fully reduced and combined 2D images, each corresponding to a wavelength between 14750 and 24930Å in steps of 5Å.

Before extraction of the stellar 1D spectra from the data cubes, unusable pixel data (residual bad pixels, nearby “negative stars” from the sky subtraction, or blending with other stars in the image) were replaced by the median value computed in a circular annulus of 2 pixels width at the radius of the defect around the trace at the wavelength they occur. The accuracy of this method was tested by applying the median substitution to good regions in a test cube. The difference between the extracted flux from the regular and the partly substituted cube was less than 1% at all wavelengths.

All spectra were extracted two times with slightly different algorithms for different purposes. (a) to be compared with template spectra requiring good recovery of the overall spectral shape and (b) to measure Br γ emission with a good signal-to-noise ratio.

(a) *Extraction with preservation of the spectral slope.* Due to the fact that adaptive optics correction produces a wavelength-dependent PSF (see Fig. 4.4), application of a custom extraction routine was necessary¹⁵. To accommodate the curved trace of each star throughout the cube (the position of the star between 1.5 and 2.4 μm can differ by up to more than 1 spatial pixels) and the changing shape of the PSF as a function of wavelength, the center of each stellar component (target and standard) was traced and fitted by a 4th-order polynomial and its wavelength-dependent FWHM_λ measured at every λ by fitting a two-dimensional Moffat profile to the stellar disk. Multiple extractions were then conducted for each target component with aperture radii equal to 1, 2, 4, 6, 8, & 10 times the measured FWHM_λ . If the target PSF appeared to be strongly elliptical or if two very close components of a multiple were extracted together, elliptical apertures were used, designed from an elliptical 2D Moffat profile fit. To make sure that the overall shape of the extracted spectrum is conserved, all extractions were compared to the result from the largest aperture ($10 \times \text{FWHM}_\lambda$) which contains close to 100% of the flux. All extractions which agree with this reference spectrum to better than 5% at all wavelengths were then examined for their noise. The extraction with the highest SNR (typically $2\text{--}4 \times \text{FWHM}_\lambda$) was selected.

(b) *Extraction with maximum signal to noise.* For the determination of Br γ flux, only local correction is necessary. Thus, the overall spectral shape does not need to be conserved and the extraction can be optimized for SNR in the Br γ region. This was achieved by using small extraction apertures ($0.5\text{--}1 \times \text{FWHM}_\lambda$). The typical improvement in SNR over the continuum-conserving extraction at $\lambda_{\text{Br}\gamma}$ is a factor of ~ 2 . In the following, I will refer to the results from (a) as *flux-conserved extraction* and from (b) as *High-SNR extraction*.

Telluric standard star spectra were extracted with the same procedures. To produce pure telluric spectra – convolved only with the instrumental profile – intrinsic absorption lines (mostly Hydrogen) and the spectral shape (\sim black body at T_{eff}) were removed. Absorption lines (except Br γ) were removed through interpolation of the continuum. Since

¹⁵Though recommended by the data reduction cookbook for the extraction of SINFONI data, *QFitsView* (<http://www.mpe.mpg.de/~ott/QFitsView/>) could not cope with the observed wavelength-dependent star location and FWHM

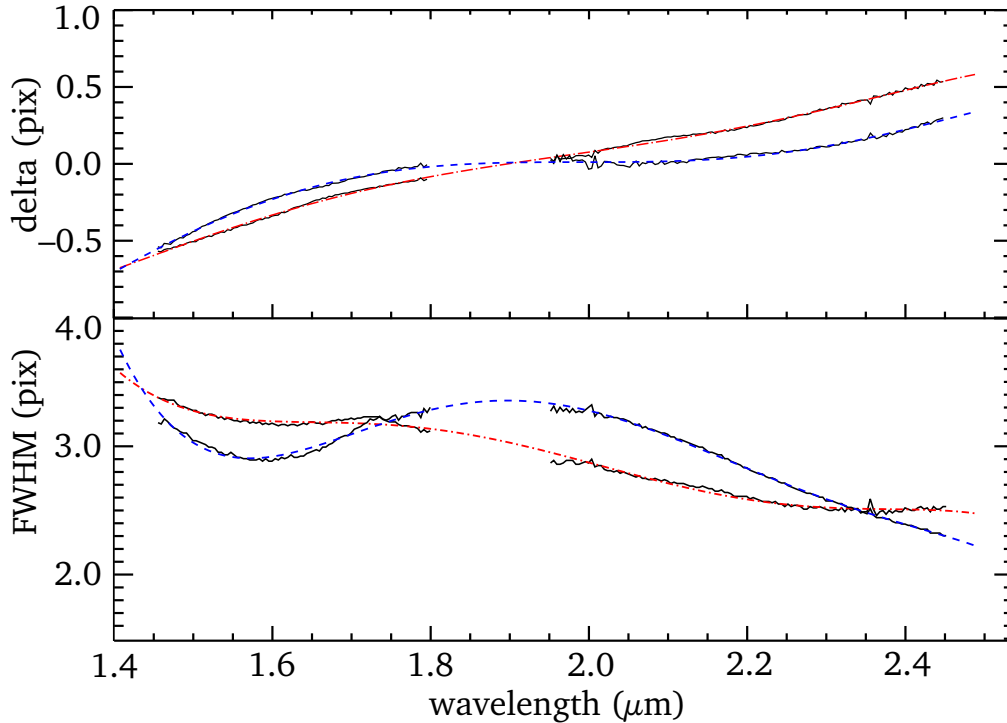


Figure 4.4: Example for the result of tracing a stellar component (here T 27 A) through a data cube. **Top panel:** The relative measured deviation from a reference pixel position are shown in black and best fits with 4th-order polynomials are indicated by the red dash-dotted and blue dashed line for the x - and y -direction, respectively. **Bottom panel:** Measured FWHM as a function of wavelength and 4th-order best fit polynomials used for extraction. Colors are the same as in the top panel (red: x , blue: y).

a careful recovery of Br γ flux is crucial for the measurement of accretion, this absorption line is removed according to the procedure used for the Br γ measurements in the ONC sample (Sect. 3.1.3), which uses an estimate of the telluric spectrum around Br γ from target spectra with neither absorption nor emission in this line. Subsequent correction for the intrinsic continuum shape of the standard stars was done by dividing blackbody spectra with temperatures according to the spectral type (Cox 2000). Fine-tuning of possible wavelength shifts of the telluric spectra in the standard and science spectra was done by a local cross-correlation of 20 pixel-wide sections of the telluric and target spectra, which were shifted to match the position of their telluric absorption features to the sub-pixel level. Finally, target spectra were divided by their corresponding *clean* telluric reference spectrum.

For two of our target multiples, CHXR 9C and CHXR 71, two epochs of data with good SNR were taken (see Table 4.1). Both data sets were reduced and extracted according to the scheme detailed above. Since no significant variability was apparent in the data, both extractions of all respective components were averaged to increase the SNR.

The final SNR of the reduced spectra depends on source brightness but never drops

below 20 anywhere in the spectral windows of H and K -band for the shape-conserved reductions except for the two sub-stellar companions. The typical SNR per pixel around Br γ in the high-SNR reduction is around 80. The spectral region of low atmospheric transparency between 18000 and 20000 Å has a low SNR and is not used for any scientific considerations in this thesis. The final reduced and extracted spectra of all multiple star components are shown in Fig. 4.5, the most important stellar absorption features (see Table 3.5) as well as Br γ are marked.

Flux calibration

After extraction, all spectra were flux calibrated with a routine similar to the one described in Sect. 3.1.3. K_s -band photometry was compared to synthetic photometry derived from convolving the uncalibrated SINFONI $H+K$ spectra with a K_s filter curve. Since the total flux of the high-SNR spectra is not conserved, these use the calibration factor derived from the flux-conserved extraction of the same target. Although flux calibration would have been possible from H -band as well (or a combination of H and K) only K_s calibration was used since the extracted K -band shows less noise and will return a better calibration for the Br γ feature at 2.166 μm .

4.2 Results

4.2.1 The color-color diagram: photometric extinctions and color excesses

Fig. 4.6 shows the $(J-H)-(H-K_s)$ and $(H-K_s)-(K_s-L')$ color-color diagrams for Cha I binaries with photometric data from Table 4.2. The data are compared to the sequence of dwarfs and giants, the CTTS locus, as well as to a sequence of K4–M9 pre-main sequence stars taken from Luhman et al. (2010). The data show a clear clustering around the tip of the PMS sequence at a spectral type $\sim\text{M1}$.

The color-color diagrams are used to derive photometric extinctions. The extinction A_V^{phot} of a target component was determined by moving it towards bluer colors along the reddening vector in the $(J-H)-(H-K_s)$ diagram¹⁶ until intersecting either the CTTS locus or the PMS sequence. To decide whether to deredden to the CTTS locus or the PMS sequence, the $(H-K_s)-(K_s-L')$ diagram was used since here the CTTS locus is clearly separate from the PMS, dwarf, and giant sequences. Targets that are clearly associated with the CTTS locus in $(H-K_s)-(K_s-L')$, i.e. fall along it or cannot otherwise be dereddened to the PMS sequence, are dereddened to the corresponding CTTS locus in $(J-H)-(H-K_s)$. All other target components are dereddened to the PMS sequence. Any targets with $J-H \lesssim 0.05$ are assigned an extinction of $A_V=0$. Uncertainties are determined from deredden-

¹⁶ $(J-H)-(H-K_s)$ is preferred over the $(H-K_s)-(K_s-L')$ diagram for the determination of extinction since interstellar extinction is stronger in JHK_s than in L' and thus results in higher precision.

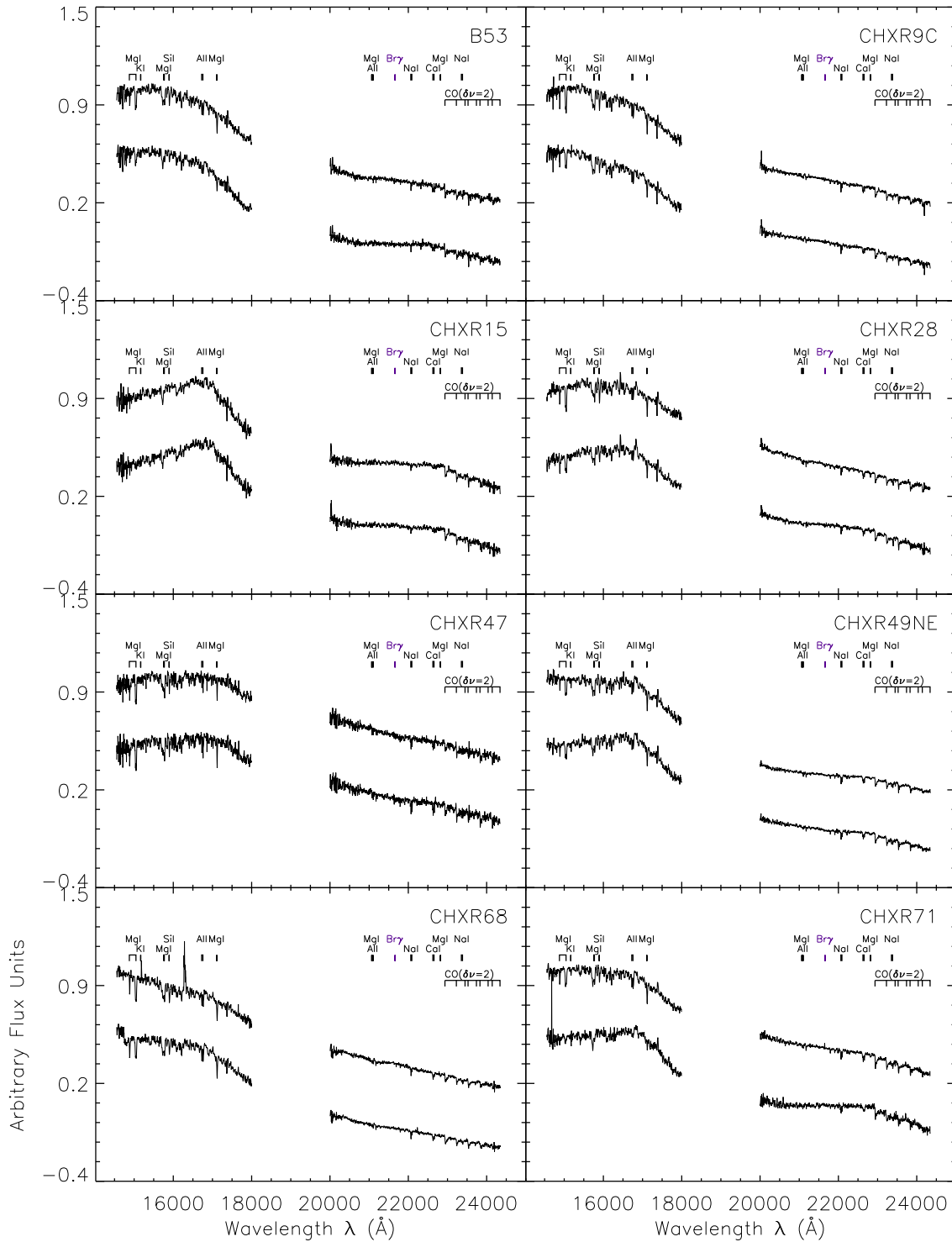


Figure 4.5: Spectroscopy of all target components observed with SINFONI. The most massive component is shown on top, the least massive component at the bottom. The most prominent absorption features of low-mass pre-main sequence stars are indicated (see Table 3.5 for a list). The spectra of CHXR73B and T 14 B are shown binned by a factor of 4.

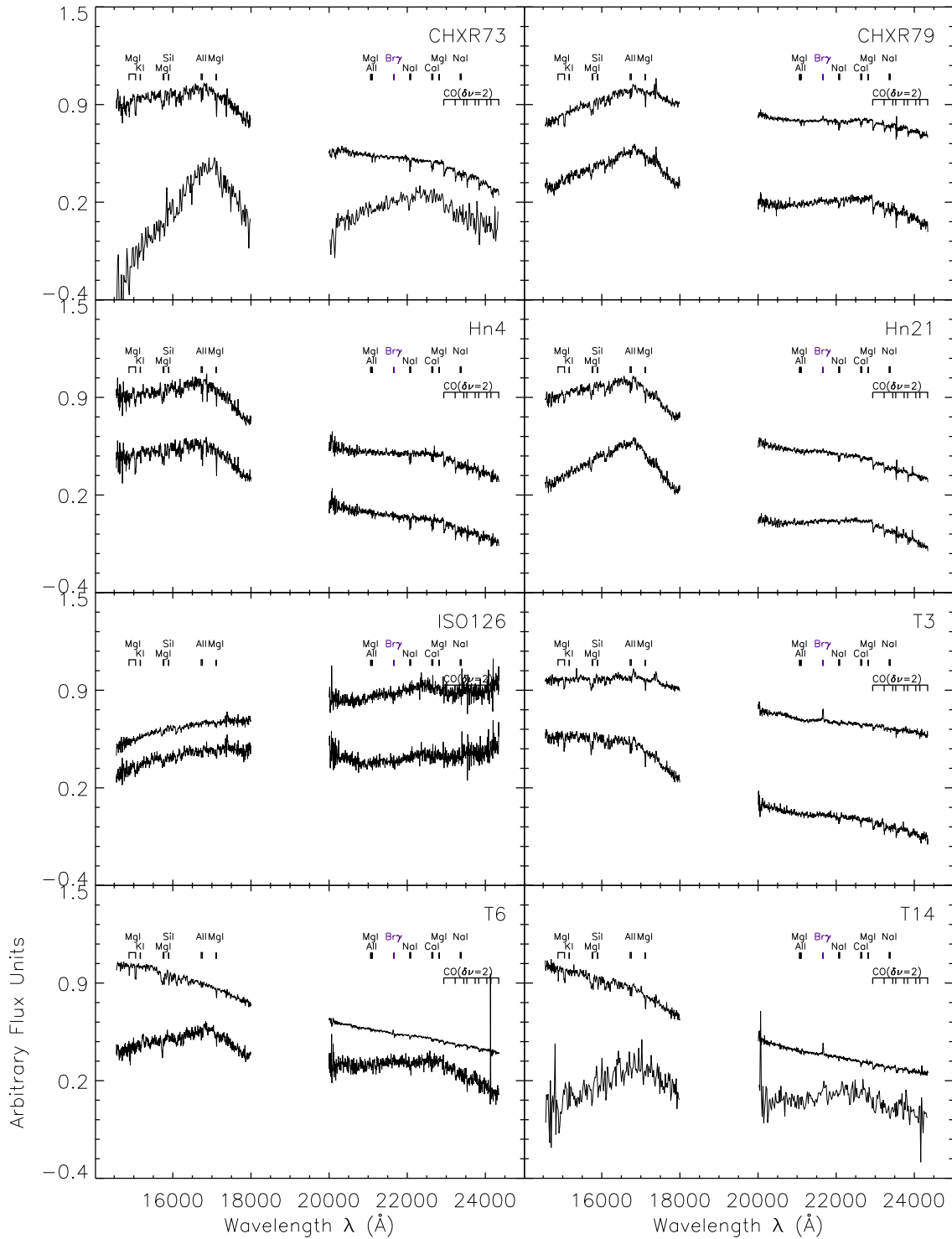


Figure 4.5: ctd.

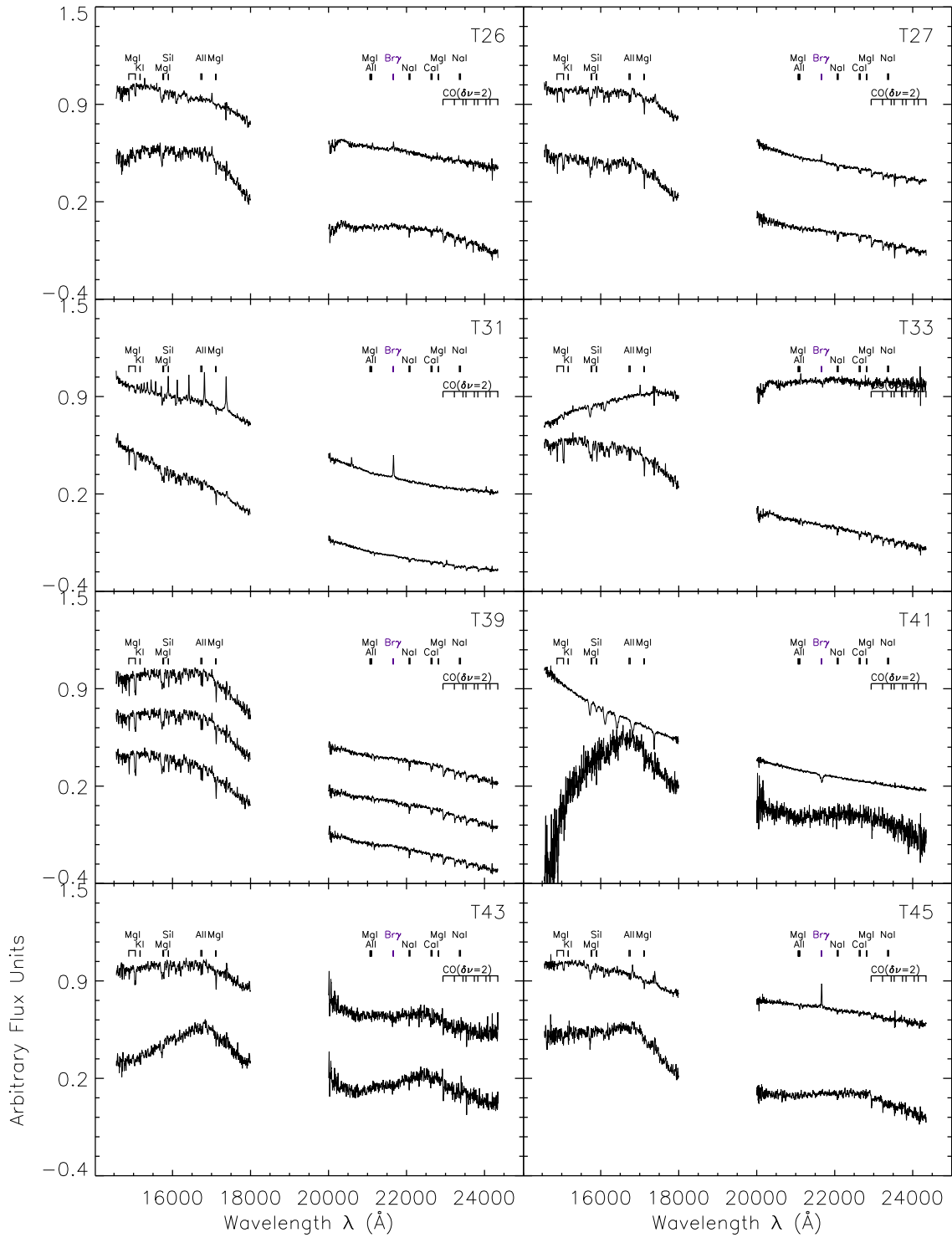


Figure 4.5: ctd.

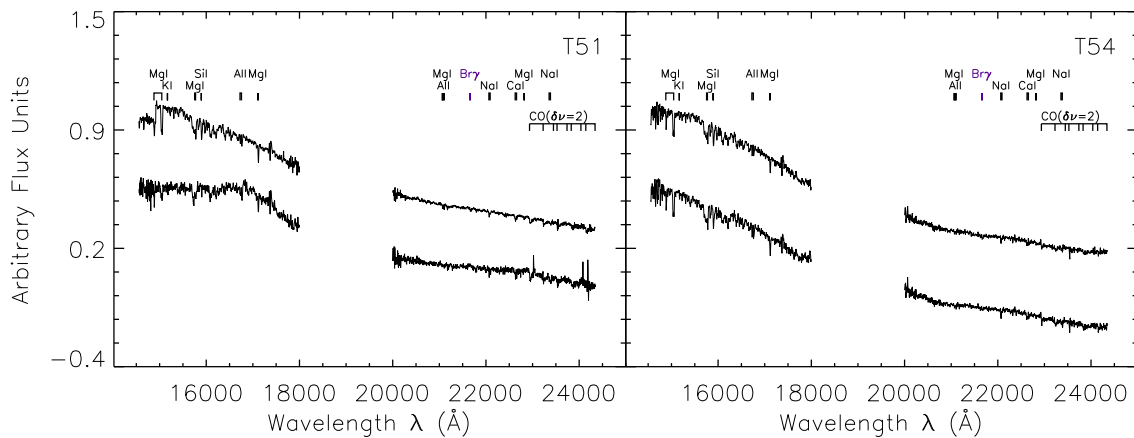


Figure 4.5: ctd.

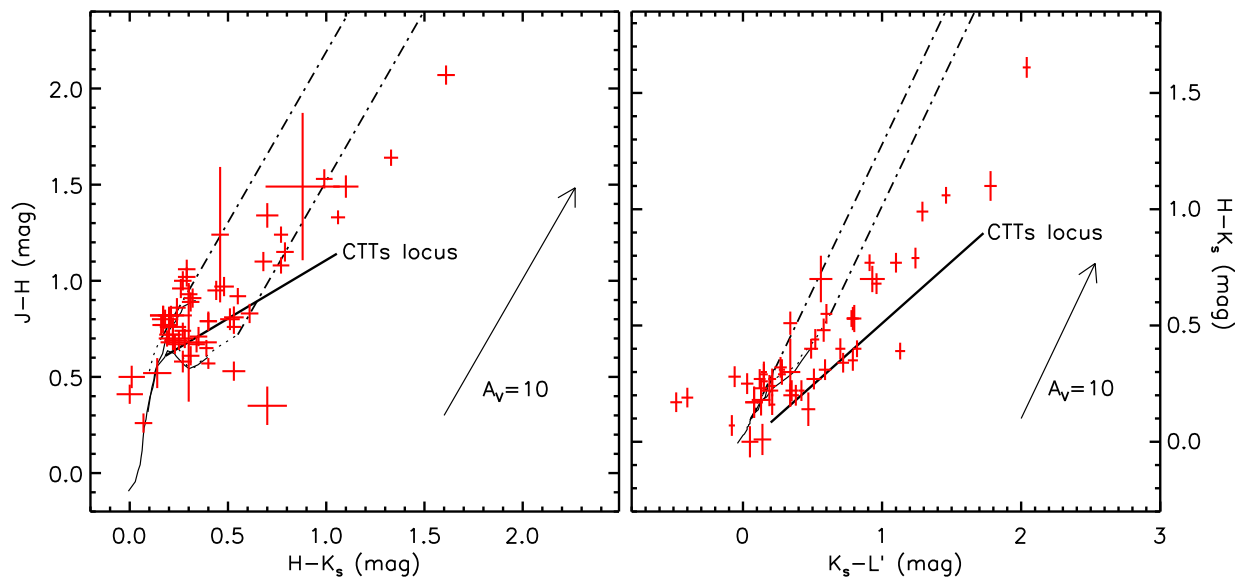


Figure 4.6: Color-color diagrams with photometric data from Table 4.2. Data is shown as red crosses, overplot are the giant and dwarf sequences (thin continuous lines) from [Bessell & Brett \(1988\)](#), the CTTs locus ([Meyer et al. 1997](#)), and a reddening vector of length $A_V = 10$ mag ([Cohen et al. 1981](#)). The dotted locus just above the dwarf sequence is the sequence derived from PMS stars in [Luhman et al. \(2010\)](#). Targets between the two dash-dotted lines can be dereddened to the PMS locus.

ing according to the uncertainties of the color measurements. The photometric extinctions A_V^{phot} are listed in Table 4.2.

Component extinctions of some of the wider binaries are published in Luhman (2007) and values typically agree to within $\Delta A_V \approx \pm 1$ mag. Luhman use a mixture of spectroscopic fitting of PMS templates in addition to near-IR dereddening similar to the method used here. Their published A_J values were converted to A_V via $A_J = 0.276 A_V$ (Cohen et al. 1981).

Color excesses were derived for all targets according to

$$E_{K_s-L'} = (K_s - L')_{\text{obs}} - 0.04 A_V - (K_s - L')_0 \quad (4.2)$$

(cf. Eq. 3.1) with reference $(K_s - L')_0$ dwarf colors, converted to the 2MASS system, from Bessell & Brett (1988) according to the spectral types in Table 4.3 (see Sect. 4.2.2). It is possible that the derived excesses over- or underestimate the real excess, since the near-IR colors of low-mass PMS stars and dwarfs of the same spectral type differ by up to a few times 0.1 mag (compare e.g. Bessell & Brett 1988 with Luhman et al. 2010). Since there are no well-calibrated $K_s - L'$ values for pre-main sequence stars available in the literature, I estimated the size of this effect by comparing PMS ($K - [3.6]$) colors (Luhman et al. 2010) to dwarf $K_s - L'$ colors and find a difference between 0.05 and 0.17 mag in the spectral type range between K4 and M6. Although the *Spitzer/IRAC* [3.6]-band and L' are not identical, this gives an indication of the magnitude of this effect. I assign systematic uncertainties of 0.2 mag to the derived $E_{K_s-L'}$ values in Table 4.2.

4.2.2 Spectral types, extinction & veiling

To measure spectral types, veiling, and to obtain another independent estimate of extinction, I compared the extracted flux-conserved spectra with dwarf spectra from the IRTF library in a similar way as done for the ONC binaries (Sect. 3.2.2). The advanced age of Cha I compared to the ONC suggests that the spectra in this sample will be even more similar to dwarf spectra. Indeed, the strong concentration of Cha I targets along the dwarf sequence in a $W(\text{Na I} + \text{Ca I}) - W(\text{CO}[2-0] + \text{CO}[4-2])$ diagram (Fig. 4.7) indicates the similarity between the depth of the photospheric absorption features and thus the surface gravity $\log g$ between dwarfs and the Cha I PMS stars. Accordingly, dwarf spectra are assumed to be suited to serve as templates and will be used for the derivation of spectral parameters.

To limit the number of templates that need to be tested for their compatibility with each target spectrum, an initial spectral type selection was done using the extinction-independent *Wilking's Q* (Wilking et al. 1999) and I_{H_2O} indices (Comerón et al. 2000). Q is measured from the ratio of fluxes at three positions $F1$ (2.07–2.13 μm), $F2$ (2.276–

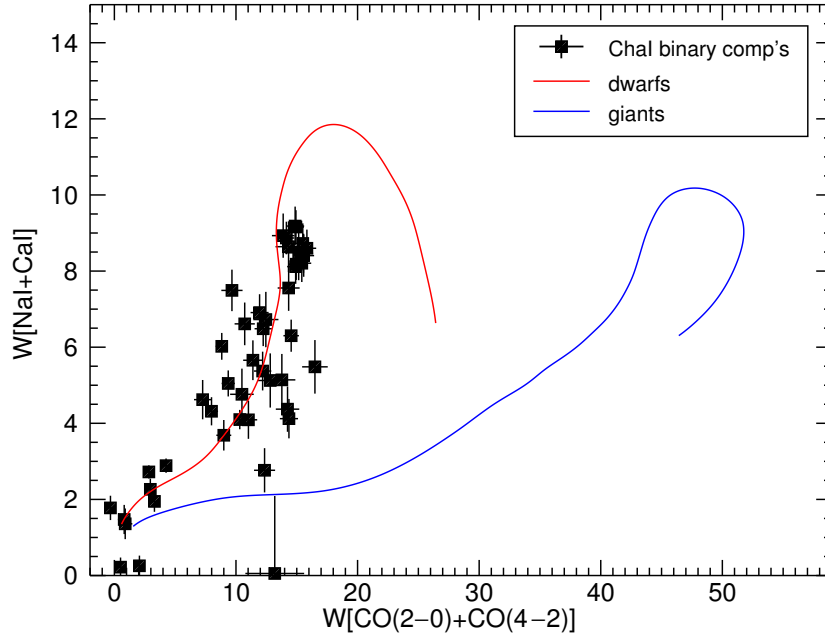


Figure 4.7: Comparison of the Cha I target components with dwarfs (red) and giants (blue) from the IRTF spectral library in terms of their equivalent widths in the mostly temperature sensitive Na I and Ca I lines and the surface gravity sensitive ^{12}CO band heads. The dwarf and giant loci are the same as in Fig. 3.4. A clear concentration of Cha I target components around the dwarf sequence can be seen validating dwarfs as suitable reference spectra. Strong veiling reduces the measured equivalent widths and explains the clustering of targets close to the origin and to the left of the dwarf sequence¹⁷.

2.285 μm), and $F3$ (2.40–2.43 μm)¹⁸ in the K -band as

$$Q = \frac{F1}{F2} \left(\frac{F3}{F2} \right)^{1.22} \quad (4.3)$$

and I_{H_2O} is measured at four positions between 1.6 and 2.3 μm (f_1, f_2, f_3, f_4 at 1.675 μm , 1.750 μm , 2.075 μm , and 2.250 μm each with a width of 0.05 μm) according to

$$I_{H_2O} = \frac{f_1}{f_2} \left(\frac{f_3}{f_4} \right)^{0.76} . \quad (4.4)$$

¹⁷A revisit of Fig. 4.7 with measured veiling values after the use of dwarf spectra as templates (Fig. 4.9) shows that all targets with $W(\text{Na I}+\text{Ca I}) < 3.5 \text{ \AA}$ and $W(\text{CO}[2-0]+\text{CO}[4-2]) < 5 \text{ \AA}$ as well as most targets to the left of the dwarf sequence are veiled with $r_K \geq 0.1$. Targets with low veiling are particularly compatible with the dwarf sequence and confirm the applicability of dwarf templates in retrospect.

¹⁸The original definition of $F3$ uses a range of 2.4–2.5 μm , extending to longer wavelengths than extracted here. The systematic error introduced by this approximation is $\approx 10\%$ ($Q_{\text{this paper}}/Q_{\text{Wilking}} \approx 0.90$) measured from the template spectra that span the whole range up to 2.5 μm . The use of a new fit to the Q -SpT relation (Fig. 4.8) accounts for this difference and enables me to infer spectral types also from the shorter wavelength range. A marginal extinction dependence may be introduced due to the different color excess ratios that apply to the 2.40–2.43 μm and 2.4–2.5 μm ranges, respectively (see e.g. the derivation of Q after Johnson & Morgan 1953). The difference, however, is small and not relevant for the use of Q in this context.

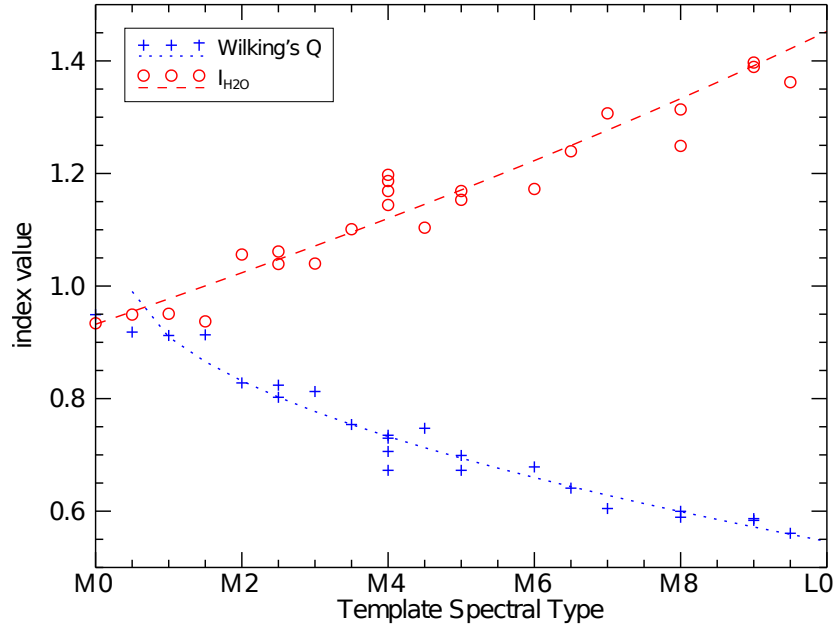


Figure 4.8: Wilking’s Q and I_{H_2O} indices after Wilking et al. (1999) and Comerón et al. (2000), measured for the dwarf template sequence from the IRTF library (Cushing et al. 2005; Rayner et al. 2009). The dashed and dotted lines are best second-order polynomial fits to the data.

A second-order polynomial was fit to both indices (see Fig. 4.8) derived from the templates as a function of spectral type assigned by the authors of the sequence (Cushing et al. 2005; Rayner et al. 2009). The two derived relations for sub-classes of M are

$$(\text{SpT}_M)_Q = 44.3 - 85.7 Q + 41.9 Q^2 \quad , \quad (4.5)$$

$$(\text{SpT}_M)_{I_{H_2O}} = -26.3 + 33.9 I_{H_2O} - 6.18 I_{H_2O}^2 \quad (4.6)$$

with a residual scatter of < 2 sub-classes. Both indices become independent of spectral type for spectral types earlier than $\sim M1$ and are used only for determinations between M1 and L0.

Q and I_{H_2O} were calculated for the flux-conserved spectra of all targets. Both spectral type estimates, $(\text{SpT}_M)_Q$ and $(\text{SpT}_M)_{I_{H_2O}}$ which typically agree to within 3 sub-classes, were averaged for each target. The subsequent detailed inspection of these and another ± 3 sub-classes was usually sufficient to find the best match between the spectral templates and the target component spectra. Targets with spectral types earlier than M1 were determined without such a pre-selection.

The final selection of the best-fitting template was done by analyzing the absolute and relative strength of multiple T_{eff} -dependent absorption features in H and K -band (e.g. Na I, Ca I, Al I, Mg I, Si I, see Table 3.5) by visual comparison of the continuum-subtracted target spectra with the selection of IRTF spectra. The resulting spectral type uncertainties are typically between 0.5 and 2 subclasses, estimated from the range of possible spectral type matches. Attempts to use an automatic spectral type determination from line ratios

did not return similarly good results. This is due to the weak strength of most absorption lines at the low spectral resolution of $R \approx 1400$ and the comparably uncertain continuum determination in the near-IR spectra.

The template with the best spectral type was modified by adding artificial reddening and veiling in 3 iterations, each with refined grids in extinction A_V , continuum excess k , and constant c according to Eq. (3.2). The best fitting parameter combination and all uncertainties are derived through χ^2 minimization (see Sect. 3.2.2 for details).

Due to the relatively wide wavelength range of ($\sim 1.45\text{--}2.5\ \mu\text{m}$) of these observations, I tested whether the veiling can safely be assumed to be independent of λ . As suggested by observations of e.g. Muzerolle et al. (2003), veiling can take the shape of a blackbody at the dust sublimation temperature. To simulate this, the constant k was multiplied with a blackbody curve of temperature 1500 K and the fitting was repeated. The new best fits were at best indistinguishable from the fitting with constant excess, but mostly visibly worse and also the best χ^2 was typically larger. Consequently, k was assumed to be constant for the derivation of r_K according to Eq. (3.4). The resulting best fitting spectral types, A_V^{spec} , and r_K are listed in Table 4.3.

Best fit templates typically fit the target spectrum very well over the wavelength range between ~ 1.7 and $\sim 2.5\ \mu\text{m}$ (see the best fit target spectra in Appendix B.2). The wavelength range between ~ 1.5 and $\sim 1.7\ \mu\text{m}$ is only fit well in $\sim 70\%$ of the cases. Part of these deviations can be explained in part by uncertainties in the spectral extraction routine which are larger at short wavelengths due to a decreased Strehl ratio (cf. the increase of FWHM with decreasing wavelength in Fig. 4.4). The majority of deviations, however, are likely due to broad water absorption features at $1.38\ \mu\text{m}$ and $1.87\ \mu\text{m}$ which produce a characteristic triangular continuum shape in young late-type spectra (e.g. Sato et al. 1992) which is not as pronounced in dwarf spectra due to their higher surface gravity. That surface gravity is indeed the reason for the deviant continuum at $< 1.7\ \mu\text{m}$ is demonstrated in Fig. 4.9 which shows that target components with the strongest bias towards the giant locus (i.e. with the lowest $\log g$, intermediate between that of dwarfs and giants) are almost exclusively stars which show strong deviations from dwarf spectra at $< 1.7\ \mu\text{m}$.

The early spectral type (B9) of T 41 A is outside the range covered by the spectral library in use. This value was copied from the *simbad*¹⁹ database. There are no further spectral values derived for this component since its discussion is outside the scope of this thesis. No spectral type could be derived for the brown dwarf candidates T 14 B and CHXR 73 B since the SNR of both spectra was too low to use spectral features for the determination of the spectral type. Assuming, however, a spectral type of M9.5 for CHXR 73 B (Luhman et al. 2006), spectral fitting could be run resulting in an extinction value of $A_V^{\text{spec}} = 1.6 \pm 0.7$ and veiling $r_K = 0.02 \pm 0.17$. The spectrum of T 33 A shows signs of strong extinction and veiling. By the shape of the continuum, it could be inferred that its spectral type is earlier than or equal to M3. Due to the strong veiling, however, photospheric features were not strong enough to reliably measure the SpT of this star. It is thus assigned SpT $< \text{M3}$ in Table 4.3 and no stellar parameters are derived. Luhman

¹⁹<http://simbad.u-strasbg.fr/simbad/>

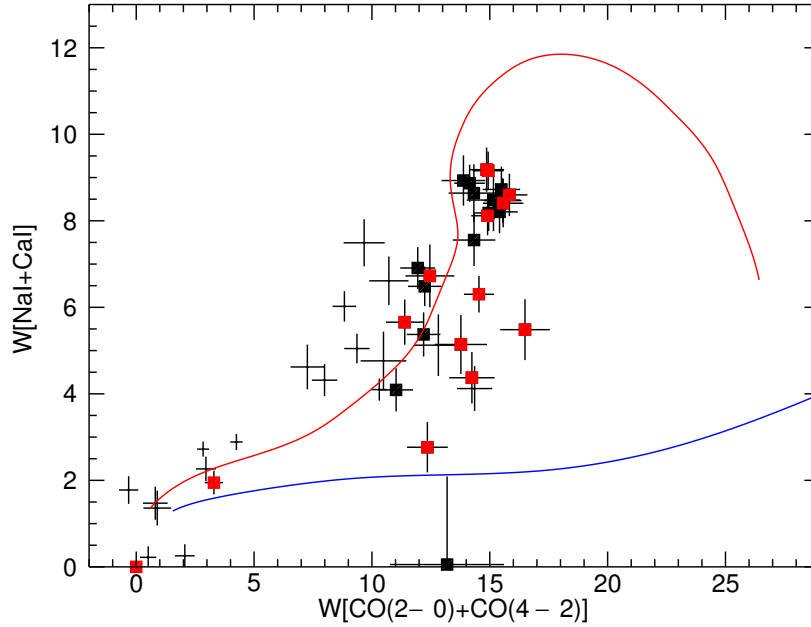


Figure 4.9: As Fig. 4.7 but target components with a continuum significantly different from that of a dwarf star between 1.45 and 1.7 μm are marked with red squares (see Appendix B.2). Low-veiling components with $r_K < 0.1$ are marked by black squares and high veiling components $r_K > 0.1$ by error bars only.

(2007) list T 33 A with a spectral type of G7 which the present data can neither confirm nor reject. The spectra of the components of ISO 126 and T 31 suffer from high veiling or extinction or both. Despite the fact that spectral typing was possible from the weak photospheric features, the spectral fitting did not return any satisfying results for these components. This might be due to a particularly large difference between the spectral shape of these targets and dwarf spectra or possible undetected observational/reduction errors.

To estimate the impact of a bad fit at wavelengths $< 1.7 \mu\text{m}$ on the parameter extraction, test fits were run in a limited wavelength range of 1.7–2.43 μm and compared with the fitting over the whole range. The changes in the measured A_V and r_K values were insignificant ($\Delta A_V < 0.3$, $\Delta r_K < 0.01$) with however larger uncertainties than when derived from the whole available wavelength range. Accordingly, dwarf templates are fit to all target components in the whole 1.45–2.43 μm range.

Photometric vs. spectroscopic extinctions

The spectroscopic measurements provide an independent estimation of the interstellar extinction in addition to the photometric extinctions from Sect. 4.2.1. In Fig. 4.10 we see a comparison between the extinction values from both derivations. While the scatter around the line of equal extinctions is quite high – deviations of 3 mag and more do appear – no strong systematic differences could be noticed. There is also no systematic difference be-

Table 4.3: Individual spectroscopic component properties

Name	Comp.	SpT	T_{eff} [K]	A_V^{spec} [mag]	r_K ($F_{K_{\text{ex}}}/F_{K_*}$)	L_* [L_{\odot}]	age [Myr]
B 53	A	M2 ± 1	3560 ± 150	0.1 ± 0.4	0.00 ± 0.09	0.19 ± 0.04	4.0 ± 4.0
	B	M4 ± 0.5 1.5	3270 ± 150	0.2 ± 0.4	0.00 ± 0.07	0.05 ± 0.01	8.0 ± 4.0 3.2
CHXR 9C	A	M1.5 ± 1	3630 ± 150	0.0 ± 0.5	0.04 ± 0.16	0.20 ± 0.03	4.4 ± 5.1 1.6
	BaBb	M2 ± 1 1.5	3560 ± 180	0.1 ± 0.5	0.05 ± 0.16	0.22 ± 0.03	3.3 ± 3.5 1.0
CHXR 15	A	M5 ± 1	3130 ± 140	0.2 ± 0.7	0.00 ± 0.15	0.06 ± 0.01	4.5 ± 2.5 0.9
	B	M5 ± 1 1.5	3130 ± 170	0.1 ± 0.6	0.00 ± 0.13	0.04 ± 0.01	6.0 ± 6.0 2.0
CHXR 28	AaAb	K7 ± 1 1.5	4060 ± 290	2.7 ± 0.4	0.02 ± 0.13	1.2 ± 0.3	1.3 ± 2.5 0.5
	B	M2.5 ± 0.5	3490 ± 110	0.4 ± 0.6	0.13 ± 0.18 0.13	0.42 ± 0.09	1.6 ± 0.4
CHXR 47	A	K5.5 ± 1 1.5	4210 ± 390	5.8 ± 0.7	0.19 ± 0.21 0.15	0.72 ± 0.14	4.5 ± 9.5 3.1
	B	K7 ± 1 1.5	4060 ± 210	5.2 ± 0.8	0.26 ± 0.24 0.18	0.47 ± 0.09	5.5 ± 6.5 3.0
CHXR 49NE	A	M2.5 ± 0.5 1	3490 ± 110	0.0 ± 0.4	0.00 ± 0.03	0.20 ± 0.04	3.4 ± 1.2 0.8
	B	M3.5 ± 1	3340 ± 110	0.0 ± 0.3	0.00 ± 0.04	0.15 ± 0.03	3.4 ± 0.6
CHXR 68	AaAb	M0 ± 1	3850 ± 180	0.3 ± 0.5	0.00 ± 0.11	0.44 ± 0.10	3.0 ± 4.0 1.4
	B	M1 ± 0.5	3710 ± 110	0.0 ± 0.2	0.00 ± 0.05	0.12 ± 0.02	12 ± 7
CHXR 71	A	M3 ± 0.5 1.5	3560 ± 270	2.3 ± 0.6	0.01 ± 0.15	0.11 ± 0.03	7.0 ± 8.0 3.5
	B	M5 ± 2	3130 ± 270	1.5 ± 0.6	0.04 ± 0.18	0.018 ± 0.003	13 ± 7
CHXR 73	A	M2.5 ± 1 1.5	3490 ± 180	1.6 ± 0.7	0.02 ± 0.17	0.09 ± 0.07	8 ± 7 5
	B
CHXR 79	A	M2 ± 1	3560 ± 150	9.6 ± 0.4	0.22 ± 0.25 0.20	0.36 ± 0.07	2.0 ± 1.0 0.5
	B	M4 ± 0.5 1	3270 ± 110	6.4 ± 1.0	0.22 ± 0.16	0.035 ± 0.007	12 ± 5.5
Hn 4	A	M4 ± 0.5 1	3270 ± 110	3.6 ± 0.5	0.01 ± 0.12	0.10 ± 0.02	4.2 ± 1.0
	B	M3 ± 1	3420 ± 150	3.5 ± 0.5	0.00 ± 0.10	0.11 ± 0.02	5.2 ± 5.0 0.7
Hn 21	A	M3.5 ± 0.5 1	3340 ± 110	2.6 ± 0.7	0.02 ± 0.14	0.11 ± 0.02	4.5 ± 2.0
	B	M6.5 ± 2 2.5	2940 ± 200	0.0 ± 0.6	0.00 ± 0.14	0.030 ± 0.006	5.5 ± 4.5 1.5
ISO 126	A	M0.5 ± 1 2	3780 ± 400	>4	≥1	0.50 ± 0.09	2.0 ± 8 1.1
	B	M0.5 ± 2 1.5	3780 ± 400	>4	≥1	0.090 ± 0.006	(23 ± 18)
T 3	A	M1.5 ± 1 2	3630 ± 320	2.2 ± 1.1	1.3 ± 1.8 0.6	0.50 ± 0.09	1.6 ± 2.3 0.8
	B	M3 ± 1 1.5	3420 ± 250	0.5 ± 0.7	0.18 ± 0.22 0.14	0.10 ± 0.02	5.8 ± 10 2.5
T 6	A	K1 ± 3 2	5080 ± 490	0.0 ± 0.9	1.5 ± 2.1 0.7	1.6 ± 0.4	10 ± 12
	B	M6 ± 1 3.5	2990 ± 320	4.6 ± 1.2	0.54 ± 0.14	0.06 ± 0.01	4.2 ± 5.8 4.0
T 14	A	K7 ± 1 0.5	4060 ± 180	0.1 ± 0.5	0.33 ± 0.28 0.20	0.67 ± 0.15	3.0 ± 3.0 1.5
	B
T 26	A	G0 ± 1 3	6030 ± 290	6.6 ± 0.9	0.18 ± 0.14 0.10	4.7 ± 1.0	7.1 ± 3.0 0.7
	BaBb	M5 ± 2 2.5	3130 ± 290	0.9 ± 0.8	0.00 ± 0.16	0.11 ± 0.02	3.0 ± 3.0 2.8
T 27	A	M1.5 ± 2 0.5	3630 ± 180	2.9 ± 0.6	0.10 ± 0.19	0.14 ± 0.03	7.0 ± 9.0 3.0
	B	M3 ± 1	3420 ± 150	2.5 ± 0.7	0.00 ± 0.12	0.09 ± 0.02	6.4 ± 4.7 2.2
T 31	A	K7 ± 3 1.5	4060 ± 460	...	(≥1)	1.6 ± 0.3	1.0 ± 3.0 0.7
	BaBb	M0 ± 1.5	3850 ± 290	...	(~0)	0.76 ± 0.10	1.5 ± 2.5 0.6
T 33	A	<M3	(≥1)
	BaBb	M0.5 ± 1 1.5	3780 ± 210	1.5 ± 0.5	0.00 ± 0.12	0.57 ± 0.13	1.8 ± 2.2 0.7
T 39	A	M2.5 ± 0.5	3490 ± 70	0.2 ± 0.4	0.00 ± 0.08	0.25 ± 0.05	2.7 ± 0.7 0.3
	B	M2 ± 0.5	3560 ± 70	0.2 ± 0.4	0.00 ± 0.07	0.20 ± 0.04	4.0 ± 1.0 1.0
	C	M2.5 ± 0.5	3490 ± 70	0.0 ± 0.3	0.00 ± 0.07	0.14 ± 0.03	4.7 ± 2.3 1.2
T 41	A	B9 ^a	10500
	B	M3.5 ± 0.5	3340 ± 70	0.0 ± 0.2	0.00 ± 0.07	0.11 ± 0.08	4.5 ± 15 1.9
T 43	A	M3.5 ± 1 2	3340 ± 290	3.4 ± 0.7	0.44 ± 0.16	0.29 ± 0.06	1.8 ± 1.2 1.6
	B	M7 ± 1 2.5	2880 ± 360	4.5 ± 0.8	0.00 ± 0.16	0.05 ± 0.01	4.0 ± 4.0 3.9
T 45	A	M1 ± 1 1.5	3710 ± 200	2.8 ± 1.2	1.5 ± 2.2 0.7	0.81 ± 0.15	1.1 ± 0.6 0.7
	B	M5 ± 2 2.5	3130 ± 210	1.6 ± 0.9	0.22 ± 0.19 0.16	0.10 ± 0.02	3.3 ± 2.9 2.9
T 51	A	K7 ± 3	4060 ± 590	1.1 ± 0.7	0.48 ± 0.40 0.23	0.76 ± 0.17	2.5 ± 13 1.2
	B	M2.5 ± 1.5	3490 ± 220	3.8 ± 0.8	0.10 ± 0.20	0.10 ± 0.02	7.2 ± 3.4 3.4
T 54	A	G8 ± 3	5507 ± 440	0.2 ± 0.5	0.00 ± 0.10	2.0 ± 0.4	16 ± 30 10
	B	K7 ± 1.5	4060 ± 310	0.0 ± 0.5	0.04 ± 0.13	0.35 ± 0.08	9.0 ± 16 6.5

^a Spectral type from *Simbad*.

Table 4.3: Individual spectroscopic component properties (ctd.)

Target	Comp.	M_* [M_\odot]	R_* [R_\odot]	$(W_{\text{Br}\gamma}^{\text{accr}})^{\text{a}}$ [Å]	disk prob.	$\log(L_{\text{acc}}/L_\odot)$	\dot{M}_{acc} [$10^{-9}M_\odot\text{yr}^{-1}$]
B 53	A	$0.37 \pm_{0.05}^{0.10}$	1.15 ± 0.05	<0.91	0.00	<-2.44	<0.45
	B	$0.20 \pm_{0.05}^{0.07}$	0.71 ± 0.03	<1.44	0.00	<-2.96	<0.16
CHXR 9C	A	$0.41 \pm_{0.06}^{0.10}$	1.14 ± 0.05	<1.03	0.00	<-2.34	<0.51
	BaBb	$0.37 \pm_{0.07}^{0.13}$	1.24 ± 0.06	<0.87	0.00	<-2.41	<0.57
CHXR 15	A	0.16 ± 0.05	0.87 ± 0.04	<1.01	0.01	<-2.88	<0.29
	B	0.14 ± 0.06	0.71 ± 0.04	<1.13	0.03	<-3.10	<0.16
CHXR 28	AaAb	0.75 ± 0.25	2.21 ± 0.16	<1.01	0.00	<-1.51	<3.64
	B	0.36 ± 0.04	1.78 ± 0.06	<1.03	0.01	<-2.01	<1.93
CHXR 47	A	$0.95 \pm_{0.20}^{0.12}$	1.60 ± 0.15	<1.76	0.17	<-1.56	<1.86
	B	$0.80 \pm_{0.22}^{0.30}$	1.39 ± 0.07	<1.78	0.02	<-1.81	<1.08
CHXR 49NE	A	0.34 ± 0.06	1.22 ± 0.04	<1.07	0.01	<-2.46	<0.50
	B	0.27 ± 0.06	1.15 ± 0.04	<1.12	0.00	<-2.45	<0.60
CHXR 68	AaAb	$0.58 \pm_{0.13}^{0.20}$	1.50 ± 0.07	<1.40	0.04	<-1.74	<1.88
	B	$0.46 \pm_{0.18}^{0.10}$	0.83 ± 0.02	<0.82	0.00	<-2.79	<0.12
CHXR 71	A	0.37 ± 0.05	0.90 ± 0.03	<0.88	0.00	<-2.77	<0.16
	B	$0.13 \pm_{0.09}^{0.08}$	0.44 ± 0.04	<1.05	0.03	<-3.51	<0.04
CHXR 73	A	0.32 ± 0.11	0.83 ± 0.04	<0.98	0.00	<-2.91	<0.13
	B	(<4.48)	0.03
CHXR 79	A	$0.38 \pm_{0.05}^{0.10}$	1.57 ± 0.07	0.92 ± 0.21	0.74	-1.53 ± 0.24	$4.88 \pm_{3.66}^{3.83}$
	B	$0.19 \pm_{0.04}^{0.14}$	0.59 ± 0.02	<1.96	0.21	<-2.98	<0.13
Hn 4	A	$0.22 \pm_{0.05}^{0.07}$	1.00 ± 0.03	<1.61	0.00	<-2.42	<0.69
	B	0.30 ± 0.08	0.95 ± 0.04	<1.72	0.00	<-2.39	<0.52
Hn 21	A	0.26 ± 0.05	0.99 ± 0.03	<0.99	0.18	<-2.81	<0.24
	B	$0.08 \pm_{0.05}^{0.10}$ ^b	0.66 ± 0.04	<1.05	0.01	<-3.22	<0.20
ISO 126	A	$0.52 \pm_{0.19}^{0.38}$	0.47 ± 0.05	(<0.75)	0.00
	B	0.50 ± 0.2	0.70 ± 0.07	(<0.65)	0.00
T 3	A	$0.42 \pm_{0.13}^{0.21}$	1.79 ± 0.16	6.52 ± 0.28	1.00	-0.62 ± 0.05	$40.9 \pm_{13.2}^{21.4}$
	B	$0.29 \pm_{0.10}^{0.13}$	0.91 ± 0.07	<1.37	0.00	<-2.45	<0.45
T 6	A	1.4 ± 0.2	1.65 ± 0.16	<0.85	0.00	<-1.37	<2.01
	B	$0.10 \pm_{0.07}^{0.11}$	0.89 ± 0.09	<2.00	0.00	<-2.55	<1.00
T 14	A	0.78 ± 0.20	1.66 ± 0.07	5.86 ± 0.33	0.00	-0.90 ± 0.04	10.7 ± 3.0
	B	0.00
T 26	A	1.7 ± 0.2	2.00 ± 0.10	5.62 ± 0.30	1.00	-0.50 ± 0.15	14.9 ± 6.4
	BaBb	$0.18 \pm_{0.08}^{0.06}$	1.13 ± 0.11	<1.18	0.01	<-2.49	<0.81
T 27	A	$0.40 \pm_{0.06}^{0.14}$	0.96 ± 0.05	1.83 ± 0.22	1.00	-2.07 ± 0.25	$0.82 \pm_{0.70}^{0.65}$
	B	0.29 ± 0.07	0.87 ± 0.04	<1.00	0.01	<-2.85	<0.17
T 31	A	$0.75 \pm_{0.35}^{0.50}$	2.55 ± 0.29	(9.35 ± 0.19)	1.00	>-1.51	>4.20
	BaBb	$0.57 \pm_{0.19}^{0.28}$	1.97 ± 0.15	(<0.87)	0.01
T 33	A	(<0.84)	0.00
	BaBb	$0.52 \pm_{0.14}^{0.18}$	1.77 ± 0.10	<0.99	0.00	<-1.83	<2.01
T 39	A	0.36 ± 0.05	1.37 ± 0.03	<1.02	0.00	<-2.17	<1.03
	B	0.38 ± 0.05	1.17 ± 0.02	<1.05	0.00	<-2.33	<0.58
	C	0.34 ± 0.05	1.04 ± 0.02	<1.12	0.01	<-2.42	<0.47
T 41	A	<0.36	0.00
	B	0.26 ± 0.07	0.99 ± 0.02	<1.28	0.00	<-2.44	<0.55
T 43	A	$0.30 \pm_{0.10}^{0.11}$	1.62 ± 0.13	<1.07	0.00	<-2.34	<0.99
	B	$0.08 \pm_{0.07}^{0.12}$ ^b	0.91 ± 0.11	<1.07	0.00	<-3.00	<0.46
T 45	A	0.49 ± 0.12	2.18 ± 0.12	12.62 ± 0.47	1.00	-0.26 ± 0.10	98 ± 35
	B	$0.18 \pm_{0.06}^{0.05}$	1.08 ± 0.07	<1.28	0.01	<-2.62	<0.58
T 51	A	0.78 ± 0.40	1.77 ± 0.26	<1.08	0.01	<-1.55	<2.56
	B	$0.32 \pm_{0.09}^{0.12}$	0.85 ± 0.05	1.11 ± 0.38	0.68	-2.67 ± 0.47	0.23 ± 0.45
T 54	A	1.3 ± 0.2	1.52 ± 0.12	<0.87	0.48	<-1.69	<0.96
	B	$0.80 \pm_{0.3}^{0.15}$	1.20 ± 0.09	<1.07	0.00	<-2.23	<0.35

^a Values in parantheses mark lower limits since no veiling could be measured.^b Masses $<0.1 M_\odot$ lie outside the scope of the *Siess et al. (2000)* models. Values are estimated through extrapolation.

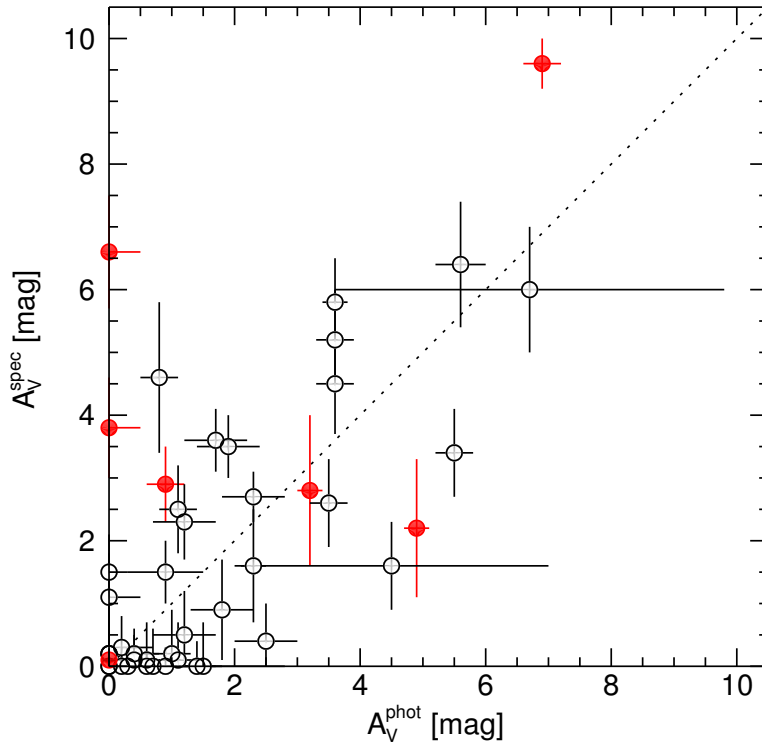


Figure 4.10: Spectroscopic versus photometric extinctions of all Cha I multiple star components. Red filled circles mark accreting components, all other components are marked with open circles. The dotted line shows equal extinctions.

tween accreting components and non-accretors visible. One of the measured spectroscopic extinctions is higher than the photometric value by more than 6 magnitudes (T 26 A). This star has a relatively large determined veiling value and the resulting fit is not as good as for most other targets, leading to less reliable constraints on the veiling. An over-estimation of veiling, however, can be the cause for an over-estimated extinction (see the correlation of best r_K and A_V in Fig. 3.5). A photometric determination of extinction using the more extinction-sensitive $J-H$ color instead of $H+K$ spectroscopy is more reliable and in the following I will use the photometrically derived values of all target components.

4.2.3 Effective temperatures & luminosities: the HR-diagram

Spectral types were converted to effective temperatures according to Schmidt-Kaler (1982) (earlier than M0) and Luhman et al. (2003) (later or equal to M0). The luminosity of each target component was estimated from its absolute M_J magnitude (assuming a distance to Cha I of 160 ± 15 pc, Whittet et al. 1997) and bolometric corrections as applied to the ONC binaries (Sect. 3.2.3). The luminosity uncertainties were calculated from the propagation of the uncertainties of all input parameters; they are dominated by the uncertainty in the distance measurement. Luminosities, effective temperatures, and stellar radii calculated

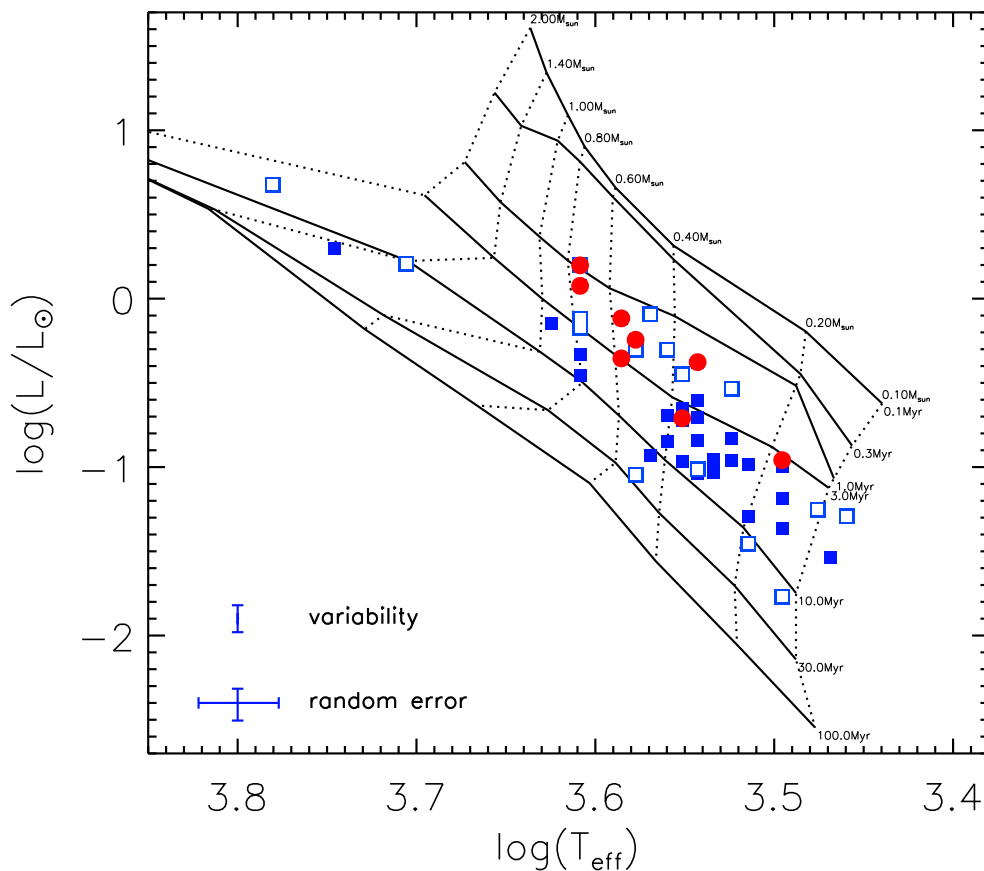


Figure 4.11: HR diagram with the isochrones of [Siess et al. \(2000\)](#). Filled red circles show spatially unresolved components, either close binary components of visual triple stars or spectroscopic binaries. Luminosities of these targets will likely appear larger than single stars at the same T_{eff} . Open blue squares show targets with strong near-IR excess ($E(K_s-L') > 0.5$ or $H-K_s > 0.6$) and filled blue squares all other components of the *Chamaeleon I* sample. In the lower left is a representation of the average random error and the luminosity uncertainty introduced by 0.2 mag variability in *J*-band ([Carpenter 2001](#)). It is striking that all targets with relatively high luminosities exhibit either strong color excess or are close binaries.

with Eq. (3.5) are listed in Table 4.3 and are used to compile the Hertzsprung-Russell diagram shown in Fig. 4.11.

Stellar masses & ages

The HR-diagram enables me to derive ages and masses of all components when comparing target locations with model isochrones. To derive the age and mass values in Table 4.3, models of [Siess et al. \(2000\)](#) were used. As all derived values depend on the choice of model for the applied isochrones, a comparison of the same data with [Palla & Stahler \(1999\)](#) isochrones is shown in Fig. 4.12. Qualitatively, there seems to be a slight bias towards younger ages in these latter models, as the sequence of low-color excess target components

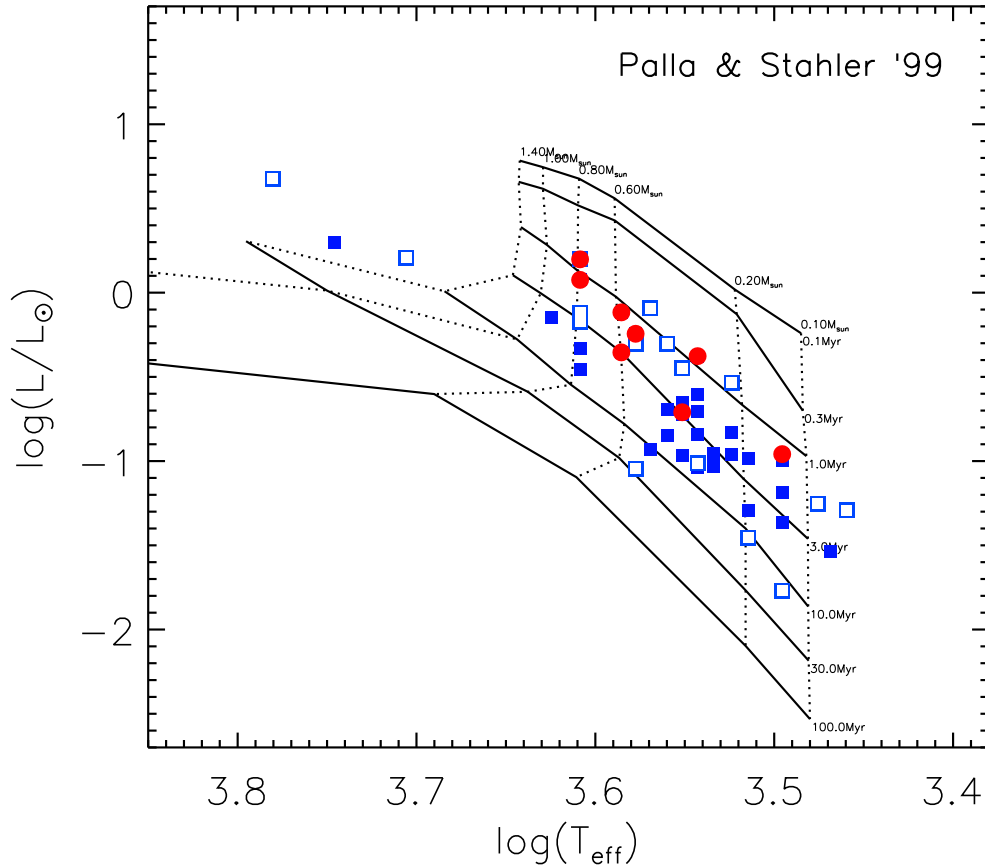


Figure 4.12: Same as Fig. 4.11 but with isochrones of Palla & Stahler (1999).

follows the 3 Myr isochrone of Palla & Stahler closely, while the same targets lie mostly below the 3 Myr isochrone of the Siess et al. (2000) models in Fig. 4.11 (see Sect. 4.3.1 for a discussion of the derived component ages). Also, masses below $\sim 0.2 M_{\odot}$ appear on average slightly less massive when derived with the Palla & Stahler models instead of those by Siess et al. (2000). In the following, the derived ages and masses from the Siess et al. isochrones will be used in order to guarantee comparability with the ONC results (Chapter 3) where the same model was applied. The differences between the inferred parameters from both sets of isochrones are likely smaller than their intrinsic systematic uncertainties. And, while most results will only be used for “order of magnitude” calculations, the inferred *mass ratios*, which will be discussed in Sect. 4.3.2, have been shown to be rather insensitive to the choice of isochrone (e.g. Lafrenière et al. 2008).

As expected, Fig. 4.11 shows that unresolved binary stars have above-average luminosities compared to individually observed components at the same T_{eff} . Depending on the brightness ratio of such close components, the derived ages can appear artificially young. The same is true for stars with strong near-IR excess. While excess is typically assumed to be weak in J -band (see e.g. Meyer et al. 1997), stars with overall strong excess emission can exhibit enough excess flux in J -band to significantly increase the estimated bolometric

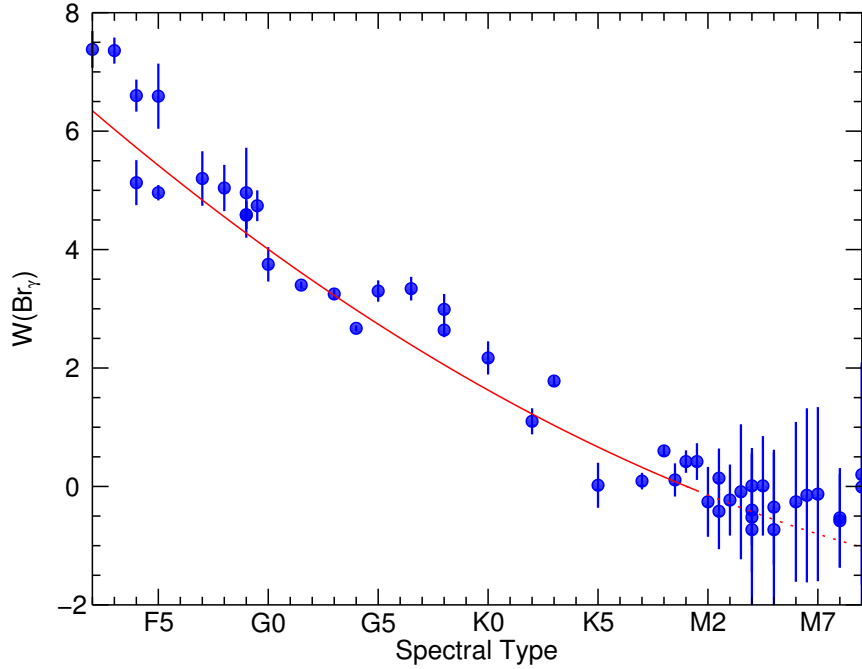


Figure 4.13: Equivalent widths of Br γ absorption lines as a function of spectral type measured from the IRTF dwarf template sequence. The red line shows our best fit (Eq. 4.7).

luminosity. Additionally, extinction might be over-estimated, as discussed in Sect. 4.3.1, which can as well lead to larger derived luminosities. These effects explain why the ten stars with the youngest derived ages are all either unresolved binaries or stars with strong color excess.

4.2.4 Accretion

Accretion activity is inferred from the existence of Br γ (21 665 Å) emission. To assess the strength of this line, the high-SNR spectral extraction is used.

Equivalent widths $W_{\text{Br}\gamma}$

Equivalent widths (Eq. 3.6) were integrated in a 56Å-wide interval around the centered Br γ peak²⁰. The continuum and noise background were estimated from regions shortward and longward of the line’s central wavelength. Br γ measurements were performed on the calibrated spectra, correcting for veiling by applying $W_\lambda = (1 + r_K) \times W_\lambda^{\text{measured}}$ (Eq. 3.7). To correct for the intrinsic Br γ absorption of spectral types earlier than M1, I measured the equivalent width in the same wavelength range for the spectral sequence of dwarf stars in the IRTF database. The correlation between $W_{\text{Br}\gamma}$ and spectral type is shown in Fig. 4.13

²⁰Note that Eq. (3.6) defines absorption features to have negative equivalent width values and emission to be positive.

Table 4.4: Equivalent widths of Br γ in dwarfs

SpT	$W_{\text{Br}\gamma}^{\text{photosph}}$ [Å]	SpT	$W_{\text{Br}\gamma}^{\text{photosph}}$ [Å]	SpT	$W_{\text{Br}\gamma}^{\text{photosph}}$ [Å]	SpT	$W_{\text{Br}\gamma}^{\text{photosph}}$ [Å]
G0	-4.00 ± 0.23	G5	-2.74 ± 0.15	K0	-1.63 ± 0.09	K5	-0.67 ± 0.06
G1	-3.74 ± 0.21	G6	-2.51 ± 0.14	K1	-1.42 ± 0.09	K6	-0.49 ± 0.05
G2	-3.48 ± 0.19	G7	-2.28 ± 0.13	K2	-1.22 ± 0.08	K7	-0.32 ± 0.05
G3	-3.23 ± 0.18	G8	-2.05 ± 0.12	K3	-1.03 ± 0.07	M0	-0.16 ± 0.05
G4	-2.98 ± 0.17	G9	-1.84 ± 0.10	K4	-0.85 ± 0.06	M1	0.00 ± 0.05

and was fit by a quadratic polynomial

$$W_{\text{Br}\gamma}^{\text{photosph}}(\text{SpT}) = (0.16 \pm 0.05) - (0.16 \pm 0.01) \times \text{SpT} + (0.0030 \pm 0.0004) \times \text{SpT}^2 \quad , \quad (4.7)$$

valid in a spectral type range between F0 and M1, with spectral types (SpT) measured as M0=0, M5=5, K0=-8, and so forth²¹. The absorption for spectral types later than M1 is small and no correction is applied here. Although a rather large correction likely applies, spectral types earlier than F0 remain uncorrected since the spectral template sequence does not reach to the earliest spectral type of this sample (T41 A, B9). The correction terms, tabulated in Table 4.4, are applied as

$$W_{\text{Br}\gamma}^{\text{accr}} = W_{\lambda} - W_{\text{Br}\gamma}^{\text{photosph}} \quad (4.8)$$

resulting in equivalent widths $W_{\text{Br}\gamma}^{\text{accr}}$ that are free of veiling and photospheric absorption. It can be assumed that the measured equivalent widths are a good indicator for the accretion, as Br γ has been found by [Antonucci et al. \(2011\)](#) to be well correlated with the accretion luminosity of young low-mass stars, better than the other examined tracers H α , Ca II, [O I], and Pa β . When the uncertainty of the equivalent width measurement was larger than the derived accretion signal, upper limits were derived from a noise measurement in the continuum surrounding $\lambda_{\text{Br}\gamma}$. The resulting fully corrected equivalent widths or upper limits are listed in Table 4.3.

To infer the presence of an accretion disk around all components, the *disk probability* was calculated from the measured $W_{\text{Br}\gamma}^{\text{accr}}$, its uncertainty, and the local noise as described in Appendix A. The values are listed in Table 4.3.

Line luminosities and mass accretion rates: $L_{\text{Br}\gamma}$, L_{acc} , & \dot{M}_{acc}

Line luminosities were derived from the flux-calibrated and dereddened spectra (Eq. 3.9) and were converted to accretion luminosities using the empirical correlation from [Muzerolle et al. \(1998a\)](#) in Eq. (3.8). Mass accretion rates \dot{M}_{acc} were calculated for all targets with significant accretion (Eq. 3.10). Upper limits for target components with no detected Br γ emission were determined from the minimum emission feature detectable with 3σ significance over the noise in the vicinity of the line. All parameters are listed in Table 4.3.

²¹Note that spectral types K8 and K9 are not used, since in the original classification by the strength of the titanium oxide bands, M0 follows directly after K7.

4.2.5 The new companion candidate to T 33 B

T 33, also known as Glass I (Glass 1979), was discovered to have a binary companion at $2''.5 \pm 0''.5$, $PA = (284 \pm 5)^\circ$ by Ghez et al. (1997). The new observations in this thesis show, for the first time, clear indications that the secondary component T 33 B itself consists of two stellar components (in the following called T 33 Ba and T 33 Bb; see Fig. 4.3). To test whether the newly detected tertiary component is a real companion, I will consider the surrounding stellar density, component colors, and proper motion of the components.

The study by Lafrenière et al. (2008) evaluates the probability of chance alignments of multiple components based on the density of stars in the 2MASS catalog in the closest $15'$ around each star of their sample. For all but the widest components they calculate a probability of $< 10^{-4}$ for chance alignments. Since this includes the $2''.4$ wide T 33 A+B system, the new component located only $0''.1$ from T 33 B must have a probability for a chance alignment considerably lower, making a physical association very likely.

The dereddened colors of both components of T 33 B are in rough agreement with PMS colors (Luhman et al. 2010) of K7 and M1 spectral type respectively. Alternatively, a spectral type of K4 can be assigned to both components assumed that they are giants (Bessell & Brett 1988). The spectral type of the combined light was derived in this thesis to be $M0.5_{-1.5}^{+1}$. As the total light from the T 33 B system is dominated by its brighter component, this confirms the PMS nature of the primary of the T 33 B subsystem, since a spectral type as early as K4 can be excluded by the detected photospheric features in $H+K$.

This leaves the question if the dimmest component Bb of the T 33 system is a background object or physically bound. This was tested through proper motion measurements of the individual components. In the ESO archive²², I was able to find two additional epochs of NACO observations taken during the last six years²³ that use a similar instrumental setup as the observations in this thesis (K_s filter, S13 camera). Together with knowledge of the proper motion of T 33 A of $\delta_{RA} = -40$ mas/yr and $\delta_{DEC} = +33$ mas/yr (Teixeira et al. 2000), common proper motion is clearly confirmed: within the ~ 5 years between the first and last of the observed epochs, both T 33 Ba and T 33 Bb move less than $0''.05$ in RA and DEC and in different directions relative to T 33 A (Fig. 4.14). The expected motion of T 33 A of $\delta_{RA} = 0''.20$ and $\delta_{DEC} = 0''.17$ in the same time span renders both components comoving with T 33 A and thus the T 33 system a physically bound triple star.

The residual motion between the components T 33 Ba & Bb is likely orbital motion. An estimate of the minimum orbital period using Newton's and Kepler's laws under the assumption of a circular orbit and that the last observation was at maximum elongation returns $P_{\min} = 102 \pm 15$ yrs. Classification of T 33 BaBb as a binary which has been hiding its binary nature through aligning its components in an inclined orbit during the last few years, explains why its binary nature has not been discovered before and why Nguyen et al. (2012) see a deviant radial velocity of T 33 B from the rest of the cluster while no signal of spectroscopic binarity was detected.

²²<http://archive.eso.org/>

²³2006-03-25 [076.C-0579(A)], 2008-02-20 [080.C-0424(A)]

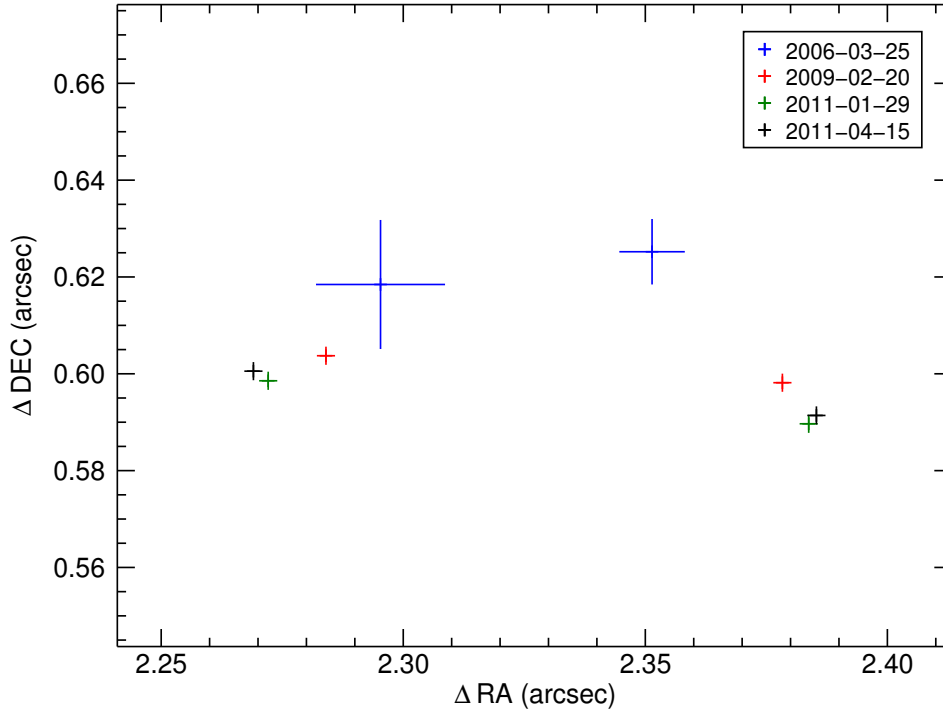


Figure 4.14: Position of T 33 Ba (right group of points) and T 33 Bb (left group) in RA and DEC relative to T 33 A at four epochs. The size of the symbols indicates the uncertainty of the relative measurement. The position of T 33 Ba & Bb at the earliest epoch has a comparably large uncertainty since both components are spatially barely resolved.

4.3 Discussion

4.3.1 Stellar parameters & sample biases

The *full*, *extended*, & *restricted* samples

The **full sample** of 26 multiple (= 52 individually detected) objects comprises targets from a broad range of binary separations, component spectral types, and observational quality. To ensure the comparability and validity of the results, I define in addition to the *full sample* of components with individually obtained spectroscopy (irrespective of the fact that they might be close binaries) two new samples, the *extended sample* and the *restricted sample*.

The extended sample. The full sample consists of all components “as observed”. This disregards the fact that some of these components may be unresolved visual or spectroscopic binaries. The *extended sample*, in contrast, is composed of all known individual components. Spectroscopic binaries as well as unresolved visual components each enter the sample as two individual components. Since not all individual stellar parameters are known, this sample will only be used for number statistics like the disk frequency (Sect. 4.3.2) where

the presence of disks in unresolved binaries can be inferred from the unresolved data. This sample will grant the most pristine view to the data, since no additional restrictions to the original component sample are applied. The extended sample consists of 62 components (19 binaries, 4 triples, and 3 quadruple stars).

The restricted sample is composed to eliminate observational and compositional biases by applying the following selection criteria. (a) Spectral types must be in the range for T Tauri stars, i.e., later than G0. (b) All target components must be stellar. It is not clear whether the formation process of brown dwarfs is identical to that of stars. To exclude the effects of possibly different initial conditions, any of the brown dwarf candidates in the sample are excluded. (c) The information must be attributable to one stellar component. A few stars in the sample could not be resolved with our adaptive optics spectroscopy or are suspected spectroscopic binary candidates. This requirement limits the restricted sample to binaries with projected separations of $\gtrsim 0''.15$ or $\gtrsim 25$ AU at the distance of Cha I.

The application of these restrictions means that some of the binary components are “singled”, meaning that only one component enters the sample. While the evolution of disks depends to first order on the existence and relative position of a stellar companion and only in second instance on the parameters of this companion (e.g., relative mass), this inclusion reduces the slight bias for primaries to have earlier spectral types than secondaries (see next paragraph and Fig. 4.15) since early-type primaries and late-type secondaries are removed.

The restricted sample comprises 43 components. If *binary* parameters shall be investigated with respect to the restricted sample, only binaries with both components in the restricted sample are considered. This *restricted binary sample* consists of 17 binaries.

Spectral types

As can be seen in the spectral type distribution in Fig. 4.15, the median spectral type of primary stars (M1.5) is earlier than that of the secondaries (M3). This is true for both the full and restricted samples. This difference can produce biases when comparing the parameters of the primary and secondary populations since many parameters, such as stellar evolutionary timescales, are mass-dependent with the more massive components evolving faster than the less massive stars. The resulting differences of the inferred parameters are discussed in the subsequent sections when they are suspected to occur.

To test whether the subsample of binary stars is representative for the population of Cha I members, I calculated the probabilities that the spectral types of primaries and secondaries are drawn from a common parent distribution with single stars of Cha I (Luhman 2004, 2007), respectively. The low KS probability of 2×10^{-5} indicates that the spectral types of primaries are rather badly compatible with those of single stars. Secondaries, however, cannot be distinguished from singles as indicated by a KS probability of 0.19. The poor compatibility of the primary stars with the single star spectral type distribution is due to a selection bias, since SINFONI observations require AO reference stars (\equiv the primaries of the binaries) to be optically bright ($V < 16.7$). This limits the latest spectral

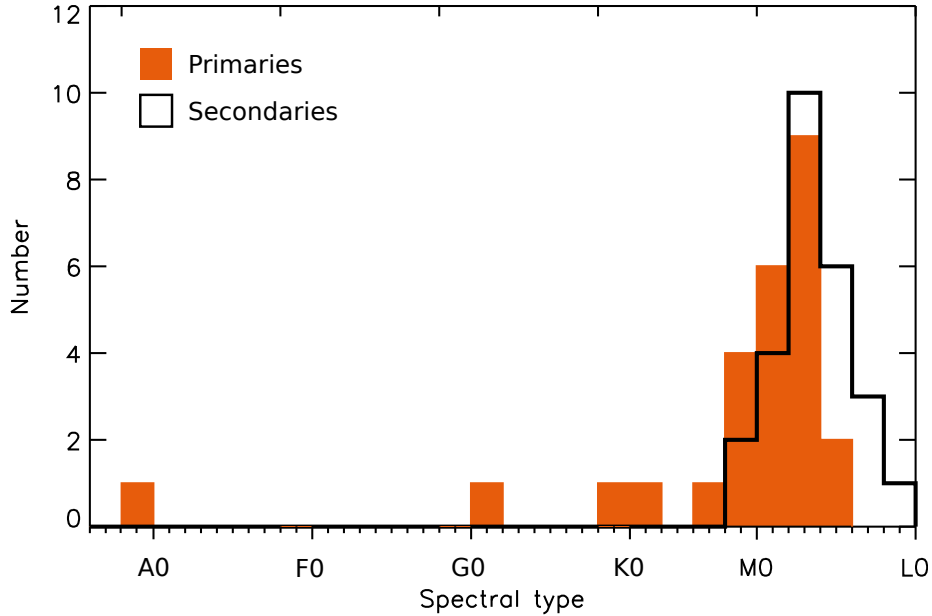


Figure 4.15: Histogram of spectral types divided into primary stars (solid orange) and secondary stars (black outline). The spectral types of secondaries are on average 1.5 sub-classes later. Unresolved close binaries in triple systems are put in as one component.

type that primaries of this sample can assume and in fact, for spectral types earlier than or equal to M4 (\equiv the apparent cut-off of primaries in Fig. 4.15), the spectral type distributions of primaries cannot be distinguished from that of single stars, with a KS probability of 92% that primaries and singles $< M4$ are drawn from the same parent distribution. Since secondary stars of binaries are not subject to this selection bias, a systematic difference between primaries and secondary/single stars of Cha I remains, which is of relevance for the comparison of the statistics of single stars with that of binary components in the subsequent sections.

Relative extinctions and ages

In Fig. 4.16, the photometric extinctions in both components of each binary are compared. While most of the extinctions are identical between the components of the same binary, those multiples with significant differences in component extinction are mostly hosts to at least one very red component with near-infrared excess $E(K_s - L') > 0.5$. If extinction is dominated by the degree of embeddedness of a binary in the molecular cloud, it is expected to be similar for both components of a binary. The presence of $K_s - L'$ color excess apparently leads to a different photometric extinction value for the respective component. Since the spectroscopically determined extinctions (see Table 4.3) show no such correlation (the values scatter almost uniformly around equal primary and secondary extinctions, though with a larger spread due to the larger uncertainties of A_V^{spec}), additional (systematic) uncertainty of the photometric extinctions as a function of color excess may be present. A

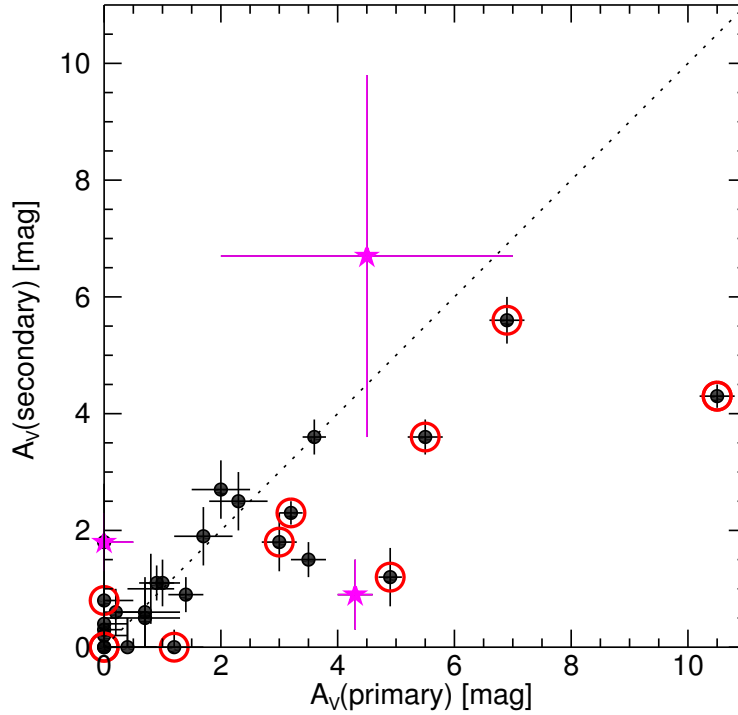


Figure 4.16: Primary vs. secondary extinctions A_V^{phot} . Target binaries with at least one component with strong near-IR color excess $E(K_s-L') > 0.5$ are marked by a red circle. The dotted line shows equal extinctions in both components. The three magenta stars (CHXR73, T 26, T 33) have at least one component without measured $E(K_s-L')$. From their very red color of $H-K > 0.6$ mag a strong near-IR excess can also be inferred for these binaries.

possible origin can either be an over-estimation of the slope of the extinction vector in the $(J-H)-(H-K_s)$ color-color diagram (Fig. 4.6) or an underestimation of the slope of the CTTS locus (which can, for example, be caused by assuming filter system transformations that do not accurately describe the filters in use²⁴) the result would be a mostly positive correlation of A_V with the color-excess, as observed. In the following, I will use the derived extinctions as measured and caution that a possible systematic uncertainty may be present with a median amplitude of 2 mag for high $E(K_s-L')$ components. If true, the luminosity of the respective components would be overestimated by on average 0.21 dex, comparable in size to the random uncertainty of the luminosity values, resulting in an age estimate that is younger than those derived in Table 4.3 by $\Delta \log \tau \approx 0.3$ at $M = 0.4 M_\odot$.

Taking these effects into consideration, the measured ages show that binary components are coeval. Fig. 4.17 compares the logarithmic isochronal primary and secondary ages from Table 4.3. Binaries with at least one component with strong color excess or an unresolved binary component are mostly located off the sequence of equal-ages. This age discrepancy is likely due to over-estimated luminosities of components with strong continuum excess or

²⁴For example, it was assumed that the NACO and 2MASS filter systems are sufficiently similar, however, they are not identical.

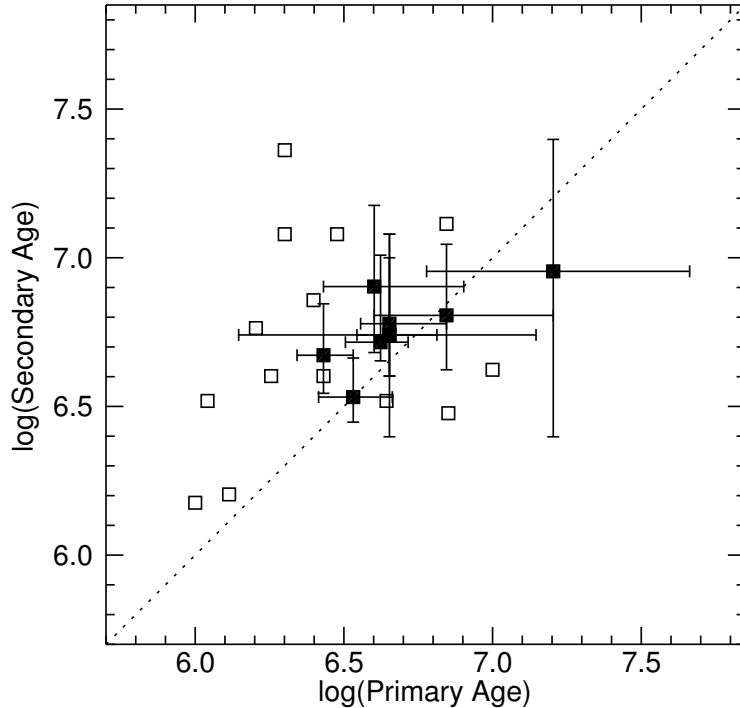


Figure 4.17: Primary age vs. secondary age in logarithmic units. Open symbols are target binaries with unreliable age measurements because they are either host at least one component with strong color-excess $E(K_s - L') > 0.5$ (or $H - K_s > 0.6$, if $K_s - L'$ could not be measured) or a spectroscopic binary component. Filled symbols with error bars are binaries with spatially separated components with low color excess.

over-estimated extinction and accordingly under-estimated ages. In contrast, all binaries with low-excess components are consistent with equal age components to within 1σ . To test whether the observations are compatible with the simultaneous formation of both components of a binary, I compare the logarithmic age differences $|\Delta \log \tau| = |\log \tau_{\text{prim}} - \log \tau_{\text{sec}}|$ after Kraus & Hillenbrand (2009). The rms scatter in $|\Delta \log \tau|$ is 0.03 dex, which is compared to 10000 randomly paired samples of the same size as the target sample, bootstrapped from the primaries and secondaries with low veiling. Only 2% of the random samples have an rms scatter smaller than 0.03 dex. The binary sample is thus more coeval than the total sample of binary components with a significance of 2.3σ .

A tendency for the less massive component to be of older age is visible in Fig. 4.17, as most points lie above the line of equal primary and secondary ages. Rather than a real feature, this is likely caused by systematics in the model isochrones or the SpT- T_{eff} conversion. Since the effect is not significant (the average logarithmic difference between the primary and secondary age is $\overline{\Delta \log \tau} = 0.09$ while one standard deviation of the scatter around the mean is 0.20) this effect is disregarded in the following.

The median inferred age of the subset of low- r_K components (excluding unresolved binaries) is 5.5 Myr, older than the 2–3 Myr derived by Luhman (2007) for a large sample of

Cha I members with models of Baraffe et al. (1998) and Chabrier et al. (2000). Even the systematically younger ages when using the Palla & Stahler (1999) models (see Fig. 4.12) produce a median age (4 Myr) which is older than the single star value. Since it is unlikely that binaries are intrinsically older than single stars of the same region, this discrepancy must be due to either sample biases or a systematic difference in the derivations of luminosities and effective temperatures. While part of the difference might be the signature of the isochrones used, I found that the luminosities derived by Luhman (2007) are systematically higher than those derived in the binary sample. Part of this difference is due to the larger distance that Luhman assumes. The increase of the distance from 160 to 168 pc requires a luminosity increase of $\Delta \log L = 0.05$ for all targets to match the observed J -band magnitudes. Furthermore, while a correction factor for unresolved binarity was applied²⁵, the study by Luhman (2007) does not account for possible excess emission in J -band which can lead to comparably high luminosities, as we see for the high-veiling components in the HR-diagram (Fig. 4.11). This can lead to an underestimation of the median age. In fact, if one includes all binary components of the present sample irrespective of their veiling into the age estimation, a median age of 4.4 Myr is derived from the Siess et al. (2000) models and 2.6 Myr from Palla & Stahler (1999). This suggests that the age quoted by Luhman (2007) is indeed underestimated. A thorough absolute age determination, however, is outside the scope of this thesis owing to the small sample size. Nevertheless, the age determination serves to confirm the similar *relative* ages (coevality) of the binary components as discussed above.

4.3.2 The evolution of disks in Cha I binary components

Disk frequency

From the number of target components with K_s-L' color excess – used as an indicator for the presence of hot dust in the inner disk – and those with significant Br γ emission – indicating ongoing accretion activity – I determine the frequency of dust and accretion disks around the components of binaries in Cha I and compare it to disks around single stars of this region.

Accretion disks. The fraction of target components harboring accretion disks is determined from the individual disk probabilities in Table 4.3 as described in the Appendix A. Some components have no good estimates for the veiling level. A correction of $W_{\text{Br}\gamma}$ is not possible for these targets and accretion strength might be significantly larger than measured. One of the reasons for an inaccessible veiling value is high veiling itself, since the line features used for veiling estimation can be reduced in depth until they blend into the continuum noise. An exclusion of these targets may accordingly bias the sample against accretors. To avoid this bias, these targets were included with a neutral disk probability of 0.5. In the following, I will consider the extended and the restricted samples.

²⁵The unresolved binary correction after Hartmann (2001) was applied under the assumption of a binary fraction of 30% in Cha I, consistent with the value found by the multiplicity study of Lafrenière et al. (2008).

The extended sample of all components returns an accretion disk fraction of $F^{\text{ext}} = 18_{-6}^{+8}\%$. This calculation is possible since all unresolved binaries except T 31 A show no Br γ emission and can be treated as consisting of two non-accreting components. T 31 A is a suspected SB2 and shows signs of accretion ($W_{\text{Br}\gamma} > 9.4 \text{ \AA}$). The uncertainty of being host to one or two accreting components is included in the calculation of the disk frequency.

The restricted sample returns a very similar frequency of $F^{\text{restr}} = 16_{-6}^{+9}\%$. Both calculations include only the information from the Br γ emission measurements. It is known that Br γ returns a lower fraction of accretors than the H α feature which, however, defines the classes of classical and weak-line T Tauri stars. This is due to the ~ 100 times lower transition probability of Br γ excitation compared to H α ²⁶. With help of the correction factor $f = 0.125$ derived in Sect. 3.3.2 and $N = 43$ components in the restricted sample, the number of CTTS with non-detected Br γ emission can be estimated to be $f/(1-f) \times (F \cdot N) \approx 1$. This increases the restricted accretion disk fraction to $F_{\text{corr}}^{\text{restr}} = 19_{-6}^{+9}\%$.

This fraction is significantly lower than the accretion disk fraction of single stars in Cha I of $F^{\text{single}} = 44 \pm 8\%$ (Mohanty et al. 2005). Assuming that binaries and single stars are born at the same time in the star formation history of a cluster, this indicates that binaries with separations of ~ 25 –1000 AU finish accreting on a shorter timescale than single stars. To investigate this trend in more detail, I divided the sample into binaries with separations closer and wider than 100 AU, close to the median separation of 119 AU of the sample. The resulting fractions of $F_{<100\text{AU}}^{\text{restr}} = 10_{-5}^{+15}\%$ and $F_{>100\text{AU}}^{\text{restr}} = 23_{-8}^{+11}\%$ show that the accretion disk fraction is particularly low in the closest binaries of the sample, less than half of the wider sample. This corroborates theoretical expectations that the timescale for viscous disk evolution is significantly shortened in binaries with separations < 100 AU, if one assumes a correlation of disk lifetime with the size of the (truncated) disk (e.g. Monin et al. 2007). The fact that the reduction of disk frequency in wide binaries is less pronounced but still significant indicates that disk lifetimes can be shortened even if the truncation of the outer disk is only weak. This is in agreement with the results from the ONC (Chapter 3), where the sample of binaries does show a reduction of accretion disk frequency despite the fact that only separations of ~ 100 –800 AU and no closer pairs could be examined due to the comparably large distance of the ONC. Further discussion and comparison of the disk frequency in Cha I with the ONC is presented in Chapter 5.

Inner dust disks. The frequency of inner dust disks is measured from the number of targets with significant $K_s - L'$ excess in the nearly simultaneous photometry. A diagram of primary and secondary $E(K_s - L')$ is shown in Fig. 4.18. As derived in Sect. 4.2.1, the systematic uncertainty of the $K_s - L'$ excess measurements is about 0.2 mag. Accordingly, $K_s - L'$ emission is in significant excess over the pure stellar color for components with $E(K_s - L') > 0.2$. There are 21_{-7}^{+17} components out of 55 with measured $K_s - L'$ colors in the extended sample which fulfill this criterion, and 20_{-6}^{+12} components in the restricted

²⁶transition probabilities are $A(\text{H}\alpha) = 4.4 \times 10^7$ and $A(\text{Br}\gamma) = 3.0 \times 10^5$ according to the NIST Atomic Spectra Database, <http://www.nist.gov/pml/data/asd.cfm>.

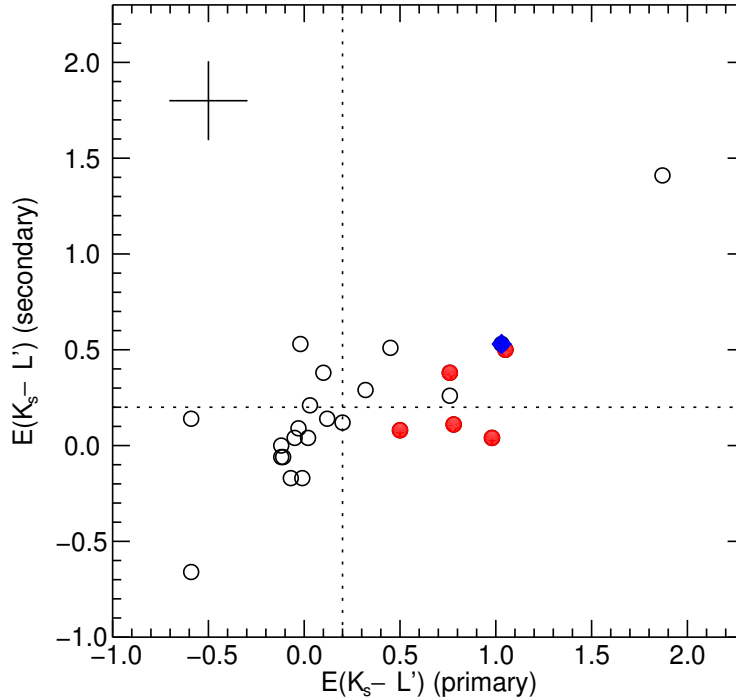


Figure 4.18: Near-infrared excess $E(K_s - L')$ for the primary and secondary components of each binary with individual component photometry. Red filled circles and blue filled diamonds are binaries with accreting primaries and secondaries respectively. Targets to the right and above the dotted lines have significant near-IR excess indicating the presence of inner disk material. A typical error bar, dominated by the systematic uncertainty of ~ 0.2 mag, is indicated in the upper left.

sample of 40 components with measured colors²⁷. The resulting inner dust disk fractions are $\mathfrak{F}^{\text{ext}} = 38_{-13}^{+31}\%$ and $\mathfrak{F}^{\text{restr}} = 50_{-15}^{+30}\%$.

The values are in good agreement with previous measurements of the disk frequency in binaries of Cha I. [Damjanov et al. \(2007\)](#) measured the frequency of targets with 8 or 24 μm excess in 15 *spatially unresolved* binaries and 2 triples in Cha I and derive a nominal frequency of multiples with disks of $\mathfrak{F} = 35_{-13}^{+15}\%$. Their value, obtained from 10–300 AU binaries, is in good agreement with the fraction of components with $K_s - L'$ excess obtained from the extended sample. And indeed, when applying the selection criteria of the restricted sample to the [Damjanov et al.](#) binary sample, the inferred hot dust disk fraction increases to 42%, since 4/5 of their binaries with separations $\lesssim 25$ AU show no signs of dust excess. This is close to the fraction found for the restricted sample of binaries in this thesis.

Both, the extended and in particular the restricted inner disk fractions of Cha I binaries are compatible with the average Cha I single star value of $\sim 47\text{--}55\%$ (with weak fluctuations depending on stellar mass) found from photometric excess in the *Spitzer/IRAC* bands

²⁷Uncertainties of the number counts were determined from targets for which $E(K_s - L') = 0.2$ is within the uncertainty limits.

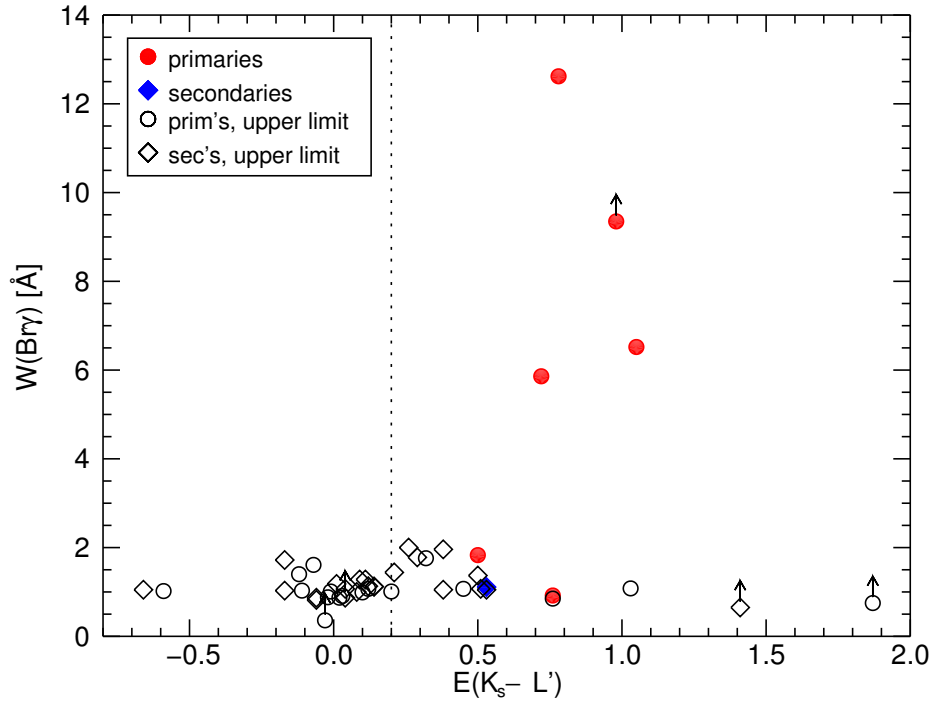


Figure 4.19: Br γ equivalent width as a function of near-IR color excess $E(K_s-L')$. Filled symbols show accretion detections, open symbols are upper limits of $W_{\text{Br}\gamma}$. Primaries and secondaries are denoted by circles and diamonds, respectively. Stars to the right of the dotted line have significant K_s-L' excess. Targets without veiling measurement can have larger $W_{\text{Br}\gamma}$ than shown here since the correction factor $(1 + r_K)$ could not be applied; they are marked with arrows.

between $3.6\ \mu\text{m}$ and $24\ \mu\text{m}$ (Luhman et al. 2008; Damjanov et al. 2007). A significant reduction of disk presence compared to single stars is mostly visible in close binaries: out of 16 components which are part of spectroscopic or visual binaries with separations $< 25\ \text{AU}$, only 3 or 4, depending on whether the spectroscopic binary T 31 A has one or two disk-bearing components, were found with significant K_s-L' excess, a fraction of 19–25%. The inclusion of close binaries explains why the extended sample shows a lower disk fraction than the restricted sample.

The correlation of inner disk presence and accretion. The fraction of inner dust disks around binary components is significantly higher than the accretion disk fraction. Figure 4.19 compares measured Br γ equivalent widths with the near-IR color excess. While all accreting components show significant color excess, 65% of the binary components with near-infrared excess show no signs of accretion in Br γ . This fraction can be corrected to be 55% with information from the literature: in agreement with the fact that only lower limits of the accretion luminosity could be measured for the two components with the

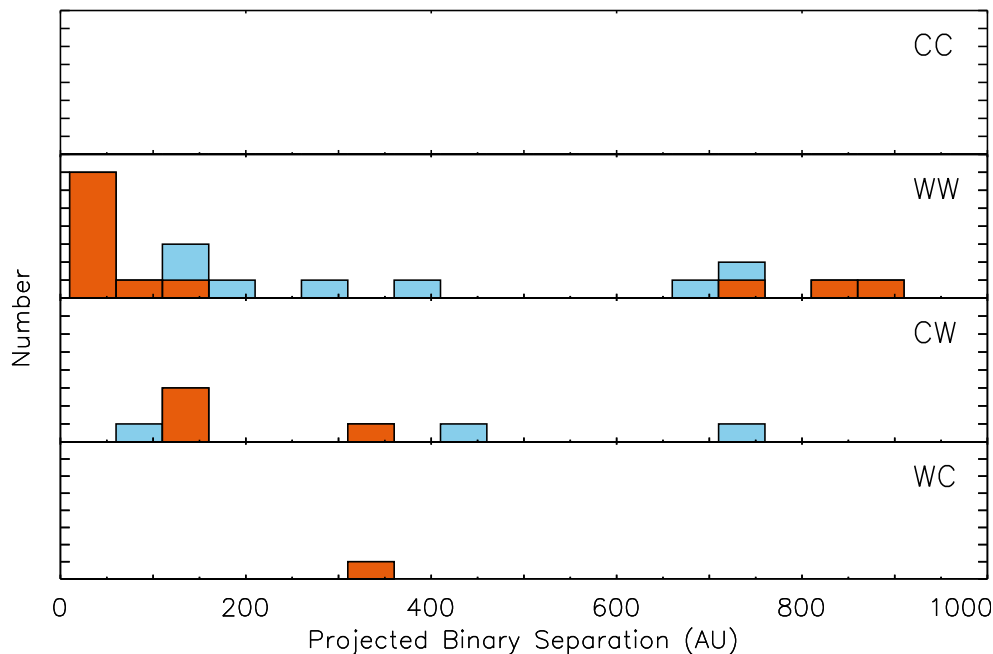


Figure 4.20: Accretion status as a function of binary separation. The red bars show the restricted sample, the combined red and blue bars represent the full sample. One tick mark on the y-axis is equivalent to one binary. The classifications CC, WW, CW, and WC refer to binaries composed of Classical and Weak-line T Tauri stars with the first and second character describing the primary and secondary component respectively. No systems with both components accreting were detected.

strongest near-IR excess, ISO 126 has been found to be accreting by $H\alpha$ studies²⁸ (Saffe et al. 2003). This fraction is significantly higher than for Cha I single stars according to the study by Damjanov et al. (2007) who find 6 of 21 stars with inner dust disks (inferred from [4.5]–[8.0] excess) without signs of accretion ($H\alpha$).

This discrepancy in the accretion and dust disk presence has been observed not only for Cha I but in multiple SFR with the conclusion that the approximately exponential decay of disk frequency is more rapid for accretion disks (time constant $\tau_{\text{acc}} \approx 2.3$ Myr) than for hot inner dust disks ($\tau_{\text{dust}} \approx 3$ Myr, see Fig. 1.4; Fedele et al. 2010). Binary companions in Cha I apparently amplify the effect that accretion disks disappear before dust disks around the same stars. Possible reasons are an inside-out disk evolution, UV irradiation from the star, or planet formation and migration. A detailed discussion follows in Chapter 5.

Differential disk evolution

Fig. 4.20 shows the separation of Cha I binaries classified by their accretion status as CC (both components accreting), WW (no accreting components), CW and WC (mixed pairs with the primary and secondary component accreting, respectively). While the ma-

²⁸While IOS 126’s $\text{Br}\gamma$ accretion signature was apparently hidden by, e.g., strong veiling (which could not be measured with the technique applied here), the stronger $H\alpha$ emission could be detected.

jority of binaries in the restricted sample were found to have no accreting components ($12_{-1}^{+3}/17 = 70_{-11}^{+18}\%$ WW), there are no CC binaries (0_{-0}^{+1}) detected and all accreting components are part of mixed systems with either an accreting primary ($4_{-2}^{+3} \times \text{CW}$) or secondary ($1_{-1}^{+0} \times \text{WC}$)²⁹. A qualitatively identical picture is posed by the full sample. The population of these classes is in good agreement with random pairing of the number of individual accretors and non-accretors in the restricted sample. About 1 CC binary would be expected, ~ 4 mixed pairs, and the rest (~ 12) WW. This indicates that the existence of a disk around one ChaI binary component has no impact on the probability of finding another disk around the other component and both components can be treated as independent in terms of their disk probability. The effect of disk synchronization that was detected for ONC binaries (Sect. 3.3.2) is not observed here. This is likely due to the older age of ChaI compared to the ONC and CC systems already evolved mostly to diskless systems. However, a preference for mixed systems with an accreting primary can be observed. The observation of suppressed WC systems compared to CW has been made in previous observations of Taurus and other star-forming regions (Monin et al. 2007), but it was not confirmed by e.g. the ONC data in this thesis ($4 \times \text{CW}$ and $3 \times \text{WC}$, Sect. 3.3.2).

The paucity of WC systems in ChaI points to either a bias against their detection or a different formation and/or evolution of secondary disks as a function of the cluster environment. Since binaries in this sample were selected from an adaptive optics search for companions, no preference for or against accreting secondary components is expected. Accretion measurements in this thesis might even be in favor of the detection of accretion in the fainter secondary spectra since the detection limit of mass accretion rate is lower the fainter the system. In fact, the only accreting secondary component in this study has the lowest detected mass accretion rate, below the upper limits of most other components (see Sect. 4.3.2 and Fig. 4.22). The fact that, independently of spectral type, secondaries systematically show no or only very weak accretion indicates that we see a real effect of the binary environment rather than a selection effect. A real paucity of mixed systems with accreting secondaries in ChaI is therefore the most plausible explanation. Assuming that close to all binaries start in a CC configuration³⁰, this observation points to a more rapid evolution of the disk around the less massive component.

While the above considerations show that the spectral type and thus the absolute mass of the binary components is unlikely to cause a preference for mixed systems, I explore the possibility that the relative disk lifetimes of primaries and secondaries are governed by the *relative masses* of the stellar components, i.e., the component mass ratios $q = M_{\text{sec}}/M_{\text{prim}}$. Fig. 4.21 shows the mass ratio as a function of binary separation, indicating also the accretion type. The diagram features mixed systems only with mass ratios below $q = 0.8$ while 5 out of 12 WW systems measure $q \gtrsim 0.8$. This suggests a mass ratio-dependent mechanism: disk truncation is stronger for the less massive secondary which may lead to a shorter disk lifetime due to an early-ceasing angular momentum transport (Artymowicz

²⁹Number uncertainties from comparison of $W_{\text{Br}\gamma} \pm \Delta W_{\text{Br}\gamma}$ with $W_{\text{Br}\gamma}^{\text{min}}$

³⁰More than 60% of all binaries in the very young (1–2 Myr; Kenyon & Hartmann 1995) Taurus association are CC (White & Ghez 2001; McCabe et al. 2006)

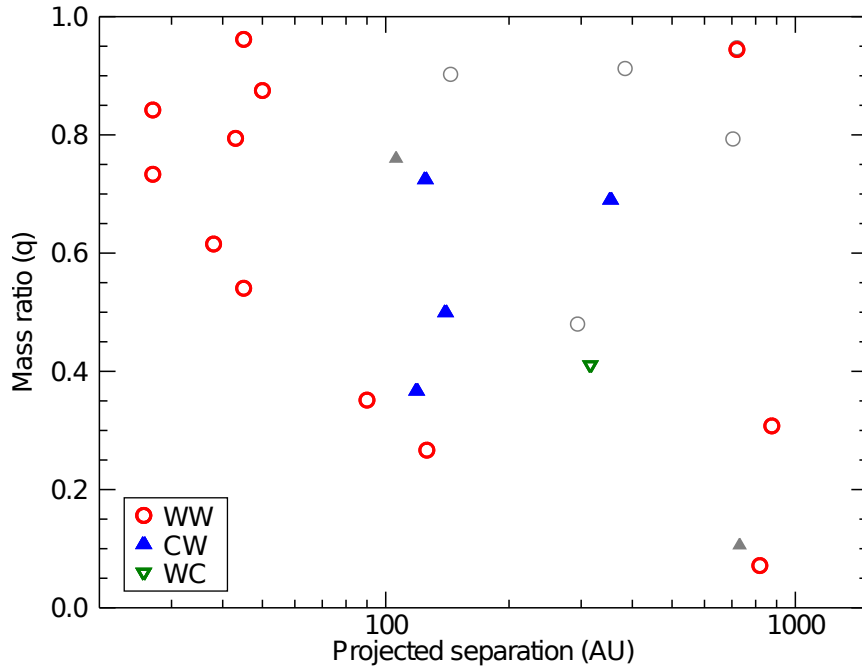


Figure 4.21: Mass ratio $q = M_{\text{sec}}/M_{\text{prim}}$ as a function of binary separation. Red open circles show binaries with two accreting components (WW), blue triangles (pointing up) show mixed systems with an accreting primary and green triangles (down) with an accreting secondary from the restricted sample. Gray symbols represent targets that are in the full sample but not in the restricted sample. There are two binaries (Hn 4, T 39 AB³¹ both WW) where the mass of the fainter component is calculated to be higher than the primary’s mass. The inverse q^{-1} is plotted for these.

& Lubow 1994). A reduction of secondary disk lifetime is in agreement with theoretical expectations (it scales with disk radius R roughly as $R^{-0.5..1}$ for a viscous disk), although a significant difference between primary and secondary disk lifetime is only expected for mass ratios $q < 0.5$ (Monin et al. 2007).

While mass ratios together with viscous disk evolution can explain at least part of the observed CW systems, always the more massive component is predicted to keep its disk for longer. Accordingly no WC systems would form. The fact that these systems are nevertheless observed might be partly due to projection effects. Disks in very wide systems that only appear close due to projection may evolve without notice of the other star if their outer tidal truncation radius is larger than the size of a typical disk, i.e., for binary separations $\gg 1000$ AU. On one hand, unrelated systems can form in any configuration since the lifetime of an individual disk can be anywhere between < 1 and ~ 10 Myr. On the other hand, WC systems might even be preferred for very wide and unrelated components, since it was found that the frequency of disks around single stars declines with increasing stellar mass (e.g. Lada et al. 2006; Carpenter et al. 2006).

³¹T 39 B is a spectroscopic binary candidate which might explain its higher inferred mass

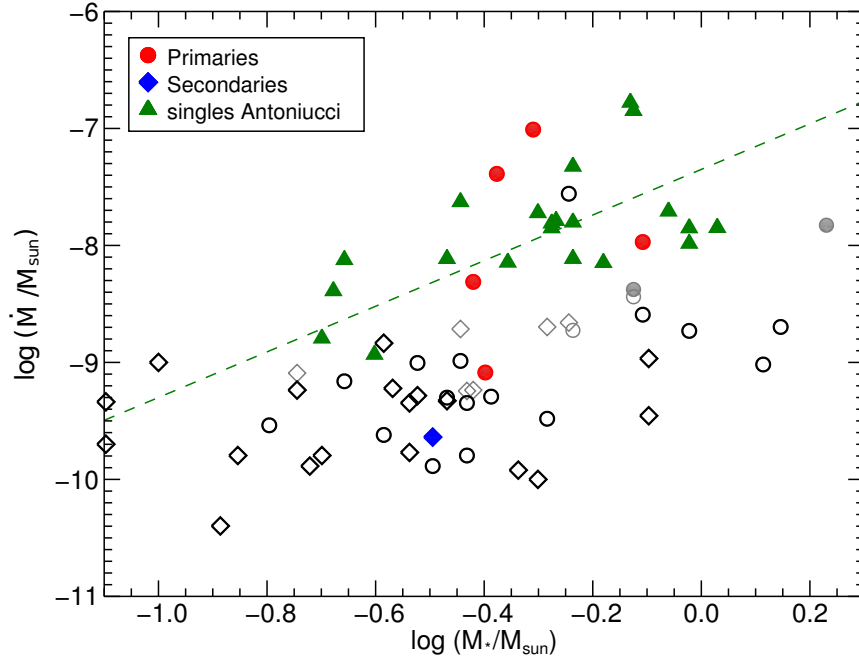


Figure 4.22: Mass accretion rate as a function of stellar mass. Filled circles and diamonds are significantly accreting primaries and secondaries of Cha I binaries, respectively. Open symbols are upper limits of undetected binary components. Colored symbols are from the restricted sample, gray symbols are in the full sample only. Green filled triangles show Cha I single stars also measured from Br γ by Antonucci et al. (2011). The authors also derive a power-law fit to their data, included as the green dashed line. Upper limit values of the Antonucci et al. non-detections are not published.

Mass accretion in Cha I binaries

Mass accretion rates are shown as function of stellar mass in Fig. 4.22. The new Cha I binary data are compared to single star mass accretion rates from Antonucci et al. (2011). As these were obtained from the same indicator, Br γ emission, no systematic biases are expected. The distributions of both populations, Cha I binary components and single stars, qualitatively agree in the $\log(\dot{M})$ – $\log(M_*)$ diagram. There are, however, too few accretors in the binary sample to statistically confirm or reject agreement with the relation $\dot{M} \propto M_*^{1.95}$ proposed by Antonucci et al. (2011).

Interestingly, all accreting components in this sample were observed at masses $\geq 0.32 M_\odot$, i.e., 100% of all accretors are among the most massive $\sim 60\%$ of all components in the binary sample. A KS-test returns a 87% chance that the masses of accretors and nonaccretors are drawn from different parent populations. This is neither due to limited sensitivity – the detection limits are mostly below the $\log(\dot{M})$ – $\log(M_*)$ relation of accretors by about 0.5 magnitudes – nor a general property of Cha I accretors: Antonucci et al. (2011) do detect single stars with masses $< 0.32 M_\odot$ with significant accretion. This corroborates the previously inferred low relevance of spectral type or mass for the existence of accretion signatures of secondary stars: since low-mass accretors $< 0.32 M_\odot$ do exist in Cha I singles

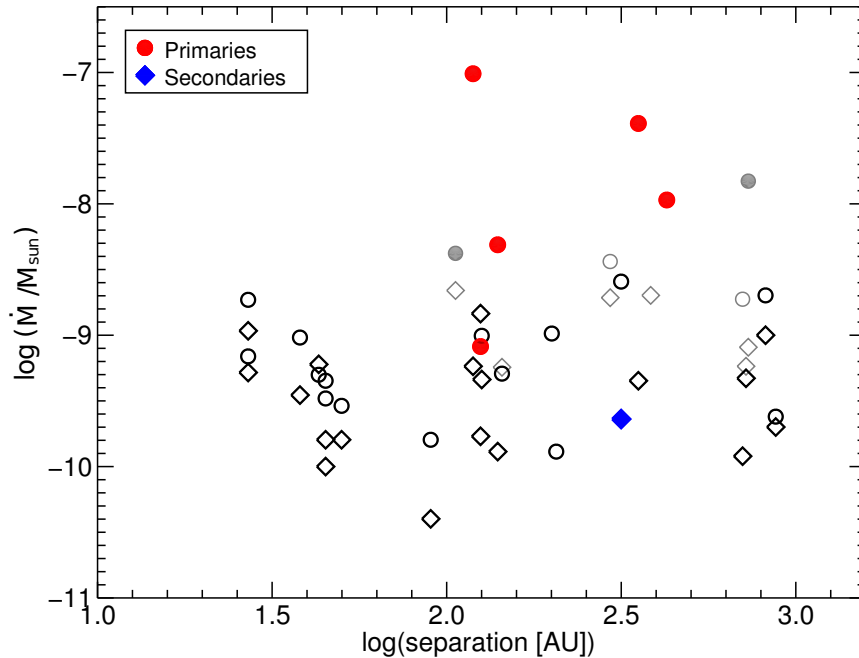


Figure 4.23: Mass accretion rate as a function of projected binary separation. Symbols as in Fig. 4.22.

but none are observed in binaries (neither primary nor secondary), it is not the lower mass of the secondary that reduces the chance of dealing with an accreting star but the presence of a more massive stellar companion is the most likely cause for the disappearance of the disk around the secondary.

While the observed dependencies suggest a dependence of accretion parameters on binary parameters, the small number of binaries in Cha I and the low fraction of accretors limits the statistical significance of these results in Chamaeleon I. Further exploration of mass accretion rates must therefore rely on the compilation of data from various star forming regions. While risking a certain level of noise due to different star formation histories and cluster environments, the better statistics can highlight the most important implications of binarity for disks and their evolution. This is further discussed in Chapter 5.

Accretion as a function of binary separation. Another interesting aspect of the effect of binarity on disks in binaries is the dependence of component accretion on binary separation. As discussed before, it is apparent from Fig. 4.23 that all accretors are part of binary systems with separations larger than ~ 100 AU. Other dependencies or correlations with binary separation, such as accretion strength or a difference between primary and secondary accretors however, are not visible in the diagram. It is likely that the poor statistics of the small sample of accretors is hiding interesting correlations and is thus prohibiting further conclusions. Furthermore, only with knowledge of the real binary separation (the projected separations provide only lower limits) and eccentricity (the outer truncation radius of a disk in an eccentric binary is defined by the semi-minor axis of the

binary orbit; Artymowicz & Lubow 1994) can useful correlations be established and the available projected “snapshot” data from a single observing epoch must always introduce a certain level of uncertainty in the inferred parameters.

4.4 Conclusions

I have presented an observational near-infrared study of the individual components of 19 T Tauri binary stars and 7 triples, including one newly resolved tertiary component, in the Chamaeleon I star forming region. The target sample covers close to all currently known multiples in the separation range between $0''.2$ and $6''$. Imaging data in JHK_sL' bands were taken with VLT/NACO together with close-in-time $1.5\text{--}2.5\mu\text{m}$ spectroscopy with VLT/SINFONI covering the accretion-induced Brackett- γ feature. The combined data set enabled me to measure the relative position, magnitude, color, spectral type, and the equivalent width of Br γ emission of each individual component. Stellar luminosities and effective temperatures were calculated which enabled me to derive stellar component masses, ages, and radii through comparison with pre-main sequence evolutionary tracks. This information was combined with the derived probabilities for the existence of hot circumstellar dust, as inferred from $K_s\text{--}L'$ color excess, and accretion disks from Br γ emission. The data enable me to derive the following conclusions:

1. The components of a binary are more coeval than random pairs of Cha I binary components with a significance of 2.3σ .
2. Components of binary stars in Cha I show signs of accretion less often than single stars in the same region. From the new data of T Tauri binaries with separations of 25–1000 AU, a fraction of $F = 19_{-6}^{+9}\%$ of all stellar components has been inferred to harbor an accretion disk. This is less than half of the single star disk fraction in Cha I of $F^{\text{single}} = 44 \pm 8\%$. Apparently, the presence of a stellar binary component causes accretion to cease earlier. A reduction of the accretion disk frequency is particularly pronounced in close binary systems of separations 25–100 AU where the accretion disk frequency $F_{<100\text{AU}} = 10_{-5}^{+15}\%$ is less than half of the accretion fraction in wider binaries (100–1000 AU, $F_{>100\text{AU}} = 23_{-8}^{+11}\%$).
3. The dust disk fraction of binary components is indistinguishable from that of single stars. $\mathfrak{F} = 50_{-15}^{+30}\%$ of all binaries with separations between 25 and 1000 AU were found with $K_s\text{--}L'$ excess, identical to the measured value in singles. The frequency of hot circumstellar dust around the components of binary systems with separations $\lesssim 25$ AU, in contrast, is reduced to $\lesssim 25\%$.
4. All accreting components were found as members of mixed pairs of accreting and non-accreting components. The presence of a disk around either binary component appears to be unrelated with the disk around the other component suggesting no synchronized disk evolution. Mixed systems were not found with equal component

masses, but their mass ratios are always below $q=0.8$. Pairs without accreting components occupy a range of mass ratios including close-to equal-mass binaries with $q > 0.8$. Different component masses and the induced stronger disk truncation of the less massive component are a possible explanation for the differential disk evolution.

5. Out of the seven identified accretors only one is a secondary star, i.e., the less massive star in the respective binary system. This is also the weakest accretor found in the sample. This suggests that accreting secondaries are rare and/or only weakly accreting. The existence of single stars with masses comparable to those of the binaries but significantly stronger accretion indicate that this is a consequence of the presence of a higher-mass stellar companion to a disk-hosting star.
6. The measured mass accretion rates of binary components agree well with the mass accretion rates of single stars of Cha I for components $> 0.3 M_{\odot}$. Accreting binary components with masses below $0.3 M_{\odot}$, however, are less frequently observed than around single stars.

Chapter 5

Binary disk evolution across different star-forming regions

The previous chapters discuss individual studies of disks around binary components in the ONC and Cha I star-forming regions. Both regions exhibit a characteristic environment for the birth and evolution of stars: while the ONC is strongly clustered with a strong radiative field from the presence of OB stars in its center, stellar densities in Cha I are low and the stellar member with the earliest spectral type is of type B6.5 (HD 96675, [Luhman 2007](#)). Furthermore, we observe both regions at different ages – binary stars of Cha I ($\sim 2\text{--}3$ Myr; [Luhman 2007](#)) have had more time to evolve towards the main sequence and their disks represent a later stage of the evolution of accretion and circumstellar dust than binaries in the ONC (~ 1 Myr; [Hillenbrand 1997](#)). The interplay of these basic parameters may explain why some of the observed binary disk parameters, such as differential disk evolution, appear different in the ONC and Cha I while other observables, like mass accretion rates, are similar. This chapter's objective is to analyze if and how the environment and age influence the evolution of disks around the components of binary stars.

Whenever possible, results from the literature are included in the discussion to draw conclusions as general as possible. Since previous studies focussed either exclusively or at least primarily on Taurus-Auriga for its proximity (140 ± 10 pc; [Kenyon et al. 1994](#)), youth ($\sim 1\text{--}2$ Myr; [Kenyon & Hartmann 1995](#)), and well accessible population of young multiple stars at low extinctions, Taurus is currently the only additional star-forming association to which data from this study can be compared. While important for studying the general process of disk evolution, high-spatial resolution surveys of a mixture of targets from various young regions and associations (e.g. [Prato et al. 2003](#)) typically do not measure enough targets per individual region to contribute statistically significant data points to the discussion of the influence of age and environment presented below.

5.1 The combined results from various star-forming regions

5.1.1 The decay of the disk frequency in binaries with age

The number of (single) stars of a star-forming region that harbor primordial dust and accretion disks drops with increasing median age of the region, from 80–100% at ~ 1 Myr to essentially 0% at $\gtrsim 10$ Myr (see Fig. 1.4). The decay of disk fraction has been found to be approximately exponential with time constants of 2.3 Myr and 3.0 Myr for the accretion disks and hot circumstellar dust, respectively (Fedele et al. 2010). Is this evolution different when nearby stellar binary companions are present? Theoretically, the truncation of the outer disk by a nearby (< 100 AU) stellar companion is expected to cause a faster disk evolution and dispersal, provided that viscosity is one of the major drivers for disk evolution (Monin et al. 2007). If the lifetime of disks around binary components is globally reduced to a fraction $f < 1$ ¹, then the decay of disk frequency should show a decay with a similar shape, though with a shorter time constant.

To investigate whether there exists a significant difference between the evolutionary timescales of disks around single stars and binary components, I use the results from the ONC and ChaI studies described in the previous Chapters 3 and 4. Additionally, I test whether data from spatially resolved studies of binaries in other SFR can be used to calculate the disk frequency around their individual components. Only a few studies exist with large enough sample sizes to derive significant statistics, all of them targeting the Taurus region (White & Ghez 2001; Hartigan & Kenyon 2003; McCabe et al. 2006). As none of these quote accretion or inner dust disk frequency measurements that can be directly included in the analysis of this thesis, I derive disk frequencies based on the number counts of target components with and without near- to mid-IR excess or H α emission or both, and compare these to large studies of single stars in Taurus in Table 5.1. Interestingly, both the disk frequency from the full samples of binary components and from the subsets of wide and close Taurus binaries ($\gtrsim 100$ AU) are distributed over a range of values despite their overlapping target samples. Nevertheless, a general trend is seen: all three studies have comparably large inferred disk fractions, in particular a disk frequency (both accretion and dust) around the components of close binaries that is considerably larger than the single star value and that of wider binaries. This suggests a preference for classical T Tauri stars in close binaries during target selection which can be due to the fact that classical T Tauri stars are typically considered more interesting in high-spatial resolution binary surveys (see also the discussion in Monin et al. 2007). A thorough *unbiased* sample composition in Taurus from the existing data must be done before accretion and dust disk fractions can enter a study like the present one. The discussion here will be confined to the two regions

¹It should be noted that f is likely a function of the binary separation, i.e., the outer disk truncation radius, since it can easily be imagined that very wide binaries leave disks essentially untruncated and their disks evolve like in single stars (i.e., $f \approx 1$). Close binaries with strongly truncated disks, in contrast, are more likely subject to disk evolution peculiarities.

Table 5.1: Fraction of dust and accretion disks of binary components in different SFR[†]

SFR	$F_{\text{acc}}^{\text{single}}$	ref. ^a	$F_{\text{acc}}^{\text{binary}}$	$F_{\text{acc}}^{<100\text{AU}}$	$F_{\text{acc}}^{>100\text{AU}}$
ONC	$(50\text{--}55) \pm 10\%$	1	$40_{-9}^{+10}\%$...	$40_{-9}^{+10}\%$
ChaI	$44 \pm 8\%$	2	$19_{-6}^{+9}\%$	$10_{-5}^{+15}\%$	$23_{-8}^{+11}\%$
Taurus (A)	$59 \pm 9\%$	2	77% (30/39)	79% (19/24)	73% (11/15)
Taurus (B)			67% (26/39)	70% (16/24)	57% (8/14)
Taurus (C)			81% (34/42)	88% (7/8)	79% (27/34)

SFR	$\mathfrak{F}_{\text{dust}}^{\text{single}}$	ref. ^a	$\mathfrak{F}_{\text{dust}}^{\text{binary}}$	$\mathfrak{F}_{\text{dust}}^{<100\text{AU}}$	$\mathfrak{F}_{\text{dust}}^{>100\text{AU}}$
ONC	55–90%	3	$59 \pm 15\%$...	$59 \pm 15\%$
ChaI	$52 \pm 6\%$	4	$50_{-15}^{+30}\%$	$38 \pm 25\%$	$62 \pm 14\%$
Taurus (A)	64% (157/247)	5	85% (35/41)	93% (25/27)	71% (10/14)
Taurus (B)	62%	6	68% (23/34)	73% (16/24)	58% (7/12)
Taurus (C)			81% (34/42)	88% (7/8)	79% (27/34)

[†] All samples are cropped to binary separations of $\sim 25\text{--}1000$ AU and approximate spectral type ranges between early K and mid to late M. Accretion was either inferred from H α emission or sensitivity-corrected Br γ . The inner dust disk fraction of the Taurus binary samples refers to the fraction of binary components with excess emission $E(K-L) > 0.2$ over a dwarf atmosphere of the same spectral type (Bessell & Brett 1988) or $K - [N]$ excess.

^a References for the single star accretion and dust disk fractions. Binary values of the ONC and Cha I are from this thesis; references for Taurus binaries as indicated (capital letters) in the first column.

REFERENCES. (A) White & Ghez 2001; (B) Hartigan & Kenyon 2003; (C) McCabe et al. 2006
(1) Fűrész et al. 2008; (2) Mohanty et al. 2005; (3) Hillenbrand et al. 1998; (4) Damjanov et al. 2007; (5) Luhman et al. 2010; (6) Fedele et al. 2010

analyzed in this thesis (ONC, Cha I) and should be revisited with existing and future data from Taurus and other SFR.

The evolution of the frequency of accretion and hot inner dust disks is explored with help of Fig. 5.1, which visualizes the calculations of the ONC and Cha I statistical data summarized in Table 5.1. *Hot circumstellar dust* appears to be only mildly or not at all reduced around the components of binary stars with projected separations between ~ 25 AU and ~ 1000 AU. Even when dividing the sample into wide (100–1000 AU) and close (25–100 AU) binaries – the closer the binary the stronger disk truncation and accordingly a possible effect on disk evolution – no clear trend of dust disk frequency is visible: while wide binaries show a disk frequency that is indistinguishable from the single star value, the disk frequency in closer binaries is only mildly reduced, by less than 1σ . *Accretion disks* show a different signature. Their frequency appears to be reduced, particularly strongly in the separation range $\sim 25\text{--}100$ AU, where the Cha I data point lies $\sim 3\sigma$ below the single star accretion disk decay curve of Fedele et al. (2010). But even wider binaries appear with a lower frequency than singles.

To quantify by how much accretion disk evolution is accelerated, I compare the ONC and Cha I binary accretion data to exponential decay curves (see the middle and bottom

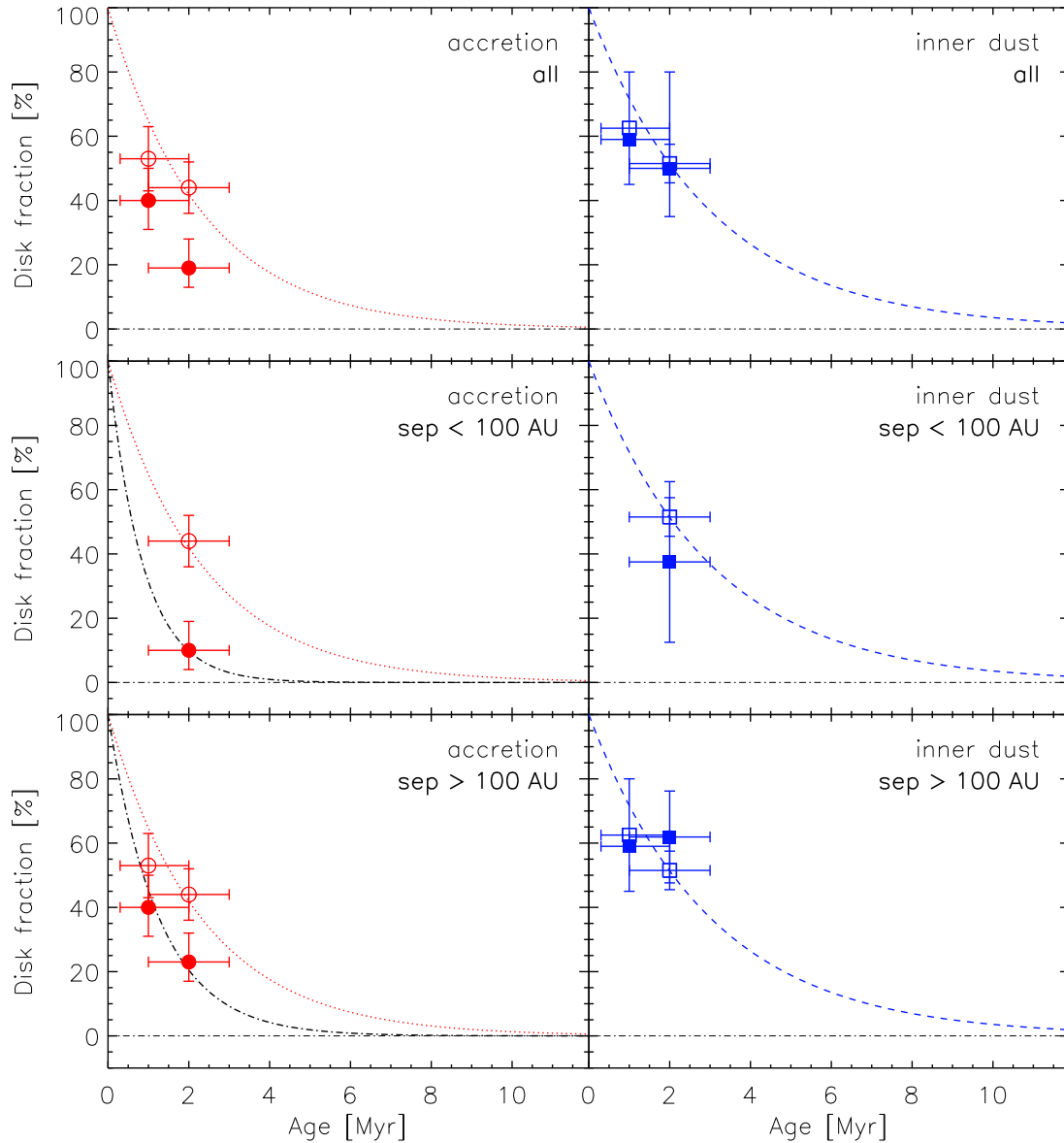


Figure 5.1: Decay of accretion and inner dust disk frequency with age with the new ONC (plotted at 1 Myr) and Cha I (2 Myr) data from this thesis. As indicated in the top-right of each sub-panel the whole (restricted) samples, close binaries (projected separations < 100 AU), and wide binaries (> 100 AU) are shown for both dust and accretion disks. The filled symbols show components of binaries, the open symbols are the comparison values measured from single stars of the same star-forming regions (Hillenbrand et al. 1998; Mohanty et al. 2005; Luhman et al. 2008). The dotted red and dashed blue lines are exponential fits (accretors: $\tau=2.3$ Myr, dust: $\tau=3$ Myr) to the disk frequencies of K0–M5 (single) stars in a number of young clusters and associations by Fedele et al. (2010). ONC binaries have no values at < 100 AU since the sample did not contain any binaries in this separation range. Exponential decay curves (dash-dotted) with time constants 0.9 Myr and 1.3 Myr are overlotted in the sub-panels of the accretor fraction of close and wide binaries, respectively.

panels in the left column of Fig. 5.1). Under the assumption that the binary disk fraction follows an exponential temporal decay like for single stars, I find that binaries are compatible with a rapid decay with a time constant $\tau_{\text{acc}}^{<100\text{AU}} = 0.9 \pm 0.5$ Myr, wider binaries with $\tau_{\text{acc}}^{>100\text{AU}} = 1.3 \pm 0.9$ Myr (uncertainties are estimated from the measurement errors of the disk fraction and age). Both values are shorter than the derived single star value of $\tau_{\text{acc}}^{\text{sing}} = 2.3$ Myr (Fedele et al. 2010) by factors of 2.6 and 1.8, respectively. Further data points are desirable to confirm the evidence for an accelerated exponential decay of disk frequency and an accordingly faster disk evolution.

Taken together, these observations draw the following picture of the impact of the presence of stellar binary companions at projected separations of ~ 25 –1000 AU on the evolution of a circumstellar disk: (i) The presence of hot inner dust is independent of the existence of a stellar companion at separations > 100 AU. (ii) Closer companions (~ 25 –100 AU) suggest a small, though not significant reduction of the disk frequency. (iii) The lifetime of accretion disks appears reduced in presence of a stellar companion between ~ 25 and 1000 AU by a factor of ~ 2 . While (iv) a strong and significant reduction is seen for close binaries < 100 AU, (v) accretion disk frequencies are found to be systematically reduced also around wider (100–1000 AU) binary components.

These results are in agreement with spatially unresolved studies which examine the frequency of disks in binary *systems* instead of the individual components (Cieza et al. 2009; Kraus et al. 2012). While this technique can cover binaries from a wider range of separations and brightness ratios since it is not limited by the spatial resolution of ground- and space-based observatories, it remains unknown whether the measured accretion is originating from one or both components of a binary. The resulting statistics is accordingly less sensitive to small changes of the overall disk frequency². Nevertheless, Kraus et al. (2012) find a significantly reduced frequency of close (< 40 AU) binary stars with signs of disks compared to single stars, in agreement with the finding by Cieza et al. (2009) that binaries in such close systems can less often be associated with mid-IR excess emission.

One caveat of the study presented in this thesis is the difference of the techniques used for the derivation of the single star and binary component accretion disk frequencies. If the correction factor f for the compensation of the lower sensitivity of Br γ is higher than assumed³ (see Sect. 3.3.2), Br γ would misclassify more classical T Tauri stars as non-accreting than anticipated. However, even if the frequency of accretors in wide binaries (> 100 AU) would prove to be as high as that of single stars, a significant reduction of accretors in closer binaries can be inferred since the relative decrease of disks around wide and close binaries in this thesis remains true. Future studies with a single star comparison sample measured with the same accretion indicator (Br γ) are required in each of the studied regions to evaluate the reduction of disk frequency with high confidence. Such a study is

²The derived frequencies of unresolved studies f_{bin} are upper limits to the component disk frequency f_{comp} since $f_{\text{bin}} = C_{\text{bin}}/N_{\text{bin}} > C_{\text{comp}}/N_{\text{comp}} = f_{\text{comp}}$, because $N_{\text{comp}} = 2N_{\text{bin}}$ but $C_{\text{comp}} < 2C_{\text{bin}}$ when N the total number of components or binaries and C the number of accretors.

³ f was inferred from the number of Br γ emission detections in previously known classical T Tauri stars using data from Folha & Emerson (2001). It can vary with the individual sensitivities to Br γ and the original H α detection.

underway by the author and his collaborators for the Chamaeleon I region. Also, expansion of the project to a wider range of SFR ages will reveal whether the observed trend for a reduced accretion disk frequency at roughly constant hot dust presence continues to old ages.

Since the optically thin gas disk extends closer to the stellar surface than circumstellar dust, the apparently accelerated gas dispersal in binary companions may be evidence for either a modified inside-out evolution of the circumstellar disk or an overall more rapid evolution of the gas content of the disk. Alternative interpretations can be adapted from Fedele et al. (2010), who discuss possible reasons for the observed different timescales of dust and accretion disk dispersal in *single* stars to be viscous evolution, potentially taking into account the UV radiation from the central star, or planet formation. If binaries enhance one of these effects, this would explain their even more extreme difference between accretion and dust disk dispersal.

Inside-out evolution of circumstellar disks is supported by theoretical considerations (e.g. Alexander et al. 2006) as well as observations; e.g. McCabe et al. (2006) see a correlation between the absence of accretion and the presence of an inner hole in the disk, as inferred from the abundance of targets with mid-IR ($K - [N]$) excess emission but without near-IR ($K - L$) excess. While a simple acceleration of inside-out disk evolution would disperse both the accretion and inner dust disk on a shorter timescale, the fact that close binarity accelerates only the dispersal of the inner (accretion) and not the near-IR-detected part of the disk would require the onset of inside-out disk dispersal to be shifted to earlier times in the stellar evolution while the speed of inside-out evolution needs to be *slower* to match the absolute lifetime of the near-IR detected disk. While in principle possible, it seems rather unlikely that dispersal timing and a deceleration of disk evolution are matched to such a high degree. While inside-out evolution is still a possible scenario for disk evolution in general, it cannot on its own be responsible for the short accretion disk lifetimes in binaries compared to the lifetime of hot circumstellar dust in the same targets.

Viscous evolution predicts a declining accretion strength with age, however, on a very long timescale > 10 Myr. Additional photoevaporation by UV radiation from the central star would result in timescales closer to the observed ones, with a short delay ($\sim 10^5$ yr) until the dust disk disperses (Clarke et al. 2001). Although a further reduction of accretion disk lifetimes in binaries compared to single stars may be possible in this framework when accounting for the additional UV irradiation by the stellar companion, the effect is very small even for a stellar companion in as little as 10 AU distance whose irradiation would already be $\gtrsim 100$ times weaker (through geometrical thinning) than that of the central star assuming that the UV processes mainly take place at distances of 1 AU from the stellar surface or closer. Additionally, although a delay between the dust and accretion disk dispersal are predicted by this theory, the timescale of $\sim 10^5$ yr is shorter than observed in both binaries and singles. Additional processes thus must be at work in the UV-switch scenario to explain the magnitude of the dust/accretion disk dispersal time discrepancy.

Another proposed mechanism by Fedele et al. (2010) is planet formation and subsequent migration to the inner region of the disk where it can stop further accretion. The larger discrepancy between accretion and dust presence in the inner disks of binaries compared

to single stars could be caused by an increased number of planets around the components of binaries compared to single stars or a more rapid inward migration. [Eggenberger & Udry \(2010\)](#) find that the planet abundance is slightly reduced. If most binaries initially form a planet that is involved in shutting off accretion, a significant fraction of these would need to be removed at a later stage. However, after planets migrate close enough to the star to interact with the accretion region they evolve essentially like single star planets and a removal through, e.g., dynamical interaction with the binary companion is unlikely given the stability of their orbits when closer to the star than $\sim 1/10$ of the binary separation ([Holman & Wiegert 1999](#)). And also a faster planet migration in binary systems is not foreseen in today's theoretical derivations as, e.g., the proposed binary-specific *Kozai migration*⁴ ([Wu & Murray 2003](#)) is too slow to have a significant impact on the planet migration within the first few Myr.

The current approaches to explain the different timescales of accretion and dust disk evolution in single stars can apparently not be modified in a straight-forward way to explain the stronger signature found in binary stars and additional concepts must be tested for their applicability to both, single and binary star disk evolution.

5.1.2 Differential disk evolution

Not only are mixed systems of accreting and non-accreting components abundant in all our samples as well as studies of other regions like Taurus (see e.g. [Monin et al. 2007](#)), but they also exhibit a remarkable binary separation distribution. In [Fig. 5.2](#) the separation distributions in the four categories CC (both components accreting), WW (no accreting components), and CW and WC (mixed systems with accreting primary and secondary, respectively) are presented for the ONC, Cha I (both from this thesis), and Taurus ([McCabe et al. 2006](#)).

Apparently, mixed systems exist at binary projected separations from below 50 AU up to several hundred AU. The significant paucity of mixed pairs with separations smaller than 200 AU that was seen in ONC binaries (see [Sect. 3.3.2](#)) is not observed in binaries of Cha I and Taurus where several mixed systems with separations < 200 AU are found. However, a systematic absence of wide CC pairs is seen in all three samples. While the distributions of mixed pairs span the whole range of separations up to 1000 AU, CC binaries are consistently found with separations below ~ 350 AU with a KS probability of only 3% that CC pairs of the combined distributions are drawn from the same parent distribution as mixed pairs. This points to a synchronization of accretion in close systems that apparently cannot be supported in wider binaries. Possible mechanisms must either sustain accretion preferably in both components of close binaries, e.g., through simultaneous feeding from a common circumbinary envelope or disk, or initial conditions were more equal in closer binaries through a more similar distribution of, e.g., angular momentum or mass or both.

⁴Kozai migration is an interplay of the Kozai mechanism, forcing a planet around a binary component on an eccentric orbit, and tidal circularization.

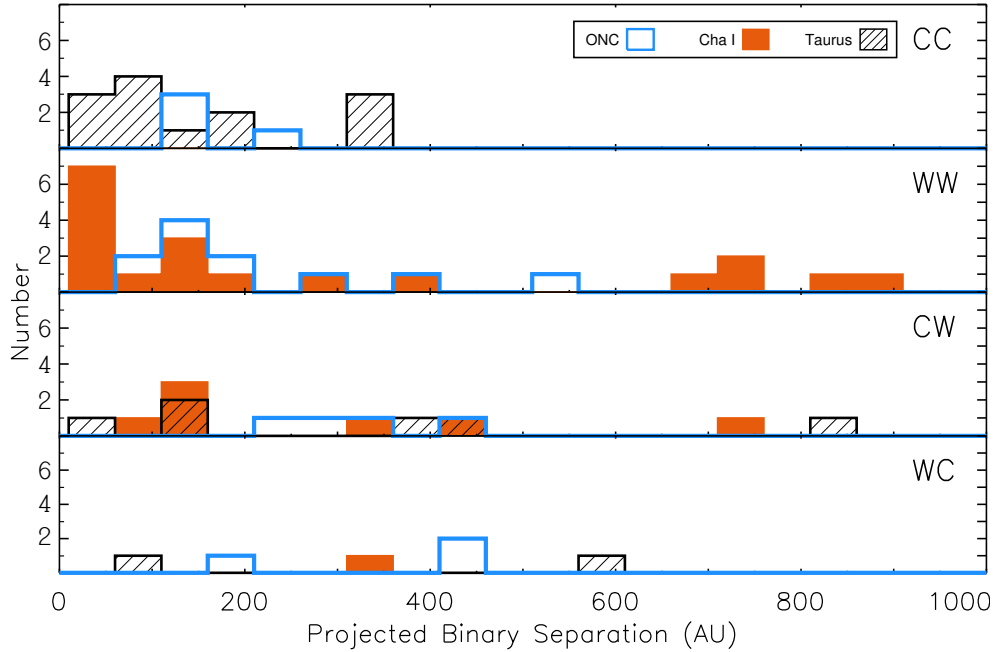


Figure 5.2: Binary accretion type as a function of the projected binary separation in three different star forming regions. Blue outline: Orion Nebula Cluster (Chapter 3); Solid orange: Chamaeleon I (Chapter 4); Black hatched: Taurus-Auriga (McCabe et al. 2006). The four categories CC, WW, CW, and WC refer to pairs of classical and weak-line T Tauri stars, and mixed systems with an accreting primary or secondary component, respectively. The sample of ONC binaries is limited to separations $\gtrsim 100$ AU, while the other two samples reach ~ 25 AU.

The largest disk-like circumbinary structure that has been observed is found around UY Aur. The inner edge of the circumbinary material is about 500 AU from the center of mass of the ~ 190 AU wide (deprojected semi-major axis) binary system (Close et al. 1998). The fact that the outer disk edge extends has a diameter of ~ 1400 AU in near-IR scattered-light images ($12''$ – $13''$ at a distance of 140 pc Close et al. 1998) and even more than twice this extent in radio observations of ^{13}CO (Duvert et al. 1998), indicates that spatially large reservoirs can exist to possibly feed the individual circumstellar disks even of relatively wide binaries (the details of the feeding mechanism were explored in a few numerical studies, e.g. Artymowicz & Lubow 1996; Günther & Kley 2002). While in loose associations like Taurus accretion synchronization can in principle be due to circumbinary material like observed around UY Aur, this model is not able to explain the synchronization of disks in binaries of dense clusters like the ONC, where dynamical interactions limit the size of disks to small outer radii of mostly < 400 AU (see the discussion in Sect. 3.3.2).

The data confirm the preference for mixed systems to have an accreting primary ($17\times\text{CW}$ vs. $7\times\text{WC}$ in the combined sample of ONC, Cha I, and Taurus), as it was already observed in earlier studies (Monin et al. 2007). This imbalance is likely to be real, since the majority of these systems were found in high-spatial resolution surveys of the three regions without preference for or against accretors. Accretion can be detected with

the same sensitivity around both components of a binary (see Sect. 4.3.2). The stronger truncation and/or external illumination of the secondary disk apparently leads to an, on average, shorter disk lifetime relative to the primary star disks.

If interpreted as an age sequence from very young (Taurus, ONC; ~ 1 Myr) to slightly older (Cha I; $\sim 2\text{--}3$ Myr), the three distributions suggest the following course of differential disk evolution: While no WW binaries were found at the youngest ages, CC have disappeared by the age of Cha I. This confirms the assumed general evolution from accreting to accretion-free binaries over the timespan of a few Myrs. The existence of mixed systems in all populations is consistent with either all or a fraction of all binaries evolving from a CC state through an intermediate mixed state and subsequently to WW. It cannot be excluded that a fraction of binary systems forms in a mixed state and remains in this state for a comparably long time. Though, with the background of the strong preference for CC systems in the younger populations this interpretation seems rather unlikely.

If the picture of a typical binary evolution from CC to WW is true, then Taurus is apparently in a younger (binary) evolutionary state than the ONC, since it has a higher fraction of CC binaries. A possible reason for a lower fraction of CC binaries in the ONC than Taurus may be stellar encounters. Simulations for the ONC and its highest density region, the Trapezium cluster, were able to show that dynamical interactions can reduce disk frequency by 5–20% over the lifetime of the ONC of ~ 1 Myr (Olczak et al. 2006). The relative dynamical youth of Taurus is also suggested by its higher binary frequency. Assuming that initially all stars are born as binaries, Marks & Kroupa (2012) show that the stellar density at a cluster’s birth is the most important parameter to determine the binary frequency observed at a later age, which simultaneously explains the low binary frequency of the dense ONC and the more than twice as high binary frequency of the loose Taurus association.

5.1.3 The independence of mass accretion rate and binarity

Mass accretion rates are found to be comparable across various star-forming regions. This is inferred from the similar locations that components of binaries in the ONC, Cha I, and Taurus (Hartigan & Kenyon 2003) assume in a $\log \dot{M}_{\text{acc}}\text{--}\log M_*$ diagram (Fig. 5.3). Together with the observation that mass accretion rates in binaries are independent of binary separations (see e.g. Fig. 4.23) and that also single stars are measured with similar mass accretion rates (Figs. 3.16 & 4.22), it can be inferred that stellar binary companions within $\sim 100\text{--}1000$ AU have no impact on mass accretion rates in young star-forming regions.

The time over which mass is accreted, however, is significantly shorter in close binaries than in single stars (Sect. 5.1.1). This observation implies a decoupling of accretion duration and strength. How can such a decoupling be explained? To feed a central star with disk material while satisfying angular momentum conservation, angular momentum needs to be transported from the inner disk outward. This can be done via viscosity and an expansion of the outer disk radius. In binary stars, free expansion is inhibited by the existence of a stellar companion which removes the outer disk material from the system by

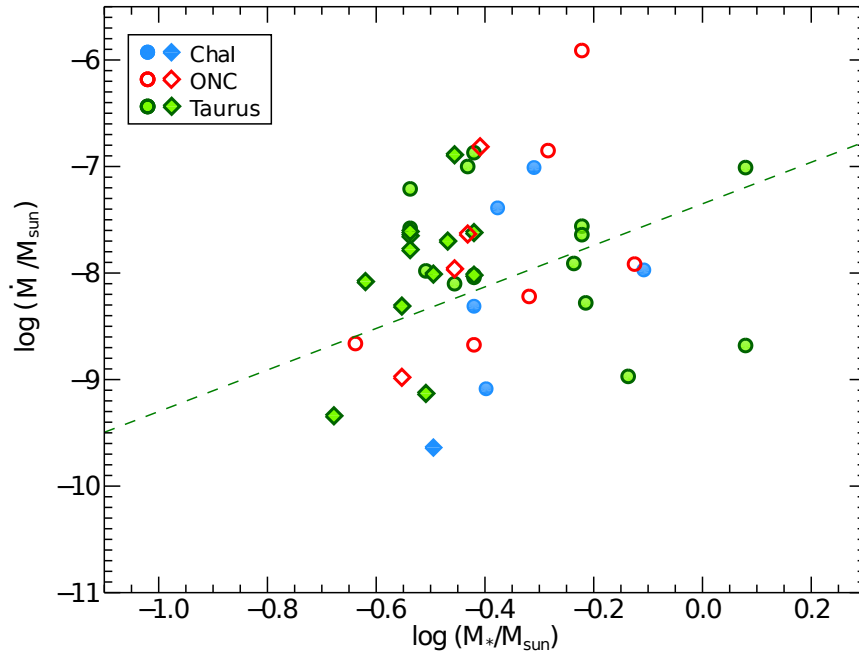


Figure 5.3: Mass accretion rate as a function of stellar mass for different SFR. Blue filled symbols are Chamaeleon I binary components, red open symbols show ONC data, and green symbols are Taurus data from [Hartigan & Kenyon \(2003\)](#). Circles show primary components and diamonds secondaries. The dashed line is the $\dot{M}_{\text{acc}}-M_*$ relation for single stars in Chal by [Antonucci et al. \(2011\)](#).

scattering or engulfing the material that crosses the disk’s edge at roughly 1/2–1/3 of the binary separation ([Artymowicz & Lubow 1994](#)). An accretion strength that is independent of disk truncation would mean that the angular momentum transport is not altered by the presence of a companion and that disk material is transported inwards at the same rate as in an untruncated, freely expanding disk. A shorter accretion disk lifetime then is a necessary consequence, since there is less material in the outer disk reservoir of a truncated disk to sustain accretion.

A concept that is consistent with a decoupling of accretion onto the star and the size of the outer disk is the *layered accretion* model ([Gammie 1996](#)). One of its features is the existence of a *dead zone* (enclosed by *live zones*) which is a region in the disk’s midplane extending radially between ~ 0.1 AU and several times 1 AU from the star which is dense and cool so that it is, unlike the rest of the disk, neither ionized by heating from the central star nor cosmic rays. Vanishing ionization, however, inhibits magnetorotational mass accretion through this region since neutral matter does not couple to the magnetic field. In this model, the mass accretion rate onto the star is determined by mass transport in the disk *inside* the inner edge of the dead zone, i.e. inside the critical radius R_c defined by the radius at which $T = 1000$ K through viscous heating. Material that resides in the outer disk will not be transported all the way to the star but mostly accumulate in the dead

zone⁵. While the predicted mass accretion rates are independent of the disk size and mass (and thus of truncation through a stellar companion), they are well consistent with the values measured for young low-mass stars ($\sim 10^{-8} M_{\odot} \text{yr}^{-1}$ to several times $10^{-7} M_{\odot} \text{yr}^{-1}$; Gammie 1996).

The existence of a dead zone could not yet be confirmed by observations since the predicted features (e.g. a characteristic drop the surface density distribution) are weak and subject to future observations with *ALMA* or the *EVLA* (Zhu et al. 2010). Also, the original model is likely incomplete, as it e.g. assumes that mass accretion rates are independent of stellar mass, in contrast to observations which show roughly a dependence $\dot{M} \propto M_*^{1.8}$ (Hartmann et al. 2006). Nevertheless, together with the supplementary studies underway (e.g. Hartmann et al. 2006; Ilgner & Nelson 2008; Zhu et al. 2010), the layered accretion model is a promising candidate to explain the apparent independence of the mass accretion rates from disk truncation by a companion as observed in the binary data of this thesis.

5.1.4 Binary disk evolution vs. planet formation

The observed reduction of accretion disk lifetime in close binaries, and thus the presence of gas in the inner disk, has necessary implications for the formation of planets. As planets are built from the material of the primordial disk, their formation must be completed before disk dispersal. The time that the formation needs is not yet fully established and currently a function of the model that is applied. The two most popular planet formation scenarios are core accretion and disk fragmentation. The former mechanism is comparably slow, it needs a few Myrs to complete planet formation and is suspected to mainly form low-mass gaseous and rocky planets (Pollack et al. 1996). Disk fragmentation through gravitational instability, in contrast, can form high-mass gas giants on timescales < 100 kyr (Boss 1997). The typical lifetimes of protoplanetary disks around single stars of up to 10 Myrs would allow either process to be responsible for the formation of the majority of planets. As discussed earlier, however, disk lifetimes are (i) reduced in close binaries compared to single stars and (ii) are typically shorter around the less massive component of a binary. If planets predominantly form through a slow process like core accretion, then their number would be reduced in close binaries and in particular their secondary stars.

Hot-Jupiter planets have been found around the components of almost 60 binary stars to date (Roell et al. 2012). The parameters of these planets exhibit a few interesting features. One is the apparent preference for high masses $\gtrsim 1 M_{\text{Jup}}$ of planets in orbit around the component of a close binary < 100 AU. Wider binaries are found with a wider range of planetary masses including those below $1 M_{\text{Jup}}$ (see in particular Fig. 3 of Duchêne 2010). Another observation is the surprisingly clear preference for the more massive binary component to host a planet – less than 5% of all planets in binaries orbit the less massive component, and only one system was found with both components orbited each by their

⁵The accumulating material will eventually be accreted in an *FU Ori*-like outburst, when the infalling material heats up to the critical temperature T_c and suddenly becomes viscous.

own planet (Roell et al. 2012). Furthermore, the overall planet frequency in close binaries is lower than in single stars, which is inferred from the finding by Eggenberger & Udry (2010) that planets are significantly ($\sim 2\sigma$) less often found in binary systems than around single stars.

When combined, the findings from the disk and planet surveys are in favor of a bimodal planet formation scenario where low-mass planets ($\lesssim 1 M_{\text{Jup}}$) form mainly through core accretion and higher-mass planets through disk fragmentation (Duchêne 2010). This would explain the absence of low-mass planets in close binaries $\lesssim 100$ AU where the disk evolutionary timescale could be too short for the formation of planets through core accretion, in particular in the short-lived secondary disks. Wider binaries have longer disk dispersal timescales, close to the ones of single stars. They could form planets with similar properties as single star planets through either process.

An alternative suggestion of Duchêne (2010) is a separation-dependent preference for either formation mechanism (instead of a mass-dependence as described above). Disk fragmentation could be triggered by the presence of a close binary companion leading to an enhanced formation of massive planets, while wide binaries would be dominated by planet formation through core accretion. The different formation processes would, however, not explain why the parameter distributions (e.g. mass) of high-mass planets in close and wide binaries are so similar.

All results based on planet statistics must be judged in the light of today's observational limitations for the detection of planets with the primarily used radial velocity technique. The contamination of the planetary radial velocity signal with the light from the secondary star makes the detection of low-mass planets in spatially unresolved binaries comparatively harder. For this reason, most previous radial velocity surveys either excluded known close binaries from their samples or are limited by significantly worse lower detection limits. Duchêne (2010) argue, however, that the observed preferences for high-mass planets in close binaries are not entirely due to observational biases but a real feature of the planetary population, based on the uniform detectability criterion of Fischer & Valenti (2005). The observed features of the population of planets around binary components might thus indeed reflect the correlations of disk presence in primaries and secondaries of T Tauri binaries.

5.2 Summary

This chapter combines new observational and previously published results from studies of the individual circumstellar disks around the components of visual binary stars in the Orion Nebula Cluster, Chamaeleon I, and Taurus star-forming regions with separations between 25 and 1000 AU. The three data sets are analyzed regarding the evolution of disk frequency with the median age of the region, the relative timescales for component disk evolution, as well as the impact of binarity on mass accretion. The new results enabled me to draw the following conclusions:

1. The frequency of accretion disks around binary components decays more rapidly than in single stars. This was inferred from the consistently lower binary accretion disk

frequency compared to single star accretion disks. The reduction of accretion disk frequency is particularly strong in close binaries of $\sim 25\text{--}100$ AU separation, where Cha I binaries show a reduction of accretion disk frequency of as much as 3σ .

2. The existence of a binary companion at $25\text{--}1000$ AU has no significant impact on the presence of hot circumstellar dust for stars with ages $\lesssim 3$ Myr. Hot circumstellar dust is measured as often in association with binary components of $25\text{--}1000$ AU binaries as around single stars.
3. The imbalance of accretion and dust disk fractions implies an accelerated evolution of the inner gas disk compared to the evolution of hot inner dust around binary components.
4. Systems of two accreting components (CC) were found with significantly smaller separations than mixed-accretion systems. The absence of CC binaries at separations wider than 350 AU implies an accretion-synchronizing mechanism of preferably close systems. This could be feeding from circumbinary material or initial conditions at formation that are particularly similar for close binary companions.
5. Mixed systems of accreting and non-accreting components do exist in all three regions and at all tested binary separations. There seems to be a preference for systems with an accreting primary.
6. Binaries evolve from pairs of classical T Tauri stars to pairs of weak-line T Tauri stars with a possible intermediate step of mixed pairs. This was inferred from the fact that the young Taurus and ONC regions show more classical T Tauri pairs than the slightly older Cha I population with its mainly weak-line population.
7. Mass accretion rates of binary components with masses $\sim 0.2 M_{\odot} \leq M_* \leq 1 M_{\odot}$ are independent of the presence of stellar companions between $\sim 100\text{--}1000$ AU. The implied independence of accretion rate and disk lifetime can be explained by a decoupling of material transport in the inner disk from the events at the outer disk edge, in agreement with e.g. layered disk models with a dead zone. Shorter disk lifetimes in binaries are possibly a consequence of the limited material in disks that are truncated by a nearby binary companion.
8. The absence of low-mass ($< 1 M_{\text{Jup}}$) planets in close (< 100 AU) binaries may be correlated with the shorter average lifetimes of secondary disks. This parallelism agrees with the hypothesis that high-mass planets $\gtrsim 1 M_{\text{Jup}}$ form through a rapid process such as disk fragmentation and low-mass planets $\lesssim 1 M_{\text{Jup}}$ form through the slower mechanism of core accretion.

Chapter 6

Conclusions & outlook

Binaries are an inevitable and abundant outcome of stellar formation. Exploration of their properties at ages of a few Myr, when remainders of the star formation process are still visible, provides information about various aspects of star formation. This naturally includes single and multiple star formation processes, but also extends to planet formation as the planets form from the circumstellar disks.

Among the most telling features of an ongoing star- and planet-forming process are the presence and the properties of circumstellar disks in the T Tauri phase. A detailed description of the distribution and evolution of their gaseous and dusty material is necessary to draw conclusions about the initial conditions present in the earliest and most fundamental star- and binary formation phases, which are hidden from view with most observational techniques. How do external processes influence the development of mass accretion? By how much does the evolution of the circumstellar material notice the presence of a stellar companion? What is the dominant planet formation process? Results from the study of circumstellar material in low-mass binaries provides crucial information to approach and eventually answer these and other open questions about stellar formation.

This thesis presents a high-spatial resolution near-infrared photometric and spectroscopic study of 52 visual low-mass multiple stars in the 1–3 Myr old Orion Nebula Cluster and Chamaeleon I star-forming regions. The observational data allow me to infer stellar parameters including effective temperatures, luminosities, masses, ages, and radii of the individual components of each multiple with projected separations between ~ 25 –1000 AU. These parameters are brought into context with the measured presence of hot circumstellar dust at the inner rim of the protoplanetary disk as inferred from the existence of near-infrared excess emission, and with the strength of ongoing accretion from the assessment of Brackett- γ line emission. The new data represent the most complete and coherent study of the individual components of binaries in the two targeted star-forming regions and are among the largest spatially-resolved studies of binaries in nearby star-forming regions to date. Data from a third region, Taurus, could be compiled from previous publications. The binary companions of the three data sets were analyzed regarding their accretion and inner dust disk frequency taking into account the median ages of the regions and with the background of the different dynamical and star formation histories.

While *single star disk evolution* has been investigated in depth in numerous previous studies, the gathered information from this thesis adds significantly to our knowledge about the evolution of protoplanetary disks in *T Tauri binary stars*. Taking into account the new results, today's picture of the evolution of disks in T Tauri binaries can be summarized as follows:

1. Binary companions truncate a disk to $\sim 1/3$ of the binary separation. This implies a significant disk truncation in binary systems smaller than a few times 100 AU and accordingly altered disk evolution compared to single star disks, since the typical sizes of untruncated disks are on the order of several times 100 AU.
2. Disk evolution in binaries is faster than in single star systems. More specifically, the evolution of disks around the components of binaries is, on average, finished after a shorter time than around singles with comparable stellar parameters. This observation is a function of binary separation, as well as the targeted disk component – circumstellar gas or dust. While binaries with separations $\lesssim 40$ AU show a reduction of both gas and dust in the disk, intermediate separation binaries between 30 and 100 AU are found with only a reduction of accretion and thus gas presence. Wide binaries >100 AU evolve mostly like single stars with only mildly reduced gas and dust content.
3. Binary components are born coevally. This is evidence against capture of formerly unrelated components as a major binary formation mechanism. Despite equal stellar component ages, the relative circumstellar disk lifetimes are not necessarily equal around both components of a binary. Either component, the more or less massive one, can be host to the longer-lived disk of a system with a preference for the more massive component to have a disk for longer. In binaries with projected separations $\lesssim 350$ AU a weak synchronization of disk evolution is apparent, i.e., a preference for disk lifetimes to be similar around both components of a binary.
4. Mass accretion rates in primordial disks are universal, i.e., they are independent of a possible truncation of the outer disk through a binary companion and of the respective star-forming environment. The duration over which a star accretes, in contrast, is a function of binary separation (see 2.), i.e. the outer truncation radius of a disk.
5. The fact that preferably the more massive binary component hosts the longer-lived disk and that disks in close binaries are generally shorter-lived correlates with the finding that planets in binaries are found almost exclusively around the more massive binary component and that almost no low-mass hot Jupiters $<1 M_{\text{Jup}}$ are found in close binaries <100 AU. A scenario in agreement with both these observations suggests that high-mass planets $\gtrsim 1 M_{\text{Jup}}$ form in a relative fast process like disk fragmentation while lower-mass planets predominantly form through slow processes like core accretion.

The above results are based on evidence from observations of a small number of star-forming regions in the Solar neighborhood, each providing access to a limited number of low-mass binary stars. Most of the results are subject to low-number statistics with accordingly large uncertainties. An immediate future task must be to enlarge samples and expand the study to additional nearby star-forming regions to broaden the scope of properties: Observations should target young and old ages up to ~ 10 Myr, strongly clustered and disperse regions, and low-mass regions as well as those with a large body of hot stars. The resulting information is a direct extension of the results discussed in this thesis and would, in addition to better statistics, help to address the following questions: *Does the observed rapid decline of disk frequency in close binary stars continue to older ages ~ 10 Myr? Do disks initially form around all binary components? Do binaries form differently in the vicinity of hot stars?* While most of the required observations are straightforward, results can be used to gauge star-, binary- and planet-formation theories through the comparison of the predicted and measured stellar, binary, and planetary parameters.

Current observations mostly explore the inner-most regions of the circumstellar disks. This is due to observational limitations: To achieve the highest spatial resolutions at the required sensitivity to detect disk signatures around close pairs of faint low-mass stars, most previous data were taken with ground-based (using adaptive optics) and space-based observations at optical and near-infrared wavelengths. This limits the deducible physics to emission from hot processes near the stellar surface. The bulk of the disk mass, however, resides at comparably large distances to the star and temperatures are accordingly low, producing no detectable signature in the infrared. *How is the disk material distributed over the components of binary stars? Is dust evolution (e.g. grain growth) in binaries accelerated to match the short inner disk lifetimes?* These questions can only be addressed with observations at sub-mm and longer wavelengths. The necessary angular resolutions of a few tenths of an arcsecond and the sensitivity to detect the small amounts of circumstellar material around T Tauri stars, however, became accessible only recently with large interferometric radio arrays like the Sub-Millimeter Array (SMA) and the Atacama Large Millimeter Array (ALMA). Pioneering effort to measure the radio emission from a number of individual binary components has been made only recently by [Harris et al. \(2012\)](#) with the SMA, yet the total amount of spatially resolved sub-mm data of T Tauri binary stars is still small. Future studies with ALMA's superior sensitivity and angular resolution will enable us to efficiently measure the circumstellar material distribution of close visual binary stars in large quantities. The combined data from multiple wavelengths is required to draw conclusions about disk evolution on all spatial scales and temperatures to eventually form a coherent picture of all the processes involved in the first few Myr of a stellar lifetime.

Appendix A

Statistical evaluation of the disk frequency

We used a Bayesian approach to derive the probability density function (PDF) of the disk frequency around the individual components of binaries in the ONC. The location of the maximum of the distribution and its width represent the most robust estimates of our disk frequency and its uncertainty, respectively. Input information comes from the measured values of the Bry equivalent width and the continuum noise measurements in each target spectrum.

A.1 Derivation of the formulae

We defined the probability density $P(\vartheta|D)$, given the data D , of the true disk frequency ϑ with $0 \leq \vartheta \leq 1$ to be in the interval $[\vartheta, \vartheta + d\vartheta]$, as

$$P(\vartheta|D) = \sum_{j=0}^n \text{prob}(\vartheta, k=j|D) \quad (\text{A.1})$$

$$= \sum_{j=0}^n \text{prob}(\vartheta|k=j, D) \cdot p_n(k=j|D) \quad . \quad (\text{A.2})$$

While $\text{prob}(\vartheta, k|D)$ describes the PDF as a function of the disk frequency ϑ and the observed number of disks k , the $\text{prob}(\vartheta|k, D)$ in (A.2) are the probability density functions PDF_k , which describe the probability density of finding the true disk frequency to be in the range $[\vartheta, \vartheta + d\vartheta]$ when the number of detected disks is fixed at k (see §A.1.1). The latter were weighted by $p_n(k|D)$ in order to account for their relative probability (see §A.1.2). To include the contributions of all possible outcomes ($0 \dots n$ disks surrounding n targets), we summed up all partial PDFs to the final PDF $P(\vartheta|D)$.

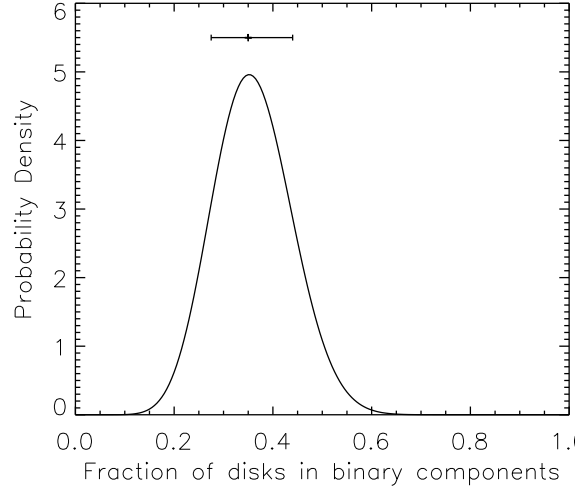


Figure A.1: The resulting ONC probability density function as a sum of the individually weighted $p(\vartheta|k, D)$. The resulting best-fit value of the disk fraction of binaries in the ONC (see bar) is $F = 0.35^{+0.09}_{-0.08}$.

A.1.1 The probability density for k disks in n targets

The PDF $\text{prob}(\vartheta|k, D)$ can be most accurately described as being binomial, since there are only two options “disk” or “no disk”. For instance, starting with Bayes’ theorem, we found that

$$p(\vartheta|k, n) = \frac{p(k|\vartheta, n) p(\vartheta|n)}{p(k|n)} \quad (\text{A.3})$$

$$= \frac{\binom{n}{k} \vartheta^k (1 - \vartheta)^{n-k}}{\frac{1}{n+1}} \cdot p(\vartheta|n) \quad (\text{A.4})$$

$$= (n + 1) \cdot \binom{n}{k} \vartheta^k (1 - \vartheta)^{n-k} \cdot \begin{cases} 1 & \text{for } 0 \leq \vartheta \leq 1 \\ 0 & \text{else} \end{cases} \quad (\text{A.5})$$

for the total number of targets n . The prior $p(\vartheta|n)$ was assumed to be uniform, since it simply describes the probability of finding a disk fraction anywhere between 0 and 1. In addition, we found that $p(k|n) = 1/(n + 1)$, since it describes the probability of selecting a solution among $n + 1$ possibilities $\{0, \dots, n\}$.

A.1.2 The weighting factors $p(k|D)$

We were able to compare the measurement of the equivalent width $W(\text{Bry})$ to the noise limit at the position of the Bry line (Table A.1). Assuming the noise and the underlying distribution of the Bry measurement to be approximately Gaussian (which can safely be assumed owing to the high photon count rates), we were able to derive the probability Π of significant Bry emission and hence a disk by integrating a Gaussian distribution

(with median $\mu = W(\text{Br}\gamma)$ and width $\sigma = \Delta W(\text{Br}\gamma)$). The lower and upper integration limits were the continuum noise and infinity, respectively. For example, if we measured an equivalent width of $1.5 \pm 0.5 \text{ \AA}$ and the continuum noise level is 1.0 \AA (i.e. right at the 1σ limit of our measurement), then the derived probability was $\Pi = 0.84$, i.e. we assigned a 16% ($\equiv 1\sigma$) probability that the system contained no disk.

Table A.1: Accretion

Name	Component	$W_{\text{Br}\gamma}^{\text{a}}$ [\AA]	$W_{\text{min}}^{\text{b}}$ [\AA]
[AD95] 1468	A	1.48 ± 0.49	1.47
	B	0.68 ± 0.56	1.62
[AD95] 2380	A	1.00 ± 0.19	0.65
	B	0.85 ± 1.12	3.51
JW 235	A	5.13 ± 0.47	1.21
	B	2.14 ± 0.54	1.59
JW 260	A	-2.11 ± 0.13	0.37
	B	-4.05 ± 0.15	0.48
JW 553	A	0.02 ± 0.14	0.44
	B	-0.26 ± 0.24	0.75
JW 566	A	0.63 ± 0.18	0.53
	B	0.45 ± 0.23	0.70
JW 598	A	-0.33 ± 0.10	0.34
	B	1.10 ± 0.66	2.06
JW 648	A	0.42 ± 0.17	0.49
	B	0.48 ± 0.31	0.84
JW 681	A	-0.38 ± 0.13	0.46
	B	0.94 ± 0.21	0.68
JW 687	A	0.09 ± 0.16	0.43
	B	-0.05 ± 0.16	0.51
JW 876	A	0.52 ± 0.18	0.54
	B	0.96 ± 0.18	0.51
JW 959	A	-1.48 ± 0.22	0.65
	B	-0.82 ± 0.25	0.76
[HC2000] 73	A	1.40 ± 0.14	0.41
	B	-0.10 ± 0.49	1.35
TCC 15	A	-0.79 ± 0.21	0.67
	B	16.69 ± 2.73	5.44
TCC 52	A	1.51 ± 0.10	0.28

Table A.1: continued.

Name	Component	$W_{\text{Bry}}^{\text{a}}$ [Å]	$W_{\text{min}}^{\text{b}}$ [Å]
	B	1.14 ± 0.14	0.40
TCC 55	A	-0.14 ± 0.20	0.63
	B	-0.24 ± 0.23	0.68
JW 63	A	-0.04 ± 0.34	1.02
	B	0.61 ± 0.43	1.17
JW 128	A	0.53 ± 0.49	1.28
	B	0.64 ± 0.49	1.28
JW 176	A	0.34 ± 0.47	1.26
	B	0.22 ± 0.58	1.47
JW 391	A	7.87 ± 0.26	0.69
	B	1.41 ± 0.48	1.32
JW 709	A	-0.16 ± 0.36	1.01
	B	0.42 ± 0.35	0.97
JW 867	A	0.91 ± 0.27	0.69
	B	2.37 ± 0.29	0.77

^a The equivalent width as measured in our spectra. No correction for veiling was applied, since W_{min} and W_{Bry} scale the same with veiling.

^b Equivalent width equivalent to $3\times$ continuum noise level around Bry. This is the assumed detection limit for significant Bry emission.

With this knowledge, we were able to derive $p_n(k|D)$, i.e. the probabilities of finding k disks in a set of n targets. We defined pairs $\{1 - \Pi_i, \Pi_i\}$ of the probabilities of finding “no disk” or “one disk” around a particular target i . The $p_n(k|D)$ were then derived by convolution (zero padded at the edges) of all $\{1 - \Pi_i, \Pi_i\}$

$$p_n(k|D) \in \{1 - \Pi_0, \Pi_0\} * \{1 - \Pi_1, \Pi_1\} * \dots * \{1 - \Pi_n, \Pi_n\} \quad . \quad (\text{A.6})$$

For illustrative purposes, the probabilities of finding 0, 1, or n disks in a sample of n was

$$p_n(0|D) = (1 - \Pi_0)(1 - \Pi_1) \dots (1 - \Pi_n) = \prod_{j=0}^n (1 - \Pi_j) \quad , \quad (\text{A.7})$$

$$p_n(1|D) = \sum_{l=0}^n \left\{ \prod_{j \neq l} (1 - \Pi_j) \cdot \Pi_l \right\} \quad , \quad (\text{A.8})$$

$$p_n(n|D) = \prod_{j=0}^n \Pi_j \quad . \quad (\text{A.9})$$

Other $p_n(k|D)$ could take more complicated forms.

A.1.3 Application to the ONC

For all calculations, we assumed that $n = 42$, which is equal to the number of target components excluding JW 260 (see Sect. 3.3.2). The individual Π_j were calculated from our Br γ measurements in Tab. A.1. The final probability density was derived from (A.2) and is depicted in Fig. A.1.

We found a best fit value of $F = 35_{-8}^{+9}\%$ for the disk frequency in the ONC binaries. The uncertainties of F are defined by the 16% ($\equiv 1\sigma$) wings of the distribution.

Appendix B

Best-fit spectral templates

B.1 ONC K-band spectra and best-fit templates

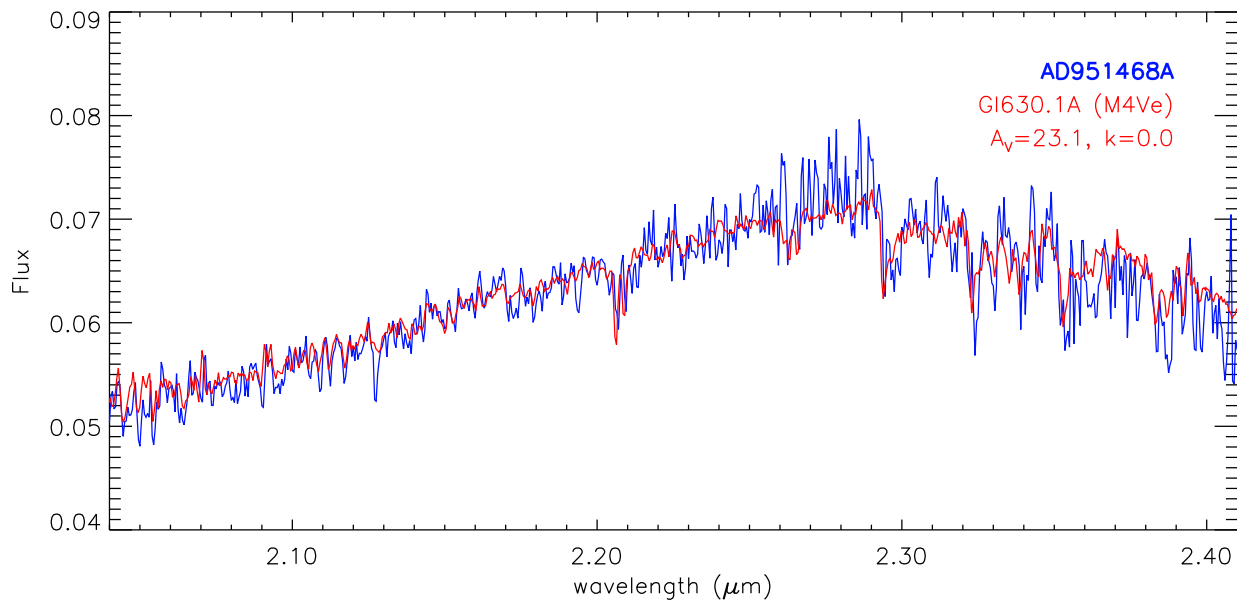


Figure B.1: The following pages present target spectra (blue) and best-fitting dwarf templates (red) for all individual component spectra of the ONC sample where spectral fitting could be accomplished. The used template spectra from the IRTF spectral library and their spectral type are indicated in the top-right of each sub-panel together with the applied modifications from the spectroscopically determined extinction and veiling.

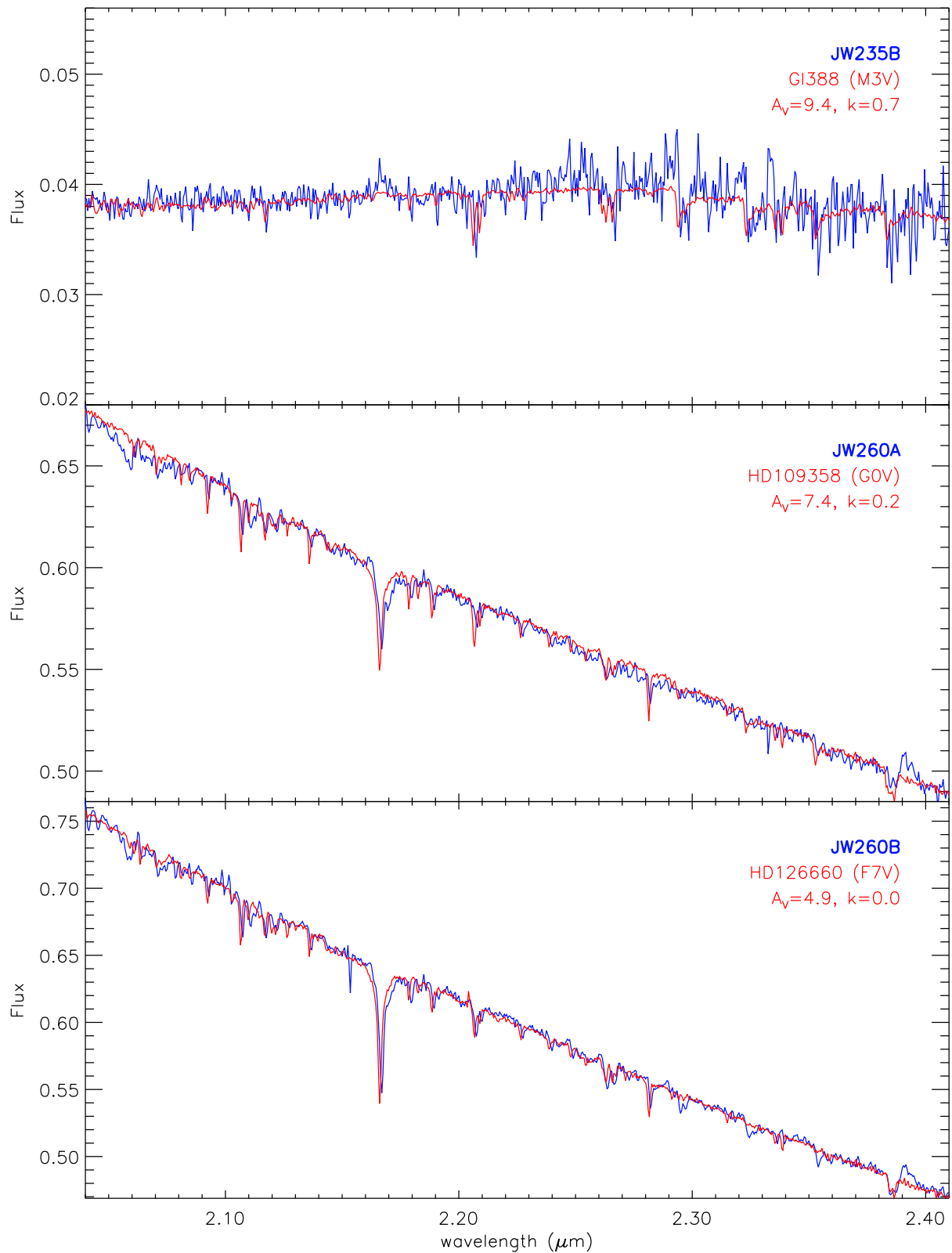


Figure B.1: (ctd.)

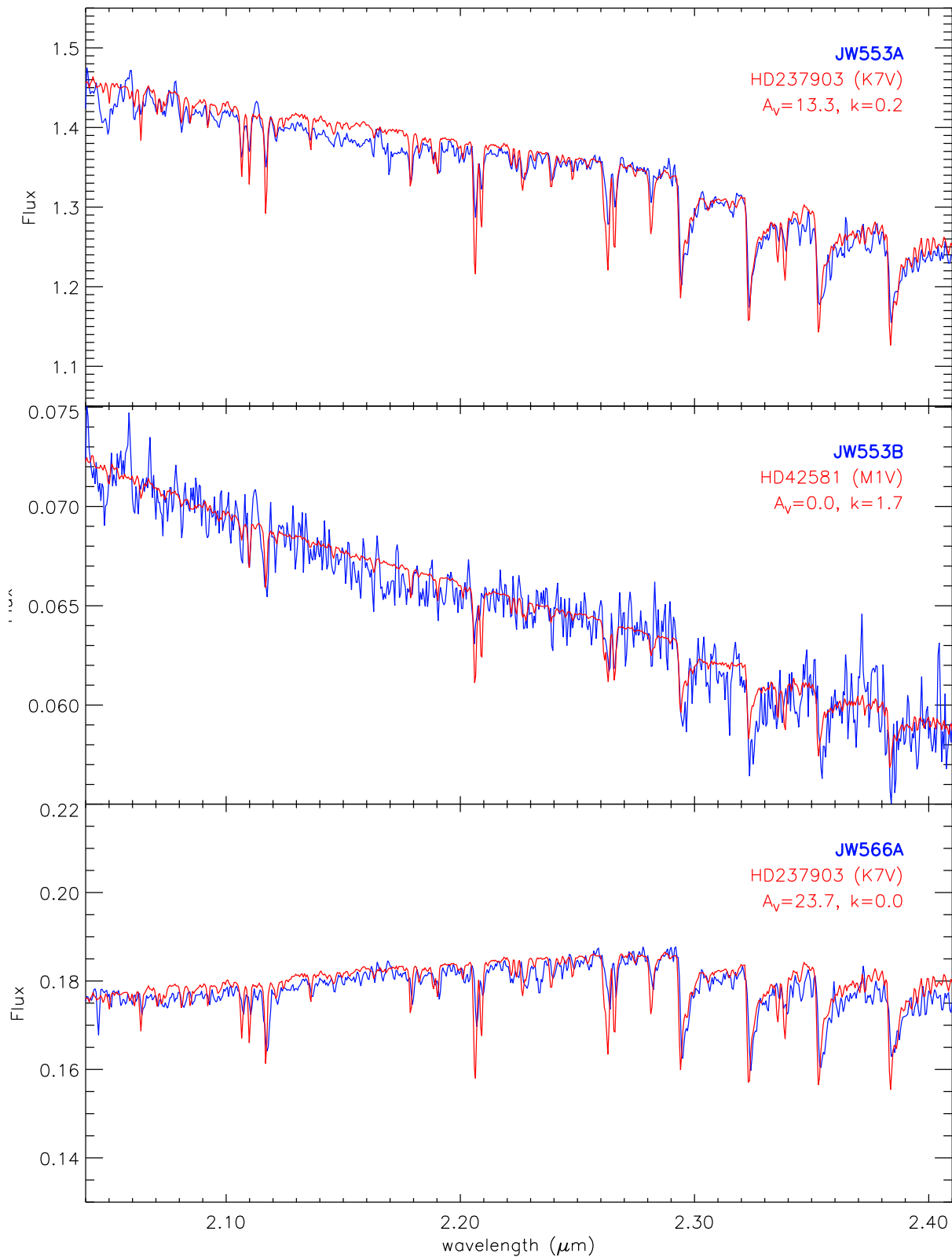


Figure B.1: (ctd.)

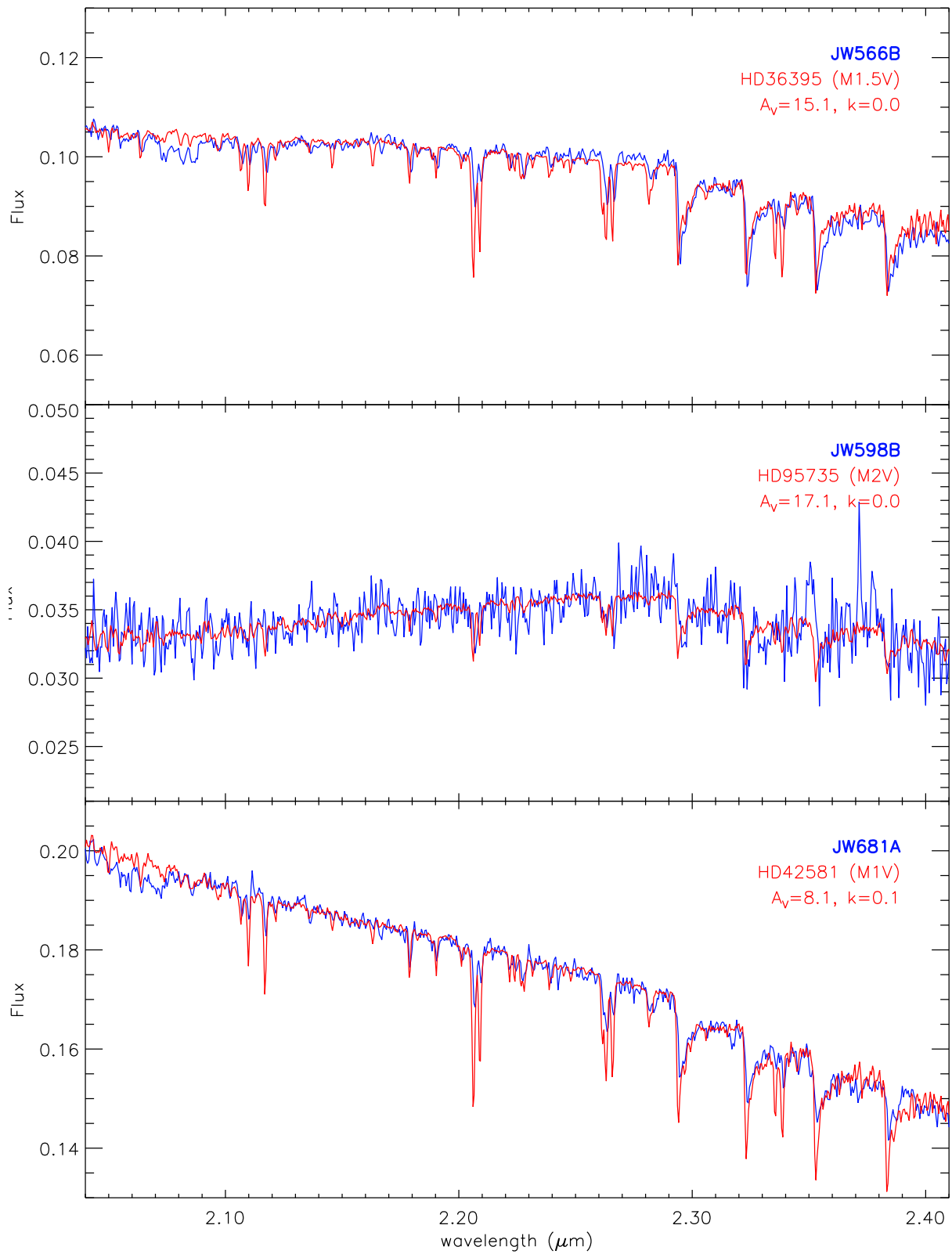


Figure B.1: (ctd.)

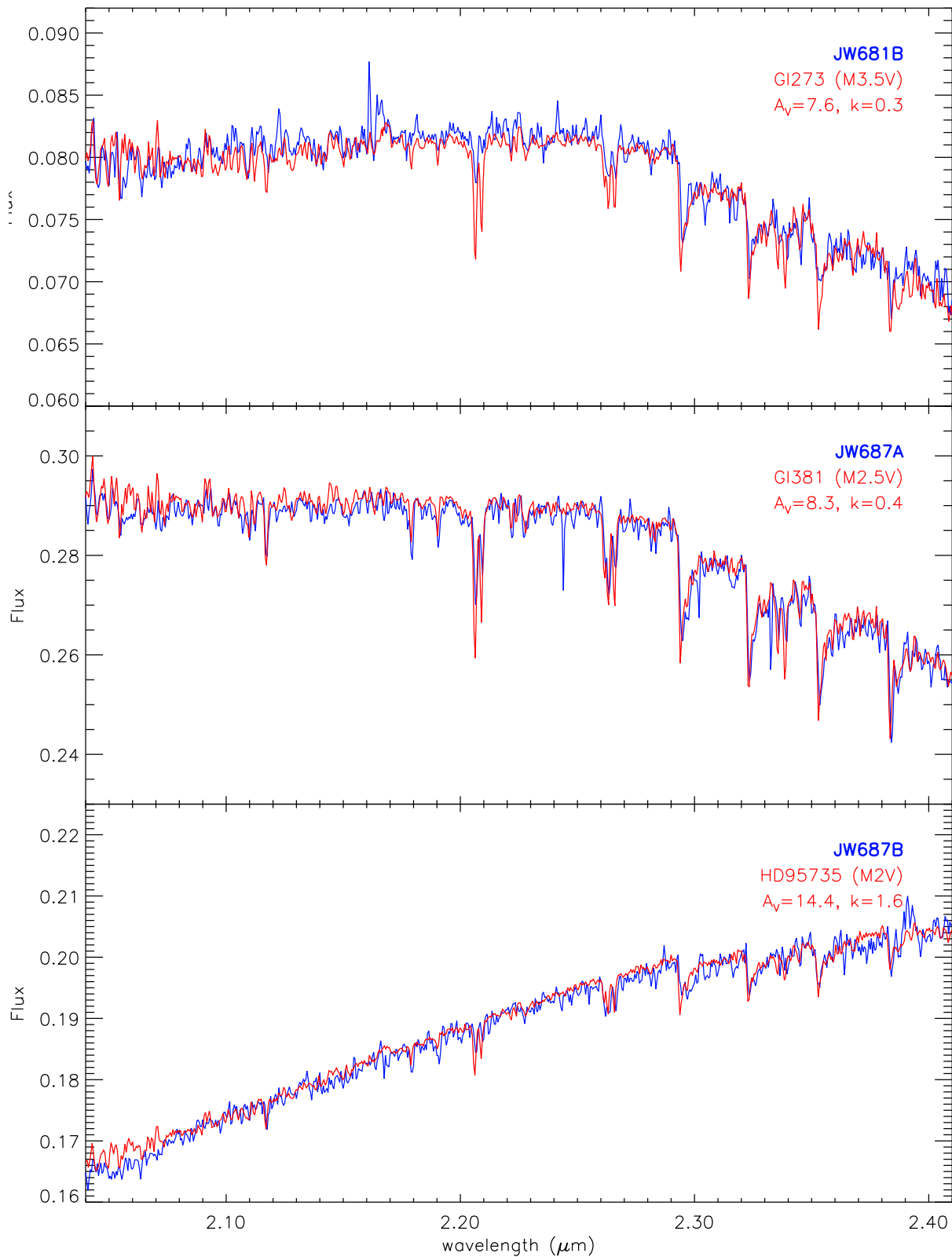


Figure B.1: (ctd.)

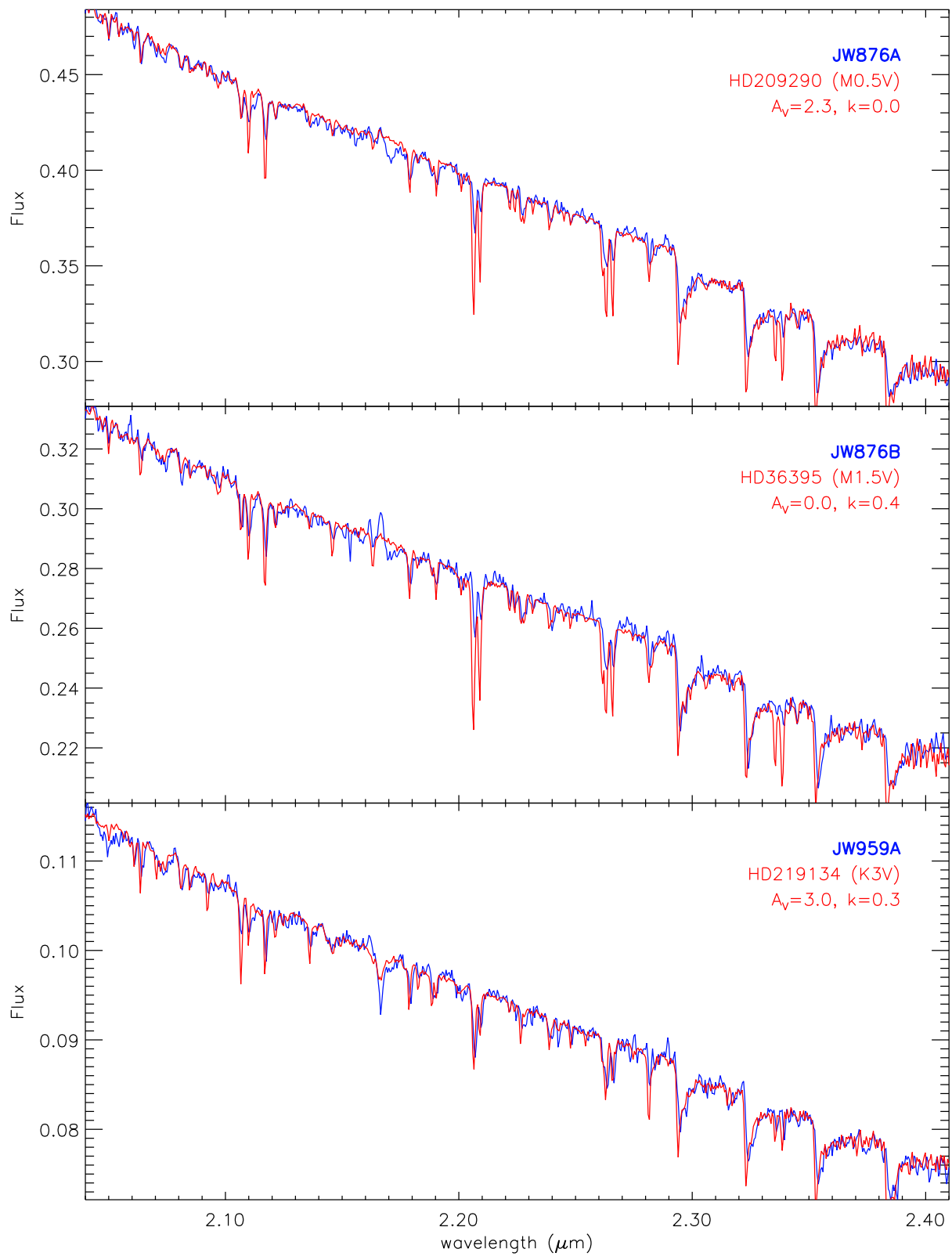


Figure B.1: (ctd.)

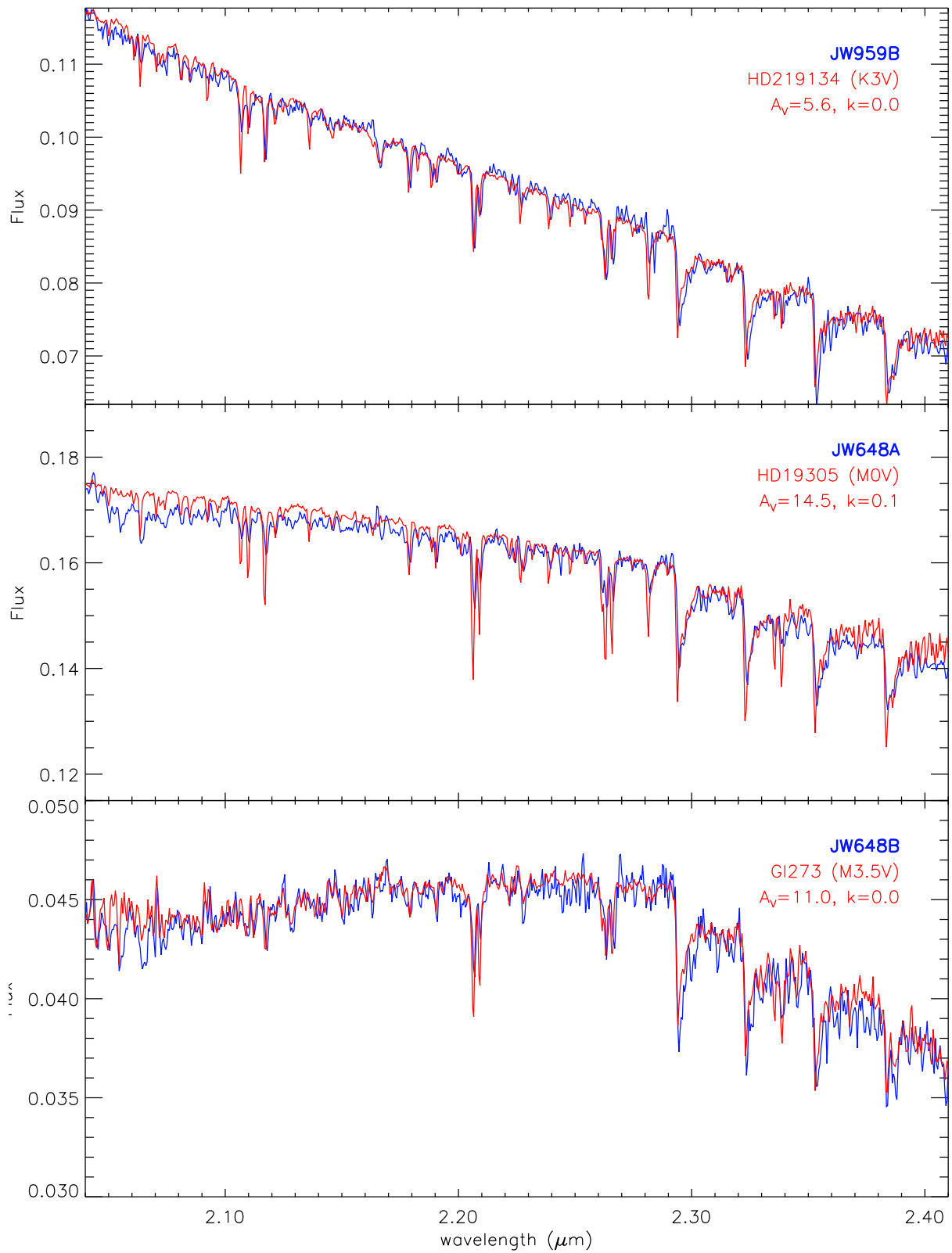


Figure B.1: (ctd.)

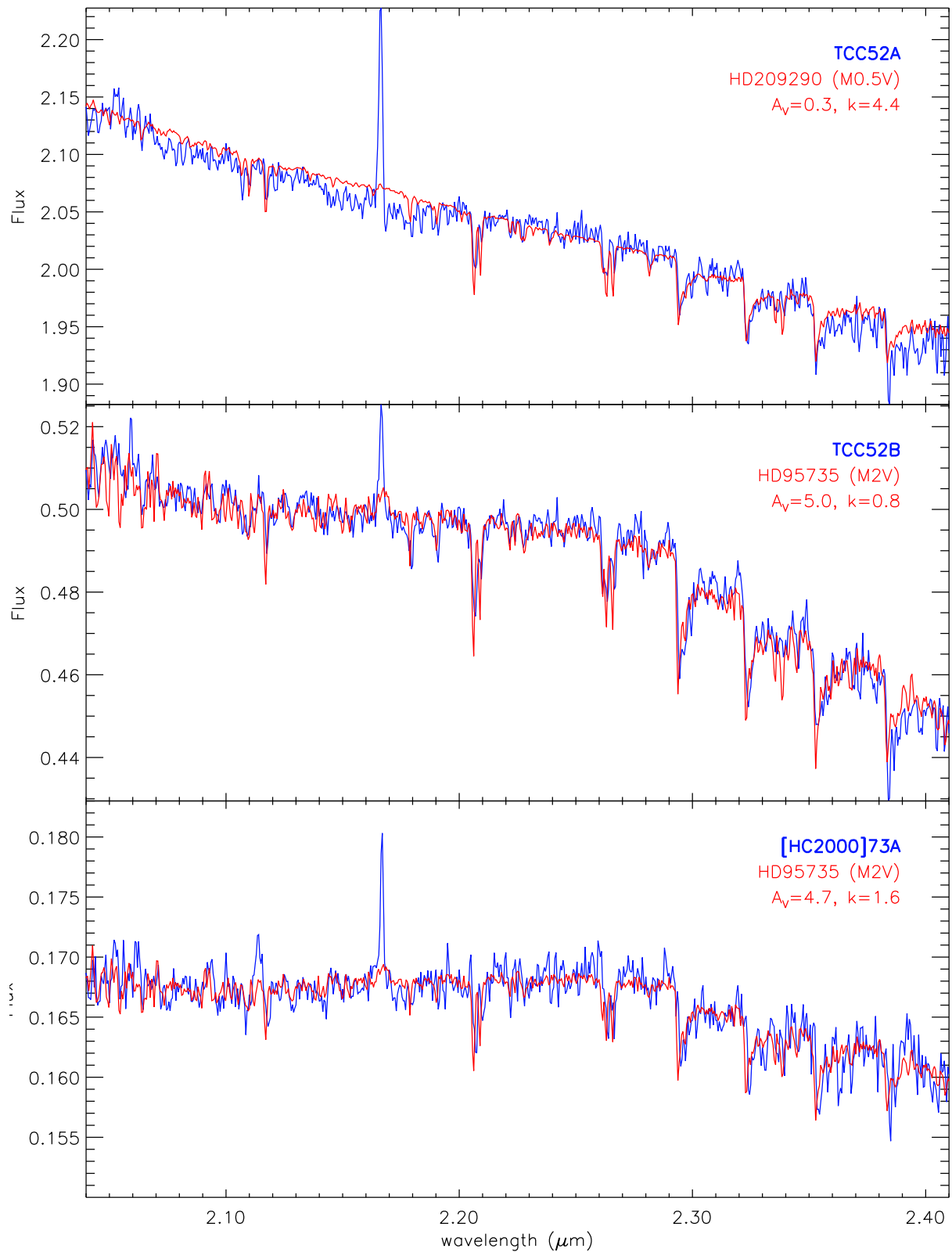


Figure B.1: (ctd.)

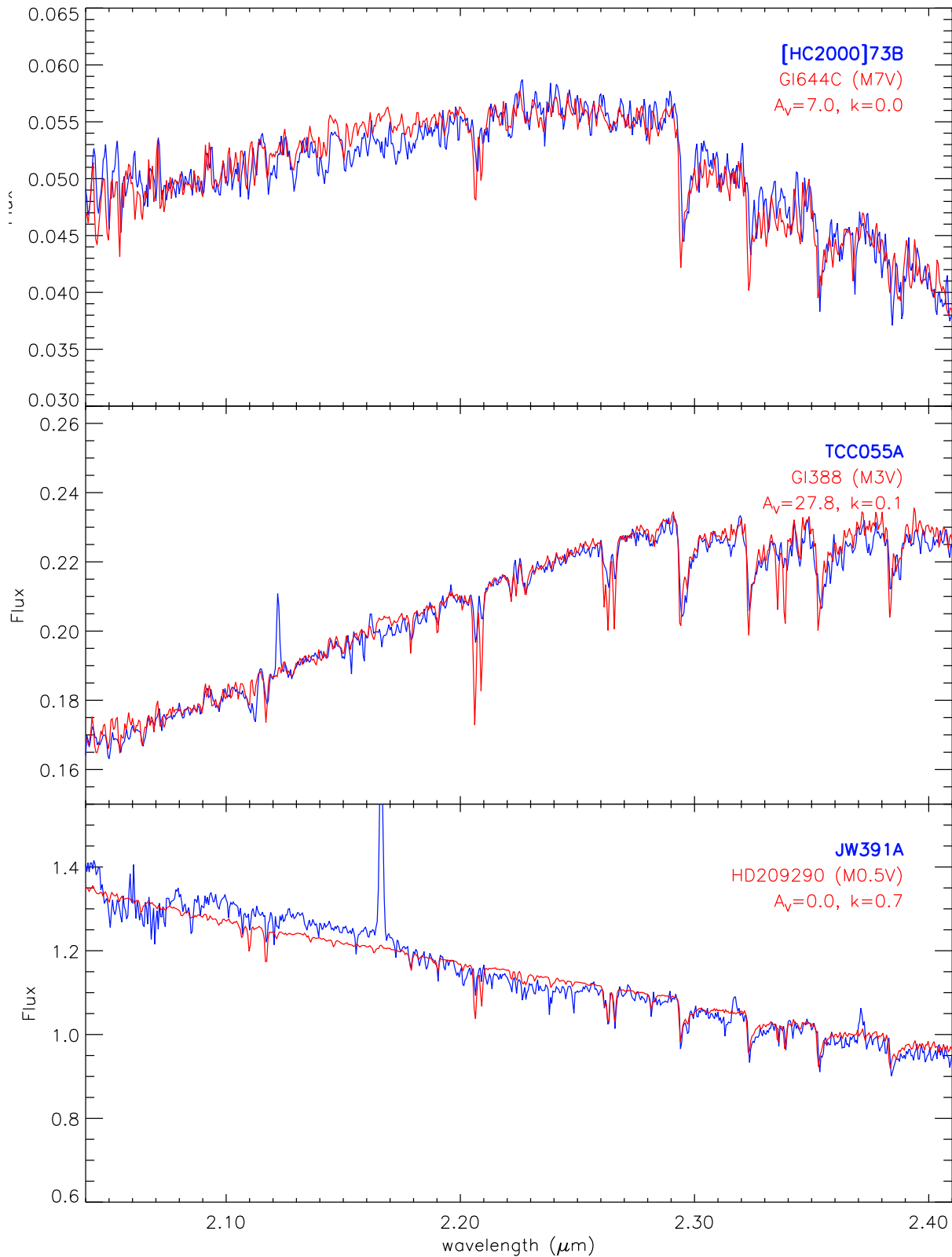


Figure B.1: (ctd.)

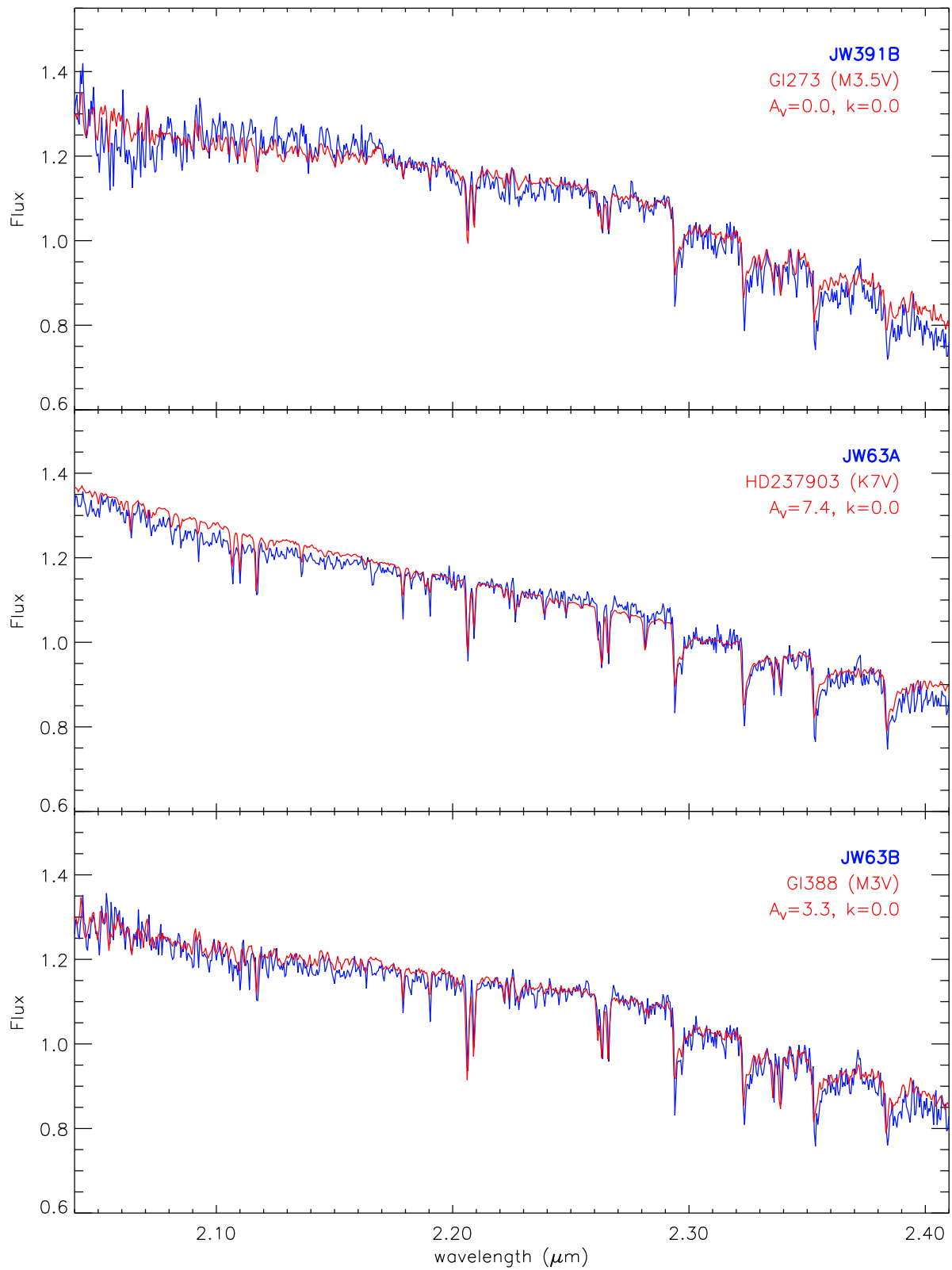


Figure B.1: (ctd.)

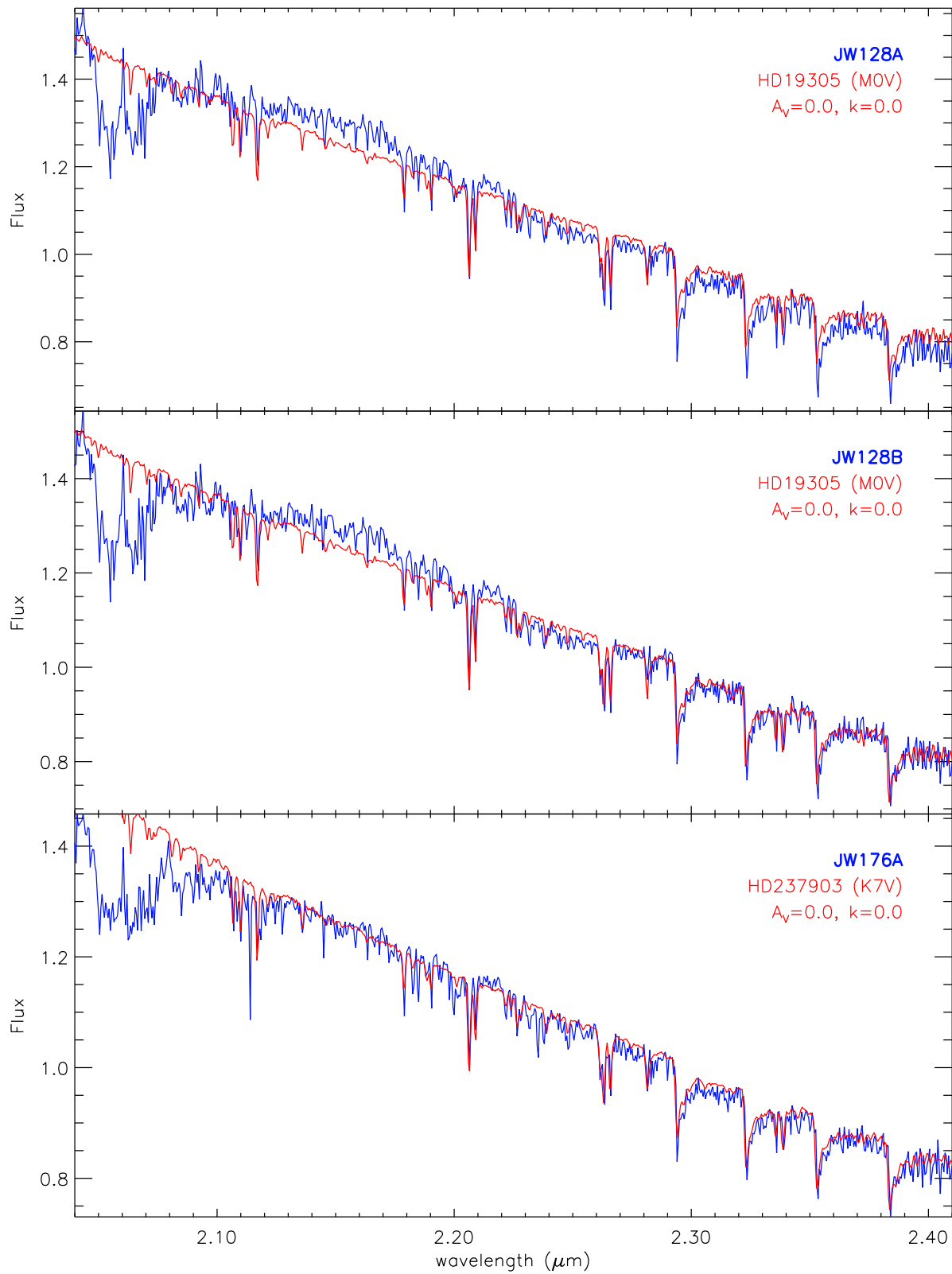


Figure B.1: (ctd.)

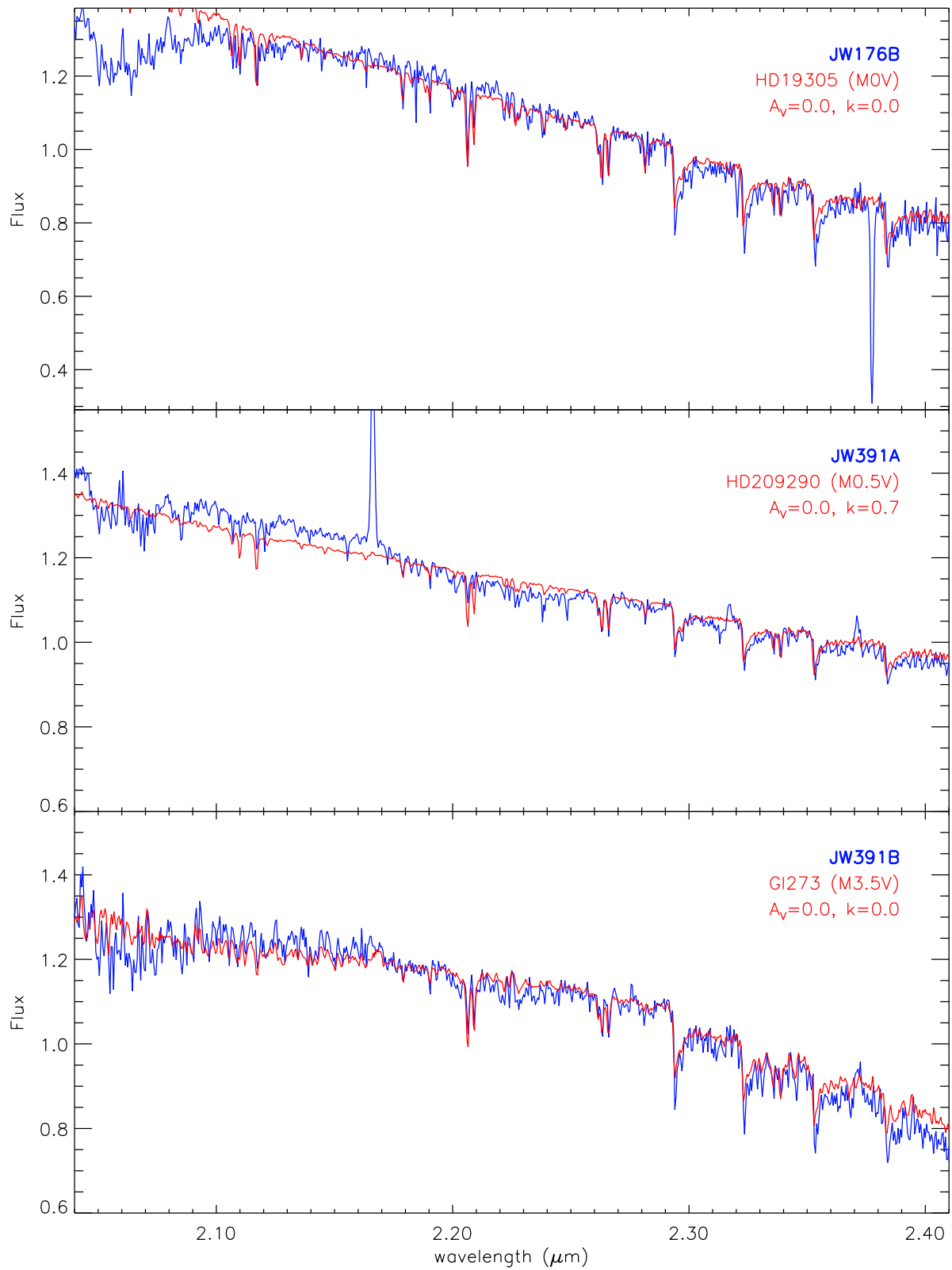


Figure B.1: (ctd.)

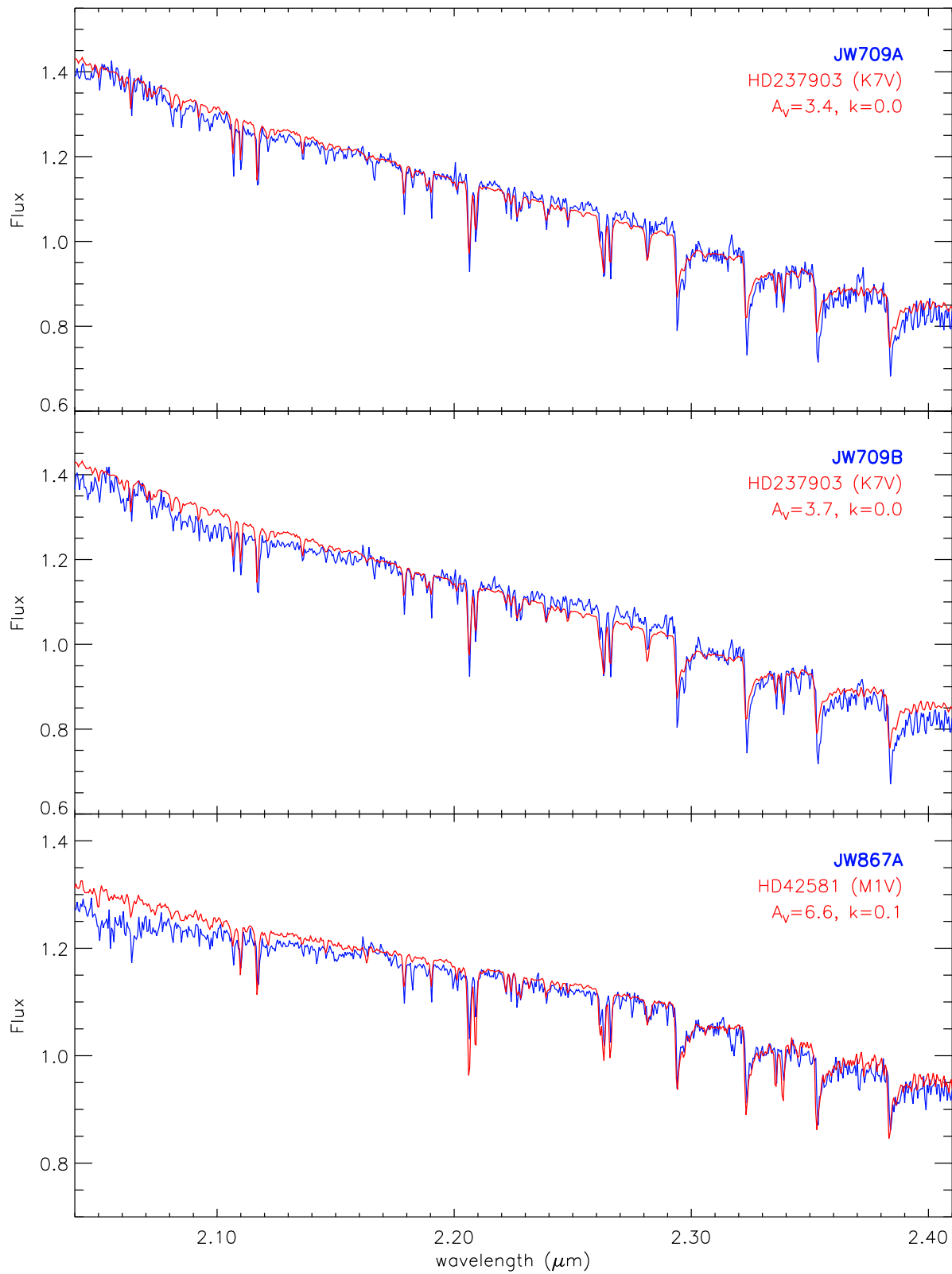


Figure B.1: (ctd.)

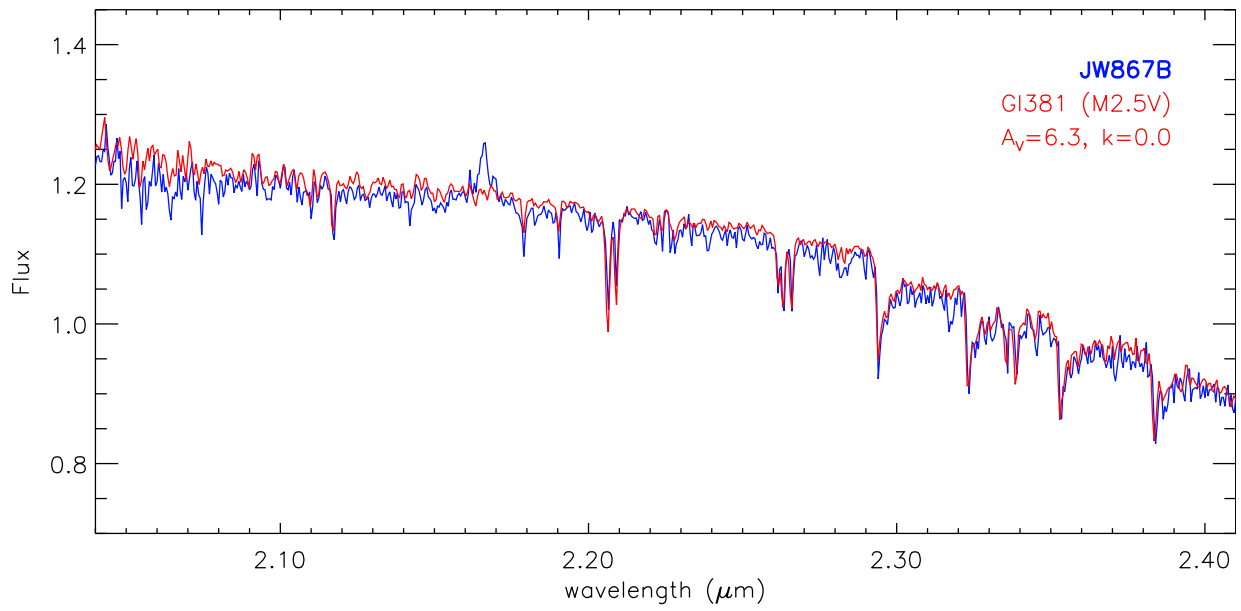


Figure B.1: (ctd.)

B.2 Best spectral template fits for all Cha I spectra

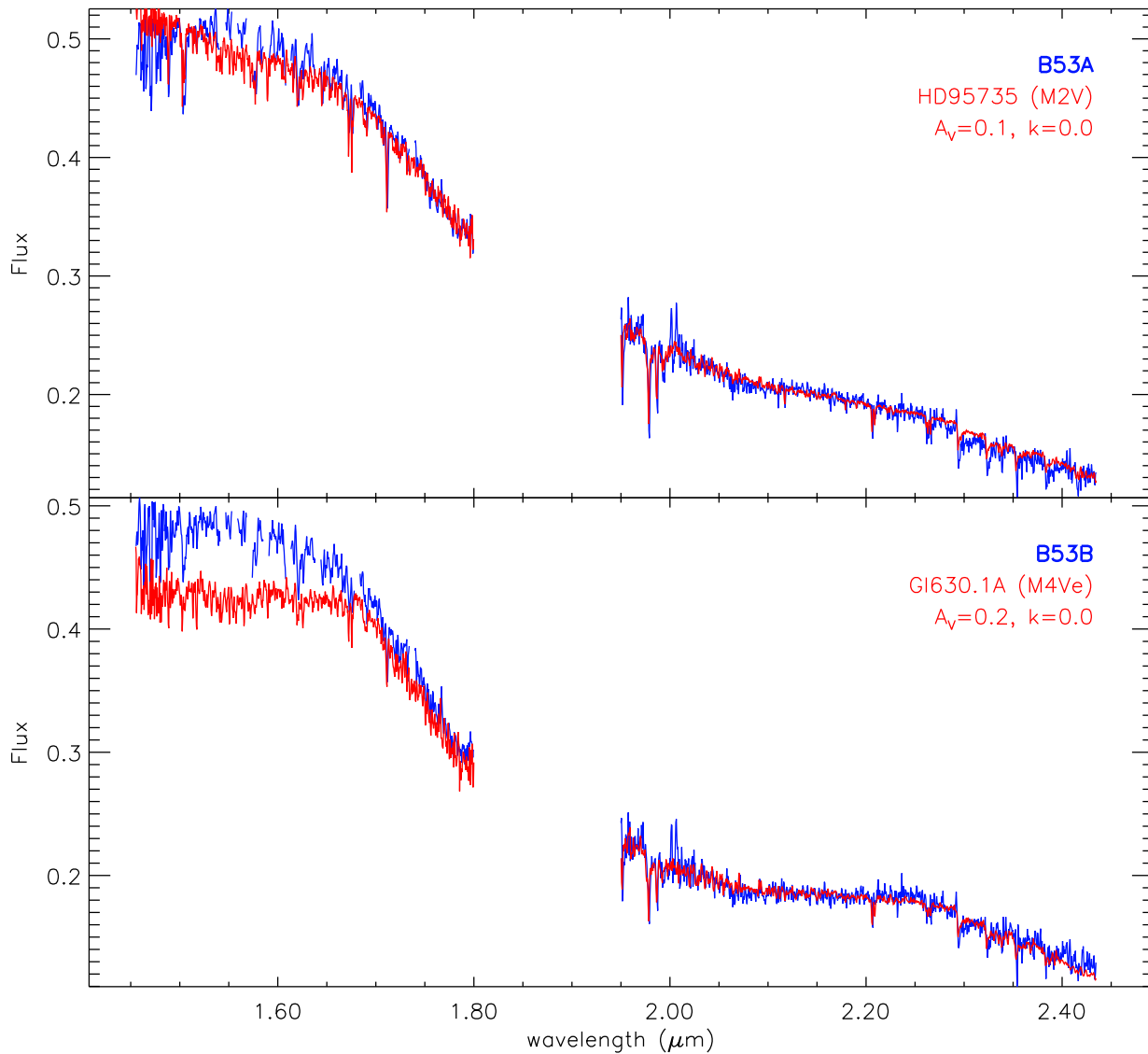


Figure B.2: Target spectra (blue) and best-fitting dwarf templates (red) for all individual component spectra of the Cha I sample where spectral fitting could be accomplished. The used template spectra from the IRTF spectral library and their spectral type are indicated in the top-right of each sub-panel together with the applied modifications in extinction and veiling.

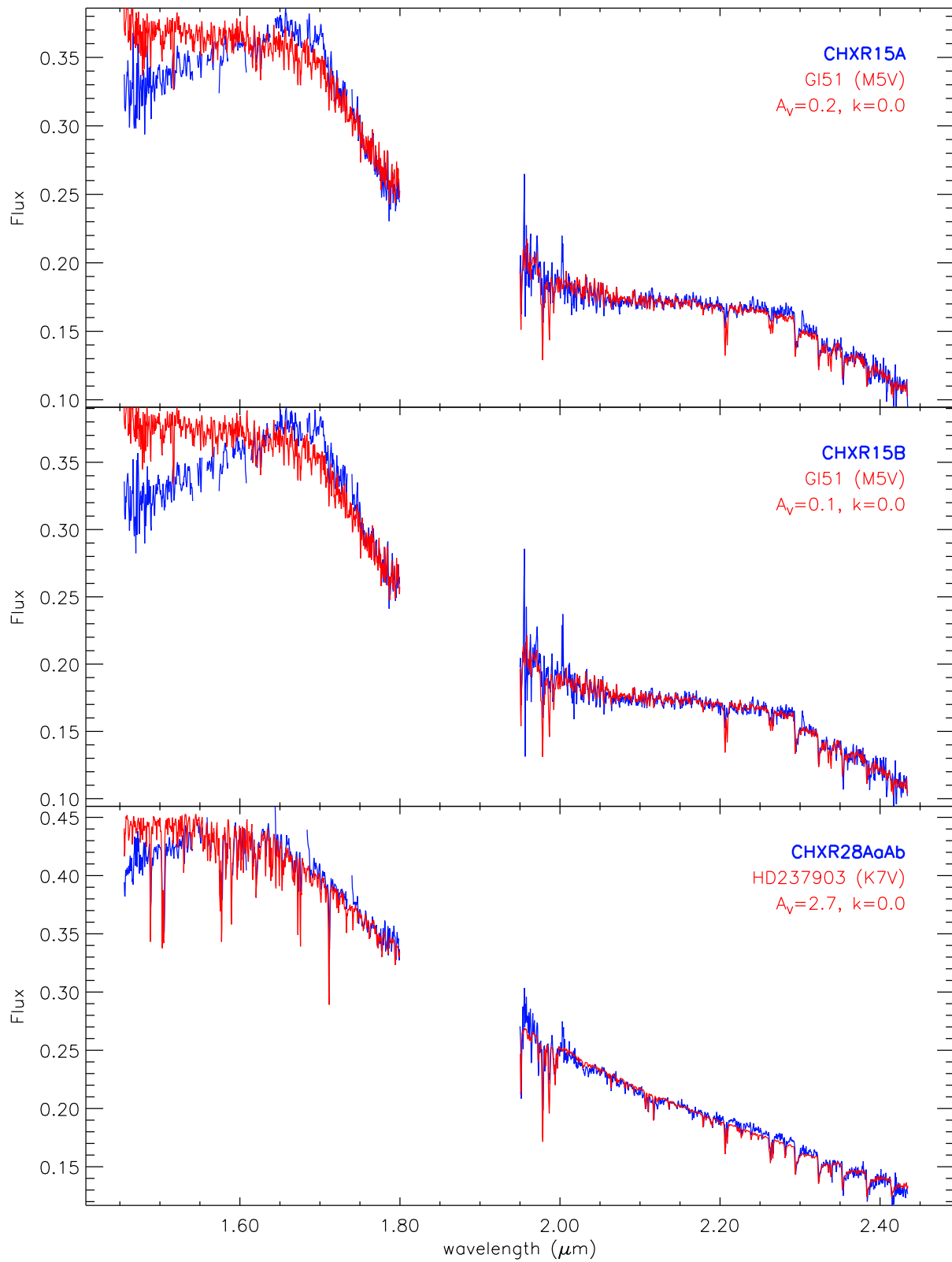


Figure B.2: (ctd.)

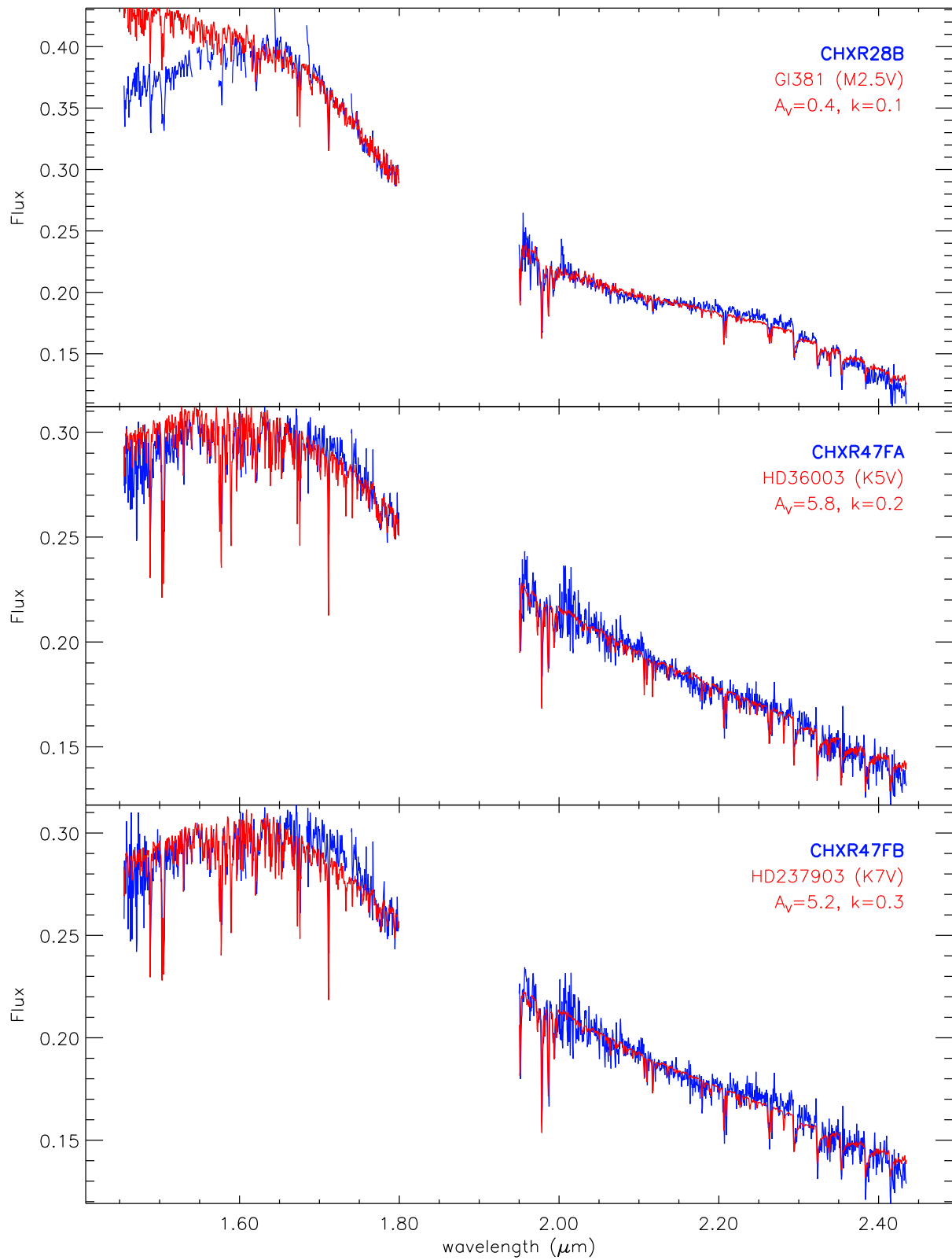


Figure B.2: (ctd.)

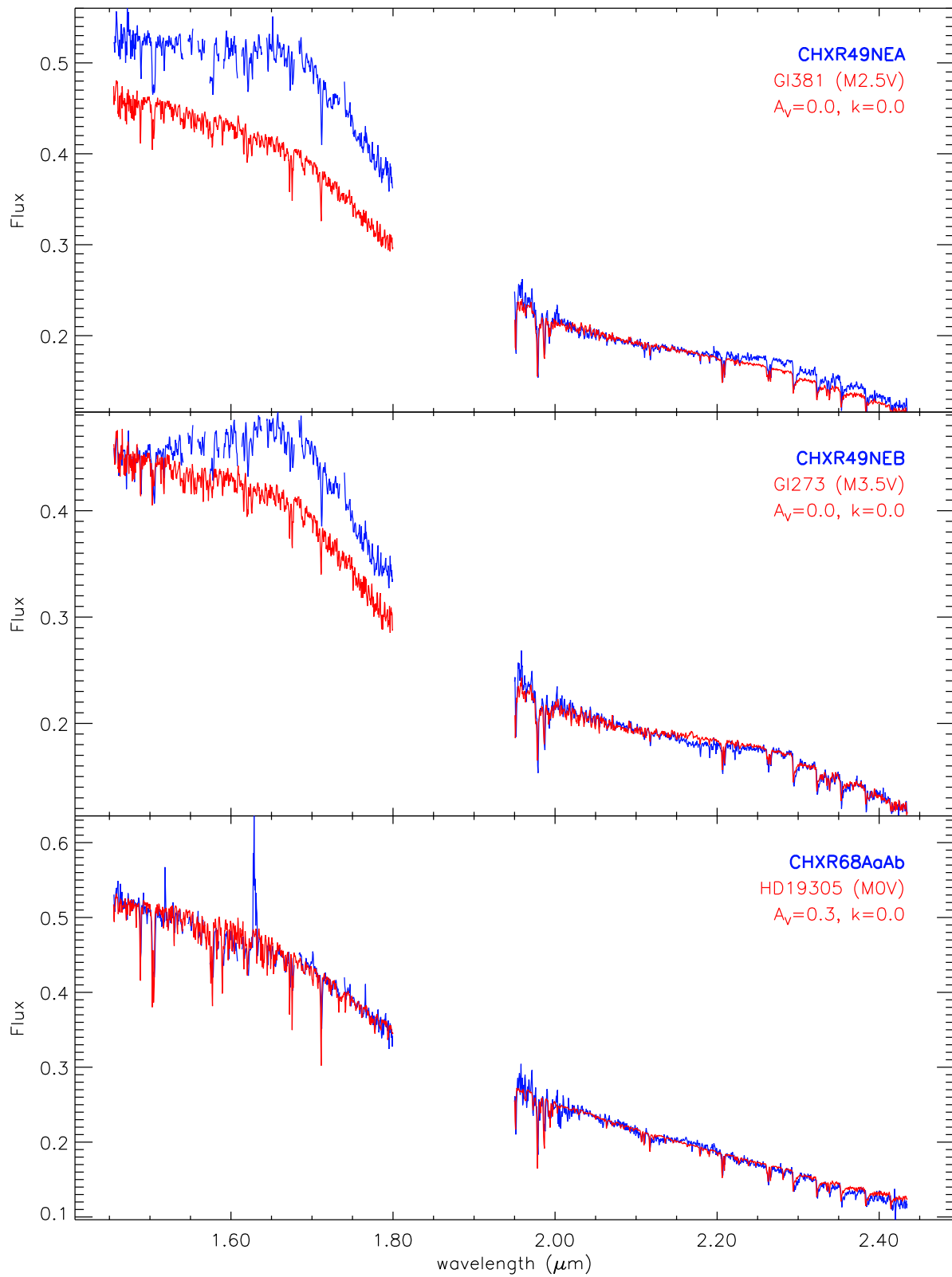


Figure B.2: (ctd.)

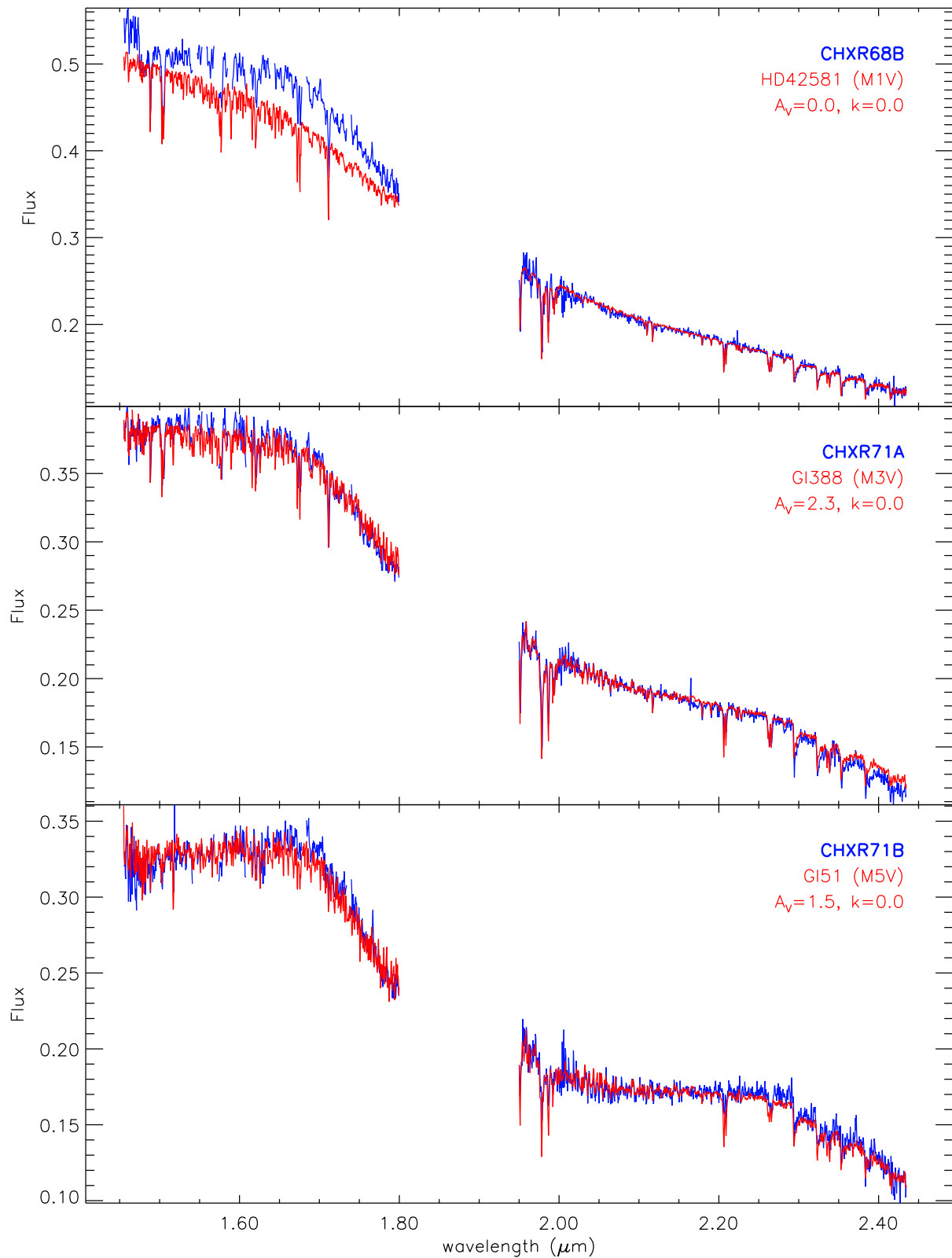


Figure B.2: (ctd.)

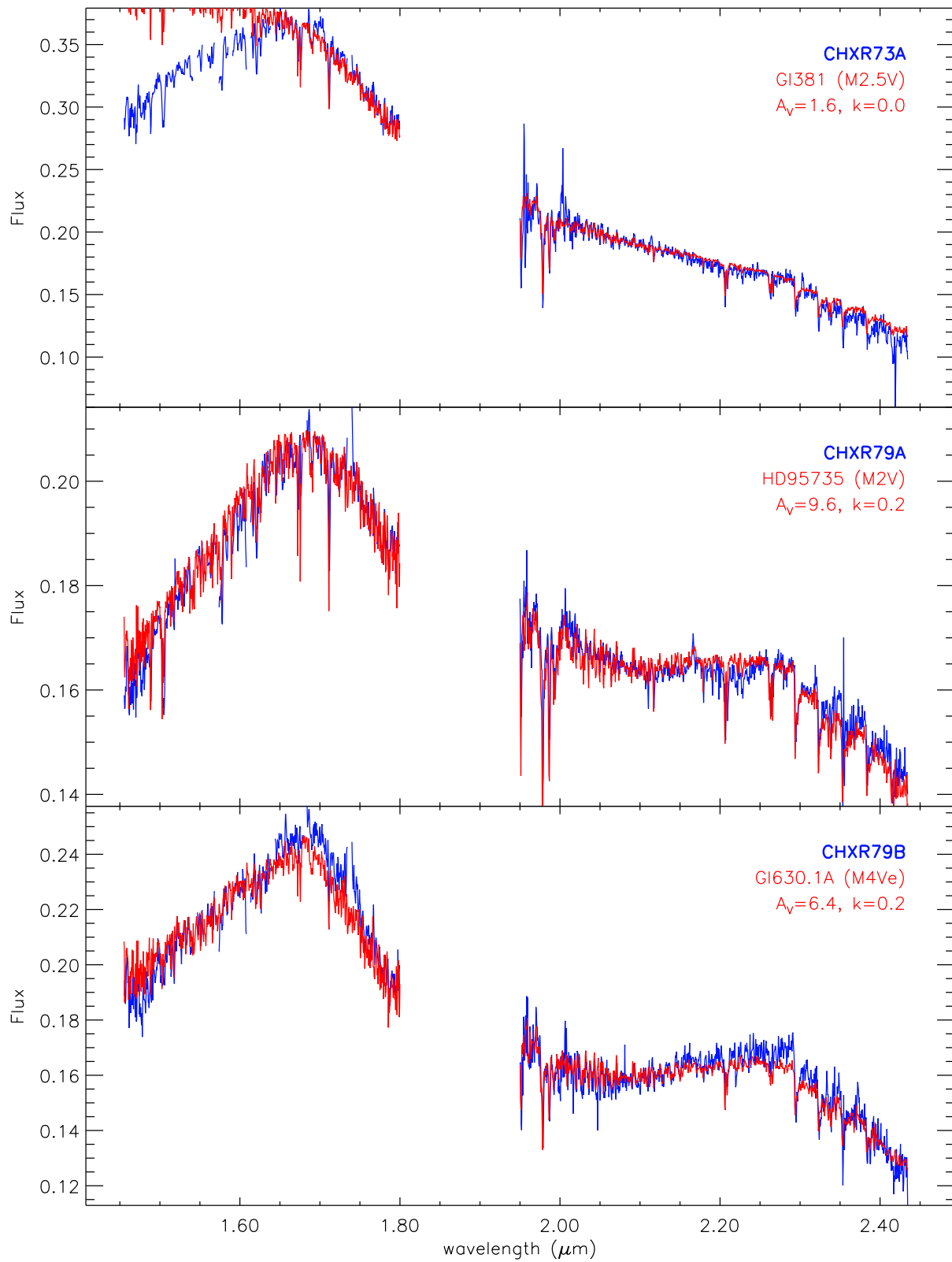


Figure B.2: (ctd.)

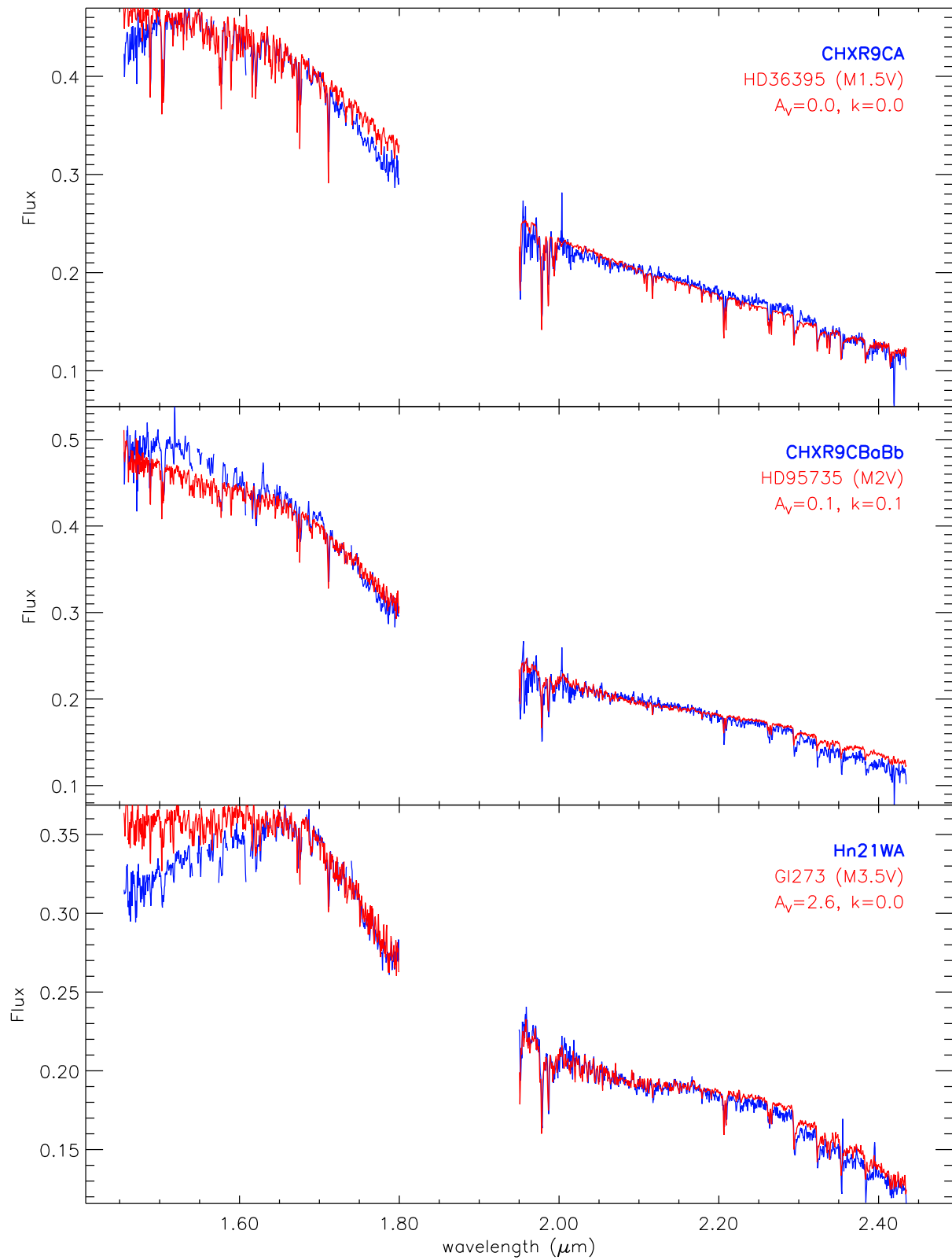


Figure B.2: (ctd.)

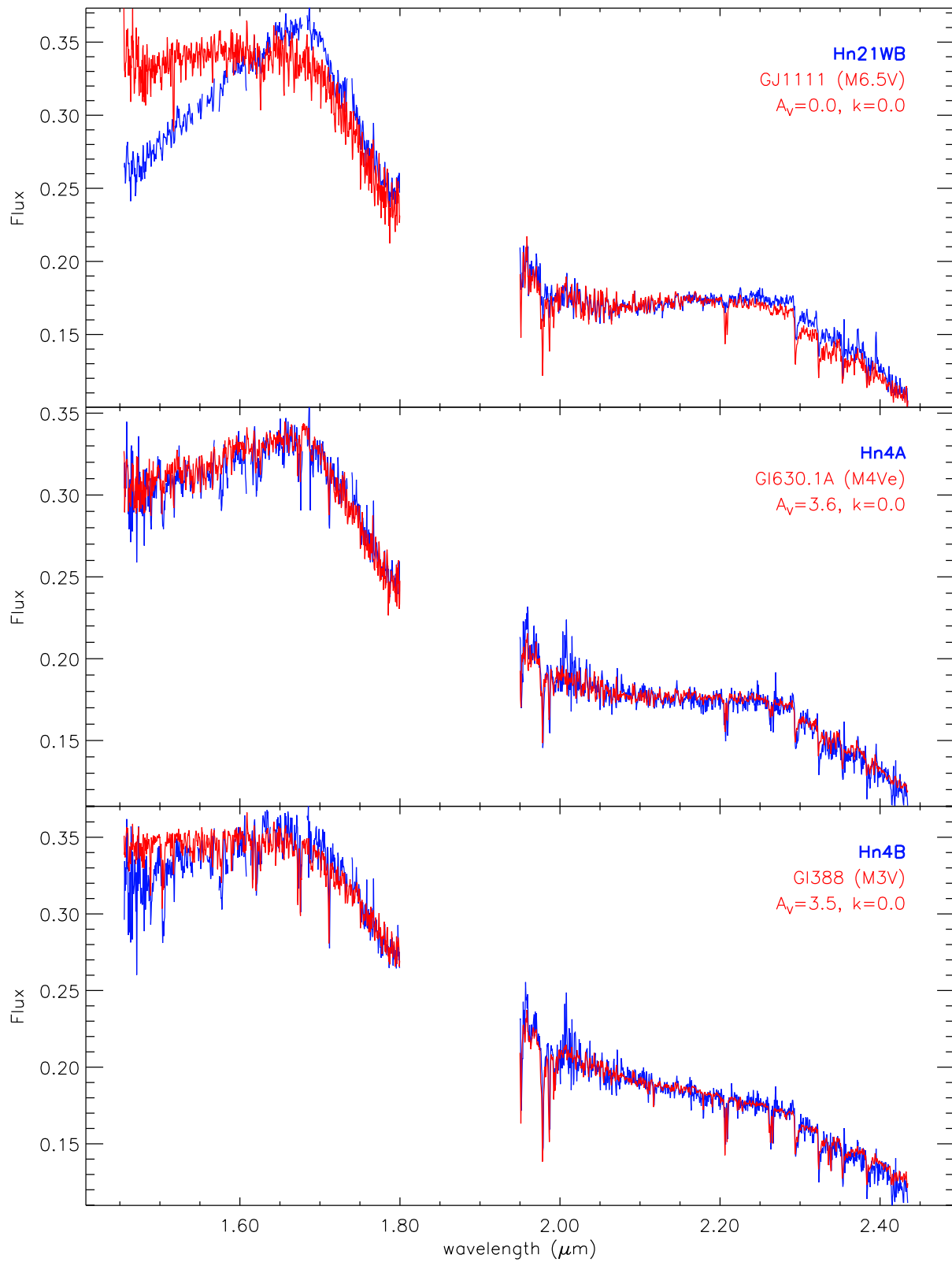


Figure B.2: (ctd.)

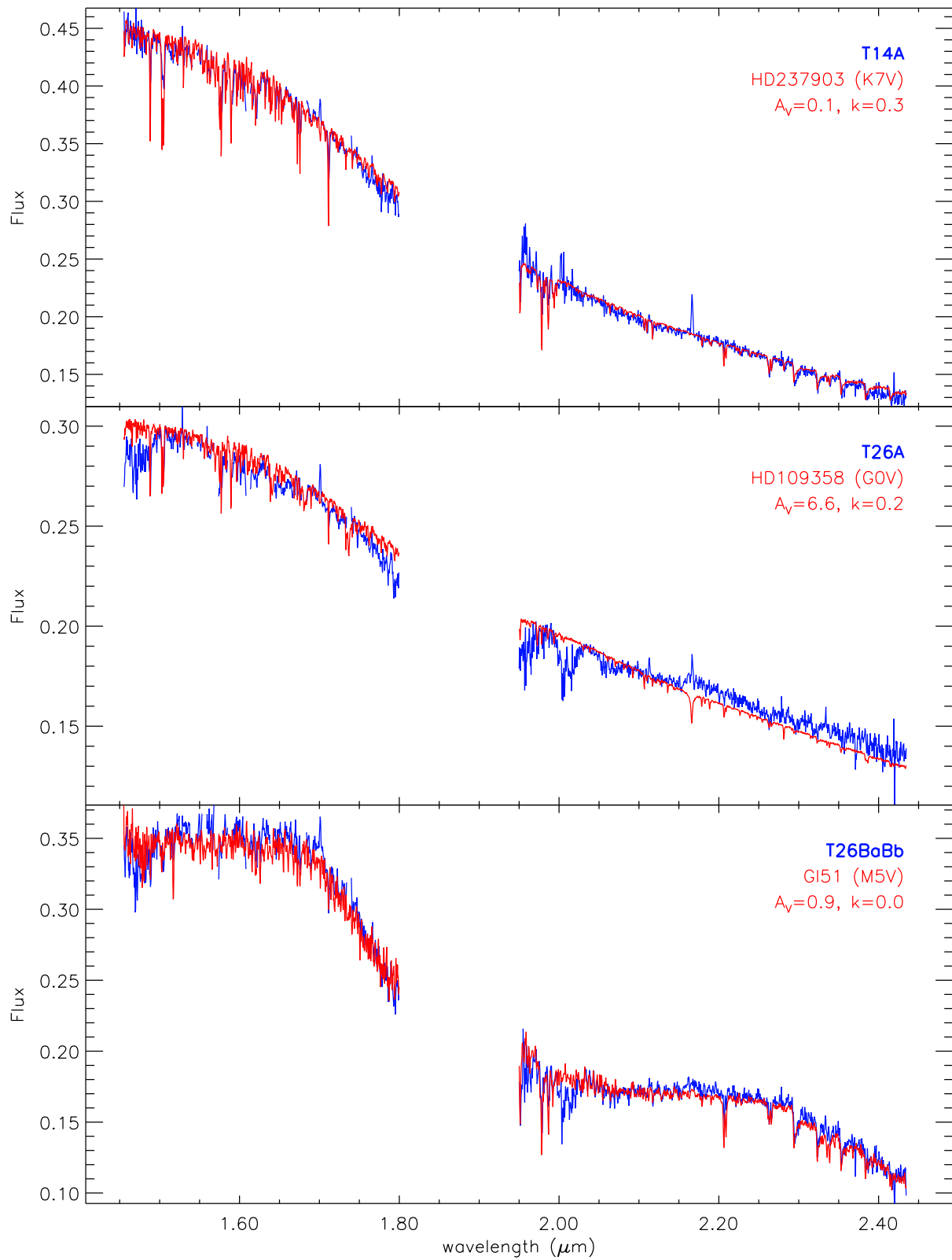


Figure B.2: (ctd.)

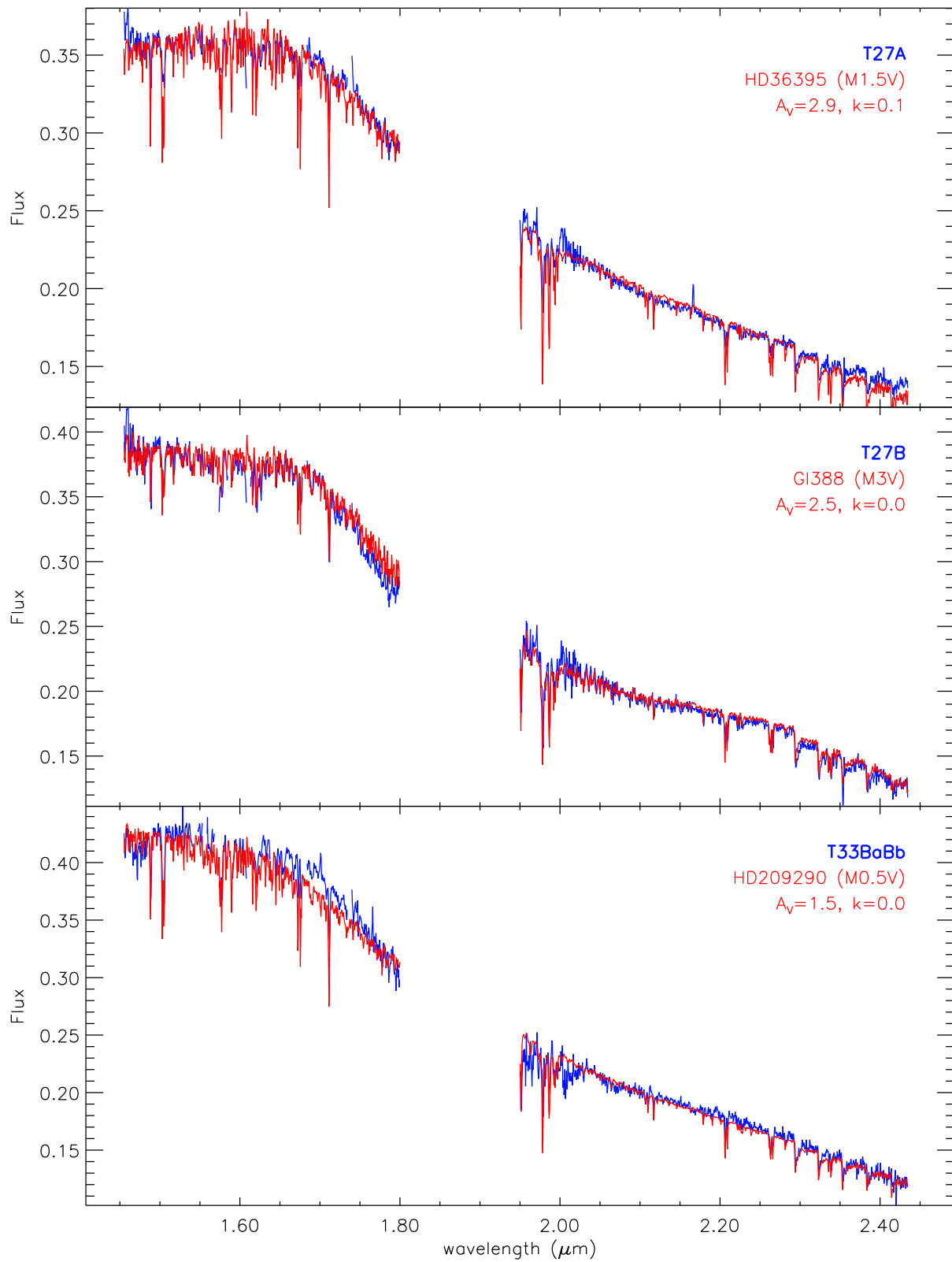


Figure B.2: (ctd.)

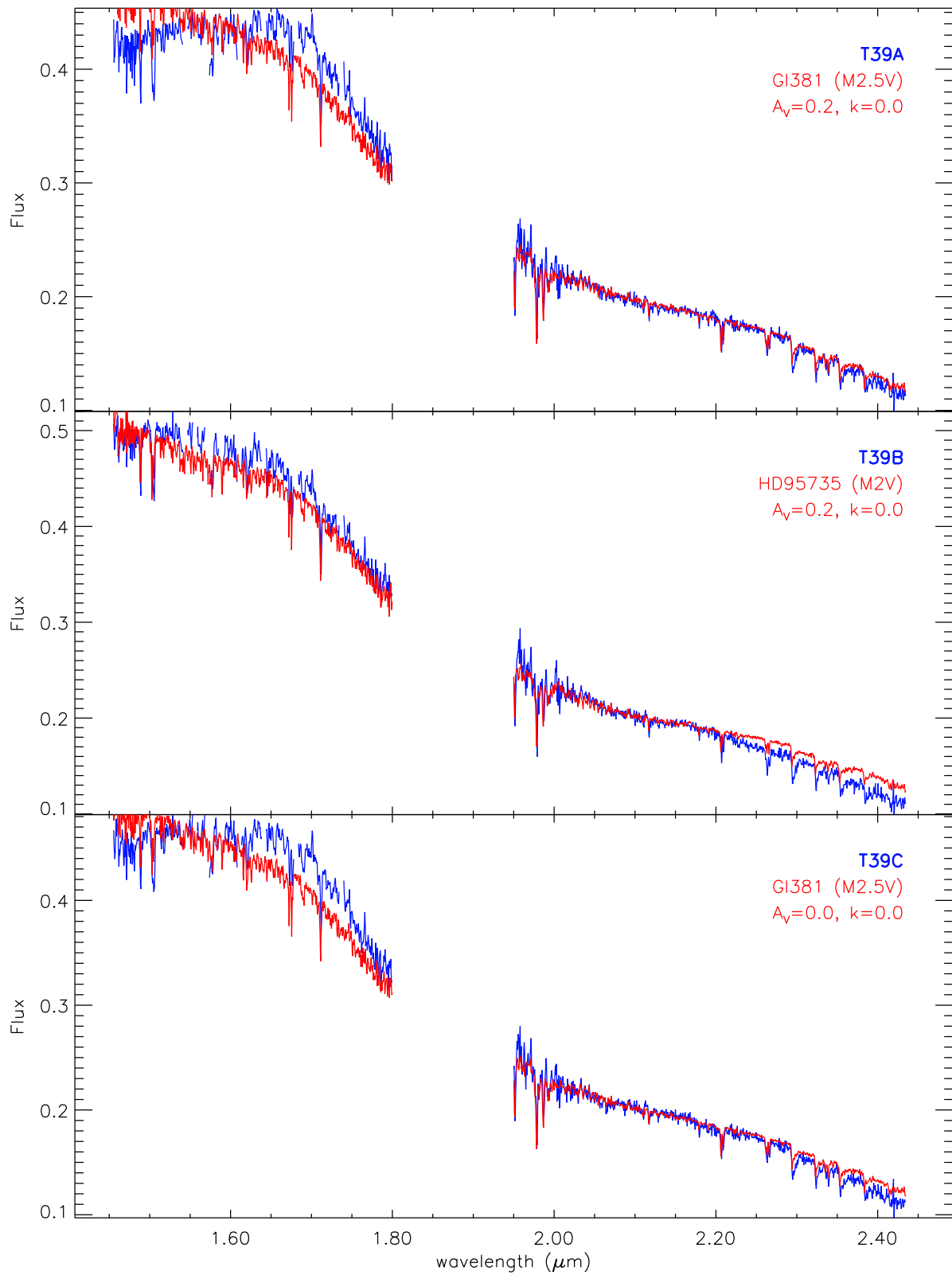


Figure B.2: (ctd.)

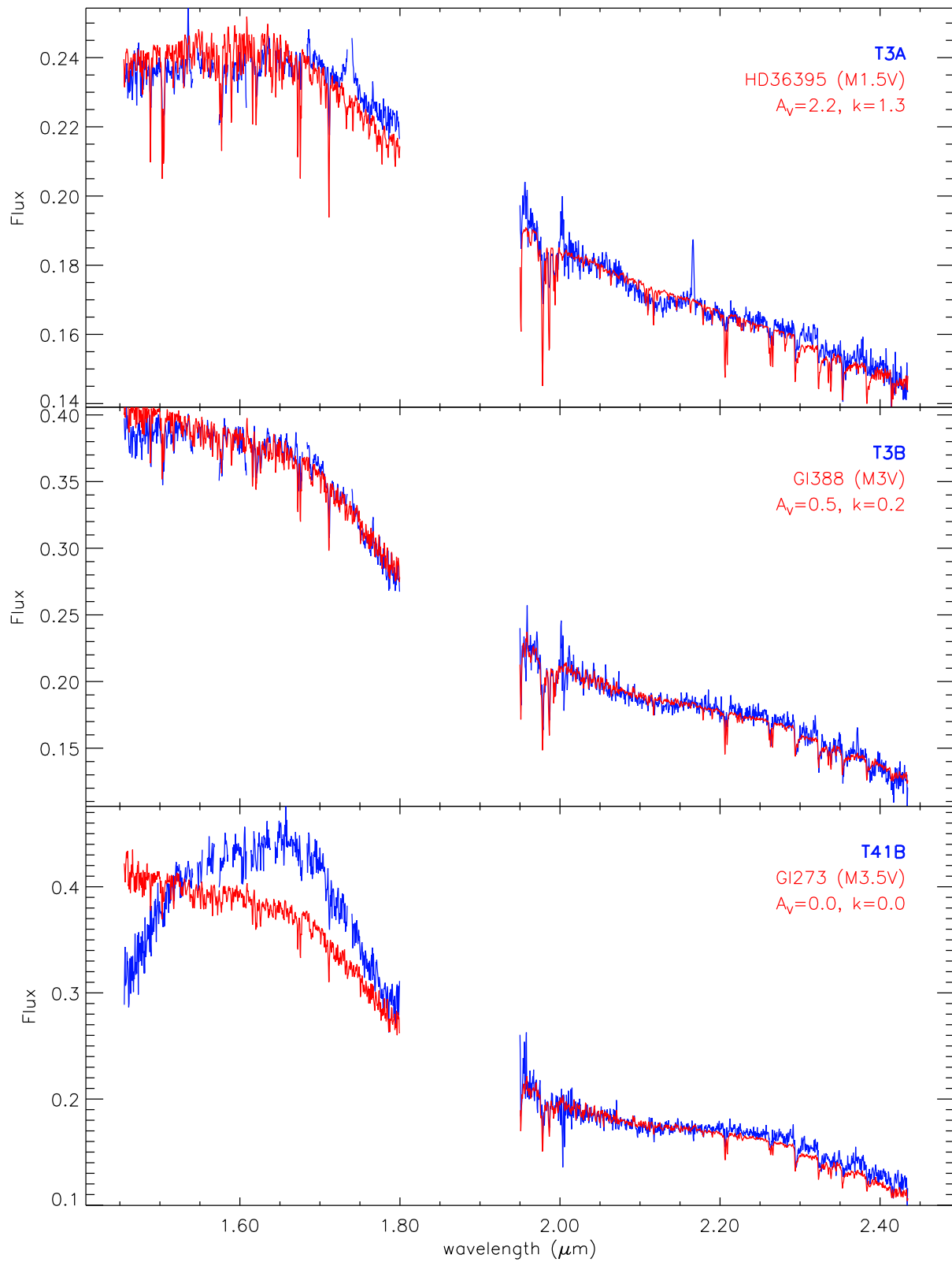


Figure B.2: (ctd.)

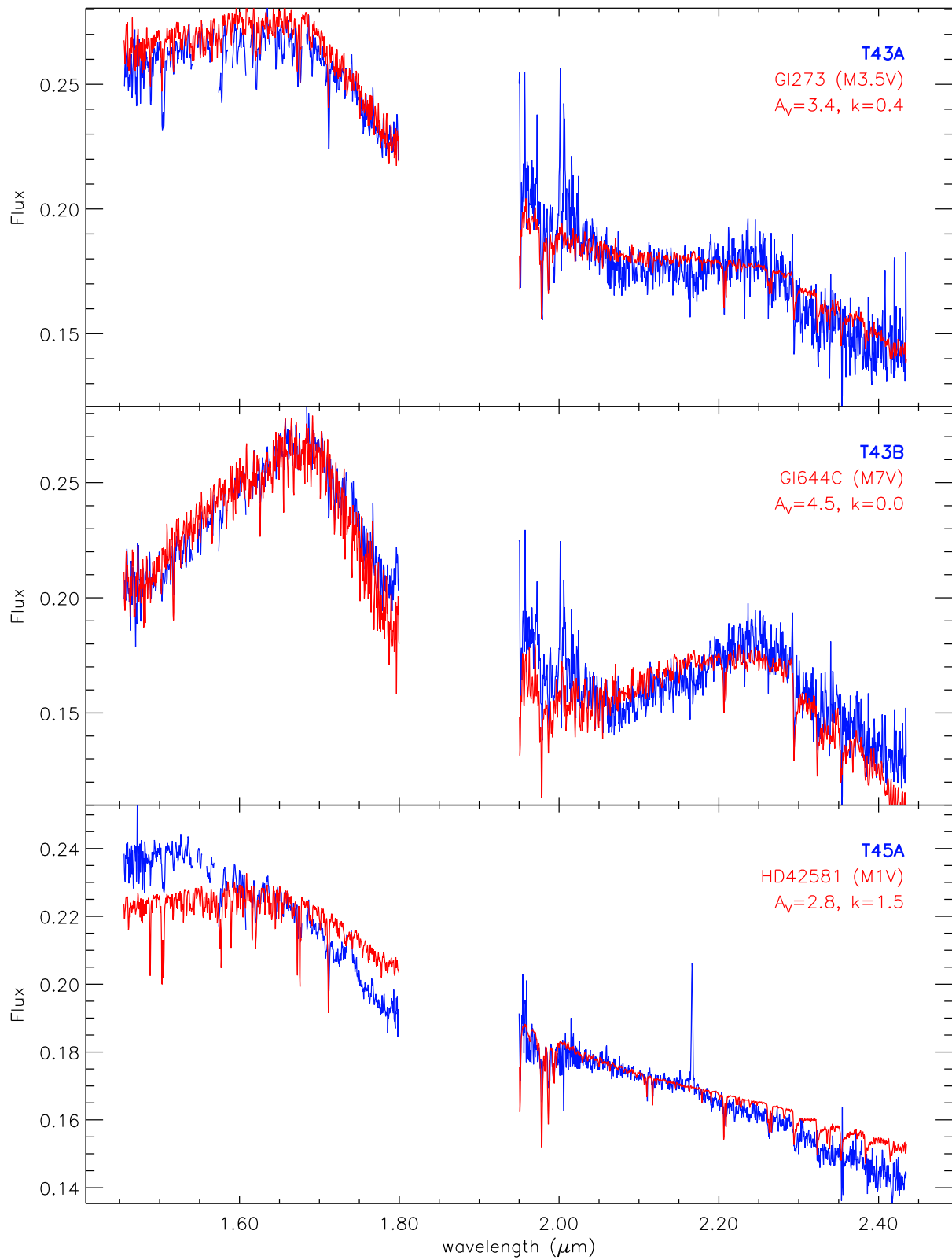


Figure B.2: (ctd.)

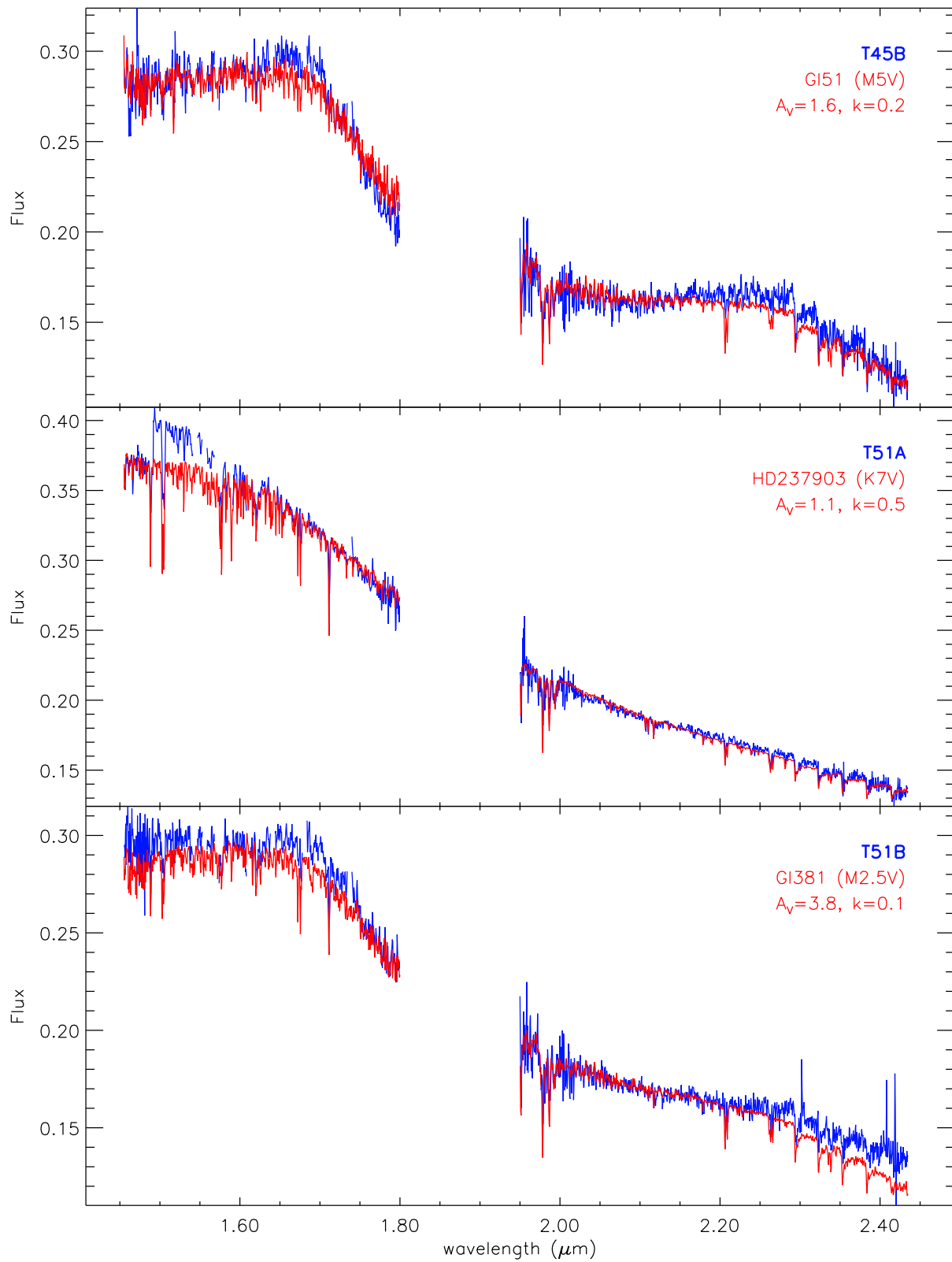


Figure B.2: (ctd.)

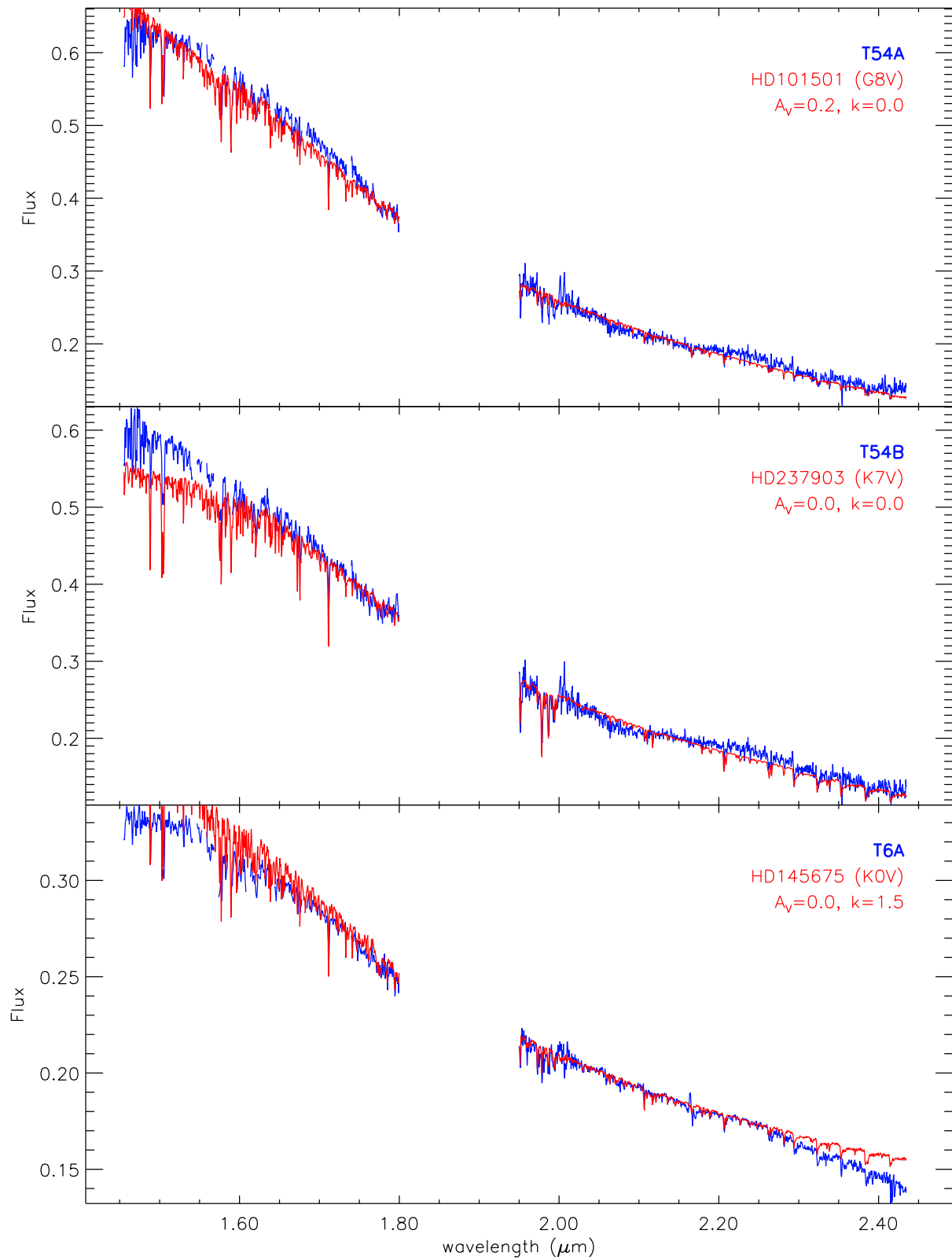


Figure B.2: (ctd.)

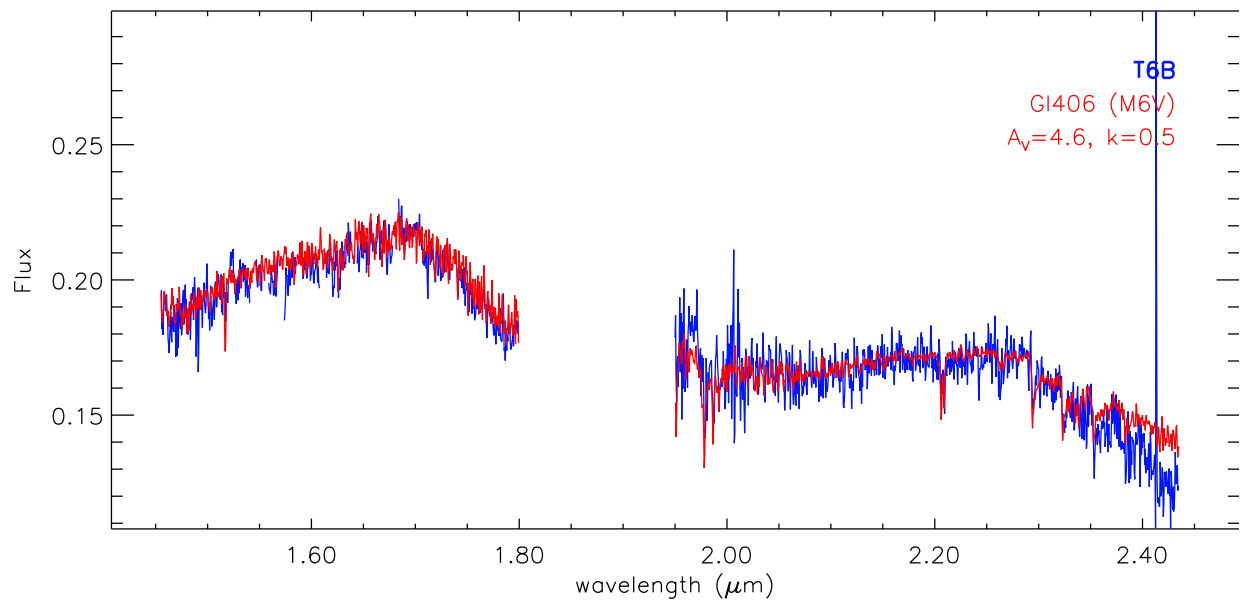


Figure B.2: (ctd.)

Bibliography

- Adams, E. R., Ciardi, D. R., Dupree, A. K., et al. 2012, *AJ*, 144, 42
- Alexander, R. D., Clarke, C. J., & Pringle, J. E. 2006, *MNRAS*, 369, 229
- Ali, B. & Depoy, D. L. 1995, *AJ*, 109, 709
- Andre, P., Ward-Thompson, D., & Barsony, M. 1993, *ApJ*, 406, 122
- Andrews, S. M. & Williams, J. P. 2005, *ApJ*, 631, 1134
- Andrews, S. M. & Williams, J. P. 2007, *ApJ*, 659, 705
- Antoniucci, S., García López, R., Nisini, B., et al. 2011, *A&A*, 534, 32
- Armitage, P. J., Clarke, C. J., & Tout, C. A. 1999, *MNRAS*, 304, 425
- Artymowicz, P. & Lubow, S. H. 1994, *ApJ*, 421, 651
- Artymowicz, P. & Lubow, S. H. 1996, *ApJ*, 467, L77
- Babcock, H. W. 1961, *ApJ*, 133, 572
- Bally, J. 2008, in *Handbook of Star Forming Regions, Volume I*, ed: B. Reipurth, 459
- Baraffe, I., Chabrier, G., Allard, F., & Hauschildt, P. H. 1998, *A&A*, 337, 403
- Barrado y Navascués, D. & Martín, E. L. 2003, *AJ*, 126, 2997
- Basri, G., Marcy, G. W., & Valenti, J. A. 1992, *ApJ*, 390, 622
- Bastian, U., Finkenzeller, U., Jaschek, C., & Jaschek, M. 1983, *A&A*, 126, 438
- Beck, T. L., Bary, J. S., & McGregor, P. J. 2010, *ApJ*, 722, 1360
- Beckers, J. M. 1988, *ESOC*, 30, 693
- Beckers, J. M. 1993, *ARA&A*, 31, 13
- Bertout, C., Basri, G., & Bouvier, J. 1988, *ApJ*, 330, 350

- Bessell, M. S. & Brett, J. M. 1988, *PASP*, 100, 1134
- Beuermann, K., Hessman, F. V., Dreizler, S., et al. 2010, *A&A*, 521, L60
- Bonnet, H., Abuter, R., Baker, A., et al. 2004, *The Messenger*, 117, 17
- Borrero, J. M. & Ichimoto, K. 2011, *Living Reviews in Solar Physics*, 8, 4
- Boss, A. P. 1997, *Science*, 276, 1836
- Bouvier, J., Alencar, S. H. P., Harries, T. J., Johns-Krull, C. M., & Romanova, M. M. 2007, in *Protostars and Planets V*, 479–494
- Bouwman, J., Lawson, W. A., Dominik, C., et al. 2006, *ApJ*, 653, L57
- Bouy, H., Kolb, J., Marchetti, E., et al. 2008, *A&A*, 477, 681
- Brandner, W., Alcalá, J. M., Kunkel, M., Moneti, A., & Zinnecker, H. 1996, *A&A*, 307, 121
- Brandner, W. & Zinnecker, H. 1997, *A&A*, 321, 220
- Cambresy, L., Epchtein, N., Copet, E., et al. 1997, *A&A*, 324, L5
- Carpenter, J. M. 2001, *AJ*, 121, 2851
- Carpenter, J. M., Hillenbrand, L. A., & Skrutskie, M. F. 2001, *AJ*, 121, 3160
- Carpenter, J. M., Hillenbrand, L. A., Skrutskie, M. F., & Meyer, M. R. 2002, *AJ*, 124, 1001
- Carpenter, J. M., Mamajek, E. E., Hillenbrand, L. A., & Meyer, M. R. 2006, *ApJ*, 651, L49
- Cederblad, S. 1946, *Meddelanden fran Lunds Astronomiska Observatorium Serie II*, 119, 1
- Chabrier, G., Baraffe, I., Allard, F., & Hauschildt, P. 2000, *ApJ*, 542, 464
- Cieza, L., Padgett, D. L., Stapelfeldt, K. R., et al. 2007, *ApJ*, 667, 308
- Cieza, L. A., Kessler-Silacci, J. E., Jaffe, D. T., Harvey, P. M., & Evans, N. J. 2005, *ApJ*, 635, 422
- Cieza, L. A., Padgett, D. L., Allen, L. E., et al. 2009, *ApJ*, 696, L84
- Clarke, C. J., Gendrin, A., & Sotomayor, M. 2001, *MNRAS*, 328, 485
- Close, L. M., Dutrey, A., Roddier, F., et al. 1998, *ApJ*, 499, 883
- Cohen, J. G., Persson, S. E., Elias, J. H., & Frogel, J. A. 1981, *ApJ*, 249, 481

- Comerón, F., Neuhäuser, R., & Kaas, A. A. 2000, *A&A*, 359, 269
- Correia, A. C. M., Udry, S., Mayor, M., et al. 2005, *A&A*, 440, 751
- Correia, S., Reipurth, B., Duchene, G., Zinnecker, H., Daemgen, S., et al. 2012, in prep.
- Correia, S., Zinnecker, H., Ratzka, T., & Sterzik, M. F. 2006, *A&A*, 459, 909
- Cox, A. N. 2000, *Allen's astrophysical quantities*, 4th edn. (New York: Springer)
- Cushing, M. C., Rayner, J. T., & Vacca, W. D. 2005, *ApJ*, 623, 1115
- Cutri, R. M., Skrutskie, M. F., van Dyk, S., et al. 2003, *VizieR Online Data Catalog*, 2246
- Da Rio, N., Robberto, M., Soderblom, D. R., et al. 2010, *ApJ*, 722, 1092
- Daemgen, S., Correia, S., & Petr-Gotzens, M. G. 2012, *A&A*, 540, 46
- Daemgen, S., Hormuth, F., Brandner, W., et al. 2009, *A&A*, 498, 567
- Daemgen, S., Petr-Gotzens, M., Correia, S., & et al. 2013, in prep.
- Daemgen, S., Siegler, N., Reid, I. N., & Close, L. M. 2007, *ApJ*, 654, 558
- Damjanov, I., Jayawardhana, R., Scholz, A., et al. 2007, *ApJ*, 670, 1337
- Davies, R. & Kasper, M. 2012, *ARA&A*, 50, 305
- Doyle, L. R., Carter, J. A., Fabrycky, D. C., et al. 2011, *Science*, 333, 1602
- Duchêne, G. 1999, *A&A*, 341, 547
- Duchêne, G. 2010, *ApJ*, 709, L114
- Duchêne, G., Monin, J.-L., Bouvier, J., & Ménard, F. 1999, *A&A*, 351, 954
- Dullemond, C. P. & Monnier, J. D. 2010, *ARA&A*, 48, 205
- Duquennoy, A. & Mayor, M. 1991, *A&A*, 248, 485
- Duschl, W. J., Gail, H.-P., & Tscharnuter, W. M. 1996, *A&A*, 312, 624
- Dutrey, A., Guilloteau, S., Duvert, G., et al. 1996, *A&A*, 309, 493
- Dutrey, A., Guilloteau, S., & Simon, M. 1994, *A&A*, 286, 149
- Duvert, G., Dutrey, A., Guilloteau, S., et al. 1998, *A&A*, 332, 867
- Eggenberger, A. & Udry, S. 2010, in *Planets in Binary Star Systems*, ed: N. Haghighipour, 1st edn., Vol. 366 (Berlin: Springer), 19

- Eggenberger, A., Udry, S., Chauvin, G., et al. 2007, *A&A*, 474, 273
- Eisenhauer, F., Abuter, R., Bickert, K., et al. 2003, *SPIE*, 4841, 1548
- Eisner, J. A., Monnier, J. D., Woillez, J., et al. 2010, *ApJ*, 718, 774
- Eisner, J. A., Plambeck, R. L., Carpenter, J. M., et al. 2008, *ApJ*, 683, 304
- Fedele, D., van den Ancker, M. E., Henning, T., Jayawardhana, R., & Oliveira, J. M. 2010, *A&A*, 510, 72
- Fischer, D. A. & Marcy, G. W. 1992, *ApJ*, 396, 178
- Fischer, D. A. & Valenti, J. 2005, *ApJ*, 622, 1102
- Folha, D. F. M. & Emerson, J. P. 2001, *A&A*, 365, 90
- Fried, D. L. 1965, *JOSA*, 55, 1427
- Fűrész, G., Hartmann, L. W., Megeath, S. T., Szentgyorgyi, A. H., & Hamden, E. T. 2008, *ApJ*, 676, 1109
- Gammie, C. F. 1996, *ApJ*, 457, 355
- Getman, K. V., Feigelson, E. D., Grosso, N., et al. 2005, *ApJSS*, 160, 353
- Ghez, A. M., McCarthy, D. W., Patience, J. L., & Beck, T. L. 1997, *ApJ*, 481, 378
- Glass, I. S. 1979, *MNRAS*, 187, 305
- Glindemann, A., Hippler, S., Berkefeld, T., & Hackenberg, W. 2000, *Experimental Astronomy*, 10, 5
- Goodwin, S. P., Kroupa, P., Goodman, A., & Burkert, A. 2007, *Protostars and Planets V*, 133
- Grankin, K. N., Melnikov, S. Y., Bouvier, J., Herbst, W., & Shevchenko, V. S. 2007, *A&A*, 461, 183
- Gullbring, E., Hartmann, L., Briceno, C., & Calvet, N. 1998, *ApJ*, 492, 323
- Günther, R. & Kley, W. 2002, *A&A*, 387, 550
- Haisch, K. E., Lada, E. A., & Lada, C. J. 2001, *ApJ*, 553, L153
- Harris, R. J., Andrews, S. M., Wilner, D. J., & Kraus, A. L. 2012, *ApJ*, 751, 115
- Hartigan, P., Edwards, S., & Ghandour, L. 1995, *ApJ*, 452, 736
- Hartigan, P. & Kenyon, S. J. 2003, *ApJ*, 583, 334

- Hartigan, P., Strom, K. M., & Strom, S. E. 1994, *ApJ*, 427, 961
- Hartmann, L. 1998, *Accretion Processes in Star Formation*, Cambridge astrophysics series No. 32 (Cambridge, UK; New York: Cambridge University Press)
- Hartmann, L. 2001, *AJ*, 121, 1030
- Hartmann, L., Avrett, E. H., Loeser, R., & Calvet, N. 1990, *ApJ*, 349, 168
- Hartmann, L., D'Alessio, P., Calvet, N., & Muzerolle, J. 2006, *ApJ*, 648, 484
- Herbig, G. H. 1960, *ApJSS*, 4, 337
- Herbig, G. H. 1962, *Advances in Astronomy and Astrophysics*, 1, 47
- Herbst, W., Herbst, D. K., Grossman, E. J., & Weinstein, D. 1994, *AJ*, 108, 1906
- Hillenbrand, L. A. 1997, *AJ*, 113, 1733
- Hillenbrand, L. A. 2005, in *A Decade of Discovery: Planets Around Other Stars*, ed: M. Livo, STScI Symposium Series No. 19
- Hillenbrand, L. A. & Carpenter, J. M. 2000, *ApJ*, 540, 236
- Hillenbrand, L. A., Strom, S. E., Calvet, N., et al. 1998, *AJ*, 116, 1816
- Holman, M. J. & Wiegert, P. A. 1999, *AJ*, 117, 621
- Ilgner, M. & Nelson, R. P. 2008, *A&A*, 483, 815
- Jeffries, R. D., Littlefair, S. P., Naylor, T., & Mayne, N. J. 2011, *MNRAS*, 1538
- Jensen, E. L. N. & Akeson, R. L. 2003, *ApJ*, 584, 875
- Jensen, E. L. N., Mathieu, R. D., & Fuller, G. A. 1996, *ApJ*, 458, 312
- Johnson, H. L. & Morgan, W. W. 1953, *ApJ*, 117, 313
- Jones, B. F. & Walker, M. F. 1988, *AJ*, 95, 1755
- Joy, A. H. 1945, *ApJ*, 102, 168
- Karo, D. P. & Schneiderman, A. M. 1978, *JOSA*, 68, 480
- Kenyon, S. J., Dobrzycka, D., & Hartmann, L. 1994, *AJ*, 108, 1872
- Kenyon, S. J. & Hartmann, L. 1995, *ApJSS*, 101, 117
- Kleinmann, S. G. & Hall, D. N. B. 1986, *ApJSS*, 62, 501
- Köhler, R., Petr-Gotzens, M. G., McCaughrean, M. J., et al. 2006, *A&A*, 458, 461

- Kraus, A. L. & Hillenbrand, L. A. 2009, *ApJ*, 704, 531
- Kraus, A. L., Ireland, M. J., Hillenbrand, L. A., & Martinache, F. 2012, *ApJ*, 745, 19
- Lada, C. J. 1987, in *Star forming regions*, IAUS No. 115 (Dordrecht: D. Reidel Publishing Co.), 1–17
- Lada, C. J. & Lada, E. A. 2003, *ARA&A*, 41, 57
- Lada, C. J., Muench, A. A., Haisch, K. E., et al. 2000, *AJ*, 120, 3162
- Lada, C. J., Muench, A. A., Luhman, K. L., et al. 2006, *AJ*, 131, 1574
- Lafrenière, D., Jayawardhana, R., Brandeker, A., Ahmic, M., & van Kerkwijk, M. H. 2008, *ApJ*, 683, 844
- Le Louarn, M., Foy, R., Hubin, N., & Tallon, M. 1998, *MNRAS*, 295, 756
- Lee, J. W., Kim, S.-L., Kim, C.-H., et al. 2009, *AJ*, 137, 3181
- Leinert, C., Zinnecker, H., Weitzel, N., et al. 1993, *A&A*, 278, 129
- Lenzen, R., Hartung, M., Brandner, W., et al. 2003, *SPIE*, 4841, 944
- Luhman, K. L. 2004, *ApJ*, 602, 816
- Luhman, K. L. 2007, *ApJSS*, 173, 104
- Luhman, K. L. 2008, in *Handbook of Star Forming Regions, Volume II*, ed: B. Reipurth, 169
- Luhman, K. L., Allen, L. E., Allen, P. R., et al. 2008, *ApJ*, 675, 1375
- Luhman, K. L., Allen, P. R., Espaillat, C., Hartmann, L., & Calvet, N. 2010, *ApJSS*, 189, 353
- Luhman, K. L., Stauffer, J. R., Muench, A. A., et al. 2003, *ApJ*, 593, 1093
- Luhman, K. L., Wilson, J. C., Brandner, W., et al. 2006, *ApJ*, 649, 894
- Lynden-Bell, D. & Pringle, J. E. 1974, *MNRAS*, 168, 603
- Mann, R. K. & Williams, J. P. 2009, *ApJ*, 694, L36
- Mann, R. K. & Williams, J. P. 2010, *ApJ*, 725, 430
- Marchetti, E., Brast, R., Delabre, B., et al. 2007, *The Messenger*, 129, 8
- Marchetti, E., Hubin, N. N., Fedrigo, E., et al. 2003, *SPIE*, 4839, 317

- Marks, M. & Kroupa, P. 2012, *A&A*, 543, 8
- McCabe, C., Ghez, A. M., Prato, L., et al. 2006, *ApJ*, 636, 932
- McCaughrean, M. J. & O'dell, C. R. 1996, *AJ*, 111, 1977
- McCaughrean, M. J. & Stauffer, J. R. 1994, *AJ*, 108, 1382
- McKee, C. F. & Ostriker, E. C. 2007, *ARA&A*, 45, 565
- Menten, K. M., Reid, M. J., Forbrich, J., & Brunthaler, A. 2007, *A&A*, 474, 515
- Meyer, M. R., Calvet, N., & Hillenbrand, L. A. 1997, *AJ*, 114, 288
- Mohanty, S., Jayawardhana, R., & Basri, G. 2005, *ApJ*, 626, 498
- Monin, J.-L., Clarke, C. J., Prato, L., & McCabe, C. 2007, *Protostars and Planets V*, 395
- Monnier, J. D., Tannirkulam, A., Tuthill, P. G., et al. 2008, *ApJ*, 681, L97
- Muench, A. A., Lada, E. A., Lada, C. J., & Alves, J. 2002, *ApJ*, 573, 366
- Mugrauer, M. & Neuhäuser, R. 2009, *A&A*, 494, 373
- Muterspaugh, M. W., Lane, B. F., Kulkarni, S. R., et al. 2010, *AJ*, 140, 1657
- Muzerolle, J., Calvet, N., Hartmann, L., & D'Alessio, P. 2003, *ApJ*, 597, L149
- Muzerolle, J., Hartmann, L., & Calvet, N. 1998a, *AJ*, 116, 2965
- Muzerolle, J., Hartmann, L., & Calvet, N. 1998b, *AJ*, 116, 455
- Natta, A., Grinin, V., & Mannings, V. 2000, *Protostars and Planets IV*, 559
- Natta, A., Testi, L., & Randich, S. 2006, *A&A*, 452, 245
- Nguyen, D. C., Brandeker, A., van Kerkwijk, M. H., & Jayawardhana, R. 2012, *ApJ*, 745, 119
- Nguyen, D. C., Scholz, A., van Kerkwijk, M. H., Jayawardhana, R., & Brandeker, A. 2009, *ApJ*, 694, L153
- O'Dell, C. R. & Wen, Z. 1994, *ApJ*, 436, 194
- O'Dell, C. R., Wen, Z., & Hu, X. 1993, *ApJ*, 410, 696
- Olczak, C., Pfalzner, S., & Spurzem, R. 2006, *ApJ*, 642, 1140
- Osterloh, M. & Beckwith, S. V. W. 1995, *ApJ*, 439, 288
- Padgett, D. L., Strom, S. E., & Ghez, A. 1997, *ApJ*, 477, 705

- Palla, F. & Stahler, S. W. 1999, *ApJ*, 525, 772
- Pallavicini, R., Golub, L., Rosner, R., et al. 1981, *ApJ*, 248, 279
- Papaloizou, J. & Pringle, J. E. 1977, *MNRAS*, 181, 441
- Petr, M. 1998, Ph.D. Thesis, University of Heidelberg
- Petr, M. G., Coude Du Foresto, V., Beckwith, S. V. W., Richichi, A., & McCaughrean, M. J. 1998, *ApJ*, 500, 825
- Petr-Gotzens, M. G. & Daemgen, S. 2012, in prep.
- Petr-Gotzens, M. G., Sterzik, M. F., Köhler, R., et al. 2008, *JPhCS*, 131, 2026
- Pollack, J. B., Hubickyj, O., Bodenheimer, P., et al. 1996, *Icarus*, 124, 62
- Prato, L., Greene, T. P., & Simon, M. 2003, *ApJ*, 584, 853
- Prato, L. & Simon, M. 1997, *ApJ*, 474, 455
- Prosser, C. F., Stauffer, J. R., Hartmann, L., et al. 1994, *ApJ*, 421, 517
- Qian, S.-B., Liao, W.-P., Zhu, L.-Y., & Dai, Z.-B. 2010a, *ApJ*, 708, L66
- Qian, S.-B., Liao, W.-P., Zhu, L.-Y., et al. 2010b, *MNRAS*, 401, L34
- Qian, S.-B., Liu, L., Liao, W.-P., et al. 2011, *MNRAS*, 414, L16
- Rabien, S., Ageorges, N., Barl, L., et al. 2010, *SPIE*, 7736, 12
- Raghavan, D., McAlister, H. A., Henry, T. J., et al. 2010, *ApJSS*, 190, 1
- Rasio, F. A. 1994, *ApJ*, 427, L107
- Rayner, J. T., Cushing, M. C., & Vacca, W. D. 2009, *ApJSS*, 185, 289
- Reiners, A. 2012, *Living Reviews in Solar Physics*, 9, 1
- Reipurth, B. 2008, *Handbook of Star Forming Regions, Volume I: the Northern Sky*, ASP Monograph Publications
- Reipurth, B., Guimarães, M. M., Connelley, M. S., & Bally, J. 2007, *AJ*, 134, 2272
- Robberto, M., Ricci, L., Da Rio, N., & Soderblom, D. R. 2008, *ApJ*, 687, L83
- Robberto, M., Soderblom, D. R., Scandariato, G., et al. 2010, *AJ*, 139, 950
- Robberto, M., Song, J., Mora Carrillo, G., et al. 2004, *ApJ*, 606, 952

- Robitaille, T. P., Whitney, B. A., Indebetouw, R., Wood, K., & Denzmore, P. 2006, *ApJSS*, 167, 256
- Roell, T., Neuhäuser, R., Seifahrt, A., & Mugrauer, M. 2012, *A&A*, 542, 92
- Rousset, G., Lacombe, F., Puget, P., et al. 2003, *SPIE*, 4839, 140
- Rucinski, S. M. 1985, *AJ*, 90, 2321
- Saffe, C., Gómez, M., Randich, S., et al. 2003, *A&A*, 409, 993
- Sato, S., Okita, K., Yamashita, T., et al. 1992, *ApJ*, 398, 273
- Sauvage, J.-F., Fusco, T., Petit, C., et al. 2010, *SPIE*, 7736, 13
- Schmidt, T. O. B., Neuhäuser, R., Seifahrt, A., et al. 2008, *A&A*, 491, 311
- Schmidt-Kaler, T. 1982, in *Landolt-Bornstein*, Vol. 2, Group VI (Berlin: Springer), 453
- Shu, F. H., Adams, F. C., & Lizano, S. 1987, *ARA&A*, 25, 23
- Siess, L., Dufour, E., & Forestini, M. 2000, *A&A*, 358, 593
- Simon, M., Close, L. M., & Beck, T. L. 1999, *AJ*, 117, 1375
- Simon, M., Ghez, A. M., Leinert, C., et al. 1995, *ApJ*, 443, 625
- Skemer, A. J., Close, L. M., Greene, T. P., et al. 2011, *ApJ*, 740, 43
- Teixeira, R., Ducourant, C., Sartori, M. J., et al. 2000, *A&A*, 361, 1143
- The Big Bang Theory. 2009, "The work song nanocluster", CBS, Warner Bros., 2009
- Tobin, J. J., Hartmann, L., Furesz, G., Mateo, M., & Megeath, S. T. 2009, *ApJ*, 697, 1103
- Tohline, J. E. 2002, *ARA&A*, 40, 349
- Tristram, K. R. W. & Prieto, M. A. 2005, in *Science with Adaptive Optics*, eds: W. Brander, M. E. Kasper (Berlin: Springer), 79
- van der Blik, N. S., Manfroid, J., & Bouchet, P. 1996, *A&AS*, 119, 547
- Vicente, S. M. & Alves, J. 2005, *A&A*, 441, 195
- Vogt, N., Schmidt, T. O. B., Neuhäuser, R., et al. 2012, arXiv:1204.3332
- Wall, J. V. 1996, *QJRAS*, 37, 519
- White, R. J. & Ghez, A. M. 2001, *ApJ*, 556, 265
- Whittet, D. C. B., Prusti, T., Franco, G. A. P., et al. 1997, *A&A*, 327, 1194

Wilking, B. A., Greene, T. P., & Meyer, M. R. 1999, *AJ*, 117, 469

Williams, J. P. & Cieza, L. A. 2011, *ARA&A*, 49, 67

Wizinowich, P. L., Le Mignant, D., Bouchez, A. H., et al. 2006, *PASP*, 118, 297

Wu, Y. & Murray, N. 2003, *ApJ*, 589, 605

Wyatt, M. C. 2008, *ARA&A*, 46, 339

Zhu, Z., Hartmann, L., & Gammie, C. 2010, *ApJ*, 713, 1143

Acknowledgements

This thesis is not the achievement of a single person. Many people helped me to accomplish the present work and accompanied me through my time as a PhD student. Since this thesis would not exist without them, I would like to take the opportunity to say *thank you*.

My deepest gratitude goes to my supervisor Monika Petr-Gotzens for the amazing support she was giving me throughout my thesis. She was always available to discuss the latest results and found always the right balance between providing guidance and giving me freedom to gain experience and develop my personal scientific style. I couldn't have wished for a better supervisor in any way. Further, I would like to thank Thomas Preibisch for taking responsibility as my thesis supervisor and for his helpful new ideas regarding any topic that I brought up to him. Special thanks go to Paula Teixeira for being my Mentor at ESO. Whenever I walked into her office she had an open ear and helpful answers to my questions, be it about science or anything else. Even after she left ESO, she was there to help me whenever she could. Thanks also to Eva Schmalzl, Steve Longmore, Peter Scicluna, and Eli Bressert for valuable comments to the manuscript.

My stay at ESO was one of the best experiences in my life. This is the result of the wonderful people that I met there and who accompanied me in calm and busy times. While essentially all students and fellows of ESO contributed to making my time as a PhD student such an enjoyable experience – too many to name them all – there are a few people that I would like to particularly thank: Thank you, Alma Ruiz Velasco, for becoming and being my friend. Camilla Juul Hansen, thank you for not only for getting me started into the adventurous world of the IMPRS but also for the good times that we had inside and outside of ESO. Further, I would like to thank Alex Böhnert for the good company during many bike rides and tea breaks, as well as Ulf Seemann and Matthias Frank for always being up for an amusing intermezzo. ESO was not the same after you left.

A vital part of my astronomical education is rooted in the offers by the International Max-Planck Research School (IMPRS). However, it is not only the school itself which I owe many thanks, but it is in particular my marvelous colleagues in the team of IMPRS student representatives. Thank you Camilla, Victor, Francesco, Henrike, Rob, Dominika, and Johannes for getting involved in the IMPRS organization with so much effort. Together, we were able to make the IMPRS in Munich even more pleasant for all participants.

I owe many thanks to my parents for their continuous support and for giving me the opportunity to pursue my favorite goal: becoming an astronomer. Finally, I would like to thank Susanne Kratzat for her love and support over all these past years. Her backing gave me relief in busy times and her cheerfulness is what will keep me going in the future.

Curriculum Vitae

Personal Data

Sebastian Daemgen

Date of birth: July 10, 1982

Nationality: German

Education

PhD in Astronomy	European Southern Observatory (ESO) Garching and Ludwig-Maximilians-University Munich, Germany. <i>Advisor: Dr. Monika Petr-Gotzens</i> <i>Thesis: The evolution of protoplanetary disks in binary systems</i>	Aug 09 – Oct 12
Diplom (=Master equivalent)	Ruprecht-Karls University of Heidelberg and Max-Planck Institute for Astronomy (MPIA), Heidelberg, Germany. <i>Advisor: Dr. Wolfgang Brandner</i> <i>Thesis: Detection and Characterization of Extra Solar Planets and Their Host Stars</i>	Oct 02 – Dec 08

Professional Experience

IMPRS Garching	International Max-Planck Research School at the European Southern Observatory, Graduate Student	Aug 09 – Aug 12
ESO Garching	DGDF scientific visitor with Dr. Monika Petr-Gotzens	Feb 09 – Jul 09
MPIA Heidelberg	Diplom (=Masters equivalent) supervised by Dr. Wolfgang Brandner	Dec 07 – Dec 08
Steward Observatory, University of Arizona	Visiting student with Dr. Laird Close	Aug 05 – Jun 06
Landessternwarte Heidelberg	Summer student with Dr. Stefan Wagner	Jul 04 – Sep 04

Honors/Fellowships

Graduate Research Fellowship	International Max-Planck Research School (IMPRS)	Aug 09 – Aug 12
Study Scholarship	Study Scholarship for Graduates and Advanced Students of All Disciplines in the academic year 2005 – 2006, Deutscher Akademischer Austauschdienst (DAAD)	Aug 05 – Jul 06
Undergraduate Scholarship	Scholarship of the online career network e-fellows.net	May 04 – Feb 09

Public Outreach

- “Ask an astronomer”, ESO Girls Day 2011
- Astronomers meet the public, Odeonsplatz, Munich, part of the event “100h of Astronomy” in the Year of Astronomy 2009
- The Lunar Eclipse 2008 live at the MPIA, public event, Heidelberg, 2008
- Guide for diverse tours through the MPIA institute, including talks about general astronomy for amateur astronomers and highschool students, 2008

Scientific Activities

- Representative of the students in the International Max-Planck Research School Garching
- Member of the local organizing committee of the conference *Formation and Early Evolution of Very Low Mass Stars and Brown Dwarfs*, ESO Garching, October 2011
- Assistant in the ESO observing proposal selection process, Nov 2009 & May 2011
- Organizer of weekly ESO student science coffee meeting
- member of the German Physical Society (DPG)

Invited Talks

- | | |
|--|--------------|
| • ETH Institute for Astronomy, Zurich, Switzerland | Nov 18, 2011 |
| • Institute for Astronomy at the University of Tübingen, Germany | Nov 07, 2011 |
| • Max-Planck Institute for Astronomy (MPIA), Heidelberg, Germany | Feb 09, 2011 |
| • European Southern Observatory (ESO), Garching, Germany | Aug 21, 2010 |

Participation in International Conferences

- VLMS2011, *Formation and Early Evolution of Very Low Mass Stars and Brown Dwarfs*, Garching, Germany, 2011
- IAUS282, *From Interacting Binaries to Exoplanets: Essential Modeling Tools*, Tatranska Lomnica, Slovakia, 2011

- Cool Stars XVI, *16th Cambridge Workshop on Cool Stars, Stellar Systems, and the Sun*, Seattle, WA, 2010
- *Putting Our Solar System in Context: Origin, Dynamical and Physical Evolution of Multiple Planet Systems*, Obergurgl, Austria, 2010
- *From Circumstellar Disks to Planetary Systems*, Garching, Germany, 2009
- Cool Stars XV, *15th Cambridge Workshop on Cool Stars, Stellar Systems, and the Sun*, St. Andrews, Scotland 2008

Refereed Publications

8. **Daemgen, S.** et al. 2012, *Protoplanetary Disks of TTauri Binaries in Chamaeleon I*, in prep.
7. Bergfors, C.; Brandner, W.; **Daemgen, S.**; Hippler, S.; Janson, M.; Kudryavtseva, N.; Geissler, K.; Henning, T. 2011, *Stellar Companions to Exoplanet Host Stars: Lucky Imaging of Transiting Planet Hosts*, submitted to MNRAS
6. Janson, M.; Hormuth, F.; Bergfors, C.; Brandner, W.; Hippler, S.; **Daemgen, S.** et al. 2012, *The AstraLux Large M-dwarf Multiplicity Survey*, ApJ, 754, 44
5. **Daemgen, S.**; Correia, S.; Petr-Gotzens, M. G. 2011, *Protoplanetary Disks of TTauri Binaries in Orion*, A&A, 540, 46
4. Bergfors, C.; Brandner, W.; Janson, M.; **Daemgen, S.**; Geissler, K.; Henning, T.; Hippler, S.; Hormuth, F.; Joergens, V.; Köhler, R. 2010, *Lucky Imaging survey for southern M dwarf binaries*, A&A, 520, 54
3. Schnupp, C.; Bergfors, C.; Brandner, W.; **Daemgen, S.**; Fischer, D.; Marcy, G.; Henning, Th.; Hippler, S.; Janson, M. 2010, *Discovery of a stellar companion to the nearby solar-analogue HD 104304*, A&A, 516, 21
2. **Daemgen, S.**; Hormuth, F.; Brandner, W.; Bergfors, C.; Janson, M.; Hippler, S.; Henning, T. 2009, *Binarity of transit host stars. Implications for planetary parameters*, A&A, 498, 567.
1. **Daemgen, S.**; Siegler, N.; Reid, I.N.; Close, L.M. 2007, *Discovery of Nine New Companions to Nearby Young M Stars with the Altair AO System*, ApJ, 654, 558.

Other Publications

7. **Daemgen, S.**; Petr-Gotzens, M. G.; Correia, S. 2011, *TTauri Binaries in Orion: evidence for accelerated and synchronized disk evolution*, IAU Symposium, 282, 452.
6. **Daemgen, S.**; Petr-Gotzens, M. G.; Correia, S. 2011, *Protoplanetary Disks of Binary Systems in Orion*, APSC, 448, 589.
5. Petr-Gotzens, M. G.; **Daemgen, S.**; Correia, S. 2010, *Proto-Planetary Disks of T Tauri Binaries in Orion: Prospects for Planet Formation*, ASPC, 435, 429.
4. Schnupp, C.; Brandner, W.; Bergfors, C.; Geissler, K. G.; **Daemgen, S.**; Hippler, S.; Hormuth, F.; Lenzen, R.; Henning, T.; Janson, M.; Pantin, E. 2010, *Characterization of Exoplanet Atmospheres in the Solar Neighbourhood with E-ELT/METIS*, ASPC, 430, 534.
3. Bergfors, C.; Brandner, W.; Janson, M.; Kudryavtseva, N.; **Daemgen, S.**; Hippler, S.; Hormuth, F.; Henning, T. 2010, *Towards Astrometric Detection of Neptune- to Earth-Mass Planets around M-Stars*, ASPC, 430, 405.
2. Hippler, S.; Bergfors, C.; Brandner, W.; **Daemgen, S.**; Henning, T.; Hormuth, F.; Huber, A.; Janson, M.; Rochau, B.; Rohloff, R.; Wagner, K. 2009, *The AstraLux Sur Lucky Imaging Instrument at the NTT*, Messenger 137, 14.
1. **Daemgen, S.**; Hormuth, F.; Janson, M.; Brandner, W.; Meyer, E.; Hippler, S.; Henning, T. 2009, *High-Resolution Imaging of Transiting Exoplanet Host Stars with AstraLux*, AIPC, 1094, 433.